# Functional Nanomaterials for Electrochemical Energy Storage in Supercapacitors

*A Thesis*

*Submitted in Partial Fulfillment of the Requirements for the Degree of*

**DOCTOR OF PHILOSOPHY**

*By*

**Bhaskar Jyoti Choudhury**


**School of Energy Science and Engineering**

**Indian Institute of Technology Guwahati**

Guwahati –781039, India

November 2022

*Dedicated*

*to*

*My Parents and Mentor*

**School of Energy Science and Engineering**
**Indian Institute of Technology Guwahati**
**Guwahati –781039, India**

# STATEMENT

I do hereby declare that the content embodied in this thesis entitled "**Functional Nanomaterials for Electrochemical Energy Storage in Supercapacitors**" is the result of investigations carried out by me in the School of Energy Science and Engineering, Indian Institute of Technology Guwahati under the guidance of Prof. Vijayanand S. Moholkar.

In keeping with the general practice of reporting scientific observations, due acknowledgments have been made wherever the work described is based on the findings of other investigators.

November, 2022

**Bhaskar Jyoti Choudhury**
**(Roll No: 166151010)**

**School of Energy Science and Engineering**
**Indian Institute of Technology Guwahati**
**Guwahati –781039, India**

# CERTIFICATE

It is certified that the work contained in the thesis entitled "**Functional Nanomaterials for Electrochemical Energy Storage in Supercapacitors**", by **Bhaskar Jyoti Choudhury** (Roll No: 166151010), has been carried out under my supervision in the School of Energy Science and Engineering, Indian Institute of Technology Guwahati and that this work has not been submitted elsewhere for a degree.

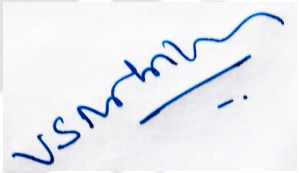

November, 2022

**Prof. Vijayanand S. Moholkar**
HAG Professor
Department of Chemical Engineering and
School of Energy Science and Engineering
Indian Institute of Technology, Guwahati
Guwahati – 781 039
Assam, India

# ACKNOWLEDGEMENTS

This thesis marks the end of my cherished memories at IIT Guwahati. Is gives me immense pleasure to express my deepest gratitude to everyone who made this possible and constantly encouraged me during my research work.

First and foremost, I express my deep sense of gratitude to my thesis supervisor ***Prof. Vijayanand S. Moholkar*** for his valuable suggestions, encouragement and constant support throughout my research work. He has provided an intriguing environment to work with freedom which cultivated my interest towards the topic. His illustrious guidance and effusive co-operation, encouraging interactions has always been a driving force for me in this project.

I would like to acknowledge my sincere gratitude to my doctoral committee members, ***Prof. T Punniyamurthy***, ***Prof. Vinayak Kulkarni***, and ***Dr. Harsh Chaturvedi*** for their insightful advices and suggestions throughput the research.

I am grateful to the faculty and staff members of School of Energy Science and Engineering for their constant help and support. I would like to acknowledge School of Energy Science and Engineering, Department of Chemical Engineering and Central Instruments Facilities (CIF) for providing various analytical facilities to carry out my research work. I am also thankful to the Indian Institute of Technology Guwahati for providing me with the state of the art infrastructure for advance level of research.

I would like to acknowledge North East Institute of Science and Technology (NEIST), Jorhat for providing required XPS analytical facility. I also acknowledge the CHNS elemental analysis facility provided by the Central Instrumentation Facility of the Indian Institutes of Science Education and Research (IISER) Bhopal and Guwahati Biotech Park.

I am thankful to my seniors (*Dr. Debarshi Mallick, Dr. Ritesh Malani, Dr. Arup Bora, Dr. Kuldeep Roy, Dr, Amit Batghare, Dr. Neha Singh, Dr. Niharika Kashyap and Dr. Philip Sainik*) for their valuable suggestions. I extend my thanks and gratitude to my colleagues (*Kajal, Udangshree, Karan, Debarshi da, Aradhana, Pushpita, Rishiraj,*

*Avinash, Komal, Umesh, Prabhutosh, Rajkumar*) for their help and enthusiastic company. I am thankful to my special friends *Sukumar, Chiranjeev and Ratnadeep* for their precious companionship and support throughout this journey.

My final words go to my beloved family for their support, care, and encouragement. I am highly indebted to my ***Maa-Deuta***, ***Mahi*** and ***Abu*** whose their endless love and blessing has made me come this far.

**Bhaskar Jyoti Choudhury**

# ABSTRACT

Energy storage systems are essential for the practical implementation of renewable energy systems because the majority of renewable energy sources are intermittent in nature. Supercapacitors (SCs) are one of the most promising energy storage devices owing to their performance characteristics, viz. high power density, rapid charge–discharge, and ultra-long cycle life. However, their usage is significantly limited by the drawbacks of low energy density. The main aim of this work is to develop advanced electrode materials for supercapacitors with improved energy density while maintaining high power density and long cycle life. This thesis reports investigations on the synthesis of four electrode materials for supercapacitors, including nanocomposites ($Fe_3O_4$/rGO and MWCNT/$MnO_2$/rGO), and carbon materials (rGO and PC–*x*). The two nanocomposites were synthesized by facile ultrasound–assisted synthesis methods. The reduced graphene oxide (rGO) was synthesized via chemical reduction of highly oxidized graphene oxide. Lastly, oxygen-enriched porous carbon (PC–*x*) was prepared by co–pyrolysis and KOH activation process from a ternary blend of biomass. These materials have been extensively characterized using standard techniques and the electrochemical performances were investigated using cyclic voltammetry (CV), galvanostatic charge-discharge (GCD), and electrochemical impedance spectrometry (EIS) techniques. The fabricated supercapacitors have been demonstrated to possess excellent electrochemical properties as follows: (1) The $Fe_3O_4$/rGO based all–solid–state supercapacitor with PVA/KOH polymer–gel electrolyte exhibited an energy density of 8.46 W h $kg^{-1}$ at a power density of 338 W $kg^{-1}$. Ternary MWCNT/$MnO_2$/rGO nanocomposite based supercapacitor with commercial–level mass loading (~12 mg $cm^{-2}$) demonstrated high specific capacitance (314.6 F $g^{-1}$ at 5 mV $s^{-1}$), energy density (21.2 W h $kg^{-1}$ at 150 W $kg^{-1}$) and excellent cycle stability at a wide cell voltage of 1.5 V in 1 M $Na_2SO_4$ electrolyte. (2) The rGO based aqueous supercapacitors (rGO–SCs) with commercial–level electrode mass loadings achieved energy densities of 15.39 W h $kg^{-1}$ (at 180 W $kg^{-1}$, 1.8 V), 21.42 W h $kg^{-1}$ (at 180 W $kg^{-1}$, 1.8 V), and 22.87 W h $kg^{-1}$ (at 210 W $kg^{-1}$, 2.1 V) in 1 M $Li_2SO_4$, redox–additive electrolyte (0.1 M $Na_2MoO_4$ + 1 M $Li_2SO_4$), and water–in–salt (11 M $NaNO_3$) electrolyte, respectively. (3) Oxygen–enriched porous carbon (PC–*x*) based aqueous supercapacitors with commercial–level mass loadings

exhibited an energy density of 22.75 W h $kg^{-1}$ (at 200 W $kg^{-1}$, 2 V) and 96.8% capacitance retention over 10000 cycles in 1 M $Li_2SO_4$. The energy density of the device was enhanced to 37.24 W h $kg^{-1}$ (at 200 W $kg^{-1}$, 2 V) in a redox–additive electrolyte (0.1 M $Na_2MoO_4$ + 1 M $Li_2SO_4$). On a whole, the results of this thesis have demonstrated the efficacy of the fabricated supercapacitors with concurrent high energy and power densities. Therefore, these materials have tremendous potential for the development of high-performance supercapacitors for commercial applications.

# CONTENTS


**Contents** i

**List of Tables** v

**List of Figures** vii

**Abbreviations** xix

**Chapter 1 Introduction and Literature Review**

1.1 Introduction 1

1.2 Supercapacitor Fundamentals 4

1.2.1 Classification of Supercapacitors 4

1.2.2 Charge Storage Mechanism of EDLCs 5

1.2.2.1 Helmholtz model 7

1.2.2.2 Gouy-Chapman or diffuse model 7

1.2.2.3 Stern model 7

1.2.3 Charge Storage Mechanism of Pseudocapacitors 9

1.3 Components of Supercapacitors 10

1.3.1 Electrode 10

1.3.2 Electrolyte 11

1.3.3 Separator 13

1.3.4 Current collector 13

1.4 Electrochemical Evaluation of Supercapacitors 13

1.4.1 Calculation of Capacitive Parameters 14

1.5 Electrode Materials for Supercapacitors 16

1.5.1 Carbon Materials 16

1.5.1.1 Activated carbon (AC) 16

1.5.1.2 Graphene 19

1.5.1.3 Carbon nanotubes (CNTs) 22

1.5.2 Metal Oxides 25

1.5.2.1 Ruthenium dioxide ($RuO_2$) 26

1.5.2.2 Manganese dioxide ($MnO_2$) 27

1.5.2.3 Iron oxide ($Fe_3O_4$) 30

1.5.3 Conducting Polymers (CPs) 33

| | | |
|---|---|---|
| | 1.5.4 Composite Materials | 35 |
| 1.6 | Aim, Approach and Scope of the Present Thesis | 39 |
| 1.7 | Thesis Outline | 40 |
| | References | 42 |
| **Chapter 2** | **Improvement of Supercapacitor Performance through Enhanced Interfacial Interactions Induced by Sonication** | |
| 2.1 | Introduction | 59 |
| 2.2 | Experimental Section | 61 |
| | 2.2.1 Materials | 61 |
| | 2.2.2 Synthesis of Reduced Graphene Oxide (rGO) | 61 |
| | 2.2.3 Synthesis of $Fe_3O_4$ Nanoparticles | 62 |
| | 2.2.4 Synthesis of $Fe_3O_4$/rGO Nanocomposite | 62 |
| | 2.2.5 Characterization Techniques | 63 |
| | 2.2.6 Fabrication of Symmetric All-Solid-State Supercapacitor | 63 |
| | 2.2.7 Electrochemical Measurements | 64 |
| 2.3 | Results and Discussion | 65 |
| | 2.3.1 Physicochemical Characterization | 65 |
| | 2.3.2 Electrochemical Performance | 74 |
| 2.4 | Conclusions | 82 |
| | References | 83 |
| **Chapter 3** | **Ultrasound-Assisted One-Pot Synthesis of Ternary MWCNT/$MnO_2$/rGO Nanocomposite for Supercapacitors with Commercial-Level Mass Loadings** | |
| 3.1 | Introduction | 89 |
| 3.2 | Experimental Section | 92 |
| | 3.2.1 Materials | 92 |
| | 3.2.2 Synthesis of Ternary MWCNT/$MnO_2$/rGO Nanocomposite | 92 |
| | 3.2.3 Synthesis of $MnO_2$/MWCNT and $MnO_2$/rGO Nanocomposites | 93 |
| | 3.2.4 Characterization Techniques | 93 |
| | 3.2.5 Electrochemical Measurements | 93 |

| | | |
|---|---|---|
| 3.3 | Results and Discussion | 94 |
| | 3.3.1 Materials Characterization | 94 |
| | 3.3.2 Electrochemical Performance | 101 |
| | 3.3.3 Physical Explanation for the Influence of Ultrasound | 112 |
| 3.4 | Conclusions | 113 |
| | References | 114 |
| **Chapter 4** | **Improved Energy Density of Reduced Graphene Oxide based Aqueous Symmetric Supercapacitors in Redox–Active and Water–in–Salt Electrolytes** | |
| 4.1 | Introduction | 121 |
| 4.2 | Experimental Section | 125 |
| | 4.2.1 Materials | 125 |
| | 4.2.2 Electrochemical Measurements | 126 |
| 4.3 | Results and Discussion | 127 |
| | 4.3.1 Physicochemical Characterization of rGO | 127 |
| | 4.3.2 Electrochemical Performance in Acidic, Alkaline, and Neutral Aqueous Electrolytes | 129 |
| | 4.3.2.1 Three–electrode cell characterization of rGO electrodes | 129 |
| | 4.1.1.1 Electrochemical performance of rGO–based symmetric supercapacitors | 134 |
| | 4.3.3 Electrochemical Performance in Redox–Active Electrolyte | 139 |
| | 4.3.3.1 Three–electrode cell characterization of rGO electrodes | 139 |
| | 4.3.3.2 Electrochemical performance of rGO–based symmetric supercapacitors | 140 |
| | 4.3.4 Electrochemical performance in “water–in–salt” or WIS electrolyte | 144 |
| | 4.3.4.1 Three–electrode cell characterization of rGO electrodes | 144 |
| | 4.3.4.2 Electrochemical performance of rGO–based symmetric supercapacitors | 145 |

| | | |
|---|---|---|
| 4.4 | Conclusions | 148 |
| | References | 149 |
| **Chapter 5** | **Biomass Blend derived Porous Carbon for Aqueous Supercapacitors with Commercial-Level Mass Loadings and Enhanced Energy Density in Redox-Active Electrolyte** | |
| 5.1 | Introduction | 155 |
| 5.2 | Experimental Section | 157 |
| | 5.2.1 Material Synthesis | 157 |
| | 5.2.2 Characterization Techniques | 159 |
| | 5.2.3 Electrochemical Measurements | 159 |
| 5.3 | Results and Discussion | 160 |
| | 5.3.1 Physicochemical Characterization | 160 |
| | 5.3.2 Electrochemical Performance in 6 M KOH Electrolyte | 168 |
| | 5.3.3 Electrochemical Performance in 1 M $Li_2SO_4$ Electrolyte | 176 |
| | 5.3.4 Electrochemical Performance in Redox-Mediated/Active electrolyte | 180 |
| 5.4 | Conclusions | 184 |
| | References | 185 |
| **Chapter 6** | **Overall Conclusions and Scope for Future Work** | |
| 6.1 | Summary of the Major Outcomes | 191 |
| 6.2 | Scope for Future Research | 194 |
| **Appendix 1** | | 197 |
| **Appendix 2** | | 207 |
| **Appendix 3** | | 221 |
| **Appendix 4** | | 233 |
| **Research Output** | | 241 |

# LIST OF TABLES


| | Table Caption | Page |
|---|---|---|
| **Chapter 1** | | |
| Table 1.1 | Summary of the capacitive performances of carbon-based electrode materials | 36 |
| Table 1.2 | Summary of capacitive performances of metal oxides and conducting polymer-based electrode materials | 37 |
| Table 1.3 | Summary of capacitive performances of composite electrode materials | 38 |
| **Chapter 5** | | |
| Table 5.1 | Elemental compositions (from XPS and CHNS analysis) and ash contents of PC-x samples | 165 |
| Table 5.2 | Porosity parameters of PC-x samples | 166 |
| **Appendix 1** | | |
| Table A1.1 | Elemental compositions of GO and rGO from CHN analysis | 197 |
| Table A1.2 | Porosity parameters of the samples | 197 |
| Table A1.3 | Magnetic parameters of the of Fe3O4 NPs and Fe3O4/rGO nanocomposite measured using vibrating sample magnetometer | 197 |
| Table A1.4 | Comparative evaluation of capacitance of symmetric solid-state supercapacitor devices | 198 |
| Table A1.5 | Comparison of electrochemical performance Fe3O4/rGO electrodes with recently reported iron oxide carbon-based electrodes | 199 |
| **Appendix 2** | | |
| Table A2.1 | BET surface area results of samples | 207 |
| Table A2.2 | Capacitive performance of binary graphene/carbon nanotube based manganese oxide nanocomposites for SCs | 208 |
| Table A2.3 | Capacitive performance of ternary graphene-carbon nanotube based manganese oxide nanocomposites for SCs | 209 |
| **Appendix 3** | | |
| Table A3.1 | Comparison of capacitive performance of graphene-based electrodes reported in our work with previous literature | 231 |
| **Appendix 4** | | |
| Table A4.1 | Composition analysis of the raw biomass samples | 233 |

| | | |
|---|---|---|
| Table A4.2 | Comparison of capacitive performance of PC–x with different carbon derived from individual biomass | 233 |
| Table A4.3 | Comparison of electrochemical performance biomass blend derived carbon with recently reported carbon materials at high electrode mass loadings | 234 |

# LIST OF FIGURES


| | Figure Caption | Page |
|---|---|---|
| **Chapter 1** | | |
| Figure 1.1 | (a) Ragone plots of energy storage devices compared to an internal combustion engine and turbines; (b) schematic representation of a supercapacitor. | 2 |
| Figure 1.2 | Schematic illustrations of charging and discharging process of supercapacitors | 3 |
| Figure 1.3 | Classification of supercapacitors | 5 |
| Figure 1.4 | Electrical double layer models: (a) Helmholtz model, (b) Gouy–Chapman model, and (c) Stern model | 6 |
| Figure 1.5 | Different types of reversible redox mechanisms that give rise to pseudocapacitance: (a) underpotential deposition, (b) redox pseudocapacitance, and (c) intercalation pseudocapacitance | 8 |
| Figure 1.6 | Construction graphs of (a) the three-electrode testing system (EW: electrochemical workstation, WE: working electrode, CE: counter electrode, RE: reference electrode), and (b) the two–electrode testing system. (Adopted from [11]) | 14 |
| Figure 1.7 | Chemical structures of graphene, graphene oxide and reduced graphene oxide (rGO) | 20 |
| Figure 1.8 | Structures of single-walled carbon nanotubes (SWCNTs) and multi-walled carbon nanotubes (MWCNTs). | 23 |
| Figure 1.9 | Crystal structures of α-, β-, γ-, δ-, and λ-$MnO_2$ | 28 |
| **Chapter 2** | | |
| Figure 2.1 | Schematic of $Fe_3O_4$/rGO nanocomposite synthesis and fabrication of all-solid-state supercapacitor | 64 |
| Figure 2.2 | (a) XRD patterns of pristine $Fe_3O_4$ NPs and $Fe_3O_4$/rGO nanocomposite (b) Raman spectra of rGO and $Fe_3O_4$/rGO nanocomposite (inset: vibration modes of $Fe_3O_4$ present in | 66 |

| | | |
|---|---|---|
| | $Fe_3O_4$/rGO) (c) Nitrogen adsorption-desorption isotherms and (d) pore size distributions of pristine $Fe_3O_4$ NPs and $Fe_3O_4$/rGO nanocomposite | |
| Figure 2.3 | TEM image of (a) $Fe_3O_4$ NPs (b) rGO sheets (c) $Fe_3O_4$/rGO nanocomposite (d) FESEM image of $Fe_3O_4$/rGO nanocomposite | 70 |
| Figure 2.4 | (a) SAED pattern (d) HRTEM and (e) elemental mapping of $Fe_3O_4$/rGO nanocomposite (carbon in red, iron in green, and oxygen in blue) | 71 |
| Figure 2.5 | (a) TG plots of rGO and $Fe_3O_4$/rGO nanocomposite (air atmosphere) (b) magnetization dependence of $Fe_3O_4$ and $Fe_3O_4$/rGO nanocomposite | 71 |
| Figure 2.6 | CV curves of (a) $Fe_3O_4$/rGO, (b) $Fe_3O_4$ ASSCs at different scan rates, (c) CV curves of ASSCs at 10 mV $s^{-1}$, and (d) specific capacitance as a function of scan rate. | 73 |
| Figure 2.7 | (a) Galvanostatic charge-discharge curves of (a) $Fe_3O_4$/rGO, (b) $Fe_3O_4$ ASSCs at different current densities, (c) specific capacitance vs. current density, and (d) cyclic performance of ASSCs | 76 |
| Figure 2.8 | (a) Ragone plot and (b) Nyquist plot of $Fe_3O_4$ and $Fe_3O_4$/rGO ASSCs | 78 |
| Figure 2.9 | (a) $C_s$ as a function of $\lambda^{-1/2}$, (b) $1/C_s$ as a function of $\lambda^{1/2}$, and (c) capacitance contribution from insertion and surface charges for ASSCs | 80 |
| **Chapter 3** | | |
| Figure 3.1 | Schematic illustration of "one-pot" ultrasound-assisted synthesis of the MWCNT/$MnO_2$/rGO nanocomposite | 94 |
| Figure 3.2 | (a) XRD patterns of (i) $MnO_2$, (ii) rGO, (iii), MWCNT, (iv) MnGC, (v) MnC, (vi) MnG; (b) Raman spectra, (c) nitrogen adsorption-desorption isotherms, and (d) pore size distribution of MnC, MnG, and MnGC nanocomposites | 96 |
| Figure 3.3 | FE-SEM images of (a-b) MnC, (c-d) MnG, and (e-f) MnGC nanocomposites in low and high resolution | 99 |

| | | |
|---|---|---|
| Figure 3.4 | TEM images of (a) MnC, (b) MnG, and (c) MnGC composites; elemental mapping of (d) MnC, (e) MnG, and (f) MnGC nanocomposites (carbon in maroon, manganese in green, and oxygen in blue). | 100 |
| Figure 3.5 | Schematic of two-electrode symmetric SC cell and the split-type cell assembly | 102 |
| Figure 3.6 | (a) Comparison of CV curves of SCs at 10 mV $s^{-1}$; CV curves of (b) MnC, (c) MnG, and (d) MnGC SCs at various scan rates; (e) specific capacitance of the SC electrodes as a function of scan rate; (f) capacitance contribution of $MnO_2$ at 5 mV $s^{-1}$ | 103 |
| Figure 3.7 | (a) Comparison of GCD curves of SCs at 1 A $g^{-1}$; GCD curves of (b) MnC, (c) MnG, and (d) MnGC SCs at different current densities; (e) specific capacitance of the SC electrodes as a function of current density; (f) long-term cyclic stability of SC cells | 107 |
| Figure 3.8 | (a) Nyquist plots (lines – EIS data recorded after 5000 cycles) and (b) Ragone plot of MnC, MnG, and MnGC SCs; (c) schematic diagram and photo of the red LED powered by two MnGC SCs connected in series | 109 |
| **Chapter 4** | | |
| Figure 4.1 | (a) Illustration of charge storage mechanisms of SCs with aqueous and redox–active electrolytes; (b) schematic representation of interactions between water molecules and cations in conventional aqueous (salt–in–water) and "water–in–salt" electrolytes. | 124 |
| Figure 4.2 | Schematic illustration of reduced graphene oxide (rGO) synthesis | 125 |
| Figure 4.3 | (a) FE–SEM, (b) TEM, and (c) elemental mapping (carbon in green, and oxygen in blue) images of rGO. | 127 |
| Figure 4.4 | Electrochemical performance of rGO electrodes using a three–electrode system in different aqueous electrolytes viz. | 128 |

| | | |
|---|---|---|
| | 1 M $H_2SO_4$, 6 M KOH, and 1 M $Li_2SO_4$: (a) CV in different electrolytes at a scan rate of 20 mV $s^{-1}$; (b) specific capacitance as a function of scan rate; (c) specific as a function of current density; (d) cycle stability in the different electrolytes. | |
| Figure 4.5 | Electrochemical performance of rGO–SCs in different aqueous electrolytes viz. 1 M $H_2SO_4$, 6 M KOH, and 1 M $Li_2SO_4$: (a) Schematic representation of two–electrode symmetric SC cell; (b) comparison of CV curves of rGO–SCs in different electrolytes; CV curves of rGO–SC in (c) 1 M $H_2SO_4$, (d) 6 M KOH, (e) 1 M $Li_2SO_4$; (f) specific capacitance of rGO electrodes as a function of scan rate. | 133 |
| Figure 4.6 | Electrochemical performance of rGO–SCs in different aqueous electrolytes, viz. 1 M $H_2SO_4$, 6 M KOH, and 1 M $Li_2SO_4$: (a) Comparison of GCD curves of rGO–SCs in different electrolytes; GCD curves of rGO–SC in (b) 1 M $H_2SO_4$, (c) 6 M KOH, (d) 1 M $Li_2SO_4$; (e) specific capacitance as a function of current density; (f) cycle stability analysis of the rGO–SCs. | 136 |
| Figure 4.7 | (a) Nyquist plots of rGO–SCs before (denoted by points) and after cycle stability (denoted by lines) tests (inset: high–frequency region); (b) Ragone plot for the rGO–SCs in different aqueous electrolytes and comparison with previously published data. | 138 |
| Figure 4.8 | Electrochemical performance of rGO–SC in redox–active electrolyte (0.1 M $Na_2MoO4$ + 1 M $Li_2SO_4$): (a) comparison of the CV curves in redox electrolyte and $Li_2SO_4$; (b) CV curves of rGO–SC at different scan rates; (c) specific capacitance as a function of scan rate; (d) comparison of the GCD curves in redox electrolyte and 1 M $Li_2SO_4$, (e) GCD curves of rGO at different current densities; (f) specific capacitance as a function of current density. | 141 |

| | | |
|---|---|---|
| Figure 4.9 | (a) cycle stability analysis of rGO–SC in redox electrolyte; (b) Ragone plot for the rGO–SC in redox electrolyte and 1 M $Li_2SO_4$ (inset: photograph of a red LED powered by the redox enhanced rGO–SC). | 144 |
| Figure 4.10 | Electrochemical performance of rGO–SC in "water–in–salt" or WIS electrolyte (11 M $NaNO_3$): (a) CV curves of rGO–SC at different scan rates; (b) specific capacitance as a function of scan rate; (c) GCD curves of rGO–SC at different current densities; (d) specific capacitance as a function of current density; (e) cycle stability analysis of the rGO–SC in WIS electrolyte; (f) Ragone plot the rGO–SC in WIS electrolyte (*inset:* photograph of a red LED powered by the 2.1 V device). | 146 |
| **Chapter 5** | | |
| Figure 5.1 | Synthesis protocol of oxygen-rich porous carbon (PC-*x*) from blends of sugarcane bagasse, water hyacinth, and yellow oleander. | 158 |
| Figure 5.2 | FE-SEM images of (a) PC-3, (b) PC-4, and (c) PC-5. TEM images of (d) PC-3, (e) PC-4, and (f) PC-5 (formation of particulate agglomerates is visible with increasing KOH/biochar ratio) | 161 |
| Figure 5.3 | (a) XRD patterns, (b) Raman spectra, and (c) XPS survey spectra of PC-*x* samples; high-resolution (d) C1s, (e) O1s, and (f) N1s spectrum of PC-4. | 163 |
| Figure 5.4 | (a) $N_2$ adsorption-desorption isotherms, and (b) pore size distribution (PSD) curves of the PC-*x* samples. | 166 |
| Figure 5.5 | Electrochemical performance of PC-*x*-SCs in 6 M KOH electrolyte: (a) schematic of symmetric supercapacitors, (b) CV curves of PC-*x*-SCs at 20 mV $s^{-1}$; CV curves of (c) PC-3-SC, (d) PC-4-SC, and (e) PC-5-SC at different scan rates; (f) specific capacitances of PC-*x* electrodes at different scan rates | 169 |
| Figure 5.6 | Electrochemical performance of PC-*x*-SCs in 6 M KOH | 171 |

| | | |
|---|---|---|
| | electrolyte: (a) GCD curves of PC-*x*-SCs at 1 A $g^{-1}$; GCD curves of (b) PC-3-SC, (c) PC-4-SC, and (d) PC-5-SC at different current densities; (e) specific capacitances of PC-*x* electrodes at different current densities, (f) cycle stability of PC-*x*-SCs | |
| Figure 5.7 | Electrochemical performance of PC-4-SC in 1 M $Li_2SO_4$: (a) CV curves of the SC at different potential windows; (b) CV of the SC curves at different scan rates; (c) specific capacitances of PC-4 electrodes at different scan rates; (d) GCD curves of the SC at different current densities; (e) specific capacitances of PC-4 electrodes at different current densities; (f) long-term cycle stability of the SC. | 177 |
| Figure 5.8 | (a) Ragone plot of PC-4-SC in 1 M $Li_2SO_4$ and comparison with carbon-based SCs in literature; (b) schematic and a digital photograph of a LED powered by PC-4-SC in 1 M $Li_2SO_4$; (c) percentage of the capacitance contribution evaluated for PC-4 in $Li_2SO_4$ electrolyte based on Trasatti's method. | 179 |
| Figure 5.9 | Electrochemical performance of PC-4-SC in the redox-mediated electrolyte (0.1 $Na_2MoO_4$ + 1 M $Li_2SO_4$): (a) comparison of CV curves of the SC in redox and $Li_2SO_4$ electrolyte; (b) CV curves at different scan rates; (c) specific capacitances of PC-4 electrodes at different scan rates (comparison with $Li_2SO_4$); (d) comparison of GCD curves of the SC in redox and $Li_2SO_4$ electrolyte; (e) GCD curves of the SC at different current densities; (f) specific capacitances of PC-4 electrodes at different current densities (comparison with $Li_2SO_4$). | 181 |
| Figure 5.10 | (a) Long-term cycle stability and (b) Ragone plot (comparison with $Li_2SO_4$) of the PC-4-SC in the redox-mediated electrolyte (0.1 $Na_2MoO_4$ + 1 M $Li_2SO_4$) | 183 |
| **Appendix 1** | | |
| Figure A1.1 | XRD plot of graphite, GO and rGO | 200 |

| | | |
|---|---|---|
| Figure A1.2 | Raman spectra of graphite, GO and rGO | 200 |
| Figure A1.3 | (a) $N_2$ adsorption-desorption isotherms of rGO (inset: BJH pore size distribution). | 201 |
| Figure A1.4 | EDS spectrum of $Fe_3O_4$/rGO nanocomposite | 201 |
| Figure A1.5 | Electrochemical performance of rGO ASSC: (a) Cyclic curves at different scan rates, (b) specific capacitance as a function of scan rate, (c) GCD curves at different current densities, , (d) specific capacitance as a function of current density. | 202 |
| Figure A1.6 | (a) Cyclic performance (at 5 $Ag^{-1}$) and (b) Nyquist plot of rGO ASSC | 202 |
| Figure A1.7 | Equivalent circuit of ASSCs | 203 |
| Figure A1.8 | (a) FE-SEM and (b) TEM images $Fe_3O_4$/rGO nanocomposite synthesized without ultrasound | 203 |
| Figure A1.9 | $N_2$ adsorption-desorption isotherms (inset: BJH pore size distribution) of $Fe_3O_4$/rGO nanocomposites synthesized without ultrasound. | 203 |
| Figure A1.10 | Comparison of (a) CV curves at 10 mV $s^{-1}$ and (b) GCD curves at 1 A $g^{-1}$ of ASSCs fabricated with $Fe_3O_4$/rGO synthesized using ultrasound-assisted method and without ultrasound. | 204 |
| **Appendix 2** | | |
| Figure A2.1 | Schematic illustration of the experimental setup for the synthesis of nanocomposites | 210 |
| Figure A2.2 | Raman spectra of pristine MWCNT and rGO | 210 |
| Figure A2.3 | Nitrogen adsorption-desorption isotherms of (a) $MnO_2$, (b) MWCNT; and pore size distribution of (c) $MnO_2$, (d) MWCNT | 211 |
| Figure A2.4 | FE-SEM images of (a) CNT (c) rGO (e) $MnO_2$ and TEM images of (b) MWCNT (d) rGO, and (f) $MnO_2$ | 212 |
| Figure A2.5 | EDX spectra of (a) MnC, (b) MnG, and (c) MnGC (the samples were dropped cast on aluminum foils and therefore a peak of Al was observed) | 213 |

| | | |
|---|---|---|
| Figure A2.6 | CV curves of the SCs at different potential windows from 1 to 1.5 V at a scan rate of 50 mV $s^{-1}$ (a) MnC, (b) MnG, and (c) MnGC | 214 |
| Figure A2.7 | (a) CV and (b) GCD curves of MWCNT SC at different scan rates and current densities; (c) CV and (d) GCD curves of rGO SC at different scan rates and current densities | 214 |
| Figure A2.8 | (a) Capacitance retention of MWCNTs and rGO SCs, (b) Nyquist plots of MWCNTs and rGO SC (lines – data after 5000 charge-discharge cycles) | 215 |
| Figure A2.9 | Electrochemical performance of $MnO_2$ SC: (a) CV and (b) GCD curves of $MnO_2$ SC at different scan rates and current densities; specific capacitance of the $MnO_2$ electrodes as a function of (c) scan rate and (d) current density; (e) Nyquist plots of $MnO_2$ | 216 |

**Appendix 3**

| | | |
|---|---|---|
| Figure A3.1 | (a) XRD patterns, (b) Raman spectra of graphene oxide (GO) and reduced graphene oxide (rGO); (c) $N_2$ adsorption-desorption isotherms, and (d) BJH pore-size distributions of rGO. | 221 |
| Figure A3.2 | Three-electrode CV curves of rGO electrode recorded at different potential windows in 1 M $Li_2SO_4$ electrolyte | 222 |
| Figure A3.3 | Electrochemical performance of rGO electrodes using three-electrode system in 1 M $H_2SO_4$ electrolyte: (a) CV curves at different scan rates from 5 to 100 mV $s^{-1}$, (b) GCD curves at different current densities from 0.5 to 5 A $g^{-1}$. | 222 |
| Figure A3.4 | Electrochemical performance of rGO electrodes using three-electrode system in 6 M KOH electrolyte: (a) CV curves at different scan rates from 5 to 100 mV $s^{-1}$, (b) GCD curves at different current densities from 0.5 to 5 A $g^{-1}$. | 223 |
| Figure A3.5 | Electrochemical performance of rGO electrodes using three-electrode system in 1 M $Li_2SO_4$ electrolyte: (a) CV curves at different scan rates from 5 to 100 mV $s^{-1}$, (b) GCD curves at different current densities from 0.5 to 5 A $g^{-1}$. | 223 |

| | | |
|---|---|---|
| Figure A3.6 | Wettability of different electrolytes on rGO electrode surface (contact angle is denoted as $\theta$) | 224 |
| Figure A3.7 | Nyquist plot of the rGO electrodes in three aqueous electrolytes viz. 1 M $H_2SO_4$, 6 M KOH, and 1 M $Li_2SO_4$ (inset: equivalent circuit) | 224 |
| Figure A3.8 | (a) CV curves of rGO in separate potential windows as positive (0 to 0.8 V) and negative (–1.0 V to 0 V) electrodes at a scan rate of 20 mV $s^{-1}$ in 1 M $Li_2SO_4$ electrolyte; (b) CV curves of rGO-SC at different potential windows in 1 M $Li_2SO_4$ electrolyte. | 225 |
| Figure A3.9 | FE-SEM images of rGO electrodes (a) before cycle stability; and after cycle stability tests in (b) $H_2SO_4$, (c) KOH, (d) $Li_2SO_4$, (e) redox-active electrolyte, and (f) water-in-salt electrolytes. | 226 |
| Figure A3.10 | Electrochemical performance of rGO electrodes using three-electrode system in redox-active electrolyte (1 M $Li_2SO_4$ + 0.1 M $Na_2MoO_4$): (a) comparison of CV curves in redox–active electrolyte and 1 M $Li_2SO_4$ at 20 mV $s^{-1}$; (b) comparison of GCD curves in redox electrolyte and 1 M $Li_2SO_4$ at 1 A $g^{-1}$; (c) CV curves at different scan rates from 5 to 100 mV $s^{-1}$, (d) GCD curves at different current densities from 0.5 to 5 A $g^{-1}$ (e) specific capacitance at various scan rates, (f) specific capacitance at various current densities. | 227 |
| Figure A3.11 | (a) CV curves of rGO in separate potential windows as positive (0 to 0.8 V) and negative (–1.0 V to 0 V) electrodes at a scan rate of 20 mV $s^{-1}$ in redox-active electrolyte; (b) CV curves of rGO-SC at different potential windows in redox-active electrolyte. | 228 |
| Figure A3.12 | Nyquist plots of rGO–SC in redox-active electrolyte (inset: high frequency region and equivalent circuit) | 228 |
| Figure A3.13 | Three-electrode CV curves of rGO electrode recorded at different potential windows in water-in-salt electrolyte (11 | 229 |

| | | |
|---|---|---|
| | M $NaNO_3$). | |
| Figure A3.14 | Electrochemical performance of rGO electrodes using three-electrode system in water-in-salt electrolyte (11 M $NaNO_3$): (a) CV curves at different scan rates from 5 to 100 mV $s^{-1}$, (b) GCD curves at different current densities from 0.5 to 5 A $g^{-1}$ (c) specific capacitance at various scan rates, (d) specific capacitance at various current densities. | 229 |
| Figure A3.15 | (a) CV curves of rGO in separate potential windows as positive (0 to 1 V) and negative (–1.1 V to 0 V) electrodes at a scan rate of 20 mV $s^{-1}$ in water-in-salt electrolyte; (b) CV curves of rGO-SC at different potential windows from 1 – 2.2 V in water-in-salt electrolyte. | 230 |
| Figure A3.16 | Nyquist plots of rGO-SC in "water–in–salt" electrolyte (inset: high-frequency region) | 230 |
| **Appendix 4** | | |
| Figure A4.1 | High resolution TEM images of (a) PC-3, (b) PC-4, and (c) PC-5 | 234 |
| Figure A4.2 | High-resolution (a) C1s, (c) O1s, and (e) N1s spectrum of PC-3; high-resolution (b) C1s, (d) O1s, and (f) N1s spectrum of PC-5 | 235 |
| Figure A4.3 | Electrochemical performance PC–*x*–SCs in 6 M KOH electrolyte: (a) Nyquist plots of PC–*x*–SCs (lines indicate EIS data after cycle stability tests and *inset*: equivalent circuit); (b) Ragone plot for PC–*x*–SCs (*inset:* a red LED powered by two symmetric PC-*x*-SC cells) | 236 |
| Figure A4.4 | GCD curves of PC-4-SC at high current densities from 10 – 20 A $g^{-1}$ in (a) 1 M $Li_2SO_4$ and (b) redox–mediated electrolyte (0.1 $Na_2MoO_4$ + 1 M $Li_2SO_4$) | 236 |
| Figure A4.5 | Nyquist plots of the PC-4-SC (lines indicate EIS spectra recorded after cycle stability tests (*inset* shows the high frequency region) in 1 M $Li_2SO_4$ and redox-mediated electrolyte (0.1 $Na_2MoO_4$ + 1 M $Li_2SO_4$). | 237 |
| Figure A4.6 | (a) plot of reciprocal of gravimetric capacitance (1/C) vs. | 237 |

square root of scan rate ($\lambda^{1/2}$); (b) plot of gravimetric capacitance (C) vs. reciprocal of square root of scan rate ($\lambda^{-1/2}$). The solid lines are linear fitting lines of data points. The algebraic equations of the fitting lines are shown in the inset.

Figure A4.7 CV curves of the PC-4-SC at different potential windows redox-mediated electrolyte (0.1 $Na_2MoO_4$ + 1 M $Li_2SO_4$) 238

भारतीय प्रौद्योगिकी संस्थान गुवाहाटी
Indian Institute of Technology Guwahati

# ABBREVIATIONS

| | |
|---|---|
| AC | Activated carbon |
| BET | Brunauer Emmett Teller |
| CNF | Carbon nanofibers |
| CNT | Carbon nanotube |
| CP | Conducting polymers |
| CV | Cyclic voltammetry |
| DMSO | Dimethyl sulfoxide |
| EDX | Energy-dispersive X-ray analysis |
| EIS | Electrochemical impedance spectroscopy |
| FESEM | Field Emission Scanning electron microscopy |
| FTIR | Fourier transform infrared spectroscopy |
| GCD | Galvanostatic charge-discharge |
| GNS | Graphene nano sheets |
| GO | Graphene oxide |
| GS | Graphene sheets |
| MWCNT | Multi wall carbon nanotube |
| PANI | Polyaniline |
| PDMS | Polydimethylsiloxane |
| PEDOT | poly-(3,4-ethylenedioxythiophene) |
| PEG | Poly ethylene glycol |
| PPy | Polypyrrole |
| PVA | poly(vinyl alcohol) |
| rGO | Reduced graphee oxide |
| SWCNT | Single wall carbon nanotube |
| SAED | Selected area electron diffraction |
| TEM | Transmission electron microscopy |
| VSM | Vibrating sample magnetometer |
| XRD | X-ray diffraction |

# CHAPTER 1

# Introduction and Literature Review

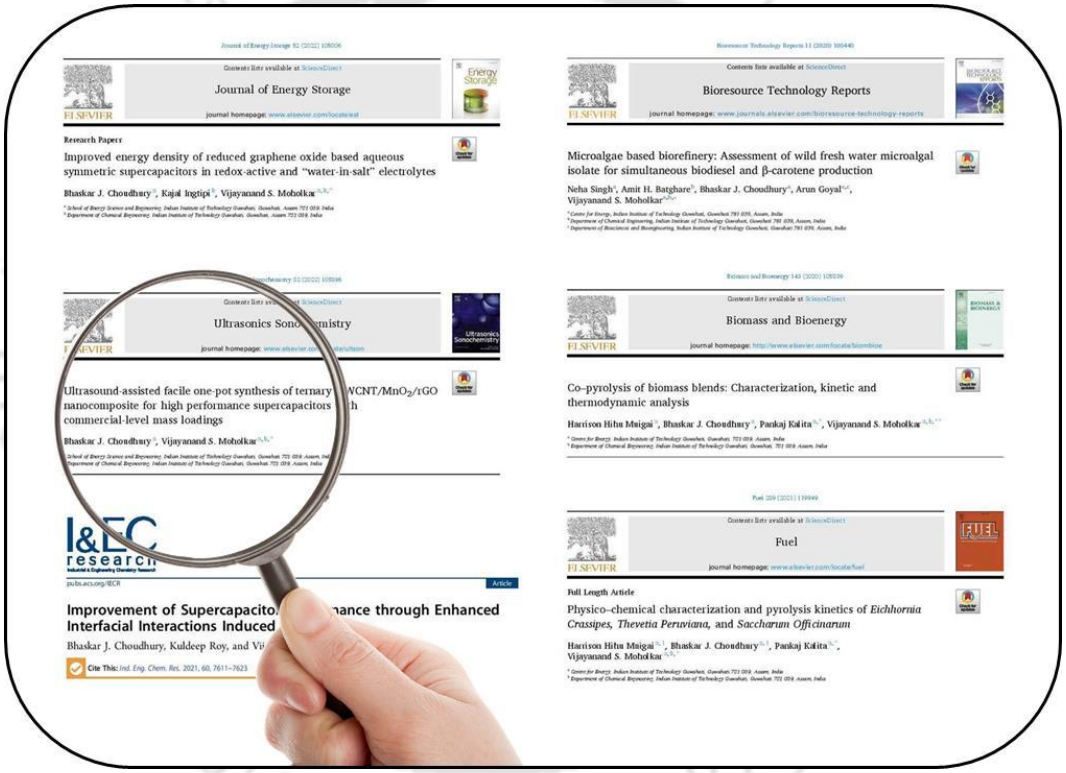

# CHAPTER 1

# INTRODUCTION AND LITERATURE REVIEW

## 1.1 INTRODUCTION

Global electricity consumption has significantly increased in recent decades due to economic growth and changing harsh weather conditions. As per the International Energy Agency (IEA), electricity production has also grown to 26936 TW h in 2019.[1] The major portion of electricity (63.1%) is generated from the combustion of fossil fuels. The extensive use of fossil fuels in electricity generation and vehicles has caused severe detrimental environmental impacts such as global warming and climate change. Moreover, fossil fuel reserves are getting exhausted very rapidly due to the increase in consumption. The diminution of fossil fuels in conjunction with their environmental impact has triggered the transition to renewable energy sources (viz. wind, solar, hydro). Several countries have pledged to reach net-zero $CO_2$ emissions by 2050 to limit the global temperature rise.[2] This goal can only be reached with a cost-effective and clean energy economy dominated by renewable sources like wind, solar and hydro in place of fossil fuels. The developments and expansion of renewable energy technologies have led to the steady growth of electricity generation from renewable energy sources over the years. In the year 2019, about 7138.6 TW h of electricity was produced from renewable sources.[1] However, intermittent electricity generation from renewable energy technologies necessitates the development of efficient and dependable electrical energy storage systems. Therefore, studies have been carried out to develop efficient and low-cost energy storage technologies for storing the electricity generated from renewable sources.

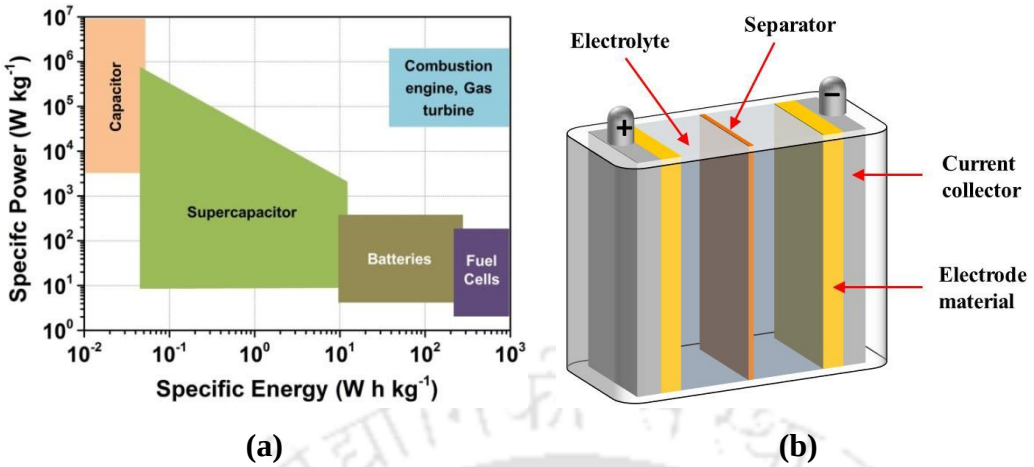


**Figure 1.1** (a) Ragone plots of energy storage devices compared to an internal combustion engine and turbines[3]; (b) schematic representation of a supercapacitor.

Electrochemical energy storage (EES) is an established approach for the storage of electricity with minimal loss and high conversion efficiency. The EES systems primarily constitute batteries, supercapacitors, and fuel cells. Among these energy storage devices, electrochemical supercapacitors or supercapacitors (SCs) have gained considerable attention for decades due to their unique performance characteristics. The Ragone plot in **Figure 1.1a** shows the comparison of different energy devices in terms of energy and power densities.[4] SCs possess several advantages, such as high power delivery, rapid charge-discharge, ultra-long cycle life, and wide operation voltages in comparison to batteries.[5,6] Conversely, the energy density of SCs (5 – 10 W h $kg^{-1}$) is much lower than that of the batteries (100 – 260 W h $kg^{-1}$).[5,7] Therefore, substantial research is underway to increase the energy density of SCs without losing power density or cycling stability. Even though the first patent on SCs was filed by Becker in 1957, the application of SCs became prevalent in the 1990s when people started to learn more about the use of SCs as a hybrid power supply.[8] At present, supercapacitors are used in applications demanding high power

uptake or delivery as well as pulsed energy, such as immediate power supply and recovery of stop-and-go systems, industrial energy management systems, frequency regulation in grids, and electric vehicles (typically used in conjunction with lithium-ion batteries).[9,10]

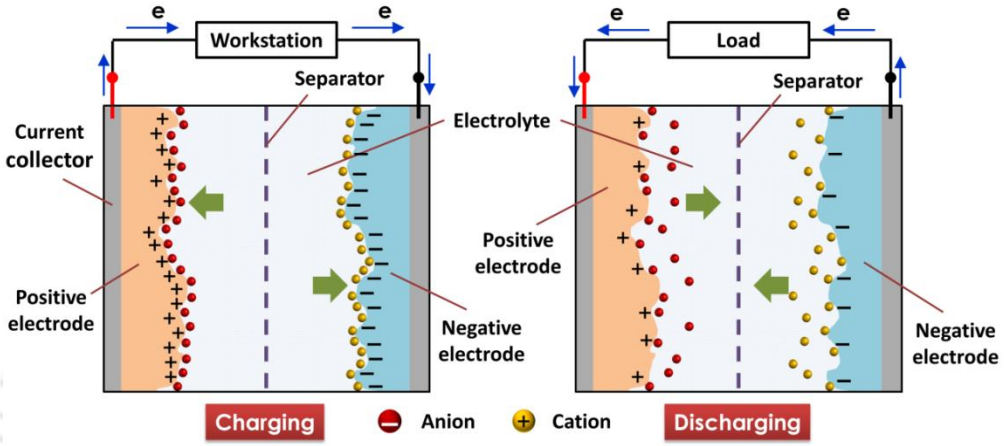


**Figure 1.2** Schematic illustrations of charging and discharging process of supercapacitors

**Figure 1.1b** depicts the main components of a supercapacitor, viz. electrodes (positive and negative), current collectors, an ion porous separator between the two electrodes, and an electrolyte filled inside the package. In commercial supercapacitors mostly activated carbon electrodes and organic electrolytes are used. Typically aqueous, organic, and ionic liquid electrolytes are used in lab-developed supercapacitors. The working of a supercapacitor is depicted in **Figure 1.2.** When the supercapacitor is charged by an electrochemical workstation, the electrons move from positive to negative electrode of the supercapacitor. At the same time, the cations and anions present in the electrolyte diffuse towards the surface of the negative and positive electrodes respectively due the driving electric field between the electrodes. During discharging, electrons move from the negative electrode towards positive

electrode by powering a load. Simultaneously the cations and anions move away from the negative and positive electrode surfaces, respectively.

## 1.2 SUPERCAPACITOR FUNDAMENTALS

### 1.2.1 Classification of Supercapacitors

Appertaining to the mechanism of energy storage SCs can be categorized into electric double-layer capacitors (EDLCs) and pseudocapacitors (PCs) (as shown in **Figure 1.3**). The charge storage in EDLCs takes place via electric double layer formation at the electrode/electrolyte interface due to adsorption and desorption of ions (electrostatically). Carbon materials are mainly used in EDLCs, which could provide porous networks with a large surface area for electrolyte ions. Pseudocapacitors on the other hand stores energy via fast reversible surface redox reactions. Typically, metal oxide (e.g. $RuO_2$, $MnO_2$, $V_2O_5$, $Fe_3O_4$, etc.) and conducting polymers (e.g. polypyrrole, poly(3,4-ethylenedioxythiophene), polyaniline, etc.) are used as pseudocapacitor electrodes. The charge storage occurs principally on the surface or near the surface of the electrode, and thus the supercapacitors exhibit fast charge-discharge characteristics along with high power density. Another kind of supercapacitors, where the charge is stored via both double layer formation and reversible surface redox reactions, is called hybrid supercapacitors (HC). HCs are divided into asymmetric, composite, and battery types (**Figure 1.3**). The asymmetric SCs are constructed using two dissimilar types of electrodes, usually one EDLC and the other pseudocapacitive electrode type. In composite-type supercapacitors, the electrodes are made of composite materials. Whereas in battery-type hybrid supercapacitors one electrode is a capacitive electrode and the other is made of battery-type material.

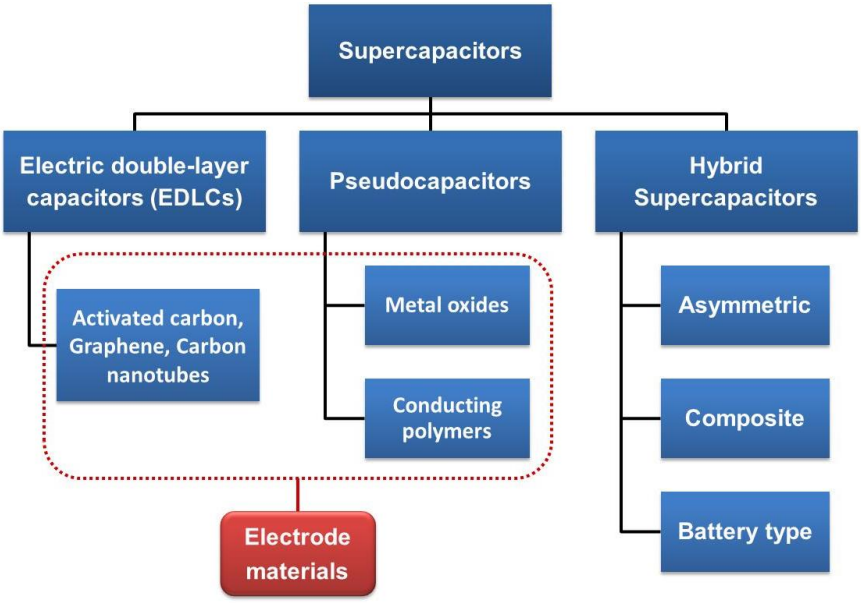


**Figure 1.3** Classification of supercapacitors

### 1.2.2 Charge Storage Mechanism of EDLCs

In EDLCs, the charge storage mechanism is electrostatic and originates from the formation of a double-layer at the electrode/electrolyte interface via adsorption/desorption of ions without any redox reactions. EDLCs capacitance intensely depends on the surface of the electrode materials, which is available for interaction with the electrolyte ions. The capacitance (C) can be expressed as:

$$C = \frac{Q}{V} = \frac{\varepsilon_r \varepsilon_o A}{d} \qquad (1.1)$$

where, $Q$ is the stored charge at the electrodes due to the potential difference $V$, $\varepsilon_r$ is the relative permittivity (dielectric constant), $\varepsilon_0$ is vacuum permittivity ($8.854 \times 10^{-12}$ F $m^{-1}$), $A$ is the surface area of electrode dipped in the electrolyte, $d$ is the effective double-layer thickness at the electrolyte/electrode interface. The value of '$d$' in EDLCs is very small (a few angstroms) in comparison to dielectric capacitors. Therefore, EDLCs exhibit high values of capacitance. The surface area of the active

material, the double-layer thickness, and the type of electrolyte influence the capacitance of EDLCs.[11]

During the charging of EDLCs, anions and cations of the electrolyte are accumulated at the respective negative and positive electrodes. This process of energy storage is highly reversible and non-faradaic in nature, which takes place due to double-layer formation at the interface of the electrode and the electrolyte. The EDLCs can store and deliver energy at a very high rate, and exhibit ultra-long cycle life with very limited capacitive fading. These features of the EDLCs can be ascribed to the faster kinetics of physical adsorption-desorption of electrolyte ions at the electrode/electrolyte ions.

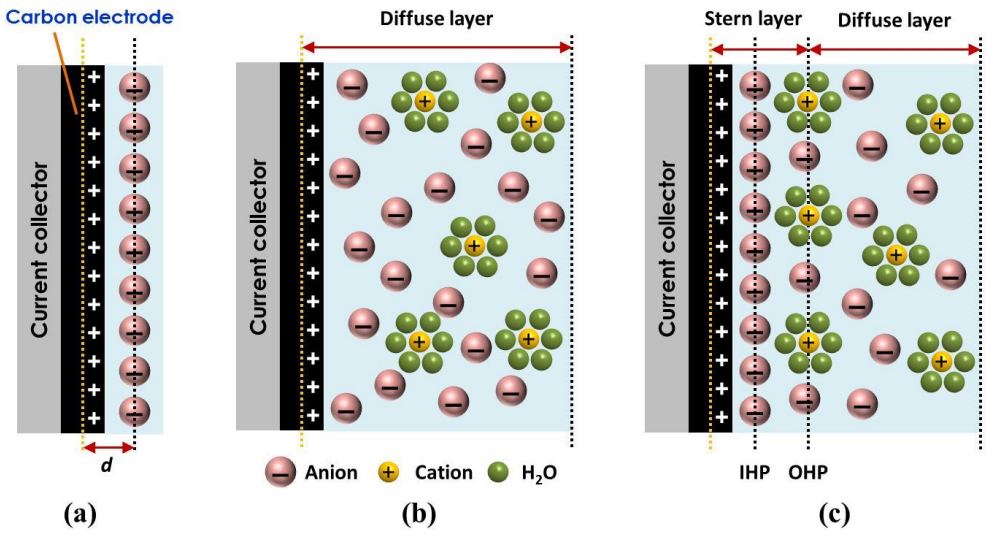


**Figure 1.4** Electrical double layer models: (a) Helmholtz model, (b) Gouy–Chapman model, and (c) Stern model

When a charged object is dipped in a liquid, an opposite charge forms on the liquid near the surface and an electric double-layer is formed. The process of electric double-layer formation could be described by various models, viz. Helmholtz model, Gouy-Chapman model, and Stern model (**Figure 1.4**).[7]

#### *1.2.2.1 Helmholtz model*

The Helmholtz double-layer model is the simplest and states that the charge of the electrode is balanced by the counterbalancing charge formed at distance '*d*' from the surface of the electrode.[12] The layer of charges on the electrode is rigidly held and the other oppositely charged (equal in magnitude) layer is fixed on the electrolyte. This model cannot properly explain the electrified interfaces.

#### *1.2.2.2 Gouy-Chapman or diffuse model*

This model suggested that although the layer of charges on the electrode is rigid, the counterbalancing layer on the electrolyte is not rigid but diffused on the electrolyte. The counterbalancing ions spread into the solution and the layer extends to some distance in the electrolyte. The thermal agitation and the movement of ions present in the solution results in non-uniform distribution of positive and negative charges in this region.[12] At higher concentrations of the electrolyte, Gouy-Chapman's theory fails to predict the charge accumulation process and overpredicts the capacitance values.

#### *1.2.2.3 Stern model*

In this model, Stern combined the views of both Helmholtz model and Gouy-Chapman model and suggested that the double-layer constitutes two regions, viz. Stern layer and diffuse layer. The Stern layer (or compact layer) is formed by the counter ions adsorbed near the electrode surface.[7,12] The specifically adsorbed ions in the Stern layer form the inner Helmholtz plane (IHP), and the weakly adsorbed ions form the outer Helmholtz plane (OHP). The second region, i.e. the diffuse layer is formed by the distribution of electrolyte ions due to the combined effect of both thermal motion and electrostatic attraction. The diffuse layer extends from the Stern layer to the neutral part of the bulk electrolyte. As per Stern theory, the total

capacitance of the electric double layer ($C_{dl}$) can be expressed by the capacitance of compact region ($C_H$) and capacitance of diffuse layer ($C_{diff}$) in series, i.e.

$$\frac{1}{C_{dl}} = \frac{1}{C_H} + \frac{1}{C_{diff}} \qquad (1.2)$$

The major features that affect the double-layer capacitance are electrode materials surface area; pore size and volume of electrode material, accessible surface area for the electrolyte ions, electrolyte properties, etc. As highly porous materials are used in EDLCs the pore structure, and pore size distribution make the double layer behavior rather complex in the pore areas, especially for the nanoporous materials. Additionally, other studies have adopted different approaches to understanding the double layer behavior in such porous materials.[13–15]

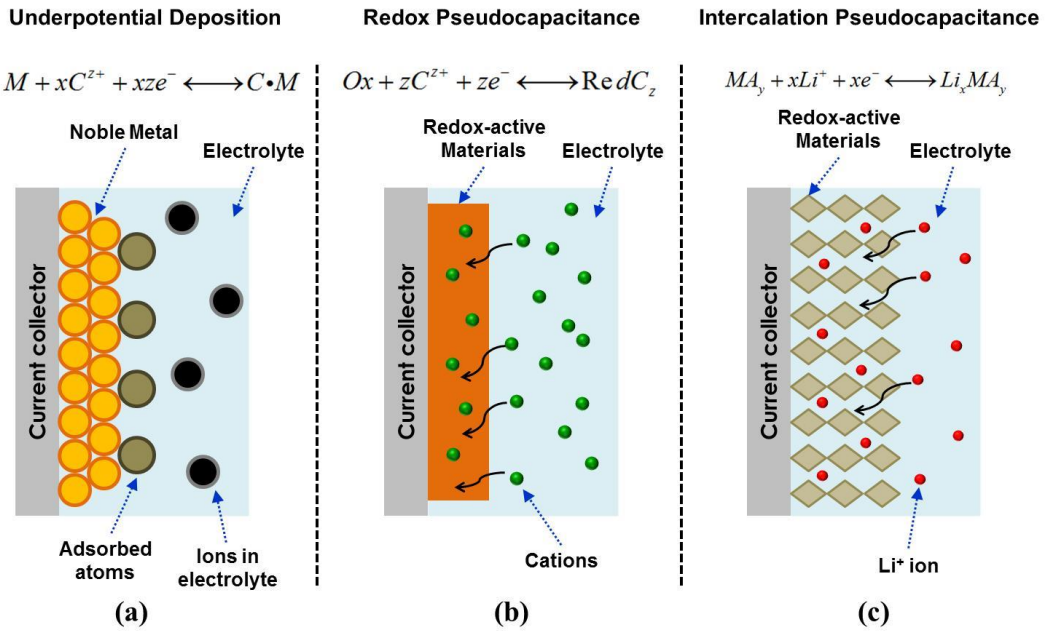


**Figure 1.5** Different types of reversible redox mechanisms that give rise to pseudocapacitance: (a) underpotential deposition, (b) redox pseudocapacitance, and (c) intercalation pseudocapacitance

### 1.2.3 Charge Storage Mechanism of Pseudocapacitors

The charge storage in pseudocapacitors takes place via surface redox or near-surface redox reactions. The plausible Faradaic mechanisms for pseudocapacitance (shown in **Figure 1.5**) are underpotential deposition, redox pseudocapacitance, and intercalation pseudocapacitance.[16]

When adsorption of metal ions results in the formation of a monolayer at the surface of another metal above their redox potential it gives rise to underpotential deposition. Conversely, redox pseudocapacitance arises when the ions get adsorbed (electrostatically) on the surface or near the surface of the electrode complemented by a faradaic charge transfer. Examples of the materials that exhibit redox pseudocapacitance are transition metal oxides (e.g. $MnO_2$, $RuO_2$, etc.) and conducting polymers (e.g. polyaniline, polypyrrole, etc.). Intercalation pseudo-capacitance arises from the intercalation of ions in the tunnels (or layers) of active materials, which is complemented by a Faradaic charge transfer without any crystallographic phase change. Intercalation pseudocapacitance varies from the intercalation process in batteries where crystallographic phase transformation takes place.

The aforementioned mechanisms of pseudocapacitance originate from different physical processes. However, their electrochemical behavior is the same, and is represented by the following relation between the electrode potential and extent of charge:

$$E = E^{o} + \frac{RT}{nF} \ln \frac{X}{1-X} \qquad (1.3)$$

where, $E$ (V) is potential, $T$ (K) is the temperature, $R$ is the universal gas constant (8.314 J $mol^{-1}$ $K^{-1}$), $n$ is the number of electrons, $F$ is Faraday's constant (96485 C

$mol^{-1}$), and $X$ is the coverage fraction of the surface or inner structure. In a linear region of $E$ vs. $X$ in Eq. (3), capacitance ($C$, F $g^{-1}$) could be expressed as:

$$C = \left(\frac{nF}{m}\right)\frac{X}{E} \tag{1.4}$$

where, $m$ is the molecular weight of active material. The term pseudocapacitance comes from the fact that the $E$ vs. $X$ plot is not fully linear in a capacitor and the capacitance is not always constant.

## 1.3 COMPONENTS OF SUPERCAPACITORS

The main components of a supercapacitor cell are the electrodes, electrolyte, separator, and current collector.

### 1.3.1 Electrode

The electrodes are made from electro-active materials, carbon materials are used in EDLCs while metal oxides and conducting polymers are used in pseudocapacitors. The electrode materials are mixed with conductive agents (e.g. carbon black) and binder materials (polytetrafluoroethylene, polyvinylidene fluoride, Nafion, etc.) to prepare a homogenous slurry, which is coated on the current collectors to prepare supercapacitor electrodes. The main work of the electrode is to store the charge when an external potential is applied. Moreover, the electrode materials should be environmentally safe and relatively inexpensive to reduce the total cost of SCs. The following parameters of the electrode materials highly influence their electrochemical performance.[17]

- *Electrical conductivity:* The high conductivity of the electrodes results in low resistance and the electrode exhibits faster electron kinetics demonstrating improved high rate capability and power density.

- *Surface area:* When the surface area of active materials is high, the electrolyte ions get additional accessible area in the electrodes to interact; thereby increasing the charge storage potential and capacitance of the electrodes.
- *Controlled porosity:* The pore size distribution of the electrode materials plays a vital role. Typically, the pore size should be more than the size of the solvated ions of the electrolytes.
- *Thermal and chemical stability:* The thermal and chemical stability of electrode material should be high, as it affects the cyclic performance of the electrodes.
- *Surface functionalities:* The introduction of surface functionalities such as oxygen, and nitrogen-containing groups in electro-active materials could increase the capacitive properties of the electrodes by promoting pseudocapacitance.

### 1.3.2 Electrolyte

Electrolytes are a very crucial part of electrochemical devices as they balance the charges between the electrodes. The capacitance, voltage, power density, energy density, etc. are dependent on the use of different types of electrolytes. The performance of the supercapacitors depends on the choice of electrolytes. The parameters for designing electrolytes are as follows:[18]

- *Electrical conductivity:* To make a supercapacitor with high electrochemical performance, the electrolyte should have conductivity and ionic mobility. Aqueous electrolytes generally have the highest ionic conductivity among different types of electrolytes. The electrolyte conductivity mainly depends on ionic mobility, ion concentration, elementary charge, and magnitude of the valence of the mobile ion charges.

- *Salt effect:* The conductivity of different salts can vary in the same solvent. Moreover, the salt concentration also affects the conductivity in the same solvent due to the number of available free ions. At optimum salt concentration, the ionic conductivity of the electrolyte could increase.
- *Solvent effect:* The viscosity and the dielectric constant of the electrolyte are the main properties that influence the conductivity of the electrolyte. The dielectric constant and the viscosity govern the dissociation of the salts and the ionic mobility, respectively. The suitable solvent should have high dielectric constant and low viscosity.
- *Electrochemical stability:* The solvent should have high electrochemical stability for cycle stability as well as the safety of the device is concerned. The components of the electrolyte and the compatibility with the electrode material influence the electrochemical stability.
- *Thermal stability:* When an SC is subjected to a repetitive charge-discharge process, it raises the operating temperature of the device, and therefore, the thermal stability of the electrolyte is very important for the safety of the device.

The electrolytes used in supercapacitors can be generally categorized as aqueous, organic, and ionic liquid electrolytes. Among the electrolytes, aqueous electrolytes are low-cost and exhibit the highest ionic conductivity but suffer from a limited potential window (1.23 V). Both organic and ionic electrolytes can operate in relatively higher potential windows (2.5–2.7 V and 3.5–4.0 V, respectively), but suffer from inferior ionic conductivity. Organic electrolytes are relatively toxic and have handling issues, while the cost of ionic electrolytes hinders their commercial application. Apart from the three aforesaid types of electrolytes, other electrolytes such as solid-state

electrolytes, mixtures of electrolytes (two similar electrolytes in different ratios), and redox-active electrolytes have been employed nowadays.[18]

### 1.3.3 Separator

The separator in a supercapacitor device avoids direct contact with the electrodes which may lead to a short circuit. The separators are insulators and should permit the movement of electrolyte ions. It wets the electrodes as well as provides mechanical support to the device. Different types of materials, viz. cellulose paper, glass fibers, ceramics, and polymer-based materials, are used as separators.

### 1.3.4 Current collector

The current collectors connect the electrodes to the outer circuit and must have excellent electrical conductivity. The current collectors should have high corrosion resistance as various types of electrolytes are used, which may cause corrosion in the current collector. The most commonly used current collector materials are aluminum, stainless steel, nickel, etc. Commonly, the electrode materials are coated onto the metallic current collector foils or sheets. Moreover, metal foams, metal mesh, carbon paper, carbon cloth, etc. are also used as current collectors. A thin layer of conductive carbon is coated on the metallic current collectors to reduce contact resistance.

## 1.4 ELECTROCHEMICAL EVALUATION OF SUPERCAPACITORS

Two different types of cell configurations are used to test the electrochemical performance of electrode materials, viz. three-electrode, and two-electrode systems. A three-electrode system (**Figure 1.6a**) constitutes a working electrode (WE), reference electrode (RE), and counter electrode (CE).[11] Three-electrode system or half-cell configuration is mainly used to study the performance of the electrode materials. The

applied voltage across the WE is measured with respect to a particular RE (for example Ag/AgCl electrode, Hg/HgO electrode, and Saturated Calomel Electrode, etc.) in the three-electrode setup. The two-electrode testing system (**Figure 1.6b**) represents a full cell configuration that consists of two electrodes (active material coated on a current collector) separated by an ion porous separator. The separator is saturated with electrolytes and prevents direct electrical contact between the electrodes. Three main electrochemical tests are used to evaluate the performance of the SCs, namely cyclic voltammetry (CV), galvanostatic charge-discharge (GCD), and electrochemical impedance spectrometry (EIS).

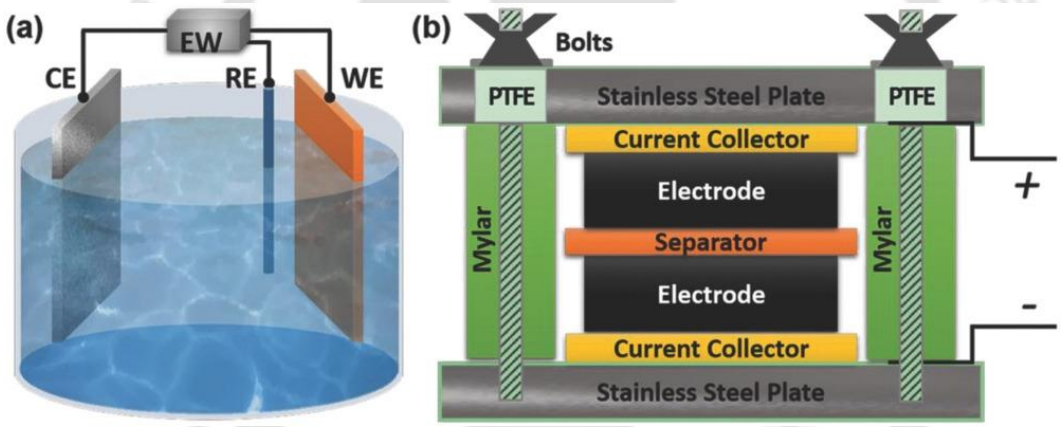


**Figure 1.6** Construction graphs of (a) the three-electrode testing system (EW: electrochemical workstation, WE: working electrode, CE: counter electrode, RE: reference electrode), and (b) the two–electrode testing system. (Adopted from [11])

### 1.4.1 Calculation of Capacitive Parameters

In a three-electrode system, The specific capacitances ($C_s$, F $g^{-1}$) can be evaluated from cyclic voltammograms as follows:[19,20]

$$C_g = \frac{\int IdV}{2\lambda m \Delta V} \qquad (1.5)$$

where, $\int IdV$ is the area under the CV curve, $I$ is the current response (A), $\Delta V$ is the potential window (V), $m$ is the mass active materials (g), and $\lambda$ indicates the voltage scan rate (V $s^{-1}$).

The more reliable value of capacitance can be obtained from the GCD tests as follows:

$$C_g = \frac{I_d \Delta t}{\Delta V} \tag{1.6}$$

where, $I_d$ (A $g^{-1}$) is the discharge current density, $\Delta t$ (s) is the time for discharging, and $\Delta V$ (V) is the potential window excluding IR drop.

For two-electrode symmetric cells, the specific capacitances of a single electrode ($C_g$, F $g^{-1}$) and symmetric supercapacitors ($C_{cell}$, F $g^{-1}$) were calculated from the respective CV and GCD using equations (1.7) and (1.8), respectively.

$$C_g = 4 \times \frac{\oint IdV}{2\lambda M \Delta V} = 4 \times C_{cell} \tag{1.7}$$

where, $M$ is the total mass of electrode materials (g) in both the electrodes and $\Delta V$ is the cell voltage (V)

$$C_g = 4 \times \frac{I_d \Delta t}{\Delta V} = 4 \times C_{cell} \tag{1.8}$$

The energy density and power density are the two main parameters of supercapacitors. The amount of total charge stored per unit mass is represented by energy density ($E_{cell}$, W h $kg^{-1}$), while the power density ($P_{cell}$, W $kg^{-1}$) defines the charge delivery rate during the discharging process. Energy and power densities of supercapacitors can be evaluated as:

$$E_{cell} = \frac{1}{2} C_{cell} V^2 \cdot \frac{1}{3.6} = \frac{I_d \int V dt}{3.6} \quad (1.9)$$

$$P_{cell} = \frac{3600E}{\Delta t} \quad (1.10)$$

## 1.5 ELECTRODE MATERIALS FOR SUPERCAPACITORS

### 1.5.1 Carbon Materials

The carbon materials offer high conductivity, large surface area, controllable pore structure, and excellent electrochemical as well as thermal stability, which makes them suitable electrode materials in EDLCs. The most commonly used carbon materials used in EDLCs are discussed below. Various carbon materials including activated carbon (AC), graphene, carbon nanotubes (CNTs), and carbon aerogels have been investigated as electrode materials for SCs.

#### *1.5.1.1 Activated carbon (AC)*

ACs are the most extensively used electrode materials for supercapacitors due to their large surface area, tunable pore structure, good electrochemical stability, and electrical properties. ACs are commonly synthesized by either physical or chemical activation of carbonaceous materials, viz. coconut shell, wood, coal, and polymers. The carbon precursors are usually treated at high temperatures ranging from 700 to 1200 °C in oxidant environments (viz. $CO_2$, steam) during the physical activation process. Conversely, chemical activation is referred to as the treatment of precursors with activating agents (such as KOH, NaOH, $H_2SO_4$, $H_3PO_4$, $ZnCl_2$, $K_2CO_3$, etc.) at relatively low temperatures (400 to 700 °C). The activation process generates the porous structure of AC in addition to the partial oxidation of the carbon surface. The

method of activation and the activation temperature and time plays a major role in tuning the pore structure and surface area of the materials. The optimization of the above-mentioned parameters can result in ACs with surface areas as high as 3000 $m^2$ $g^{-1}$.[21–23] It has been observed that ACs exhibit a wide range of pore sizes: (i) micropores (< 2 nm), (ii) mesopores (2–50 nm), and (iii) macropores (> 50 nm). Typically, a large surface area should provide higher capacitance. However, Kierzek et al.[24] obtained smaller specific capacitance (7–11 μF $cm^{-2}$) than the theoretical double-layer capacitance (15–25 μF $cm^{-2}$) for AC. Their study revealed that the whole surface area of the pores is not accessible to electrolytes thereby limiting the charge accumulation and capacitance. Hence, several other features such as pore size distribution, pore shape, surface functional groups and conductivity of the carbon materials significantly influence their capacitive performance in addition to specific surface area. The greater degree of activation could result in large pore volume and low density, which in turn will adversely affect the volumetric energy density and power delivery [12].

Studies have shown that ACs exhibit high specific capacitances in aqueous electrolytes (100 – 300 F $g^{-1}$) in comparison to organic electrolytes (100 – 120 F $g^{-1}$). The reasons for lower capacitance in organic electrolytes are the low ionic conductivity of organic electrolytes as well as the larger sizes of electrolyte ions in organic solutions. The low ionic conductivity, large ionic size together with the electrochemical affinity between the carbon surface and the organic electrolyte results in underutilization of the pore structure of the electrodes during the charge storage. The high capacitance values of ACs in aqueous electrolytes are given herewith by few examples: Sugarcane bagasse-derived carbon (2905.4 $m^2$ $g^{-1}$) prepared via KOH activation has demonstrated a high capacitance of 301.9 F $g^{-1}$ at 1 A $g^{-1}$ in an aqueous

electrolyte.[25] Chitosan-based AC (1582 $m^2$ $g^{-1}$)[26] prepared using $CuCl_2$ as the activating agent exhibited a capacitance of 252 F $g^{-1}$ at 0.5 A $g^{-1}$. Cai et al.[27] reported the $ZnCl_2$+$FeCl_3$ based activation of Moringa oleifera stems to prepare AC (2250 $m^2$ $g^{-1}$) and obtained a capacitance of 311 F $g^{-1}$ at 0.1 A $g^{-1}$. However, the cell voltages of SCs in aqueous electrolytes are limited by thermodynamic decomposition limit of water splitting (1.23 V). Therefore, the energy density of the aqueous electrolytes-based SCs is low. The organic electrolytes provide high cell voltages up to 2.7 V together, and therefore, the commercial SCs are usually constructed with organic electrolytes and AC electrodes. As a result of the high cell voltage, SCs in organic electrolyte exhibits high energy density in comparison to that in aqueous electrolyte.

The surface functional groups present in the ACs also enhance the capacitive performance by improving the wettability of the carbon surface by the electrolyte as well as contribution of pseudocapacitance. Different types of heteroatoms such as nitrogen, oxygen, and sulfur-containing groups are usually introduced on the carbon surface to provide additional faradaic charge transfer. Li et al.[28] prepared nitrogen-doped AC (1615 $m^2$ $g^{-1}$) from Macadamia nutshell by KOH-based activation process. The nitrogen-doped AC showed a specific capacitance of 229.7 F $g^{-1}$, which was 2.33 folds higher than that of the AC without nitrogen doping. However, studies have also reported that some surface functionality could result in high self-discharge, instability, and increased series resistance.[29] Additionally, acidic functionalities and moisture present on the surface of ACs could cause aging of the electrodes in organic electrolytes. Therefore, it is important to optimize the content of surface functional groups of ACs in addition to the pores structure for superior and stable electrochemical performance.

In summary, ACs are extensively used as electrode materials in commercial supercapacitors due to their high power delivery and long cycle life. However, the low energy densities have restricted their applications to certain niche markets. Therefore, it is essential to obtain an optimal and narrow pore size distribution for maximum utilization of the surface area of the electrode pores as well as controlled surface functionality for designing high energy density AC-based supercapacitors with long cycle life.

#### *1.5.1.2 Graphene*

Graphene is a 2-D material with exceptional properties, viz. excellent conductivity (charge carrier mobility = 250000 $cm^2$ $V^{-1}$ $s^{-1}$), mechanical strength (mechanical stiffness = 1 TPa), large surface area (2630 $m^2$ $g^{-1}$) and favorable pore size distributions.[30,31] These salient properties of graphene have led to the development of graphene-based electrode materials for various applications including SCs and batteries. There are several methods to synthesize graphene, viz. mechanical exfoliation (scotch tape method), chemical vapor deposition (CVD) on metal foil substrates (Ni, Cu, etc.), epitaxial growth on silicon carbide substrate, exfoliation of graphite in organic solvents and exfoliation and reduction of chemically oxidized graphite. The graphene synthesized by CVD or micromechanical exfoliation has the best quality with fewer basal plane defects and few-layered (single or bilayer sheets) structures. However, the high cost of these methods limits their applications for large-scale production of graphene for energy storage applications. The reduction of chemically oxidized graphene can produce graphene materials of relatively lower quality but at larger scales and low cost. In this process, graphite oxide (GO) is first prepared by oxidation of graphene either by Hummers, Brodie, or Staudenmaier methods. Graphite oxide contains various oxygen-containing functionalities such as

hydroxyl, epoxy, and carbonyl groups. Afterward, the GO is exfoliated and reduced by either chemical reduction (with hydrazine, sodium borohydride, hydroiodic acid, etc.) or thermal treatment to restore the electrical conductivity and the surface area. The final product obtained after the reduction process is reduced graphene oxide (rGO) which contains a very small amount of residual oxygen groups (depending upon the degree of reduction). The chemical structures of graphene, graphene oxide and rGO are shown in **Figure 1.7**.

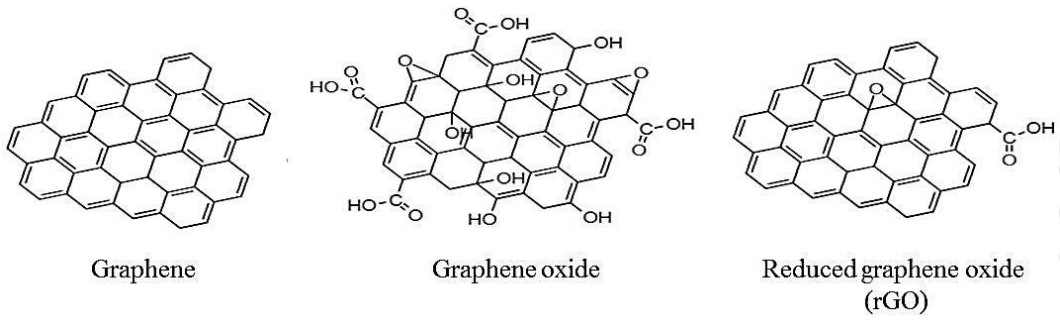


**Figure 1.7** Chemical structures of graphene, graphene oxide and reduced graphene oxide (rGO)

Theoretically, graphene can exhibit a capacitance of 550 F $g^{-1}$, which is the highest intrinsic capacitance attainable by carbon-based materials. However, the actual capacitance obtained from the graphene is far from its theoretical value due to the unwanted restacking of graphene sheets reducing the accessible surface area for the electrolyte ions. Stoller et al.[32] synthesized rGO from hydrazine reduction of graphene oxide, and the as-synthesized rGO-based electrodes exhibited gravimetric capacitances of 135 and 99 F $g^{-1}$ in aqueous KOH and organic (TEABF4/AN) electrolytes, respectively. Later, Wang et al.[33] used a gas-phase hydrazine reduction route to synthesize rGO with lesser agglomeration and obtained a higher capacitance of 205 F $g^{-1}$ in a KOH electrolyte. Lee et al. [34] used precursor-assisted chemical vapor

deposition (CVD) to synthesize mesoporous graphene nanoball for supercapacitor electrodes and achieved a capacitance of 206 F $g^{-1}$ in $H_2SO_4$ electrolyte. Vivekchand et al. [35] thermally reduced graphene oxide at 1050 °C and the resultant rGO (925 $m^2$ $g^{-1}$) exhibited a capacitance of 117 F $g^{-1}$ in $H_2SO_4$ electrolyte. However, the application of such a high-temperature process is energy-intensive. Later, Jian et al. [36] studied the effect of temperature (200 – 900 °C) on thermal reduction of GO and obtained the maximum capacitance of 315 F $g^{-1}$ (in 6 M KOH electrolyte) at the annealing temperature of 200 °C. This high capacitance is attributed to the high content of residual oxygen-containing functional groups, which contribute to pseudocapacitance.

Various strategies have been used to prevent the restacking of the graphene layers so that the maximum surface area of the graphene can be utilized for energy storage. These strategies include the addition of surfactants, spacer materials, crumpling of graphene sheets, 3D structure formation, etc.[37–40] Zhang et al.[38] reported improvement capacitance of rGO with surfactant intercalation in rGO sheets and a capacitance of 194 F $g^{-1}$ was obtained with TBAOH stabilized graphene in 2 M $H_2SO_4$ electrolyte. The surfactant not only lowered the re-stacking of rGO sheets but also increased the wettability of the rGO electrodes as well. Spacer materials such as carbon black and carbon nanotubes have been used to reduce the self-aggregation of graphene sheets, which enabled a larger accessible surface area for the electrolyte ions and increased the capacitance.[40,41] However, local aggregation graphene sheets are inescapable, which is a major hurdle to increasing the capacitance. Dey et al.[42] synthesized copper foam (CuF) integrated three-dimensional rGO electrodes (3DrGO@CuF) which exhibited a high specific capacitance of 623 F $g^{-1}$ (at 1 A $g^{-1}$). However, in this case, CuF also contributed to the total capacitance along with

3DrGO. El-Kady et al.[43] reported a larger-based unique strategy for the reduction of GO. The resultant product was laser-scribed graphene (LSG) film which possessed 3D open networks, high conductivity (1738 S $m^{-1}$) together with a specific surface area (1520 $m^2$ $g^{-1}$). The efficient pore structure of these LSG enabled efficient charge mitigation inside the whole electrodes, and thus, the LSG electrodes exhibited high capacitance (276 F $g^{-1}$) and energy densities while maintaining high power densities in ionic liquid electrolytes. It has been also reported that the preparation of graphene sheets with wrinkled or crumpled sheet morphologies reduces aggregation and can provide much better capacitive performance in comparison to 2D graphene sheets.[37,44] In addition, SCs fabricated with crumpled graphene morphologies have shown better capacitance even at higher electrode mass loadings.[37] Similar to activated carbons, heteroatom doping in graphene can also enhance the capacitance of graphene with an additional faradaic contribution. For example, Liu et al.[45] synthesized nitrogen-doped graphene (nitrogen content of 2.95), which exhibited a capacitance of 205.3 F $g^{-1}$ in comparison to 170 F $g^{-1}$ of pristine rGO in KOH electrolyte.

#### *1.5.1.3 Carbon nanotubes (CNTs)*

Carbon nanotubes (CNTs) are 1-D carbon materials with hollow cylindrical shapes consisting of hexagonal carbon networks. CNTs have been explored as electrode materials for EDLCs owing to their unique tubular structure, superior electrical conductivity, high porosity, and charge transport capability, good mechanical and chemical stability. Usually, CNTs are categorized into single-walled carbon nanotubes (SWCNTs) and multi-walled carbon nanotubes (MWCNTs). The structures of SWCNTs and MWCNTs are shown in **Figure 1.8**. The open-ended tubular structure of CNTs is advantageous for electrolyte percolation and ion diffusion. However, the capacitance of CNT-based electrodes is limited due to the low surface

area of the CNTs as compared to that of graphene and ACs. Therefore, efforts have been made to improve the electrochemical performance of CNTs by improving the specific surface area along with surface modifications with functional groups.

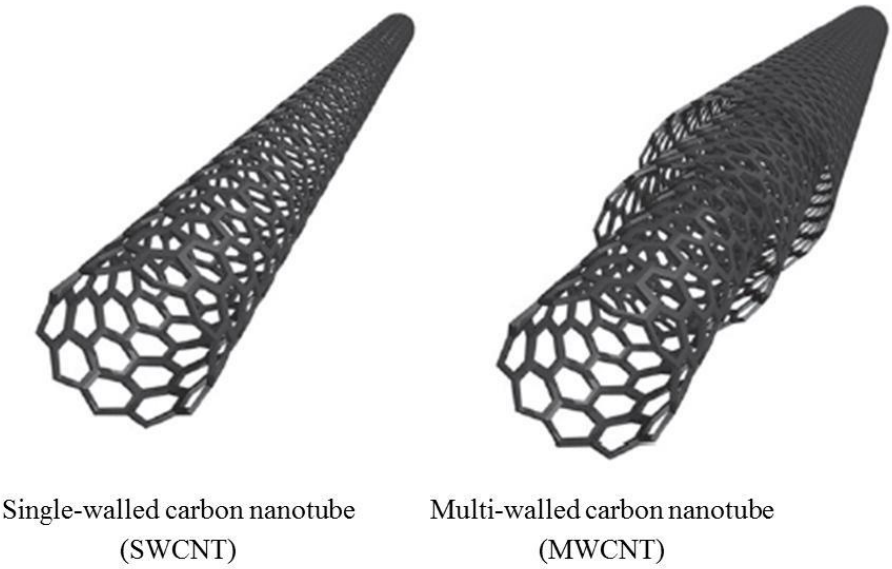


**Figure 1.8** Structures of single-walled carbon nanotubes (SWCNTs) and multi-walled carbon nanotubes (MWCNTs). (Adopted from [46])

Niu et al.[47] functionalized the catalytically grown MWCNTs with nitric acid and prepared binder-free MWCNT-based sheet electrodes for SCs. These functionalized MWCNT-based electrodes exhibited a surface area of 430 $m^2 g^{-1}$ and a specific capacitance of 102 F $g^{-1}$ in 38 wt % $H_2SO_4$ electrolyte. In another study, An et al.[48] reported the synthesis of SWCNTs via a DC arc-discharge process. The electrodes fabricated by mixing the SWCNTs and poly(vinylidene chloride) binder were annealed at 500–1000 °C. It was observed that the specific capacitance and rate capability increased with annealing temperature. The highest specific capacitance of 180 F $g^{-1}$ and an energy density of 6.5 W h $kg^{-1}$ was obtained at high power density of 20 kW $kg^{-1}$ in a 7.5 N KOH electrolyte. In another study, Frackowiak et al. [49]

improved the surface area of MWCNTs to 1035 $m^2$ $g^{-1}$ by KOH activation process and investigated the capacitive performances of these materials in aqueous and organic electrolytes. The activated samples exhibited significantly higher capacitance compared to the non-activated MWCNTs. Well aligned MWCNTs with 1–10 μm length and 5–100 nm diameter were grown on aluminum and silicon substrates by a pyrolytic method.[50] The MWCNTs coated aluminum electrodes showed a high volumetric capacitance of 120 F $cm^{-3}$ and a high power density of 700 kW $L^{-1}$ at an energy density of 26 W h $L^{-1}$. Chen et al. [51] used a CVD technique to uniformly grow CNTs on the surface of graphite foil and these electrodes exhibited a specific capacitance of 115.7 F $g^{-1}$ (at 100 mV $s^{-1}$) in 1 M $H_2SO_4$ electrolyte. Heteroatom doping has also been explored to improve the electrochemical performance of CNT-based SC electrodes. For example, Gueon and Moon [52] reported a 3.1× increase in specific capacitance with nitrogen-doped CNTs (nitrogen content 11.2 at.%) compared to that of the pristine CNTs.

Several studies have reported superior capacitive performance for aligned CNTs as compared to entangled CNTs.[53–56] The better performance of aligned CNTs is due to their unbundled structures, presence of abundant mesopores, and rapid ion transportation due to low resistance. Hata and coworkers[56] synthesized vertically aligned SWNTs via a water-assisted chemical vapor deposition technique with a specific surface area of 1300 $m^2$ $g^{-1}$. These SWCNT-based electrodes displayed a wide operating voltage of 4 V and high energy density of 94 Wh $kg^{-1}$ and power density of up to 210 kW $kg^{-1}$ in organic electrolyte. Kim et al.[53] synthesized vertically aligned double-walled CNTs grown on carbon papers and reported high electrochemical performance, viz. specific capacitance of 200 F $g^{-1}$, the maximum energy density of 20 Wh $kg^{-1,}$ and power density of 40 kW $kg^{-1}$ in 1 M $H_2SO_4$

electrolyte. Saghafi et al.[54] reported vertically aligned carbon nanotubes (VACNTs) grown on highly n-doped silicon substrates prepared via plasma-enhanced CVD process. The fabricated VACNT-based electrode exhibited a specific capacitance of 70 F $g^{-1}$, as compared to 8 F $g^{-1}$ of entangled carbon nanotube-based electrode in 0.5 M KCl electrolyte.

CNTs are a good choice for free-standing SCs electrodes because of their resilient and robust framework. Flexible and stretchable SCs with CNT-based electrodes have been explored to shed light on a wide range of stretchable energy storage devices. In addition, CNTs have been utilized to prevent the restacking of graphene sheets. Various methods such as CVD, hydrothermal treatment, electrophoretic deposition, etc. have been employed to prepare hybrid graphene/CNTs films.[57–59] The hybrids of 2D graphene materials and 1D CNTs have displayed improved electrochemical and mechanical properties compared to each of the individual components.

### 1.5.2 Metal Oxides

Metal oxides are regarded as promising electrode materials for PCs owing to their high specific capacitance and energy density resulting from surface redox reactions. To date, various metal oxides viz. $RuO_2$, $MnO_2$, $Fe_3O_4$, NiO, $V_2O_5$, etc. have been investigated as electrode materials for SCs. Among these metal oxides, $RuO_2$, $MnO_2$, and $Fe_3O_4$ have shown excellent capacitive performances. Nevertheless, most metal oxides have low electrical conductivity and thus the capacitances obtained from the metal oxide-based electrodes are far from the theoretical limit. Therefore, these materials are incorporated with conductive carbon materials to prepare composite materials to obtain superior performance.

### *1.5.2.1 Ruthenium dioxide ($RuO_2$)*

Ruthenium dioxide ($RuO_2$) has gotten a lot of interest as the most promising pseudocapacitor electrode material because of its low resistivity and great chemical and thermal stability.[60] $RuO_2$ offers a high theoretical specific capacitance under a wide operational potential (1.4 V) owing to its high electrical conductivity and multiple valance states for electron transition, i.e. $Ru^{2+}$, $Ru^{3+}$, $Ru^{4+,}$ and $Ru^{6+}$ [61]. However, the high cost and low abundance of $RuO_2$ significantly hinder its commercial application in SCs. It has been reported that amorphous $RuO_2$ exhibits higher specific capacitance than crystalline $RuO_2$ due to the presence of more electro-active sites. The double-layer capacitance accounts for about 10% of the charge stored in $RuO_2$ electrodes, whereas the majority is contributed by pseudocapacitance [62]. The protonation charge storage mechanism of $RuO_2$ can be described as:

$$RuO_2 + xH^+ + xe^- \longleftrightarrow RuO_{2-x}(OH)_x, 0 < x < 2 \qquad \text{(R 1.1)}$$

Many factors influence the performance of $RuO_2$, including crystallinity, water content, and particle size. It has been reported that the hydrous form of $RuO_2$ (i.e. $RuO_2{\cdot}xH_2O$) exhibits higher capacitance in comparison to the anhydrous form. Zheng et al. reported a hydrous $RuO_2$ electrode with an amorphous phase that can reach 720 F $g^{-1}$ after annealing at 150 °C.[63] When they raised the annealing temperature to convert $RuO_2$ to the crystalline phase, the specific capacitance drastically dropped to 19.2 F $g^{-1}$ at 400 °C. These findings revealed that protons can easily permeate into the hydrous $RuO_2$ in the amorphous phase, but that intercalation into a well-crystallized structure is difficult. Sugimoto et al.[61] attempted to explain the phenomena of the enhanced capacitance of $RuO_2{\cdot}xH_2O$. They proposed that anhydrous $RuO_2$ particles clump together with no available micropores for ion diffusion, whereas hydrous $RuO_2$ particles are smaller and have hydrated micropores

between them, allowing for good ion transport. As a result, the water content of $RuO_2$ is critical, as it is responsible for fast ionic conduction through the porous structure, which improves capacitive performance. Zheng et al.[64] electrodeposited $RuO_2.xH_2O$ thin-film electrodes on a titanium substrate, which exhibited excellent cycle stability, and good power capabilities with a high electrode specific capacitance of 786 F $g^{-1}$. Moreover, nanotubular arrayed electrodes of $RuO_2 \cdot xH_2O$ synthesized via anodic deposition technique achieved a high specific capacitance of 1300 F $g^{-1}$.

Due to the high cost of ruthenium oxide, several studies have focused on combining it with other low-cost materials. Moreover, pristine $RuO_2$ particles tend to agglomerate together, reducing their electrochemical performance dramatically [65]. In this context, various $RuO_2$/carbon composites were investigated as electrode materials for SCs for better energy-storage capacities and lower costs.[66] These composites benefit from the use of both the Faradaic and non-Faradaic mechanisms and exhibit large charge storage capacities. For instance, Naoi et al.[67] synthesized nanosized hydrous $RuO_2$/ketjen black composites using in situ sol-gel methods and reported a maximum specific capacitance of 821 $Fg^{-1}$. Similarly, laser-scribed graphene/$RuO_2$ nanocomposite-based electrodes displayed ultrahigh-specific capacitances up to 1139 F $g^{-1}$ [68].

#### *1.5.2.2 Manganese dioxide ($MnO_2$)*

Manganese dioxide is a viable substitute for $RuO_2$ because of its low cost, abundance, and environmental safety compared to other metal oxides, as well as the high theoretical specific capacitance of 1370 F $g^{-1}$.[69] The main charge storage processes for manganese oxides are pseudocapacitive (Faradic) reactions on the electrode surface and in the bulk of the electrode. Electrolyte cations (C+ = $H^+$, $Li^+$, $Na^+$, and $K^+$) adsorb on the surface of manganese oxide in the surface Faradaic reaction:[70,71]

$$(MnO_2)_{surface} + C^+ + e^- \longleftrightarrow (MnOOC)_{surface} \quad \text{(R 1.2)}$$

The bulk Faradaic reaction is based on electrolyte ion intercalation/deintercalation in the bulk manganese oxide:[70,71]

$$MnO_2 + C^+ + e^- \longleftrightarrow MnOOC \quad \text{(R 1.3)}$$

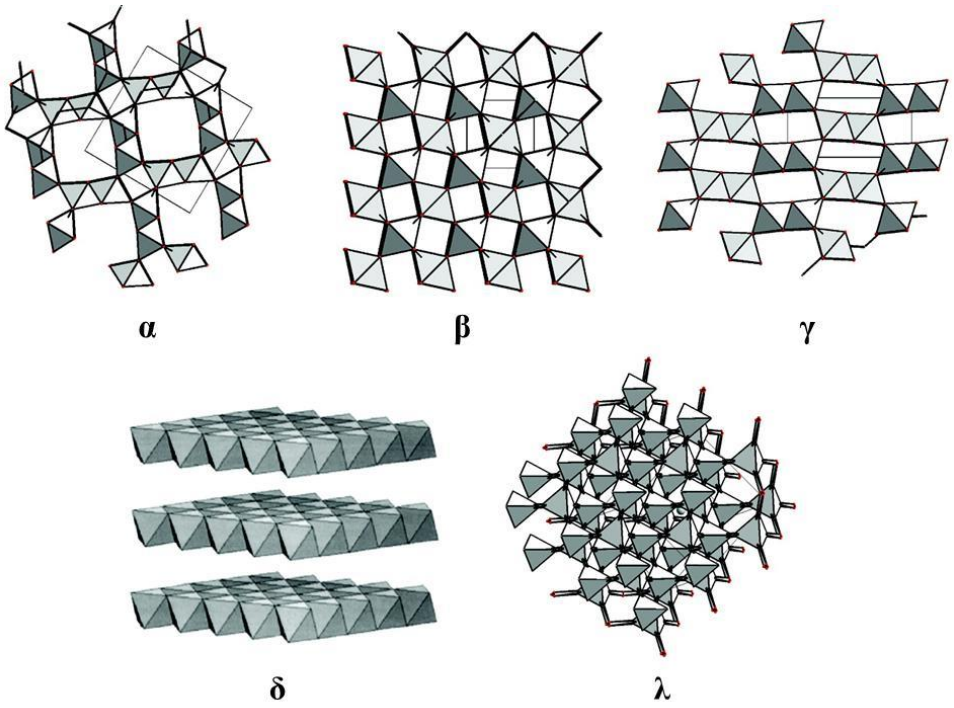


**Figure 1.9** Crystal structures of α-, β-, γ-, δ-, and λ-$MnO_2$ (Reproduced with permission [72]. Copyright 2008, ACS)

For the first time, Lee and Goodenough[73] reported $MnO_2$-based supercapacitors in aqueous electrolytes. The pseudocapacitive performance of manganese dioxides is influenced by physical and chemical factors.[74,75] The microstructure is primarily responsible for cycling stability, whereas the chemical hydrated state is primarily responsible for specific capacitance.[76] The crystallographic phases of $MnO_2$ (viz. α, β, γ, δ, and λ phases) influence the electrochemical performance of $MnO_2$. The α, β, and γ have a 1D tunnel structure, whereas δ and λ have 2D and 3D tunnel structures,

respectively (shown in **Figure 1.9**). Brousse et al.[77] and Devaraj et al.[72] investigated the capacitance of various $MnO_2$ structures in $K_2SO_4$ and $Na_2SO_4$ electrolytes, respectively, and reported that the specific capacitance of $MnO_2$ varies in the order of $\alpha \cong \delta > \gamma > \lambda > \beta$. It was perceived that the α and δ phase of $MnO_2$ possesses larger tunnel size in the crystal structure compared to other phases, which facilitate insertion of electrolyte ions during charge-discharge and resulted in higher capacitances.[72]

In addition to the crystal structure, the morphology of $MnO_2$ plays an important role in determining the capacitive performance. Therefore, $MnO_2$ nanostructures of different morphologies, viz. nanorods,[78] hollow spheres,[79] nanoflowers,[80] nanowires,[81] etc., have been explored as SC electrodes. These nanostructures displayed improved specific capacitance and rate capability along with good cycle stability. The 1D $MnO_2$ nanostructures (e.g. nanowires, nanorods, nanorods, etc.) can benefit from the rapid charge transport along the axial direction and shorter lengths of ion diffusion and electronic transport. For example, Li et al.[82] synthesized ultra-long α-$MnO_2$ nanowires by a facile hydrothermal route and these nanowire electrodes exhibited a specific capacitance of 345 F $g^{-1}$. On the other hand, 2D $MnO_2$ nanostructures can achieve enhanced capacitive performance due to high specific surface area and the presence of abundant electro-active sites available for surface redox reactions. For example, Liu et al.[83] synthesized single-layer $MnO_2$ nanosheets via a template-free method and the synthesized $MnO_2$ sheets displayed a high specific capacitance of 868 F $g^{-1}$.

In spite of its high theoretical capacitance, the low electrical conductivity of $MnO_2$ ($10^{-5}$ – $10^{-6}$ S $cm^{-1}$) hinders its charge transfer dynamics.[84,85] As a result, specific capacitances reported in the literature for pristine $MnO_2$ are far less as compared to the theoretical limit. In this context, combining $MnO_2$ with conductive

carbon materials in the form of composites is an efficient technique to improve the electrochemical performance and overcome the poor conductivity of $MnO_2$.[86–89] The carbon component not only increases the conductivity and electrochemical stability but also facilitates the diffusion of electrolyte ions. Besides, these $MnO_2$/carbon composites enable maximum utilization of the active surface area of the $MnO_2$ which is useful for effective charge transport. Consequently, enhanced capacitance, high cycle stability, and rate capability can be obtained from $MnO_2$/carbon nanocomposite-based electrodes. For instance, Chen et al.[90] reported $MnO_2$/rGO nanocomposite-based electrodes with a specific capacitance of 234.8 F $g^{-1}$ at 0.1 A $g^{-1}$ and excellent cycle stability (100% of capacitance retention over 20,000 cycles) in $Na_2SO_4$ electrolyte. Bai et al.[91] synthesized 3D-graphene/$MnO_2$ foam and obtained a specific capacitance of 333.4 F $g^{-1}$ at 0.2 A $g^{-1}$ along with good cycle stability. Wang et al.[92] fabricated stretchable supercapacitor electrodes of CNT-$MnO_2$ nanosheet composites, which exhibited a specific capacitance of 323.9 F $g^{-1}$ at 1.9 A $g^{-1}$ and 93.1% capacitance retention over 6000 cycles. Heteroatom-doped activated carbon/$MnO_2$ composite electrodes prepared by Wadekar et al.[93] exhibited a specific capacitance of 424 F $g^{-1}$, at a current density of 1 A $g^{-1}$. In another study, Ozkan et al.[94] synthesized ternary graphene/MWCNT/$MnO_2$ nanowire (GMM) composite grown on Ni foam via CVD and bath deposition method. The GMM-based electrodes demonstrated ultra-high specific capacitance of 1108.79 F $g^{-1}$, a superior energy density of 391.7 W h $kg^{-1}$, and 97.94% capacitance retention over 13,000 cycles at a wide operational potential window of 1.6 V in $Li_2SO_4$ electrolytes.

#### *1.5.2.3 Iron oxide ($Fe_3O_4$)*

$Fe_3O_4$ is a good pseudocapacitive material with a high theoretical capacitance ~ 2299 F $g^{-1}$.[95] Besides, the natural abundance, low cost, and environmental

compatibility of $Fe_3O_4$ are added merits. However, in practice, the specific capacitance values achieved using magnetite electrodes are far less due to low conductivity and the agglomeration of the $Fe_3O_4$ particles. For the first time, Wu et al.[96] investigated the capacitive performance of $Fe_3O_4$-based electrodes in different aqueous electrolytes. They obtained the highest specific capacitance of 510 F $g^{-1}$ and a wide operational potential window of 1.2 V in $Na_2SO_3$ electrolyte. The charge storage mechanism of $Fe_3O_4$ electrodes in $Na_2SO_3$ electrolyte can be expressed as:

$$FeO + SO_3^{2-} \longleftrightarrow FeSO_4 + 2e^- \quad \text{(R 1.4)}$$

$$2Fe^{II}O + SO_3^{2-} \longleftrightarrow \left(Fe^{III}O\right)^+ SO_3^{2-} \left(Fe^{III}O\right)^+ + 2e^- \quad \text{(R 1.5)}$$

Firstly, a faster surface redox reaction of sulphur was observed and given by Eq. (1.4). Secondly, oxidation/reduction redox reaction between Fe(II) and Fe(III) was observed (Eq. 1.5) along with probable intercalation of $SO_3^{2-}$ ions between the iron oxide layers for balancing the extra charge. Thereafter, Wang et al.[97] investigated the capacitance mechanism of $Fe_3O_4$ in $Na_2SO_3$, $Na_2SO_4$, and KOH electrolytes using X-ray photoelectron spectroscopy (XPS), and electrochemical quartz-crystal microbalance analysis. The specific capacitances of $Fe_3O_4$ electrodes were 170, 25, and 3 F $g^{-1}$ in $Na_2SO_3$, $Na_2SO_4$, and KOH electrolytes, respectively. It was apparent that the capacitance of $Fe_3O_4$ in $Na_2SO_3$ electrolyte is a combined effect of both the EDLC and pseudocapacitance involving successive reduction of specifically adsorbed $SO_3^{2-}$ ions as follows:

$$2SO_3^{2-} + 3H_2O + 4e^- \longleftrightarrow S_2O_3^{2-} + 6OH^- \quad \text{(R 1.6)}$$

$$S_2O_3^{2-} + 3H_2O + 8e^- \longleftrightarrow 2S^{2-} + 6OH^- \quad \text{(R 1.7)}$$

In the $Na_2SO_4$ electrolyte, the entire capacitance originated from double layer formation, whereas the small capacitance in the KOH electrolyte was caused by the

surface oxidation of $Fe_3O_4$ electrodes. In another study, Li and Liu[98] synthesized $Fe_3O_4$ nanorod films on Ti foils via hydrothermal and annealing methods. They used Dunn's method[99] to segregate the surface capacitive contribution from the capacitance originating from diffusion-controlled insertion process. The results of Dunn's method revealed the charge storage in $Fe_3O_4$ in $Li_2SO_4$ is mostly contributed by the insertion of $Li^+$ in the bulk, due to which the $Fe_3O_4$ nanorod electrodes suffered from poor rate capability. Wang et al.[100] synthesized amorphous $Fe_3O_4$ nanoparticles (NPs) via an ultrasound-assisted route using $FeCl_3$ and ethanolamine. The $Fe_3O_4$ nanoparticles displayed a high capacitance of 335 F $g^{-1}$ at 0.4 A $g^{-1}$, 100% capacitance retention over 2000 cycles, and good rate capability (in 1 M $Na_2SO_3$ electrolyte). Additionally, Zhao et al. synthesized zero-dimensional (0D) nanoparticles and one-dimensional (1D) nanowires of $Fe_3O_4$ via a hydrothermal method employing the spray deposition technique to prepare films.[101] The 1D $Fe_3O_4$ nanowires displayed a specific capacitance of 106 F $g^{-1}$ whereas the capacitance of $Fe_3O_4$ nanoparticles was 12 F $g^{-1}$.

Although $Fe_3O_4$ has high theoretical capacitance, the actual capacitances obtained from pristine $Fe_3O_4$-based supercapacitors are far less than the theoretical prediction. This unsatisfactory performance could be attributed to the poor conductivity and limited surface area (due to self–aggregation) of $Fe_3O_4$ particles. Therefore, many studies have focused on the composites of $Fe_3O_4$ and high surface areas of conductive carbon materials like porous carbon, activated carbon, graphene, carbon nanofibers, carbon nanotubes, etc. For example, Liu et al. [102] synthesize $Fe_3O_4$/GS nanocomposite paper employing vacuum filtration followed by a thermal reduction process. The optimized $Fe_3O_4$/GS composite paper (~ 64.8% $Fe_3O_4$ loading) with a surface area of 310 $m^2$ $g^{-1}$ displayed a specific capacitance of 368 F $g^{-1}$ at 1 A $g^{-1}$ and high cycle stability.

### 1.5.3 Conducting Polymers (CPs)

Conducting polymers and their derivatives have been widely researched as potential electrode materials for SCs. The high conductivity, fast charge-discharge environmental stability, and exceptional energy storage capacity make the CPs suitable electrode materials for SCs. The capacitance of CPs is primarily dependent on the redox processes. During the charge-discharge process in CP electrodes, redox reactions occur both at the surface as well as at the bulk of the material. However, these redox reactions do not involve any phase transformation. A conducting polymer must have charge carriers, charge mobility, simple kinetics, and readily available solvated counterions in order to achieve both high conductivity and electrochemical capacitance.[103] The charge carrier concentration in a CPs is increased via either removing electrons from the valence band (p-doping) or electron insertion into the conduction (n-doping) band via oxidation and reduction respectively. CPs are thus classified into two categories, viz. known as n-doped (negatively charged CPs) and p-doped (negatively charged CPs). It should be noted that CPs can only function properly within a certain potential range, and working outside of that range may induce CP degradation. As a result, selecting a proper prospective window is critical to CP-based electrodes. The most widely used conjugated CPs for SC applications are polypyrrole (PPy), polyaniline (PANI), and 3,4-ethylenedioxythiophene (PEDOT). PANI and PPy have been most extensively investigated due to their accessible redox states, high electrical conductibility, and tunable physical properties. Both PANI and PPy are essentially p-doped due to their low n-doping potentials, and therefore, they are used as positive electrode materials.

The high theoretical specific capacitance (~ 2,000 F $g^{-1}$ in $H_2SO_4$) and unique redox and acid-base doping/de-doping properties of PANI makes it a very attractive

PC material. Essentially, the electrochemical performance of PANI is collectively contributed by both its surface area and electron transfer reactions associated with the benzenoid and quinoid groups. Sivakumar et al.[104] used interfacial polymerization technique to synthesize PANI nanofibers and investigated their capacitive performance in 1 M $H_2SO_4$ electrolyte using a two-electrode cell. Although a high specific capacitance of 554 F $g^{-1}$ (1 A $g^{-1}$) was obtained, the cycle stability was significantly low for the PANI electrodes. Li et al.[105] investigated the theoretical and experimental capacitance of PANI in $H_2SO_4$ electrolyte. They reported that the experimentally obtained specific capacitance of PANI was only 30% of the theoretical value (2000 F $g^{-1}$). PPy is another extensively used CPs that have advantages like relatively high capacitance and facile synthesis. Li and Yang[106] used methyl orange-$FeCl_3$ complex as the self-degradable template to synthesize flexible PPy via a chemical oxidation method. The as-synthesized film consisted of PPy nanotubes (length of 5–6 μm and diameter 50–60 nm) when the molar ratio of $FeCl_3$ to monomer ratio was 0.5 and the film displayed a specific capacitance of 576 F $g^{-1}$ (at 0.2 A $g^{-1}$) in 1 M KCl electrolyte. Rajesh et al.[107] deposited phytic acid-doped polypyrrole thin films on stainless steel (SS) and titanium (Ti) substrates through an electro-polymerization method. The films deposited on SS and Ti substrates exhibited specific capacitances of 297, and 343 F $g^{-1}$ at 5 mV $s^{-1}$, respectively in 1 M $H_2SO_4$ electrolyte.

Although pure CPs have several unique features, their standalone application in high-performance SCs is limited due to the poor stabilities during the charging and discharging process. Large volumetric swelling and shrinking during the charge-discharge process lead to structural collapse of the CP electrodes, which results in capacitance fading and poor cycle life. To overcome the issue of mechanical

degradation as well as to improve the cycle stability, composite electrodes based on CPs and other electro-active materials are synthesized. As compared to pure CPs, these composites exhibit superior capacitive performance.

### 1.5.4 Composite Materials

In the previous sections, we have discussed various electrode materials used in supercapacitors. **Tables 1.1** and **1.2** summarize the capacitive performances of different materials, viz. carbon materials, metal oxides, and conducting polymers. Each of these materials has its own merits and shortcomings. To achieve superior electrochemical performances, hybrid composite materials are prepared by combing different (two or more) materials. This hybrid composite material exhibit enhanced electrochemical performance by benefiting from the advantages of each individual component. Also, the rationally designed structure of these composites could substantially alleviate the electrochemical properties via a synergistic effect. In practice, pseudocapacitive materials like oxides/conducting polymers are combined with carbon materials to obtain composite materials with enhanced conductivity, high stability, better charge transport properties, etc. These features ultimately result in excellent capacitive performances (viz. high specific capacitance, rate capability, and cycling life) for the composite-based supercapacitors. The electrochemical performances of various composites such as $MnO_2$/graphene, $RuO_2$/carbon fiber, CNT/cubic $Fe_3O_4$, PANI/carbon sphere, etc. have been summarized in **Table 1.3**.

**Table 1.1** Summary of the capacitive performances of carbon-based electrode materials

| Electrode Material | Electrolyte | Specific Capacitance | Cycle stability | Ref. |
|---|---|---|---|---|
| Thermally reduced graphene | 30 wt.% KOH | 150 F $g^{-1}$ at 0.1 A $g^{-1}$ | 100% after 500 cycles | 108 |
| B-doped rGO | 6 M KOH | #200 F $g^{-1}$ at 0.1 A $g^{-1}$ | 95% after 4500 cycles | 109 |
| rGO/CF film | 1 M $H_2SO_4$ | 214 F $g^{-1}$ at 0.5 A $g^{-1}$ | 90% after 10000 cycles | 110 |
| rGO on carbon cloth | 1 M $H_2SO_4$ | #185.7 F $g^{-1}$ at 1.3 A $g^{-1}$ | 60.5 after 3000 cycles | 111 |
| 3DrGO@Cu foam | Phosphate buffer | 623 F $g^{-1}$ at 1.3 A $g^{-1}$ | 100% after 2000 cycles | 112 |
| N/P-rGO | 6 M KOH | 165 F $g^{-1}$ at 0.1 A $g^{-1}$ | 91% after 2000 cycles | 113 |
| Exfoliated Graphene | 30 wt.% KOH | 264 F $g^{-1}$ at 0.1 A $g^{-1}$ | 97% after cycles | 114 |
| Graphene hydrogels | 5 M KOH | 220 F $g^{-1}$ at 1 A $g^{-1}$ | 92% after 2000 cycles | 115 |
| Holey graphene | EMIMB$F_4$/AN | 298 F $g^{-1}$ at 1 A $g^{-1}$ | 91% after 10000 cycles | 116 |
| KOH activated rGO | BMIM $BF_4$/AN | #166 F $g^{-1}$ at 5.7 A $g^{-1}$ | 100% after 10000 cycles | 117 |
| N-doped graphene | TEA $BF_4$/AN | 280 F $g^{-1}$ at 1 A $g^{-1}$ | 99.8% after 10000 cycles | 118 |
| N-doped graphene hydrogel | 5 M KOH | #131.1 F $g^{-1}$ at 80 A $g^{-1}$ | 95.2% after 4000 cycles | 119 |
| Graphene aerogels | 0.5 M $H_2SO_4$ | 325 F $g^{-1}$ at 1 A $g^{-1}$ | 98% after 10000 cycles | 120 |
| SWCNT | $Et_4NBF_4$/PC | #160 F $g^{-1}$ at 1 A $g^{-1}$ | 96.4% after 1000 cycles | 56 |
| VACNT | 0.5 M KCl | 70 F$g^{-1}$ at 5 A $g^{-1}$ | 90% after 1000 cycles | 54 |
| Functionalized CNT | 0.075 M HQ + $H_2SO_4$ | 3199 F $g^{-1}$ at 5 mV $s^{-1}$ | 70% after 350 cycles | 121 |
| N-doped CNTs | 6 M KOH | 205 F $g^{-1}$ at 1 A $g^{-1}$ | 92.8% after 1000 cycles | 122 |
| N-doped spherical CNT | 1 M $H_2SO_4$ | 215 F $g^{-1}$ at 0.2 A $g^{-1}$ | 99% after 1500 cycles | 52 |
| 3D CNT-aerogel | 1 M $H_2SO_4$ | 160.8 F $g^{-1}$ at 0.5 mA | 94.7% after 10000 cycles | 123 |
| Lignin-derived AC | 6 M KOH | 312 F $g^{-1}$ at 1 A $g^{-1}$ | 98% after 20000 cycles | 25 |
| Grapefruit peel derived AC | 1M H2SO4 | 311 F $g^{-1}$ at 0.1 A $g^{-1}$ | 94.05 % after 10000 cycles | 124 |
| Soybean lecithin derived AC | 1 M KOH | 285 F $g^{-1}$ at 0.5 A $g^{-1}$ | 92% after 20000 cycles | 125 |
| Chitosan derived AC | 6 M KOH | 252 F $g^{-1}$ at 0.5 $g^{-1}$ | 99.3% after 10000 cycles | 26 |
| Rape pollen derived AC | 6 M KOH | 390 F $g^{-1}$ at 0.5 A $g^{-1}$ | 92.9% after 10000 cycles | 126 |
| Fallen leaves derived AC | 6 M KOH | 223 F $g^{-1}$ at 0.5 A $g^{-1}$ | 100 % after 2000 cycles | 127 |
| Potato waste derived AC | 2 M KOH | 255 F $g^{-1}$ at 1 A $g^{-1}$ | 93.7% after 5000 cycles | 128 |
| Sugarcane bagasse derived AC | 6 M KOH | #142.1 F $g^{-1}$ at 0.5 A $g^{-1}$ | 93.9% after 5000 cycles | 129 |
| Sunflower stalk derived AC | 6 M KOH | 365 F $g^{-1}$ 0.5 A $g^{-1}$ | 95% after 15 000 cycles | 130 |
| Pine nut shell derived AC | 6 M KOH | 324 F $g^{-1}$ at 0.05 A $g^{-1}$ | 94.6% after 10000 cycles | 131 |
| Polymer-derived N-doped AC | 6 M KOH | 250 F $g^{-1}$ at 0.5 A $g^{-1}$ | 95.75% after 10000 cycles | 132 |

EMIMBF4: 1-ethyl-3-methylimidazolium tetrafluoroborate; AN: acetonitrile; BMIM $BF_4$: 1-butyl-3-methyl-imidazolium tetrafluoroborate; TEA $BF_4$: tetraethylammonium-tetrafluoroborate, Et4NBF4: Tetraethylammonium-tetrafluoroborate; PC: propylene carbonate; HQ: hydroquinone, # two-electrode data

**Table 1.2** Summary of capacitive performances of metal oxides and conducting polymer-based electrode materials

| Electrode Material | Electrolyte | Specific Capacitance | Cycle stability | Ref. |
|---|---|---|---|---|
| $RuO_2 \cdot nH_2O$ | 0.5 M $H_2SO_4$ | 786 F $g^{-1}$ at 100 μA $cm^{-2}$ | 95% after 200 cycles | 64 |
| mulberry-like $RuO_2$ | 1 M $H_2SO_4$ | 400 F·$g^{-1}$ at 0.2 A·$g^{-1}$ | 84.7% after 6000 cycles | 133 |
| $RuO_x \cdot nH_2O$ | 0.5 M $H_2SO_4$ | 1340 F·$g^{-1}$ at 25 mV·$s^{-1}$ | | 134 |
| Amorphous $RuO_2$ | 0.5 M $H_2SO_4$ | 551 F·$g^{-1}$ at 5 mV·$s^{-1}$ | | 135 |
| α-$MnO_2$ nanorods | 1 M $Na_2SO_4$ | 182 F $g^{-1}$ at 2 A $g^{-1}$ | 100% after 2000 cycles | 78 |
| $MnO_2$ nanowires on Ni foam | 6 M KOH | 641 F $g^{-1}$ at 2 A $g^{-1}$ | 97% after 2000 cycles | 81 |
| α-$MnO_2$ nanowires | 0.5 M $Na_2SO_4$ | 345 F $g^{-1}$ at 1 A $g^{-1}$ | 100% after 2000 cycles | 82 |
| Single-layer $MnO_2$ nanosheets | 1 M $Na_2SO_4$ | 868 F $g^{-1}$ at 3 A $g^{-1}$ | 91% after 10000 cycles | 83 |
| α-$MnO_2$ nanoneedles | 1 M $Na_2SO_4$ | 289 F $g^{-1}$ at 0.5 A $g^{-1}$ | 88% after 10000 cycles | 136 |
| Multidimensional $MnO_2$ | 1 M $Na_2SO_4$ | 311.52 F $g^{-1}$ at 0.3 A $g^{-1}$ | 80% after 2000 cycles | 137 |
| Hollow $MnO_2$ nanofibers | 1 M $Na_2SO_4$ | 291 F $g^{-1}$ at 1 A $g^{-1}$ | 90.9% after 5000 cycles | 138 |
| $Fe_3O_4$ nanorod film | 2.5 M $Li_2SO_4$ | 314 F $g^{-1}$ at 5 mV·$s^{-1}$ | | 98 |
| Amorphous $Fe_3O_4$ | 1 M $Na_2SO_3$ | 335.5 F $g^{-1}$ at 0.4 A $g^{-1}$ | 43.3% after 2000 cycles | 100 |
| $Fe_3O_4$ nanorods | 1 M $Na_2SO_3$ | 208.6 F $g^{-1}$ at 0.5 A $g^{-1}$ | 73.2 % after 500 cycles | 139 |
| $Fe_3O_4$ nanodiscs | 6 M KOH | 920 F $g^{-1}$ at 1.5 A $g^{-1}$ | 87.8% after 10000 cycles | 140 |
| $Fe_3O_4$ nanoparticles | 2 M $Na_2SO_3$ | 336 F $g^{-1}$ at 1 A $g^{-1}$ | 80.4% after 1000 cycles | 141 |
| $Fe_2O_3$ nanoneedles | 1 M $Na_2SO_4$ | 418.7 F $g^{-1}$ at 10 mV $s^{-1}$ | 93.3% after 5000 cycles | 142 |
| Mesoporous $Fe_2O_3$ | 1 M KOH | 469 F$g^{-1}$ at 2 m$Vs^{-1}$ | 84% after 2000 cycles | 143 |
| NiO nanobelts | 2 M KOH | 600 F $g^{-1}$ at 5 A $g^{-1}$ | 94% after 2000 cycles | 144 |
| Hollow nanostructures composed of NiO nanosheets | 2 M KOH | 642 F $g^{-1}$ at 3 A $g^{-1}$ | 94.4% after 1000 cycles | 145 |
| Porous hollow $Co_3O_4$ | 3 M KOH | 1100 F $g^{-1}$ at 1.25 A $g^{-1}$ | 95.1% after 6000 cycles | 146 |
| $Co_3O_4$nanowire | 2 M KOH | 754 F $g^{-1}$ at 2 A $g^{-1}$ | 100% after 4000 cycles | 147 |
| $V_2O_5$ nanosheets | 1 M $Na_2SO_4$ | 451 F $g^{-1}$ at 0.5 A $g^{-1}$ | 90% after 4000 cycles | 148 |
| $V_2O_5$ nanowires | 1 M $Na_2SO_4$ | 832 F $g^{-1}$ at 1 A $g^{-1}$ | 94.6% after 10000 cycles | 149 |
| PANI nanowires | 1 M $HClO_4$ | 950 F $g^{-1}$ at 1 A $g^{-1}$ | 78% after 500 cycles | 150 |
| Polypyrrole film | 1 M KCl | 576 F $g^{-1}$ at 0.2 A $g^{-1}$ | 82% after 1000 cycles | 106 |
| Polythiophene thin films | 0.1 M $LiClO_4$ in PC | 252 F $g^{-1}$ at 5 mV $s^{-1}$ | 85% after 1000 cycles | 151 |
| Polyethylenedioxythiophene (PEDOT) paper | PVA–$H_2SO_4$ | [#]115 F $g^{-1}$ at 0.4 mA $cm^{-2}$ | 91% after 2500 cycles | 152 |

[#] two-electrode data

**Table 1.3** Summary of capacitive performances of composite electrode materials

| Electrode Material | Electrolyte | Specific Capacitance | Cycle stability | Ref. |
|---|---|---|---|---|
| Laser-scribed graphene/$RuO_2$ | 1 M $H_2SO_4$ | 1139 F $g^{-1}$ at 30 A $g^{-1}$ | 93% after 4000 cycles | 68 |
| GO/ $RuO_2$ aerogel | 3 M $H_2SO_4$ | 328.6 F $g^{-1}$ at 5 mV $s^{-1}$ | 82.81% after 5000 cycles | 153 |
| $RuO_2$/carbon fiber | 2 M $H_2SO_4$ | 544 F $g^{-1}$ at 2 mV $s^{-1}$ | 97% after 2000 cycles | 154 |
| $RuO_2$/charcoal-derived carbon | 2 M $H_2SO_4$ | 510 F $g^{-1}$ at 1 A $g^{-1}$ | 87.05% after 3000 cycles | 155 |
| $RuO_2$-graphene -CNT | 3 M KOH | 480.3 F $g^{-1}$ at 0.5 mA $cm^{-2}$ | 92.7% after 10000 cycles | 156 |
| rGO/$MnO_x$ | 0.5 M $Na_2SO_4$ | 202 F $g^{-1}$ at 1 mV $s^{-1}$ | 106% after 115000 cycles | 86 |
| $MnO_2$/CNT | 1 M $Na_2SO_4$ | 257.8 F $g^{-1}$ at 2 mV $s^{-1}$ | 63% after 800 cycles | 157 |
| $MnO_2$/3D porous carbon | 1 M $Na_2SO_4$ | 139.6 F $g^{-1}$ at 300 mA $g^{-1}$ | 92.3% after 1000 cycles | 158 |
| Graphene aerogel/$MnO_2$ | 3 M LiCl | 231.9 F $g^{-1}$ at 0.5 mA $cm^{-2}$ | 92.9% after 20,000 cycles | 159 |
| Graphene/$MnO_2$/CNT | 1 M $Na_2SO_4$ | 288 F $g^{-1}$ at 50 mV $s^{-1}$ | 95% after 1000 cycles | 160 |
| $MnO_2$–rGO/Carbon fiber paper | 0.5 M $Na_2SO_4$ | 393 F $g^{-1}$ at 0.1 A $g^{-1}$ | 98.5% after 2000 cycles | 161 |
| $Fe_3O_4$-carbon nanosheets | 1 M $Na_2SO_3$ | 163.4 F $g^{-1}$ at 1 A $g^{-1}$ | 93% after 5000 cycles | 162 |
| CNT/cubic $Fe_3O_4$ | 6 M KOH | 117.2 F $g^{-1}$ at 10 mA $cm^{-2}$ | 91% after 500 cycles | 163 |
| $FeO_x$/CNF | 1 M $Na_2SO_4$ | 436 F·$g^{-1}$ at 1 A·$g^{-1}$ | 89% after 5000 cycles | 164 |
| $Fe_3O_4$/Nitrogen-Doped Carbon | 3 M KOH | 522.7 F $g^{-1}$ at 0.5 A $g^{-1}$ | 91.9% after 5000 cycles | 165 |
| NiO/graphene oxide | 0.5 M KOH | 569 F $g^{-1}$ at 5 A $g^{-1}$ | 100% after 3000 cycles | 166 |
| NiO encapsulated nitrogen-rich carbon hollow spheres | 1 M KOH | 1130 F $g^{-1}$ at 2.27 A $g^{-1}$ | 100% after 50000 cycles | 167 |
| 3D graphene/$Co_3O_4$ | 2 M KOH | 1100 F $g^{-1}$ at 10 A $g^{-1}$ | 100% after 1000 cycles | 168 |
| $Co_3O_4$/N-doped carbon hollow spheres | 2 M KOH | 581 F $g^{-1}$ at 1 A $g^{-1}$ | 95.2% after 5000 cycles | 169 |
| Graphene /$V_2O_5$ | 1 M $LiClO_4$/PC | 384 F $g^{-1}$ at 0.1 A $g^{-1}$ | 82.2% after 10000 cycles | 170 |
| Carbon coated $V_2O_5$ nanorods | 0.5 M $K_2SO_4$ | 487 $Fg^{-1}$ at 0.5 $Ag^{-1}$ | 84% after 2000 cycles | 171 |
| $Fe_2O_3$/N-rGO | 1 M KOH | 618 F $g^{-1}$ at 0.5 $Ag^{-1}$ | 56.7% after 5000 cycles | 172 |
| α-$Fe_2O_3$/rGO | 1 M KOH | 903 F $g^{-1}$ at 1 A $g^{-1}$ | 70% after 1000 cycles | 173 |
| $Fe_2O_3$/hemp straw-based porous carbon | 6 M KOH | 256 F $g^{-1}$ at 1 A $g^{-1}$ | 72.6% after 1000 cycles | 174 |
| polyaniline deposited on hollow carbon spheres | 1 M $H_2SO_4$ | 435 F $g^{-1}$ at 0.5 A $g^{-1}$ | 60% after 2000 cycles | 175 |
| graphene/polypyrrole | 1 M LiCl/PVA | #414 F $g^{-1}$ at 0.2 mA $cm^{-2}$ | 95.7% after 10000 cycles | 176 |
| Nitrogen-doped graphene and conducting polymer PEDOT | PVA-$H_2SO_4$ | #536 F $g^{-1}$ at 0.5 A $g^{-1}$ | 125% after 3000 cycles | 177 |

# two-electrode data

## 1.6 AIM, APPROACH AND SCOPE OF THE PRESENT THESIS

Based on the discussion given in previous sections, it could be perceived that primary challenge of research and development in supercapacitors is to improve the energy density while retaining high power density and excellent cycle life. The energy density of supercapacitors can be augmented by increasing the capacitance and/or widening the cell voltage. Although high operational voltages can be obtained in organic and ionic liquid electrolytes, these electrolytes are cost-prohibitive, flammable, and possess environmental concerns. In this context, low-cost, highly conductive, and environment–friendly aqueous electrolytes are appealing and safer alternatives. Essentially, the electrode material plays a pivotal role in the electrochemical performance of the supercapacitors. This thesis focuses on the development of high energy density supercapacitors (with commercial-level mass loadings) using advanced electrode materials. In addition, various electrolyte modification techniques have been also studied to augment the energy density.

The following approach has been undertaken for exploring new routes for synthesis efficient materials:

a) Synthesis of nanostructured electrode materials using various protocols, viz. ultrasound-assisted method, co-pyrolysis and activation, etc.

b) Physicochemical characterization of synthesized materials with a variety of analytical methods, including field emission scanning electron microscopy (FE-SEM), transmission electron microscopy (TEM), X-ray diffraction (XRD), energy-dispersive X-ray spectroscopy (EDX), Raman spectroscopy, Brunauer–Emmett–Teller (BET) surface area analysis, etc.

c) Preparation of electrode slurry by mixing the active materials with conductive agent and binder. The slurry is coated on a current collector substrate and dried.

Next, working electrodes of designed sizes are punched out for supercapacitor cell assembly

d) Assembling of supercapacitor cells and investigation of its electrochemical performance using standard electrochemical techniques, viz. cyclic voltammetry (CV), galvanostatic charge-discharge (GCD), and electrochemical impedance spectroscopy (EIS).

## 1.7 THESIS OUTLINE

This thesis comprises of six chapters. The brief summaries of the contents of these chapters are given below:

**Chapter 1:** This chapter presents general introduction and fundamentals of supercapacitors including the charge storage mechanisms, various components, and electrochemical investigation techniques. Subsequently, a brief review of the state–of–the–art literature on various promising supercapacitor electrode materials and their electrochemical performances has been presented. Finally, the broad aim, approach, and scope of the present thesis have been outlined.

**Chapter 2:** This chapter presents a facile ultrasound-assisted synthesis of $Fe_3O_4$/reduced graphene oxide (rGO) nanocomposites for supercapacitor applications. The $Fe_3O_4$/rGO nanocomposite has been extensively characterized using standard techniques, viz. XRD, Raman spectroscopy, FE-SEM, TEM, BET, etc. All-solid-state supercapacitors were fabricated using $Fe_3O_4$/rGO electrodes and PVA/KOH gel electrolyte, and the electrochemical performances were investigated. The merits of ultrasound-assisted synthesis method for improved capacitive performance of $Fe_3O_4$/rGO have been discussed.

**Chapter 3:** This chapter describes ultrasound-assisted synthesis of a ternary nanocomposite of multi-walled carbon nanotube (MWCNT)/$MnO_2$/ rGO as well as binary nanocomposites of $MnO_2$/rGO and $MnO_2$/MWCNT. Various standard physicochemical characterizations were performed to deduce properties of these nanocomposites. Electrochemical performances of the nanocomposites have been investigated at commercial-level electrode mass loadings.

**Chapter 4:** This chapter provides an eco–friendly and sustainable approach for developing high–energy–density aqueous supercapacitors. Firstly, capacitive performances of rGO-based symmetric supercapacitors (rGO–SCs) with commercial–level electrode mass loadings have been investigated in different aqueous electrolytes. The energy densities of the rGO–SCs have been augmented with two facile strategies: (i) using pseudo faradaic contributions from redox-active electrolyte, and (ii) widening the cell voltage using a low–cost water–in–salt (WIS) electrolyte.

**Chapter 5:** This chapter demonstrates a scalable synthesis of oxygen-enriched porous carbon (PC–*x*) via co-pyrolysis and KOH activation of a ternary mixture of biomass (viz. sugarcane bagasse, water hyacinth, and yellow oleander). The synthesized PC–*x* have been characterized using standard techniques. The influence of KOH/char weight ratio (*x*) on the micro/mesopore volume, surface functionalities, and capacitive performances were studied. High voltage supercapacitors were assembled in neutral aqueous electrolytes and electrochemical performances were evaluated. Furthermore, the energy density of the device was augmented using a redox-active electrolyte.

**Chapter 6:** This chapter provides an overview of all studies in this thesis. A critical comparison is made of various approaches adopted for efficient supercapacitor fabrication, viz. using new techniques of sonication or use of activated carbon derived

from biomass or new redox-active and water-in-salt electrolytes. The merits and shortfalls of these approaches have been discussed. Based on the results of the present study, scope for future research in the area supercapacitors has been outlined.

## REFERENCES


(1) Transformation – Key World Energy Statistics 2021 – Analysis - IEA https://www.iea.org/reports/key-world-energy-statistics-2021/transformation#electricity-generation (accessed Feb 4, 2022).

(2) Net Zero by 2050 – Analysis - IEA https://www.iea.org/reports/net-zero-by-2050 (accessed Feb 4, 2022).

(3) Winter, M.; Brodd, R. J. What Are Batteries, Fuel Cells, and Supercapacitors? *Chem. Rev.* **2004**, *104* (10), 4245–4269.

(4) Wang, J. G.; Kang, F.; Wei, B. Engineering of MnO2-Based Nanocomposites for High-Performance Supercapacitors. *Prog. Mater. Sci.* **2015**, *74*, 51–124.

(5) Zhong, C.; Deng, Y.; Hu, W.; Qiao, J.; Zhang, L.; Zhang, J. A Review of Electrolyte Materials and Compositions for Electrochemical Supercapacitors. *Chem. Soc. Rev.* **2015**, *44* (21), 7484–7539.

(6) Wei, L.; Sevilla, M.; Fuertes, A. B.; Mokaya, R.; Yushin, G. Hydrothermal Carbonization of Abundant Renewable Natural Organic Chemicals for High-Performance Supercapacitor Electrodes. *Adv. Energy Mater.* **2011**, *1* (3), 356–361.

(7) González, A.; Goikolea, E.; Barrena, J. A.; Mysyk, R. Review on Supercapacitors: Technologies and Materials. *Renew. Sustain. Energy Rev.* **2016**, *58*, 1189–1206.

(8) Zhang, Q.-Z.; Zhang, D.; Miao, Z.-C.; Zhang, X.-L.; Chou, S.-L. Research Progress in $MnO_2$ -Carbon Based Supercapacitor Electrode Materials. *Small* **2018**, *14* (24), 1702883.

(9) Shao, Y.; El-Kady, M. F.; Sun, J.; Li, Y.; Zhang, Q.; Zhu, M.; Wang, H.; Dunn, B.; Kaner, R. B. Design and Mechanisms of Asymmetric Supercapacitors. *Chem. Rev.* **2018**, *118* (18), 9233–9280.

(10) Miller, J. R.; Simon, P. Materials Science: Electrochemical Capacitors for Energy Management. *Science (80-. ).* **2008**, *321* (5889), 651–652.

(11) Wu, Z.; Li, L.; Yan, J. M.; Zhang, X. B. Materials Design and System Construction for Conventional and New-Concept Supercapacitors. *Adv. Sci.* **2017**, *4* (6), 1600382.

(12) Zhang, L.; Zhao, X. S. Carbon-Based Materials as Supercapacitor Electrodes. *Chem. Soc. Rev.* **2009**, *38* (9), 2520–2531.

(13) Huang, J.; Sumpter, B. G.; Meunier, V. A Universal Model for Nanoporous Carbon Supercapacitors Applicable to Diverse Pore Regimes, Carbon Materials, and Electrolytes. *Chem. - A Eur. J.* **2008**, *14* (22), 6614–6626.

(14) Huang, J.; Sumpter, B. G.; Meunier, V. Theoretical Model for Nanoporous Carbon Supercapacitors. *Angew. Chemie* **2008**, *120* (3), 530–534.

(15) de Levie, R. On Porous Electrodes in Electrolyte Solutions. I. Capacitance Effects. *Electrochim. Acta* **1963**, *8* (10), 751–780.

(16) Augustyn, V.; Simon, P.; Dunn, B. Pseudocapacitive Oxide Materials for High-Rate Electrochemical Energy Storage. *Energy Environ. Sci.* **2014**, *7* (5), 1597–1614.

(17) Zhi, M.; Xiang, C.; Li, J.; Li, M.; Wu, N. Nanostructured Carbon-Metal Oxide Composite Electrodes for Supercapacitors: A Review. *Nanoscale* **2013**, *5* (1), 72–88.

(18) Pal, B.; Yang, S.; Ramesh, S.; Thangadurai, V.; Jose, R. Electrolyte Selection for Supercapacitive Devices: A Critical Review. *Nanoscale Adv.* **2019**, *1* (10), 3807–3835.

(19) Zhang, S.; Pan, N. Supercapacitors Performance Evaluation. *Adv. Energy Mater.* **2015**, *5* (6), 1401401.

(20) Choudhury, B. J.; Roy, K.; Moholkar, V. S. Improvement of Supercapacitor Performance through Enhanced Interfacial Interactions Induced by Sonication. *Ind. Eng. Chem. Res.* **2021**, *60* (20), 7611–7623.

(21) Raymundo-Piñero, E.; Kierzek, K.; Machnikowski, J.; Béguin, F. Relationship between the Nanoporous Texture of Activated Carbons and Their Capacitance Properties in Different Electrolytes. *Carbon N. Y.* **2006**, *44* (12), 2498–2507.

(22) Endo, M.; Maeda, T.; Takeda, T.; Kim, Y. J.; Koshiba, K.; Hara, H.; Dresselhaus, M. S. Capacitance and Pore-Size Distribution in Aqueous and Nonaqueous Electrolytes Using Various Activated Carbon Electrodes. *J. Electrochem. Soc.* **2001**, *148* (8), A910.

(23) Qu, D.; Shi, H. Studies of Activated Carbons Used in Double-Layer

Capacitors. *J. Power Sources* **1998**, *74* (1), 99–107.

(24) Kierzek, K.; Frackowiak, E.; Lota, G.; Gryglewicz, G.; Machnikowski, J. Electrochemical Capacitors Based on Highly Porous Carbons Prepared by KOH Activation. *Electrochim. Acta* **2004**, *49* (4), 515–523.

(25) Zhang, L.; You, T.; Zhou, T.; Zhou, X.; Xu, F. Interconnected Hierarchical Porous Carbon from Lignin-Derived Byproducts of Bioethanol Production for Ultra-High Performance Supercapacitors. *ACS Appl. Mater. Interfaces* **2016**, *8* (22), 13918–13925.

(26) Deng, X.; Zhao, B.; Zhu, L.; Shao, Z. Molten Salt Synthesis of Nitrogen-Doped Carbon with Hierarchical Pore Structures for Use as High-Performance Electrodes in Supercapacitors. *Carbon N. Y.* **2015**, *93*, 48–58.

(27) Cai, Y.; Luo, Y.; Dong, H.; Zhao, X.; Xiao, Y.; Liang, Y.; Hu, H.; Liu, Y.; Zheng, M. Hierarchically Porous Carbon Nanosheets Derived from Moringa Oleifera Stems as Electrode Material for High-Performance Electric Double-Layer Capacitors. *J. Power Sources* **2017**, *353*, 260–269.

(28) Li, Z.; Liang, Q.; Yang, C.; Zhang, L.; Li, B.; Li, D. Convenient Preparation of Nitrogen-Doped Activated Carbon from Macadamia Nutshell and Its Application in Supercapacitor. *J. Mater. Sci. Mater. Electron.* **2017**, *28* (18), 13880–13887.

(29) Pandolfo, A. G.; Hollenkamp, A. F. Carbon Properties and Their Role in Supercapacitors. *J. Power Sources* **2006**, *157* (1), 11–27.

(30) Compton, O. C.; Nguyen, S. T. Graphene Oxide, Highly Reduced Graphene Oxide, and Graphene: Versatile Building Blocks for Carbon-Based Materials. *Small* **2010**, *6* (6), 711–723.

(31) Lemine, A. S.; Zagho, M. M.; Altahtamouni, T. M.; Bensalah, N. Graphene a Promising Electrode Material for Supercapacitors—A Review. *Int. J. Energy Res.* **2018**, *42* (14), 4284–4300.

(32) Stoller, M. D.; Park, S.; Yanwu, Z.; An, J.; Ruoff, R. S. Graphene-Based Ultracapacitors. *Nano Lett.* **2008**, *8* (10), 3498–3502.

(33) Wang, Y.; Shi, Z.; Huang, Y.; Ma, Y.; Wang, C.; Chen, M.; Chen, Y. Supercapacitor Devices Based on Graphene Materials. *J. Phys. Chem. C* **2009**, *113* (30), 13103–13107.

(34) Lee, J. S.; Kim, S. I.; Yoon, J. C.; Jang, J. H. Chemical Vapor Deposition of Mesoporous Graphene Nanoballs for Supercapacitor. *ACS Nano* **2013**, *7* (7),

6047–6055.

(35) Vivekchand, S. R. C.; Rout, C. S.; Subrahmanyam, K. S.; Govindaraj, A.; Rao, C. N. R. Graphene-Based Electrochemical Supercapacitors. *J. Chem. Sci. 2008 1201* **2008**, *120* (1), 9–13.

(36) Zhao, B.; Liu, P.; Jiang, Y.; Pan, D.; Tao, H.; Song, J.; Fang, T.; Xu, W. Supercapacitor Performances of Thermally Reduced Graphene Oxide. *J. Power Sources* **2012**, *198*, 423–427.

(37) Luo, J.; Jang, H. D.; Huang, J. Effect of Sheet Morphology on the Scalability of Graphene-Based Ultracapacitors. *ACS Nano* **2013**, *7* (2), 1464–1471.

(38) Zhang, K.; Mao, L.; Zhang, L. L.; On Chan, H. S.; Zhao, X. S.; Wu, J. Surfactant-Intercalated, Chemically Reduced Graphene Oxide for High Performance Supercapacitor Electrodes. *J. Mater. Chem.* **2011**, *21* (20), 7302–7307.

(39) Shao, Y.; El-Kady, M. F.; Wang, L. J.; Zhang, Q.; Li, Y.; Wang, H.; Mousavi, M. F.; Kaner, R. B. Graphene-Based Materials for Flexible Supercapacitors. *Chem. Soc. Rev.* **2015**, *44* (11), 3639–3665.

(40) Yan, J.; Wei, T.; Shao, B.; Ma, F.; Fan, Z.; Zhang, M.; Zheng, C.; Shang, Y.; Qian, W.; Wei, F. Electrochemical Properties of Graphene Nanosheet/Carbon Black Composites as Electrodes for Supercapacitors. *Carbon N. Y.* **2010**, *48* (6), 1731–1737.

(41) Yang, S. Y.; Chang, K. H.; Tien, H. W.; Lee, Y. F.; Li, S. M.; Wang, Y. S.; Wang, J. Y.; Ma, C. C. M.; Hu, C. C. Design and Tailoring of a Hierarchical Graphene-Carbon Nanotube Architecture for Supercapacitors. *J. Mater. Chem.* **2011**, *21* (7), 2374–2380.

(42) Dey, R. S.; Hjuler, H. A.; Chi, Q. Approaching the Theoretical Capacitance of Graphene through Copper Foam Integrated Three-Dimensional Graphene Networks. *J. Mater. Chem. A* **2015**, *3* (12), 6324–6329.

(43) El-Kady, M. F.; Strong, V.; Dubin, S.; Kaner, R. B. Laser Scribing of High-Performance and Flexible Graphene-Based Electrochemical Capacitors. *Science (80-. ).* **2012**, *335* (6074), 1326–1330.

(44) Yan, J.; Liu, J.; Fan, Z.; Wei, T.; Zhang, L. High-Performance Supercapacitor Electrodes Based on Highly Corrugated Graphene Sheets. *Carbon N. Y.* **2012**, *50* (6), 2179–2188.

(45) Liu, Y. Z.; Li, Y. F.; Su, F. Y.; Xie, L. J.; Kong, Q. Q.; Li, X. M.; Gao, J. G.;

Chen, C. M. Easy One-Step Synthesis of N-Doped Graphene for Supercapacitors. *Energy Storage Mater.* **2016**, *2*, 69–75.

(46) John, J.; Gravel, E.; Namboothiri, I. N. N.; Doris, E. Advances in Carbon Nanotube-Noble Metal Catalyzed Organic Transformations. *Nanotechnol. Rev.* **2012**, *1* (6), 515–539.

(47) Niu, C.; Sichel, E. K.; Hoch, R.; Moy, D.; Tennent, H. High Power Electrochemical Capacitors Based on Carbon Nanotube Electrodes. *Appl. Phys. Lett.* **1998**, *70* (11), 1480.

(48) An, K. H.; Kim, W. S.; Park, Y. S.; Moon, J.-M.; Bae, D. J.; Lim, C.; Lee, Y. S.; Lee, Y. H. Electrochemical Properties of High-Power Supercapacitors Using Single-Walled Carbon Nanotube Electrodes**. *Adv. Funct. Mater.* **2001**, *11* (5), 387–392.

(49) Frackowiak, E.; Delpeux, S.; Jurewicz, K.; Szostak, K.; Cazorla-Amoros, D.; Béguin, F. Enhanced Capacitance of Carbon Nanotubes through Chemical Activation. *Chem. Phys. Lett.* **2002**, *361* (1–2), 35–41.

(50) Emmenegger, C.; Mauron, P.; Züttel, A.; Nützenadel, C.; Schneuwly, A.; Gallay, R.; Schlapbach, L. Carbon Nanotube Synthesized on Metallic Substrates. *Appl. Surf. Sci.* **2000**, *162–163*, 452–456.

(51) Chen, J. H.; Li, W. Z.; Wang, D. Z.; Yang, S. X.; Wen, J. G.; Ren, Z. F. Electrochemical Characterization of Carbon Nanotubes as Electrode in Electrochemical Double-Layer Capacitors. *Carbon N. Y.* **2002**, *40* (8), 1193–1197.

(52) Gueon, D.; Moon, J. H. Nitrogen-Doped Carbon Nanotube Spherical Particles for Supercapacitor Applications: Emulsion-Assisted Compact Packing and Capacitance Enhancement. *ACS Appl. Mater. Interfaces* **2015**, *7* (36), 20083–20089.

(53) Kim, B.; Chung, H.; Kim, W. Supergrowth of Aligned Carbon Nanotubes Directly on Carbon Papers and Their Properties as Upercapacitors. *J. Phys. Chem. C* **2010**, *114* (35), 15223–15227.

(54) Saghafi, M.; Mahboubi, F.; Mohajerzadeh, S.; Holze, R. Preparation of Vertically Aligned Carbon Nanotubes and Their Electrochemical Performance in Supercapacitors. *Synth. Met.* **2014**, *195*, 252–259.

(55) Zhang, H.; Cao, G.; Yang, Y.; Gu, Z. Comparison Between Electrochemical Properties of Aligned Carbon Nanotube Array and Entangled Carbon Nanotube

Electrodes. *J. Electrochem. Soc.* **2008**, *155* (2), K19.

(56) Izadi-Najafabadi, A.; Yasuda, S.; Kobashi, K.; Yamada, T.; Futaba, D. N.; Hatori, H.; Yumura, M.; Iijima, S.; Hata, K. Extracting the Full Potential of Single-Walled Carbon Nanotubes as Durable Supercapacitor Electrodes Operable at 4 V with High Power and Energy Density. *Adv. Mater.* **2010**, *22* (35), E235–E241.

(57) Zhang, C.; Peng, Z.; Lin, J.; Zhu, Y.; Ruan, G.; Hwang, C. C.; Lu, W.; Hauge, R. H.; Tour, J. M. Splitting of a Vertical Multiwalled Carbon Nanotube Carpet to a Graphene Nanoribbon Carpet and Its Use in Supercapacitors. *ACS Nano* **2013**, *7* (6), 5151–5159.

(58) Yang, S. Y.; Chang, K. H.; Tien, H. W.; Lee, Y. F.; Li, S. M.; Wang, Y. S.; Wang, J. Y.; Ma, C. C. M.; Hu, C. C. Design and Tailoring of a Hierarchical Graphene-Carbon Nanotube Architecture for Supercapacitors. *J. Mater. Chem.* **2011**, *21* (7), 2374–2380.

(59) You, B.; Wang, L.; Yao, L.; Yang, J. Three Dimensional N-Doped Graphene – CNT Networks for Supercapacitor. *Chem. Commun.* **2013**, *49* (44), 5016–5018.

(60) Huang, H.-S.; Chang, K.-H.; Suzuki, N.; Yamauchi, Y.; Hu, C.-C.; C-W Wu, K.; Huang, H.; C-W Wu, K.; Chang, K.; Hu, C.; Suzuki, N.; Yamauchi, Y. Evaporation-Induced Coating of Hydrous Ruthenium Oxide on Mesoporous Silica Nanoparticles to Develop High-Performance Supercapacitors. *Small* **2013**, *9* (15), 2520–2526.

(61) Sugimoto, W.; Iwata, H.; Yokoshima, K.; Murakami, Y.; Takasu, Y. Proton and Electron Conductivity in Hydrous Ruthenium Oxides Evaluated by Electrochemical Impedance Spectroscopy: The Origin of Large Capacitance. *J. Phys. Chem. B* **2005**, *109* (15), 7330–7338.

(62) Wang, G.; Zhang, L.; Zhang, J. A Review of Electrode Materials for Electrochemical Supercapacitors. *Chem. Soc. Rev.* **2012**, *41* (2), 797–828.

(63) Zheng, J. P.; Cygan, P. J.; Jow, T. R. Hydrous Ruthenium Oxide as an Electrode Material for Electrochemical Capacitors. *J. Electrochem. Soc.* **1995**, *142* (8), 2699–2703.

(64) Zheng, Y. Z.; Ding, H. Y.; Zhang, M. L. Hydrous–Ruthenium–Oxide Thin Film Electrodes Prepared by Cathodic Electrodeposition for Supercapacitors. *Thin Solid Films* **2008**, *516* (21), 7381–7385.

(65) Zhang, J.; Jiang, J.; Li, H.; Zhao, X. S. A High-Performance Asymmetric

Supercapacitor Fabricated with Graphene-Based Electrodes. *Energy Environ. Sci.* **2011**, *4* (10), 4009–4015.

(66) Jiang, H.; Ma, J.; Li, C. Mesoporous Carbon Incorporated Metal Oxide Nanomaterials as Supercapacitor Electrodes. *Adv. Mater.* **2012**, *24* (30), 4197–4202.

(67) Naoi, K.; Ishimoto, S.; Ogihara, N.; Nakagawa, Y.; Hatta, S. Encapsulation of Nanodot Ruthenium Oxide into KB for Electrochemical Capacitors. *J. Electrochem. Soc.* **2009**, *156* (1), A52.

(68) Hwang, J. Y.; El-Kady, M. F.; Wang, Y.; Wang, L.; Shao, Y.; Marsh, K.; Ko, J. M.; Kaner, R. B. Direct Preparation and Processing of Graphene/RuO2 Nanocomposite Electrodes for High-Performance Capacitive Energy Storage. *Nano Energy* **2015**, *18*, 57–70.

(69) Wei, W.; Cui, X.; Chen, W.; Ivey, D. G. Manganese Oxide-Based Materials as Electrochemical Supercapacitor Electrodes. *Chem. Soc. Rev.* **2011**, *40* (3), 1697–1721.

(70) Zhu, J.; Shi, W.; Xiao, N.; Rui, X.; Tan, H.; Lu, X.; Hng, H. H.; Ma, J.; Yan, Q. Oxidation-Etching Preparation of MnO2 Tubular Nanostructures for High-Performance Supercapacitors. *ACS Appl. Mater. Interfaces* **2012**, *4* (5), 2769–2774.

(71) Zhang, Q.-Z.; Zhang, D.; Miao, Z.-C.; Zhang, X.-L.; Chou, S.-L. Research Progress in MnO2–Carbon Based Supercapacitor Electrode Materials. *Small* **2018**, *14* (24), 1702883.

(72) Devaraj, S.; Munichandraiah, N. Effect of Crystallographic Structure of MnO2 on Its Electrochemical Capacitance Properties. *J. Phys. Chem. C* **2008**, *112* (11), 4406–4417.

(73) Lee, H. Y.; Goodenough, J. B. Supercapacitor Behavior with KCl Electrolyte. *J. Solid State Chem.* **1999**, *144* (1), 220–223.

(74) Toupin, M.; Brousse, T.; Bélanger, D. Influence of Microstucture on the Charge Storage Properties of Chemically Synthesized Manganese Dioxide. *Chem. Mater.* **2002**, *14* (9), 3946–3952.

(75) Kim, H.; Popov, B. N. Synthesis and Characterization of MnO2-Based Mixed Oxides as Supercapacitors. *J. Electrochem. Soc.* **2003**, *150* (3), D56.

(76) Chang, J. K.; Huang, C. H.; Lee, M. T.; Tsai, W. T.; Deng, M. J.; Sun, I. W. Physicochemical Factors That Affect the Pseudocapacitance and Cyclic

Stability of Mn Oxide Electrodes. *Electrochim. Acta* **2009**, *54* (12), 3278–3284.

(77) Brousse, T.; Toupin, M.; Dugas, R.; Athouël, L.; Crosnier, O.; Bélanger, D. Crystalline MnO2 as Possible Alternatives to Amorphous Compounds in Electrochemical Supercapacitors. *J. Electrochem. Soc.* **2006**, *153* (12), A2171.

(78) Su, X.; Yang, X.; Yu, L.; Cheng, G.; Zhang, H.; Lin, T.; Zhao, F. H. A Facile One-Pot Hydrothermal Synthesis of Branched α-MnO2 Nanorods for Supercapacitor Application. *CrystEngComm* **2015**, *17* (31), 5970–5977.

(79) Xu, M.; Kong, L.; Zhou, W.; Li, H. Hydrothermal Synthesis and Pseudocapacitance Properties of α-MnO2 Hollow Spheres and Hollow Urchins. *J. Phys. Chem. C* **2007**, *111* (51), 19141–19147.

(80) Jiang, H.; Li, C.; Sun, T.; Ma, J. A Green and High Energy Density Asymmetric Supercapacitor Based on Ultrathin MnO2 Nanostructures and Functional Mesoporous Carbon Nanotube Electrodes. *Nanoscale* **2012**, *4* (3), 807–812.

(81) Raut, S. D.; Mane, H. R.; Shinde, N. M.; Lee, D.; Shaikh, S. F.; Kim, K. H.; Kim, H. J.; Al-Enizi, A. M.; Mane, R. S. Electrochemically Grown MnO2 Nanowires for Supercapacitor and Electrocatalysis Applications. *New J. Chem.* **2020**, *44* (41), 17864–17870.

(82) Li, W.; Liu, Q.; Sun, Y.; Sun, J.; Zou, R.; Li, G.; Hu, X.; Song, G.; Ma, G.; Yang, J.; Chen, Z.; Hu, J. MnO2 Ultralong Nanowires with Better Electrical Conductivity and Enhanced Supercapacitor Performances. *J. Mater. Chem.* **2012**, *22* (30), 14864–14867.

(83) Liu, Z.; Xu, K.; Sun, H.; Yin, S. One-Step Synthesis of Single-Layer MnO2 Nanosheets with Multi-Role Sodium Dodecyl Sulfate for High-Performance Pseudocapacitors. *Small* **2015**, *11* (18), 2182–2191.

(84) Wei, W.; Cui, X.; Chen, W.; Ivey, D. G. Manganese Oxide-Based Materials as Electrochemical Supercapacitor Electrodes. *Chem. Soc. Rev.* **2011**, *40* (3), 1697–1721.

(85) Zhi, J.; Reiser, O.; Huang, F. Hierarchical MnO2 Spheres Decorated by Carbon-Coated Cobalt Nanobeads: Low-Cost and High-Performance Electrode Materials for Supercapacitors. *ACS Appl. Mater. Interfaces* **2016**, *8* (13), 8452–8459.

(86) Wang, Y.; Lai, W.; Wang, N.; Jiang, Z.; Wang, X.; Zou, P.; Lin, Z.; Fan, H. J.; Kang, F.; Wong, C.-P.; Yang, C. A Reduced Graphene Oxide/Mixed-Valence

Manganese Oxide Composite Electrode for Tailorable and Surface Mountable Supercapacitors with High Capacitance and Super-Long Life. *Energy Environ. Sci.* **2017**, *10* (4), 941–949.

(87) Yao, J.; Pan, Q.; Yao, S.; Duan, L.; Liu, J. Mesoporous MnO2 Nanosphere/Graphene Sheets as Electrodes for Supercapacitor Synthesized by a Simple and Inexpensive Reflux Reaction. *Electrochim. Acta* **2017**, *238*, 30–35.

(88) Zheng, X.; Zhou, X.; Xu, J.; Zou, L.; Nie, W.; Hu, X.; Dai, S.; Qiu, Y.; Yuan, N. Highly Stretchable CNT/MnO2 Nanosheets Fiber Supercapacitors with High Energy Density. *J. Mater. Sci.* **2020**, *55* (19), 8251–8263.

(89) Chai, Y.; Li, Z.; Wang, J.; Mo, Z.; Yang, S. Construction of Hierarchical Holey Graphene/MnO2 Composites as Potential Electrode Materials for Supercapacitors. *J. Alloys Compd.* **2019**, *775*, 1206–1212.

(90) Chen, Y.; Zhang, J.; Li, M.; Yang, C.; Zhang, L.; Wang, C.; Lu, H. Strong Interface Coupling and Few-Crystalline MnO2/Reduced Graphene Oxide Composites for Supercapacitors with High Cycle Stability. *Electrochim. Acta* **2018**, *292*, 115–124.

(91) Bai, X. L.; Gao, Y. L.; Gao, Z. Y.; Ma, J. Y.; Tong, X. L.; Sun, H. Bin; Wang, J. A. Supercapacitor Performance of 3D-Graphene/MnO2 Foam Synthesized via the Combination of Chemical Vapor Deposition with Hydrothermal Method. *Appl. Phys. Lett.* **2020**, *117* (18), 183901.

(92) Wang, Q.; Ma, Y.; Liang, X.; Zhang, D.; Miao, M. Flexible Supercapacitors Based on Carbon Nanotube-MnO2 Nanocomposite Film Electrode. *Chem. Eng. J.* **2019**, *371*, 145–153.

(93) Wadekar, P. H.; Khose, R. V.; Pethsangave, D. A.; Some, S. Waste-Derived Heteroatom-Doped Activated Carbon/Manganese Dioxide Trio-Composite for Supercapacitor Applications. *Energy Technol.* **2020**, *8* (6), 1901402.

(94) Wang, W.; Guo, S.; Bozhilov, K. N.; Yan, D.; Ozkan, M.; Ozkan, C. S. Intertwined Nanocarbon and Manganese Oxide Hybrid Foam for High-Energy Supercapacitors. *Small* **2013**, *9* (21), 3714–3721.

(95) Nithya, V. D.; Sabari Arul, N. Progress and Development of Fe3O4 Electrodes for Supercapacitors. *J. Mater. Chem. A* **2016**, *4* (28), 10767–10778.

(96) Wu, N. L.; Wang, S. Y.; Han, C. Y.; Wu, D. S.; Shiue, L. R. Electrochemical Capacitor of Magnetite in Aqueous Electrolytes. *J. Power Sources* **2003**, *113*

(1), 173–178.

(97) Wang, S.-Y.; Ho, K.-C.; Kuo, S.-L.; Wu, N.-L. Investigation on Capacitance Mechanisms of Fe3O4 Electrochemical Capacitors. *J. Electrochem. Soc.* **2006**, *153* (1), A75.

(98) Li, R.; Liu, J. Mechanistic Investigation of the Charge Storage Process of Pseudocapacitive Fe3O4 Nanorod Film. *Electrochim. Acta* **2014**, *120*, 52–56.

(99) Brezesinski, T.; Wang, J.; Tolbert, S. H.; Dunn, B. Ordered Mesoporous α-MoO3 with Iso-Oriented Nanocrystalline Walls for Thin-Film Pseudocapacitors. *Nat. Mater. 2010 92* **2010**, *9* (2), 146–151.

(100) Wang, L.; Zhang, X.; Wang, S.; Li, Y.; Qian, B.; Jiang, X.; Yang, G. Ultrasonic-Assisted Synthesis of Amorphous Fe3O4 with a High Specific Surface Area and Improved Capacitance for Supercapacitor. *Powder Technol.* **2014**, *256*, 499–505.

(101) Zhao, X.; Johnston, C.; Crossley, A.; Grant, P. S. Printable Magnetite and Pyrrole Treated Magnetite Based Electrodes for Supercapacitors. *J. Mater. Chem.* **2010**, *20* (36), 7637–7644.

(102) Liu, M.; Sun, J. In Situ Growth of Monodisperse Fe3O4 Nanoparticles on Graphene as Flexible Paper for Supercapacitor. *J. Mater. Chem. A* **2014**, *2* (30), 12068–12074.

(103) Bryan, A. M.; Santino, L. M.; Lu, Y.; Acharya, S.; D'Arcy, J. M. Conducting Polymers for Pseudocapacitive Energy Storage. *Chem. Mater.* **2016**, *28* (17), 5989–5998.

(104) Sivakkumar, S. R.; Kim, W. J.; Choi, J. A.; MacFarlane, D. R.; Forsyth, M.; Kim, D. W. Electrochemical Performance of Polyaniline Nanofibres and Polyaniline/Multi-Walled Carbon Nanotube Composite as an Electrode Material for Aqueous Redox Supercapacitors. *J. Power Sources* **2007**, *171* (2), 1062–1068.

(105) Li, H.; Wang, J.; Chu, Q.; Wang, Z.; Zhang, F.; Wang, S. Theoretical and Experimental Specific Capacitance of Polyaniline in Sulfuric Acid. *J. Power Sources* **2009**, *190* (2), 578–586.

(106) Li, M.; Yang, L. Intrinsic Flexible Polypyrrole Film with Excellent Electrochemical Performance. *J. Mater. Sci. Mater. Electron.* **2015**, *26* (7), 4875–4879.

(107) Rajesh, M.; Raj, C. J.; Kim, B. C.; Cho, B. B.; Ko, J. M.; Yu, K. H.

Supercapacitive Studies on Electropolymerized Natural Organic Phosphate Doped Polypyrrole Thin Films. *Electrochim. Acta* **2016**, *220*, 373–383.

(108) Du, X.; Guo, P.; Song, H.; Chen, X. Graphene Nanosheets as Electrode Material for Electric Double-Layer Capacitors. *Electrochim. Acta* **2010**, *55* (16), 4812–4819.

(109) Han, J.; Zhang, L. L.; Lee, S.; Oh, J.; Lee, K. S.; Potts, J. R.; Ji, J.; Zhao, X.; Ruoff, R. S.; Park, S. Generation of B-Doped Graphene Nanoplatelets Using a Solution Process and Their Supercapacitor Applications. *ACS Nano* **2013**, *7* (1), 19–26.

(110) Huang, Y.; Shen, C.; Tang, Z.; Shi, T.; Zheng, S.; Lin, L. Mass Loading-Independent Energy Storage with Reduced Graphene Oxide and Carbon Fiber. *ChemElectroChem* **2019**, *6* (24), 6009–6015.

(111) Guo, G.; Shen, L.; Li, X.; Cao, Y.; Sun, Y.; Xiong, Z. Tunable Reduction Degree of Stacked Lamellar RGO Film for Application in Flexible All-Solid-State Supercapacitors. *Diam. Relat. Mater.* **2020**, *106*, 107845.

(112) Dey, R. S.; Hjuler, H. A.; Chi, Q. Approaching the Theoretical Capacitance of Graphene through Copper Foam Integrated Three-Dimensional Graphene Networks. *J. Mater. Chem. A* **2015**, *3* (12), 6324–6329.

(113) Wang, C.; Zhou, Y.; Sun, L.; Zhao, Q.; Zhang, X.; Wan, P.; Qiu, J. N/P-Codoped Thermally Reduced Graphene for High-Performance Supercapacitor Applications. *J. Phys. Chem. C* **2013**, *117* (29), 14912–14919.

(114) Lv, W.; Tang, D. M.; He, Y. B.; You, C. H.; Shi, Z. Q.; Chen, X. C.; Chen, C. M.; Hou, P. X.; Liu, C.; Yang, Q. H. Low-Temperature Exfoliated Graphenes: Vacuum-Promoted Exfoliation and Electrochemical Energy Storage. *ACS Nano* **2009**, *3* (11), 3730–3736.

(115) Zhang, L.; Shi, G. Preparation of Highly Conductive Graphene Hydrogels for Fabricating Supercapacitors with High Rate Capability. *J. Phys. Chem. C* **2011**, *115* (34), 17206–17212.

(116) Xu, Y.; Lin, Z.; Zhong, X.; Huang, X.; Weiss, N. O.; Huang, Y.; Duan, X. Holey Graphene Frameworks for Highly Efficient Capacitive Energy Storage. *Nat. Commun. 2014 51* **2014**, *5* (1), 1–8.

(117) Zhu, Y.; Murali, S.; Stoller, M. D.; Ganesh, K. J.; Cai, W.; Ferreira, P. J.; Pirkle, A.; Wallace, R. M.; Cychosz, K. A.; Thommes, M.; Su, D.; Stach, E. A.; Ruoff, R. S. Carbon-Based Supercapacitors Produced by Activation of

Graphene. *Science (80-. ).* **2011**, *332* (6037), 1537–1541.

(118) Jeong, H. M.; Lee, J. W.; Shin, W. H.; Choi, Y. J.; Shin, H. J.; Kang, J. K.; Choi, J. W. Nitrogen-Doped Graphene for High-Performance Ultracapacitors and the Importance of Nitrogen-Doped Sites at Basal Planes. *Nano Lett.* **2011**, *11* (6), 2472–2477.

(119) Chen, P.; Yang, J. J.; Li, S. S.; Wang, Z.; Xiao, T. Y.; Qian, Y. H.; Yu, S. H. Hydrothermal Synthesis of Macroscopic Nitrogen-Doped Graphene Hydrogels for Ultrafast Supercapacitor. *Nano Energy* **2013**, *2* (2), 249–256.

(120) Jung, S. M.; Mafra, D. L.; Lin, C. Te; Jung, H. Y.; Kong, J. Controlled Porous Structures of Graphene Aerogels and Their Effect on Supercapacitor Performance. *Nanoscale* **2015**, *7* (10), 4386–4393.

(121) Wang, G.; Liang, R.; Liu, L.; Zhong, B. Improving the Specific Capacitance of Carbon Nanotubes-Based Supercapacitors by Combining Introducing Functional Groups on Carbon Nanotubes with Using Redox-Active Electrolyte. *Electrochim. Acta* **2014**, *115*, 183–188.

(122) LI, L.-X.; TAO, J.; GENG, X.; AN, B.-G. Preparation and Supercapacitor Performance of Nitrogen-Doped Carb...: Ingenta Connect. *Acta Physico-Chimica Sin.* **2013**, *23* (1), 111–116.

(123) Li, Y.; Kang, Z.; Yan, X.; Cao, S.; Li, M.; Guo, Y.; Huan, Y.; Wen, X.; Zhang, Y. A Three-Dimensional Reticulate CNT-Aerogel for a High Mechanical Flexibility Fiber Supercapacitor. *Nanoscale* **2018**, *10* (19), 9360–9368.

(124) Wang, Y.-Y.; Hou, B.-H.; Lü, H.-Y.; Lü, C.-L.; Wu, X.-L. Hierarchically Porous N-Doped Carbon Nanosheets Derived From Grapefruit Peels for High-Performance Supercapacitors. *ChemistrySelect* **2016**, *1* (7), 1441–1447.

(125) Demir, M.; Saraswat, S. K.; Gupta, R. B. Hierarchical Nitrogen-Doped Porous Carbon Derived from Lecithin for High-Performance Supercapacitors. *RSC Adv.* **2017**, *7* (67), 42430–42442.

(126) Liu, S.; Liang, Y.; Zhou, W.; Hu, W.; Dong, H.; Zheng, M.; Hu, H.; Lei, B.; Xiao, Y.; Liu, Y. Large-Scale Synthesis of Porous Carbon via One-Step CuCl2 Activation of Rape Pollen for High-Performance Supercapacitors. *J. Mater. Chem. A* **2018**, *6* (25), 12046–12055.

(127) Li, Y. T.; Pi, Y. T.; Lu, L. M.; Xu, S. H.; Ren, T. Z. Hierarchical Porous Active Carbon from Fallen Leaves by Synergy of K2CO3 and Their Supercapacitor Performance. *J. Power Sources* **2015**, *299*, 519–528.

(128) Ma, G.; Yang, Q.; Sun, K.; Peng, H.; Ran, F.; Zhao, X.; Lei, Z. Nitrogen-Doped Porous Carbon Derived from Biomass Waste for High-Performance Supercapacitor. *Bioresour. Technol.* **2015**, *197*, 137–142.

(129) Chen, R.; Yu, M.; Sahu, R. P.; Puri, I. K.; Zhitomirsky, I. The Development of Pseudocapacitor Electrodes and Devices with High Active Mass Loading. *Adv. Energy Mater.* **2020**, *10* (20), 1903848.

(130) Wang, X.; Yun, S.; Fang, W.; Zhang, C.; Liang, X.; Lei, Z.; Liu, Z. Layer-Stacking Activated Carbon Derived from Sunflower Stalk as Electrode Materials for High-Performance Supercapacitors. *ACS Sustain. Chem. Eng.* **2018**, *6* (9), 11397–11407.

(131) Guan, L.; Pan, L.; Peng, T.; Gao, C.; Zhao, W.; Yang, Z.; Hu, H.; Wu, M. Synthesis of Biomass-Derived Nitrogen-Doped Porous Carbon Nanosheests for High-Performance Supercapacitors. *ACS Sustain. Chem. Eng.* **2019**, *7* (9), 8405–8412.

(132) Yang, M.; Long, X.; Li, H.; Chen, H.; Liu, P. Porous Organic-Polymer-Derived Nitrogen-Doped Porous Carbon Nanoparticles for Efficient Oxygen Reduction Electrocatalysis and Supercapacitors. *ACS Sustain. Chem. Eng.* **2019**, *7* (2), 2236–2244.

(133) Yu, F.; Pang, L.; Wang, H. X. Preparation of Mulberry-like RuO2 Electrode Material for Supercapacitors. *Rare Met.* **2021**, *40* (2), 440–447.

(134) Hu, C.-C.; Chen, W.-C.; Chang, K.-H. How to Achieve Maximum Utilization of Hydrous Ruthenium Oxide for Supercapacitors. *J. Electrochem. Soc.* **2004**, *151* (2), A281.

(135) Gujar, T. P.; Shinde, V. R.; Lokhande, C. D.; Kim, W. Y.; Jung, K. D.; Joo, O. S. Spray Deposited Amorphous RuO2 for an Effective Use in Electrochemical Supercapacitor. *Electrochem. commun.* **2007**, *9* (3), 504–510.

(136) Davoglio, R. A.; Cabello, G.; Marco, J. F.; Biaggio, S. R. Synthesis and Characterization of α-MnO2 Nanoneedles for Electrochemical Supercapacitors. *Electrochim. Acta* **2018**, *261*, 428–435.

(137) Bai, X.; Tong, X.; Gao, Y.; Zhu, W.; Fu, C.; Ma, J.; Tan, T.; Wang, C.; Luo, Y.; Sun, H. Hierarchical Multidimensional MnO2 via Hydrothermal Synthesis for High Performance Supercapacitors. *Electrochim. Acta* **2018**, *281*, 525–533.

(138) Xu, K.; Li, S.; Yang, J.; Hu, J. Hierarchical Hollow MnO2 Nanofibers with Enhanced Supercapacitor Performance. *J. Colloid Interface Sci.* **2018**, *513*,

448–454.

(139) Liu, J.; Liu, S.; Zhuang, S.; Wang, X.; Tu, F. Synthesis of Carbon-Coated Fe3O4 Nanorods as Electrode Material for Supercapacitor. *Ionics (Kiel).* **2013**, *19* (9), 1255–1261.

(140) Khan, A. J.; Khan, A.; Javed, M. S.; Arshad, M.; Asim, S.; Khalid, M.; Siyal, S. H.; Hussain, S.; Hanif, M.; Liu, Z. Surface Assembly of Fe3O4 Nanodiscs Embedded in Reduced Graphene Oxide as a High-Performance Negative Electrode for Supercapacitors. *Ceram. Int.* **2020**, *46* (11), 19499–19505.

(141) Mao, Y.; Zhou, B.; Peng, S. Magnetite Ultrafine Particles/Porous Reduced Graphene Oxide in Situ Grown onto Ni Foam as a Binder-Free Electrode for Supercapacitors. *RSC Adv.* **2020**, *10* (35), 20753–20764.

(142) Li, Y.; Xu, J.; Feng, T.; Yao, Q.; Xie, J.; Xia, H. Fe2O3 Nanoneedles on Ultrafine Nickel Nanotube Arrays as Efficient Anode for High-Performance Asymmetric Supercapacitors. *Adv. Funct. Mater.* **2017**, *27* (14), 1606728.

(143) Kore, R. M.; Lokhande, B. J. A Robust Solvent Deficient Route Synthesis of Mesoporous Fe2O3 Nanoparticles as Supercapacitor Electrode Material with Improved Capacitive Performance. *J. Alloys Compd.* **2017**, *725*, 129–138.

(144) Wang, B.; Chen, J. S.; Wang, Z. Y.; Madhavi, S.; Lou, X. W.; Wang, B.; Song Chen, J.; Wang, Z.; Madhavi, S.; Wen Lou, X. Green Synthesis of NiO Nanobelts with Exceptional Pseudo-Capacitive Properties. *Adv. Energy Mater.* **2012**, *2* (10), 1188–1192.

(145) Zhang, G.; Yu, L.; Hoster, H. E.; Lou, X. W. Synthesis of One-Dimensional Hierarchical NiO Hollow Nanostructures with Enhanced Supercapacitive Performance. *Nanoscale* **2013**, *5* (3), 877–881.

(146) Zhang, Y. Z.; Wang, Y.; Xie, Y. L.; Cheng, T.; Lai, W. Y.; Pang, H.; Huang, W. Porous Hollow Co 3 O 4 with Rhombic Dodecahedral Structures for High-Performance Supercapacitors. *Nanoscale* **2014**, *6* (23), 14354–14359.

(147) Xia, X. H.; Tu, J. P.; Zhang, Y. Q.; Mai, Y. J.; Wang, X. L.; Gu, C. D.; Zhao, X. B. Freestanding Co 3O 4 Nanowire Array for High Performance Supercapacitors. *RSC Adv.* **2012**, *2* (5), 1835–1841.

(148) Zhu, J.; Cao, L.; Wu, Y.; Gong, Y.; Liu, Z.; Hoster, H. E.; Zhang, Y.; Zhang, S.; Yang, S.; Yan, Q.; Ajayan, P. M.; Vajtai, R. Building 3D Structures of Vanadium Pentoxide Nanosheets and Application as Electrodes in Supercapacitors. *Nano Lett.* **2013**, *13* (11), 5408–5413.

(149) Liang, K.; Tang, X.; Hu, W.; Yang, Y. Ultrafine V2O5 Nanowires in 3D Current Collector for High-Performance Supercapacitor. *ChemElectroChem* **2016**, *3* (5), 704–708.

(150) Wang, K.; Huang, J.; Wei, Z. Conducting Polyaniline Nanowire Arrays for High Performance Supercapacitors. *J. Phys. Chem. C* **2010**, *114* (17), 8062–8067.

(151) Patil, B. H.; Jagadale, A. D.; Lokhande, C. D. Synthesis of Polythiophene Thin Films by Simple Successive Ionic Layer Adsorption and Reaction (SILAR) Method for Supercapacitor Application. *Synth. Met.* **2012**, *162* (15–16), 1400–1405.

(152) Anothumakkool, B.; Soni, R.; Bhange, S. N.; Kurungot, S. Novel Scalable Synthesis of Highly Conducting and Robust PEDOT Paper for a High Performance Flexible Solid Supercapacitor. *Energy Environ. Sci.* **2015**, *8* (4), 1339–1347.

(153) Korkmaz, S.; Kariper, A.; Karaman, O.; Karaman, C. The Production of RGO/RuO2 Aerogel Supercapacitor and Analysis of Its Electrochemical Performances. *Ceram. Int.* **2021**, *47* (24), 34514–34520.

(154) Chung, M. Y.; Lo, C. T. High-Performance Binder-Free RuO2/Electrospun Carbon Fiber for Supercapacitor Electrodes. *Electrochim. Acta* **2020**, *364*, 137324.

(155) Zhang, Y.; Park, S. J. Incorporation of RuO2 into Charcoal-Derived Carbon with Controllable Microporosity by CO2 Activation for High-Performance Supercapacitor. *Carbon N. Y.* **2017**, *122*, 287–297.

(156) Kong, S.; Cheng, K.; Ouyang, T.; Gao, Y.; Ye, K.; Wang, G.; Cao, D. Facile Electrodepositing Processed of RuO2-Graphene Nanosheets-CNT Composites as a Binder-Free Electrode for Electrochemical Supercapacitors. *Electrochim. Acta* **2017**, *246*, 433–442.

(157) Jin, Y.; Chen, H.; Chen, M.; Liu, N.; Li, Q. Graphene-Patched CNT/MnO2 Nanocomposite Papers for the Electrode of High-Performance Flexible Asymmetric Supercapacitors. *ACS Appl. Mater. Interfaces* **2013**, *5* (8), 3408–3416.

(158) Yang, G.; Park, S. J. MnO2 and Biomass-Derived 3D Porous Carbon Composites Electrodes for High Performance Supercapacitor Applications. *J. Alloys Compd.* **2018**, *741*, 360–367.

(159) Yao, B.; Chandrasekaran, S.; Zhang, J.; Xiao, W.; Qian, F.; Zhu, C.; Duoss, E. B.; Spadaccini, C. M.; Worsley, M. A.; Li, Y. Efficient 3D Printed Pseudocapacitive Electrodes with Ultrahigh MnO2 Loading. *Joule* **2019**, *3* (2), 459–470.

(160) Cheng, Y.; Lu, S.; Zhang, H.; Varanasi, C. V.; Liu, J. Synergistic Effects from Graphene and Carbon Nanotubes Enable Flexible and Robust Electrodes for High-Performance Supercapacitors. *Nano Lett.* **2012**, *12* (8), 4206–4211.

(161) Sawangphruk, M.; Srimuk, P.; Chiochan, P.; Krittayavathananon, A.; Luanwuthi, S.; Limtrakul, J. High-Performance Supercapacitor of Manganese Oxide/Reduced Graphene Oxide Nanocomposite Coated on Flexible Carbon Fiber Paper. *Carbon N. Y.* **2013**, *60*, 109–116.

(162) Liu, D.; Wang, X.; Wang, X.; Tian, W.; Liu, J.; Zhi, C.; He, D.; Bando, Y.; Golberg, D. Ultrathin Nanoporous Fe3O4-Carbon Nanosheets with Enhanced Supercapacitor Performance. *J. Mater. Chem. A* **2013**, *1* (6), 1952–1955.

(163) Guan, D.; Gao, Z.; Yang, W.; Wang, J.; Yuan, Y.; Wang, B.; Zhang, M.; Liu, L. Hydrothermal Synthesis of Carbon Nanotube/Cubic Fe3O4 Nanocomposite for Enhanced Performance Supercapacitor Electrode Material. *Mater. Sci. Eng. B Solid-State Mater. Adv. Technol.* **2013**, *178* (10), 736–743.

(164) Samuel, E.; Joshi, B.; Jo, H. S.; Kim, Y. Il; An, S.; Swihart, M. T.; Yun, J. M.; Kim, K. H.; Yoon, S. S. Carbon Nanofibers Decorated with FeOx Nanoparticles as a Flexible Electrode Material for Symmetric Supercapacitors. *Chem. Eng. J.* **2017**, *328*, 776–784.

(165) Li, L.; Jia, C.; Shao, Z.; Wang, J.; Wang, F.; Wang, W.; Wang, H.; Zu, D.; Wu, H. $Fe_3O_4$ /Nitrogen- Doped Carbon Electrodes from Tailored Thermal Expansion toward Flexible Solid- State Asymmetric Supercapacitors. *Adv. Mater. Interfaces* **2019**, *6* (21), 1901250.

(166) Wu, M. S.; Lin, Y. P.; Lin, C. H.; Lee, J. T. Formation of Nano-Scaled Crevices and Spacers in NiO-Attached Graphene Oxide Nanosheets for Supercapacitors. *J. Mater. Chem.* **2012**, *22* (6), 2442–2448.

(167) Kim, S. Y.; Jeong, H. M.; Kwon, J. H.; Ock, I. W.; Suh, W. H.; Stucky, G. D.; Kang, J. K. Nickel Oxide Encapsulated Nitrogen-Rich Carbon Hollow Spheres with Multiporosity for High-Performance Pseudocapacitors Having Extremely Robust Cycle Life. *Energy Environ. Sci.* **2014**, *8* (1), 188–194.

(168) Dong, X. C.; Xu, H.; Wang, X. W.; Huang, Y. X.; Chan-Park, M. B.; Zhang,

H.; Wang, L. H.; Huang, W.; Chen, P. 3D Graphene-Cobalt Oxide Electrode for High-Performance Supercapacitor and Enzymeless Glucose Detection. *ACS Nano* **2012**, *6* (4), 3206–3213.

(169) Liu, T.; Zhang, L.; You, W.; Yu, J.; Liu, T.; Zhang, L.; You, W.; Yu, J. Core–Shell Nitrogen-Doped Carbon Hollow Spheres/Co3O4 Nanosheets as Advanced Electrode for High-Performance Supercapacitor. *Small* **2018**, *14* (12), 1702407.

(170) Liu, Z.; Zhang, H.; Yang, Q.; Chen, Y. Graphene / V2O5 Hybrid Electrode for an Asymmetric Supercapacitor with High Energy Density in an Organic Electrolyte. *Electrochim. Acta* **2018**, *287*, 149–157.

(171) Saravanakumar, B.; Purushothaman, K. K.; Muralidharan, G. V2O5 / Nitrogen Enriched Mesoporous Carbon Spheres Nanocomposite as Supercapacitor Electrode. *Microporous Mesoporous Mater.* **2018**, *258*, 83–94.

(172) Ma, Z.; Huang, X.; Dou, S.; Wu, J.; Wang, S. One-Pot Synthesis of Fe2O3 Nanoparticles on Nitrogen-Doped Graphene as Advanced Supercapacitor Electrode Materials. *J. Phys. Chem. C* **2014**, *118* (31), 17231–17239.

(173) Quan, H.; Cheng, B.; Xiao, Y.; Lei, S. One-Pot Synthesis of α-Fe2O3 Nanoplates-Reduced Graphene Oxide Composites for Supercapacitor Application. *Chem. Eng. J.* **2016**, *286*, 165–173.

(174) Jiang, X.; Shi, G.; Wang, G.; Mishra, P.; Du, J.; Zhang, Y. Fe2O3/Hemp Straw-Based Porous Carbon Composite for Supercapacitor Electrode Materials. *Ionics (Kiel).* **2020**, *26* (8), 4039–4051.

(175) Shen, K.; Ran, F.; Zhang, X.; Liu, C.; Wang, N.; Niu, X.; Liu, Y.; Zhang, D.; Kong, L.; Kang, L.; Chen, S. Supercapacitor Electrodes Based on Nano-Polyaniline Deposited on Hollow Carbon Spheres Derived from Cross-Linked Co-Polymers. *Synth. Met.* **2015**, *209*, 369–376.

(176) Chen, J.; Wang, Y.; Cao, J.; Liao, L.; Liu, Y.; Zhou, Y.; Ouyang, J. H.; Jia, D.; Wang, M.; Li, X.; Li, Z. Pulsed Electrochemical Fabrication of Graphene/Polypyrrole Composite Gel Films for High Performance and Flexible Supercapacitors. *Electrochim. Acta* **2020**, *361*, 137036.

(177) Teng, H.; Song, J.; Xu, G.; Gao, F.; Luo, X. Nitrogen-Doped Graphene and Conducting Polymer PEDOT Hybrids for Flexible Supercapacitor and Electrochemical Sensor. *Electrochim. Acta* **2020**, *355*, 136772.

# CHAPTER 2

## Improvement of Supercapacitor Performance through Enhanced Interfacial Interactions Induced by Sonication

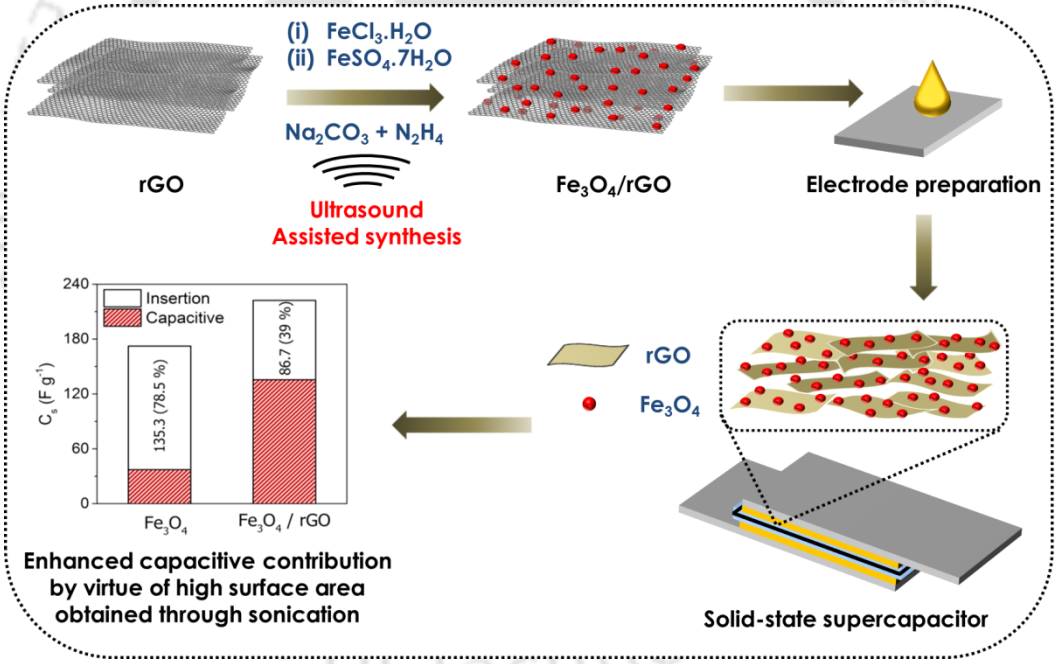

# CHAPTER 2

# IMPROVEMENT OF SUPERCAPACITOR PERFORMANCE THROUGH ENHANCED INTERFACIAL INTERACTIONS INDUCED BY SONICATION

## 2.1 INTRODUCTION

$Fe_3O_4$ has gained immense interest as a pseudocapacitive electrode material.[1] The high theoretical specific capacitance of $Fe_3O_4$ (2299 F $g^{-1}$) along with its low cost, less toxicity, and natural abundance makes it a promising supercapacitor electrode material. However, the specific capacitance values obtained for pristine $Fe_3O_4$ electrodes are far less than the theoretical values. This is due to the poor conductivity and the low surface area resulting from the agglomeration of the $Fe_3O_4$ particles. Therefore, many studies have focused on the composites of $Fe_3O_4$ and high surface areas of conductive carbon materials like porous carbon, activated carbon, graphene, carbon nanofibers, carbon nanotubes, etc. [2–5] Among the carbon materials, graphene has shown great potential in energy storage applications owing to its properties, viz. high surface area (2630 $m^2$ $g^{-1}$), superior mechanical strength, excellent electrical and thermal conductivity, etc.[6] Graphene and its primary derivatives namely graphene oxide (GO) and reduced graphene oxide (rGO) have been comprehensively investigated for various energy storage applications.[7,8] It is known that electro-active materials with large surface area and mesoporous structure could accommodate more electrolyte ions and facilitate charge transport for faster surface redox reactions.[9] Therefore graphene-based composites can demonstrate enhanced capacitive performance due to their large surface area, good electrical

conductivity, and high chemical stability.[10–14] Moreover, the layered structure of graphene acts as a substrate for the growth of various functional materials during the synthesis of nanocomposites. Various studies have shown that graphene-based $Fe_3O_4$ nanocomposites have demonstrated excellent capacitance performance.[1,4,15] It has been reported that the electrochemical performance of these nanocomposites is affected by the morphology and surface area interaction between graphene and $Fe_3O_4$ particles. Previous literature reports several synthesis methods, viz. solvothermal, hydrothermal, electrodeposition, solution precipitation, hydrogen reduction, microwave irradiation, etc. for preparation of graphene-$Fe_3O_4$ based composite.[1,4,15] Many of these methods are rather complex and some of them require high temperatures and longer time duration. This necessitates the formulation of novel synthesis protocols that are simpler and less energy-intensive.

In the present work, we have synthesized a relatively high surface area $Fe_3O_4$/rGO nanocomposite via a novel ultrasound-assisted method. Ultrasound (37 kHz) was used to effectively disperse rGO nanosheets and to facilitate the nucleation of $Fe_3O_4$ nanoparticles (NPs) on rGO. The use of ultrasound resulted in lesser aggregation of $Fe_3O_4$ nanoparticles as well as the better distribution of $Fe_3O_4$ particles on the surface of the crumpled rGO sheets. Symmetric all-solid-state supercapacitors (ASSCs) have been fabricated using as-synthesized $Fe_3O_4$/rGO nanocomposite as electrode material. The capacitive performances of ASSCs were investigated with different electrochemical techniques. The high surface area of the $Fe_3O_4$/rGO nanocomposite achieved through the novel ultrasound-assisted technique is manifested in improved electrochemical performance of the SC devices, as explained in subsequent sections.

## 2.2 EXPERIMENTAL SECTION

### 2.2.1 Materials

Graphite powder (< 20 μm), hydrazine hydrate ($N_2H_4$, 50–60%), poly(vinyl alcohol) (PVA), polytetrafluoroethylene (PTFE, 60 wt% dispersion in $H_2O$), and sodium carbonate anhydrous ($Na_2CO_3$) were obtained from Sigma Aldrich (India). Ferric chloride hexahydrate ($FeCl_3 \cdot 6H_2O$), sulphuric acid ($H_2SO_4$, 98%), ferrous sulfate heptahydrate ($FeSO_4 \cdot 7H_2O$), hydrogen peroxide ($H_2O_2$, 30%), potassium permanganate ($KMnO_4$), and hydrochloric acid (HCl, 35%) were purchased from Himedia Ltd. (India). Carbon black (Super P® Conductive) was purchased from Alfa-Aesar (USA). Ultrapure water was used for all the experiments.

### 2.2.2 Synthesis of Reduced Graphene Oxide (rGO)

Graphite oxide was synthesized by oxidizing graphite in concentrated $H_2SO_4$ acid using a modified Hummers method.[16] Briefly, concentrated $H_2SO_4$ (90 mL) was added to graphite (3 g) powder in around–bottom flask and vigorously stirred for 30 min. $KMnO_4$ (12 g) was added slowly into the solution keeping the flask in an ice bath to control the reaction temperature. The reaction temperature was then raised to 40 °C using an oil bath with continuous stirring for 6 h. The thickened dark brown reaction mixture was cooled, followed by addition of ultrapure water (400 mL) while maintaining the reaction flask in the ice bath. Further, $H_2O_2$ solution was added dropwise until the color of suspension turned to bright yellow. The suspension was filtered and washed with HCl (0.1 M) solution and ethanol. The as-synthesized graphite oxide was further washed with ultrapure water until neutral pH was obtained and vacuum dried at 60 ºC.

The graphite oxide was exfoliated in ultrapure water (500 mL) using sonication (37 kHz, 100 W) for 2 h to obtain a colloidal suspension of graphene oxide (3 mg $mL^{-1}$). Hydrazine hydrate (5 mL) was added to reduce the graphene oxide and the solution was continuously stirred for 8 h using an oil bath at 85 ºC. The resultant black coloured reduced graphene oxide (rGO) suspension was filtered and the solids were washed with HCl (0.1 M) solution followed by ultrapure water wash till neutral pH was obtained. The solids were oven-dried at 70 ºC.

### 2.2.3 Synthesis of $Fe_3O_4$ Nanoparticles

In a typical procedure to synthesize magnetite ($Fe_3O_4$) nanoparticles, $FeCl_3 \cdot 6H_2O$ (1.1 g) and $FeSO_4 \cdot 7H_2O$ (0.6 g) were completely dissolved in ultrapure water (100 mL) using bath sonication. An aqueous solution of sodium carbonate (1 M, 100 mL) was slowly added to the above solution followed by dropwise addition of hydrazine hydrate (2 mL) under continued sonication. After 15 min of further sonication, the solution was transferred to an oil bath and continuously stirred at 80 °C. The oil bath was removed after 1 h and the solution was cooled to room temperature. An agglomerated black mass of $Fe_3O_4$ nanoparticles precipitated and a permanent magnet was used to collect the particles. The obtained $Fe_3O_4$ nanoparticles were cleaned by repeated washing with ultrapure water and dried in vacuum for 12 h (at 70 °C).

### 2.2.4 Synthesis of $Fe_3O_4$/rGO Nanocomposite

The reduced graphene oxide powder (300 mg) was dispersed in ultrapure water (100 mL) using sonication for 30 min. Then $FeCl_3 \cdot 6H_2O$ (1.1 g) and $FeSO_4 \cdot 7H_2O$ (0.6 g) were added to the dispersion and further sonicated for 30 min. Sodium carbonate (1 M, 100 mL) and hydrazine hydrate (2 mL) were subsequently

added and the reaction mixture was heated at 80 °C for 1 h. Afterward, the solution cooled to room temperature and $Fe_3O_4$/rGO nanocomposite was magnetically separated, washed, and vacuum dried.

### 2.2.5 Characterization Techniques

The crystal structures of synthesized materials were investigated using Rigaku powder X-ray diffractometer (Model: Smart Lab, Cu Kα, λ = 1.54178 Å). Raman spectra were recorded using a Horiba Jobin Vyon Raman system (Model LabRam HR) with 514 nm laser to study the structural information of synthesized materials. The $N_2$ adsorption-desorption isotherms for the samples were recorded using a Micromeritics surface area analyzer (Model: Tristar II). The specific surface and pores size distributions (PSD) were obtained from the $N_2$ isotherms using Brunauer-Emmett-Teller (BET) and Barrett-Joyner-Halenda (BJH) methods, respectively. Zeiss field emission scanning electron microscope (FE-SEM) (Model:-Sigma 300) and a JEOL transmission electron microscope (TEM) (Model: JEM 2100) were used to observe the surface morphology of the synthesized nanomaterials. The weight ratio of $Fe_3O_4$ in the composite was determined using thermogravimetric analysis using a Netzsch thermogravimetric analyzer (Model: TG 209 F1 Libra). The magnetic behaviour of the $Fe_3O_4$ and $Fe_3O_4$/rGO nanocomposite was evaluated using a Lakeshore vibrating sample magnetometer (Model: 7410 series). CHNS elemental analysis was performed using an Elementar CHNS analyzer (Model: vario EL cube).

### 2.2.6 Fabrication of Symmetric All-Solid-State Supercapacitor

The electrode slurry for supercapacitors was prepared by making synthesized material ($Fe_3O_4$ or $Fe_3O_4$/rGO, 80 wt%) with carbon black (12 wt%) and PTFE dispersion (8 wt% PTFE content). The prepared slurry was coated onto a stainless

steel foil (thickness ~ 200 μm) and dried in vacuum at 70 °C. Prior to the electrode slurry coating, the stainless foil (current collector) was roughened using emery paper and properly cleaned by sonication in acetone. ASSCs were fabricated by assembling two similar electrodes (1.5 cm x 1.5 cm) using PVA/KOH as polymer gel electrolyte with a separator (cellulose filter paper) in between (**Figure 2.1**). The PVA/KOH electrolyte was prepared as follows: PVA (3 g) and KOH (3 g) were dissolved in 30 mL ultrapure water under continuous stirring at 90 °C until the solution became clear.

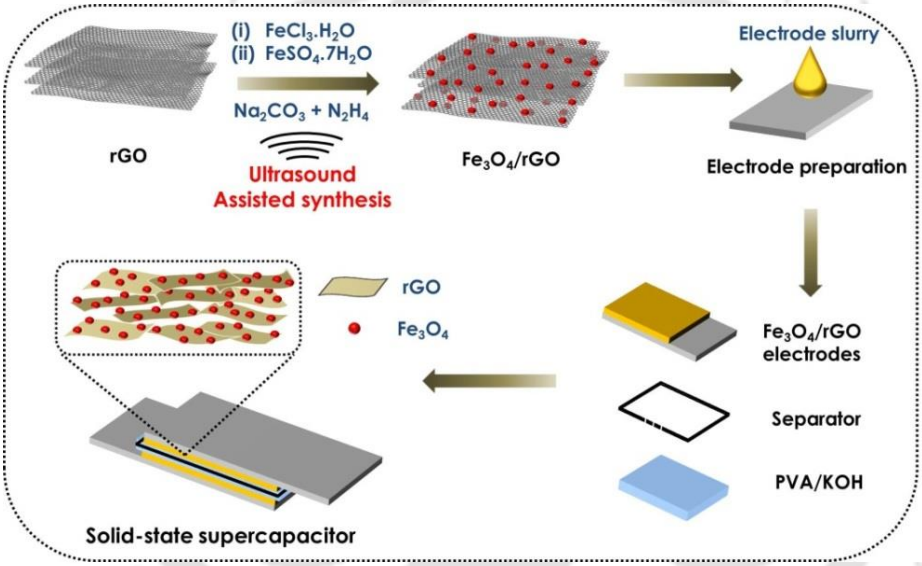


**Figure 2.1** Schematic of $Fe_3O_4$/rGO nanocomposite synthesis and fabrication of all-solid-state supercapacitor

### 2.2.7 Electrochemical Measurements

The electrochemical performances of ASSCs were evaluated using a M204 Potentiostat/Galvanostat (Metrohm Autolab). The widely used electrochemical techniques viz. cyclic voltammetry (CV), galvanostatic charge–discharge (GCD), and electrochemical impedance spectrometry (EIS) were used to assess the performance parameters of the solid-state supercapacitor devices.

The gravimetric specific capacitances of the ASSCs ($C_{cell}$, F $g^{-1}$) were calculated from the CV and GCD curves using equations 1.7 and 1.8, respectively as described in section 1.4.1 in **Chapter 1**. The two other two key parameters ASSCs, viz. energy (E, W h $kg^{-1}$), and power densities (P, W $kg^{-1}$), were calculated from GCD curves using equations 1.9 and 1.10, respectively (described in section 1.4.1 in **Chapter 1)**.

## 2.3 RESULTS AND DISCUSSION

### 2.3.1 Physicochemical Characterization

The structure and phase information of the synthesized nanomaterials were investigated using XRD measurements. The diffraction patterns were recorded over a 2θ range of 10° to 70° at 5° $min^{-1}$ scan rate. **Figure 2.2a** shows the diffraction patterns of $Fe_3O_4$ and $Fe_3O_4$/rGO. The diffraction peaks of $Fe_3O_4$ were noticed at 2θ = 30.20°, 35.50°, 43.23°, 53.61°, 57.15°, 62.72°, and 74.35°, corresponding to (2 2 0), (3 1 1), (4 0 0), (4 2 2), (5 1 1), (4 4 0) and (5 3 3) planes of magnetite face-centered cubic structure, respectively (JCPDS 72−2303).[3] In the diffraction pattern of the $Fe_3O_4$/rGO composite, a hump at 2θ = 24.64° was observed, which can be assigned to (0 0 2) plane of rGO (interlayer spacing ~ 0.36 nm). The presence of all the diffraction peaks of magnetite along with rGO confirms the coexistence of rGO and $Fe_3O_4$ in the nanocomposite. This type of X-ray diffraction pattern for $Fe_3O_4$/rGO composites is well reported in the existing literature.[2] The XRD patterns of graphite, graphene oxide (GO), and rGO oxide is shown in **Figure A1.1** (**Appendix A**). The XRD pattern of GO exhibits a sharp peak at 2θ = 9.62° corresponding to an interlayer spacing (*d*-spacing) of ~ 0.92 nm. This high *d*-spacing is attributed to the presence of oxygen functionalities and intercalated water molecules in the interlayers of GO. In the XRD

pattern of rGO, the peak at 9.62° disappeared and a broad peak was observed at about 2θ = 24° corresponding to (0 0 2) plane with a d-spacing of ~ 0.36 nm. The decrease in d-spacing of rGO is essentially due to the removal of oxygen-containing functional groups during the reduction process. The smaller peak observed at about 2θ = 42.5° corresponds to the (1 0 0) plane and the absence of any other peaks indicates the purity of the synthesized rGO.

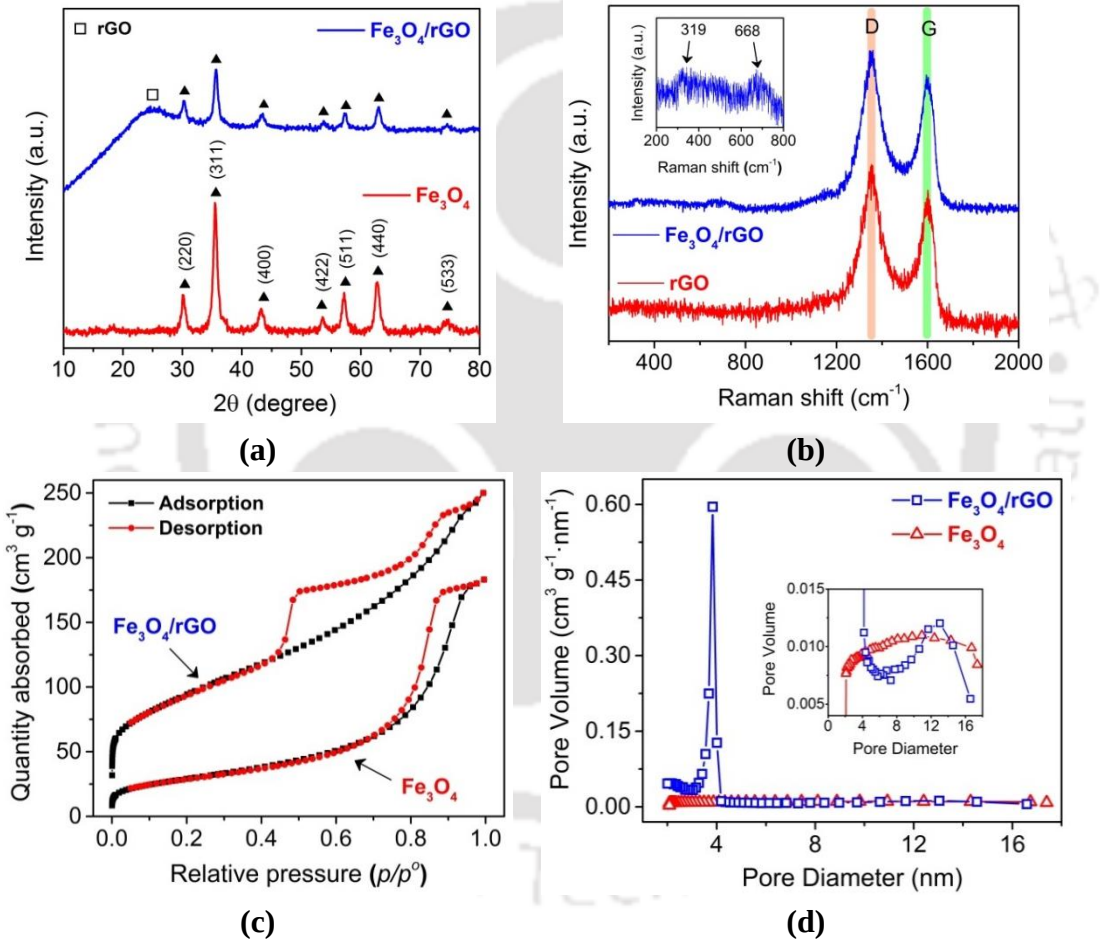


**Figure 2.2** (a) XRD patterns of pristine $Fe_3O_4$ NPs and $Fe_3O_4$/rGO nanocomposite (b) Raman spectra of rGO and $Fe_3O_4$/rGO nanocomposite (inset: vibration modes of $Fe_3O_4$ present in $Fe_3O_4$/rGO) (c) Nitrogen adsorption-desorption isotherms and (d) pore size distributions of pristine $Fe_3O_4$ NPs and $Fe_3O_4$/rGO nanocomposite

Elemental composition of graphene oxide and rGO obtained from CHN elemental analysis is shown in **Table A1.1** (**Appendix A**). The contents of C and O in graphene oxide were revealed as 41.5 and 55.3 wt%, respectively. Similarly, contents of C and O in rGO were 89.0 and 8.5 wt%, respectively. Thus, elemental analysis results confirmed the effective reduction of graphene oxide using hydrazine to form rGO (as indicated by a drastic reduction in oxygen content).

The synthesized materials were investigated with the Raman spectroscopy technique to characterize the structural features as it is a well-versed technique for characterizing carbon materials and composites. The Raman spectra of rGO and $Fe_3O_4$/rGO in **Figure 2.2b** show two prominent peaks at ~1351 for D-band and ~1602 $cm^{-1}$ for G-band, respectively.[17] The ratio of intensity ($I_D/I_G$) of these two bands provides information about the degree of the disordered ($sp^3$ hybridized) to the ordered ($sp^2$ hybridized) carbon domains. The $I_D/I_G$ ratio for rGO increased to 1.12 from 0.87 for GO (**Figure A1.2, Appendix 1**), which is due to the introduction of defects in the lattice of GO during the reduction process using hydrazine. In the case of $Fe_3O_4$/rGO nanocomposite, the $I_D/I_G$ ratio was ~ 1.13. This minimal increase in the $I_D/I_G$ value could be due to the growth of $Fe_3O_4$ in the rGO surface. Existing literature suggests the defect sites in the rGO surface could play a pivotal role in the nucleation of $Fe_3O_4$ nanoparticles by hindering their agglomeration of crystallites during formation.[13] The inset in **Figure 2.1b** shows two more peaks at 319 and 668 $cm^{-1}$ for $Fe_3O_4$/rGO composite along with the presence of G and D bands of rGO. The presence of $E_g$ (319 $cm^{-1}$) and $A_{1g}$ (668 $cm^{-1}$) vibration modes in $Fe_3O_4$ further confirmed the growth of magnetite on rGO.[18]

The specific surface area of electrode materials is a major characteristic that influences their electrochemical performance. The $N_2$ adsorption-desorption isotherms

of $Fe_3O_4$/rGO composite and pristine $Fe_3O_4$ are represented in **Figure 2.2c**. The isotherm for $Fe_3O_4$ was observed to be type II and BET surface area was found to be ~ 105 $m^2$ $g^{-1}$ with a pore volume of 0.27 $cm^3$ $g^{-1}$. As per IUPAC classification, an H3 type hysteresis loop was observed for the magnetite sample, which could be due to the presence of slit-type pores in the aggregates of magnetite particles. Type II isotherms were observed for $Fe_3O_4$/rGO nanocomposite, with a high BET specific surface area of ~ 332 $m^2$ $g^{-1}$ and pore volume of 0.27 $cm^3$ $g^{-1}$. The H2 type of hysteresis was observed for the composite, which can be attributed to the complex mesoporous structure of the rGO in the composite. The pore size distribution of the synthesized materials was obtained using the Barrett–Joyner–Halenda (BJH) model from the desorption isotherms (**Figure 2.2d**). The average pore diameter for the $Fe_3O_4$ and $Fe_3O_4$/rGO nanocomposite was found to be 9.2 and 4.3 nm, respectively. The $N_2$ adsorption-desorption isotherms of rGO (**Figure A1.3, Appendix 1**) were identified to be type IV isotherms with H2 type of hysteresis loop. The BJH pore size distribution (inset of **Figure A1.3, Appendix 1**) plot revealed that the majority of the pore volume of rGO is contributed by pores in the range of 3-4 nm size. The BET surface area, total pore volume, and average pore diameter of the rGO were obtained to be 555.20 $m^2$ $g^{-1}$, 0.47 $cm^3$ $g^{-1}$, and 3.57 nm respectively. Therefore, the narrow pore size distribution of the $Fe_3O_4$/rGO nanocomposite is due to the introduction of rGO, which drastically increased the number of mesopores in the composite thereby increasing the surface area. It is well reported that electrode materials with pore size distribution within 2-5 nm have demonstrated higher capacitive performance. Such kind of mesoporous structures can easily facilitate pathways for electrolyte ions to reach the core of the material during the charge storage process improving supercapacitor performance.[9,19] Therefore, during the electrochemical reaction; the

high surface area of the synthesized $Fe_3O_4$/rGO nanocomposite could offer abundant active sites for the electrolytes. Also, the high pore volume resulting from mesopores of the composite could facilitate easy access for the electrolyte ions resulting in improved electrochemical performance.[20]

The high surface area (332 $m^2$ $g^{-1}$) of the nanocomposite is attributed to uniform unfolding of graphene nanosheets under intense microconvection generated by sonication. The magnitude of this convection in time and spatial scale can be determined as follows: using calorimetric technique,[21] the acoustic pressure amplitude in the ultrasound bath was determined as 1.5 bar (or 150 kPa). The microstreaming velocity (i.e. the oscillatory velocity of the fluid elements induced by ultrasound wave) is given as: $u = \frac{P_A}{\rho c}$, where $P_A$ = acoustic pressure amplitude, ρ = density of the medium, $c$ = sonic velocity through the medium. Substituting the relevant values in context of present study: $P_A$ = 150 kPa, ρ = 1000 kg $m^{-3}$, c = 1481 m $s^{-1}$ gives u = 0.101 m $s^{-1}$, which is typically equivalent to mechanical agitation of ~ 100 rpm. The amplitude of oscillation of the fluid elements (a) is determined as: $u = 2\pi fa$. Substituting u = 0.101 m $s^{-1}$, $f$ = 37 kHz yields $a$ = 0.43 μm. So intense convection on such a small spatial scale is highly effective in unfolding the graphene nanosheets. Moreover, such microconvection is also useful in inducing uniform nucleation of $Fe_3O_4$ particles on the surface of graphene sheets.

The TEM images were used to investigate the morphology of $Fe_3O_4$ NPs and $Fe_3O_4$/rGO nanocomposites, as seen in **Figures 2.3a-c**. The morphologies of $Fe_3O_4$ particles in **Figure 2.3a** reveals that irregular spherical particles of $Fe_3O_4$ (size: 20–30 nm) were formed. The bare rGO sheets and distribution of $Fe_3O_4$ in the rGO sheets could be seen in the TEM image of the $Fe_3O_4$/rGO composite in **Figure 3b, c**.

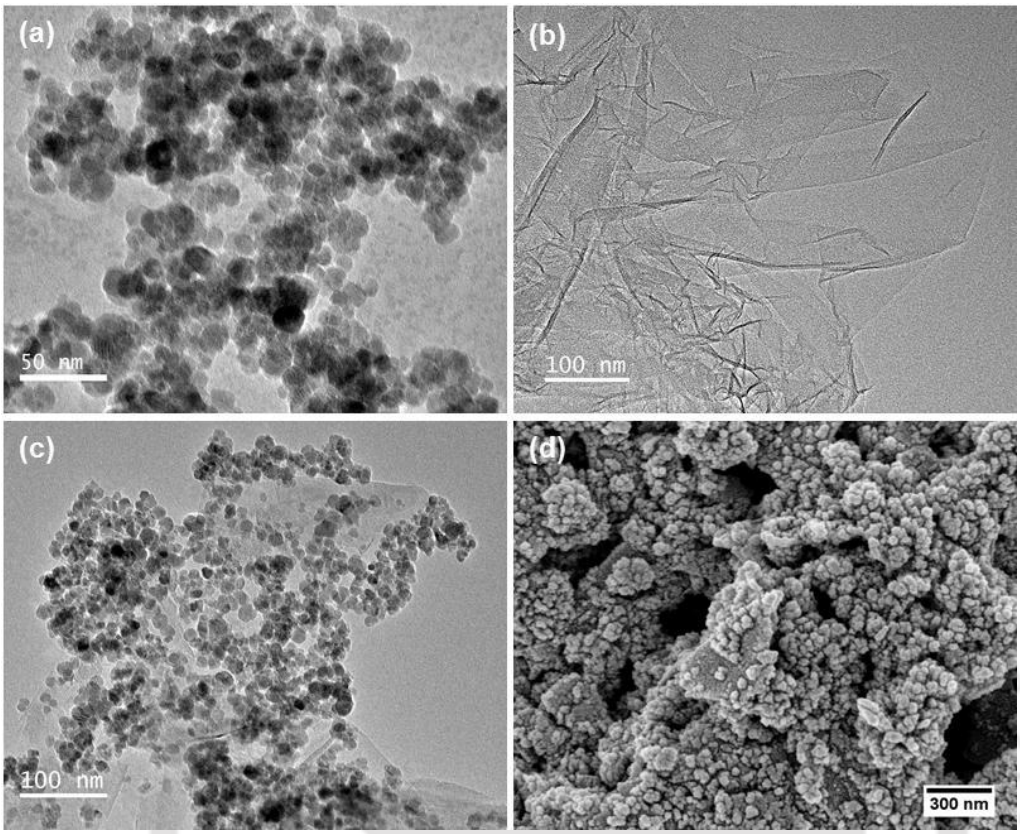


**Figure 2.3** TEM image of (a) $Fe_3O_4$ NPs (b) rGO sheets (c) $Fe_3O_4$/rGO nanocomposite (d) FESEM image of $Fe_3O_4$/rGO nanocomposite

The FESEM image of the nanocomposite in **Figure 2.3d** shows numerous $Fe_3O_4$ particles distributed on the rGO surface supporting the formation of the $Fe_3O_4$/rGO composite. The selected area diffraction (SAED) pattern $Fe_3O_4$/rGO composite as shown in Figure 4a infers the polycrystalline nature of the composite. The planes of $Fe_3O_4$, viz. (2 2 0), (3 1 1), (4 0 0), (4 2 2), (5 1 1), and (4 4 0), were identified in the SAED pattern of the composite, which could be correlated to the obtained XRD results. The high-resolution TEM images (HR-TEM) of the $Fe_3O_4$/rGO nanocomposite (**Figure 2.4b**) shows the fringe spacing ~ 0.296 and ~0.253 nm, which corresponds to two planes of $Fe_3O_4$ i.e. (2 2 0) and (3 1 1), respectively. The elemental mapping of the $Fe_3O_4$/rGO composite in **Figure 2.4c** in the selected area

confirmed the presence of C, Fe, and O elements in the composite. The EDS (**Figure A1.4, Appendix 1**) study of the composite also further confirmed the presence of C, Fe, and O in the composite.

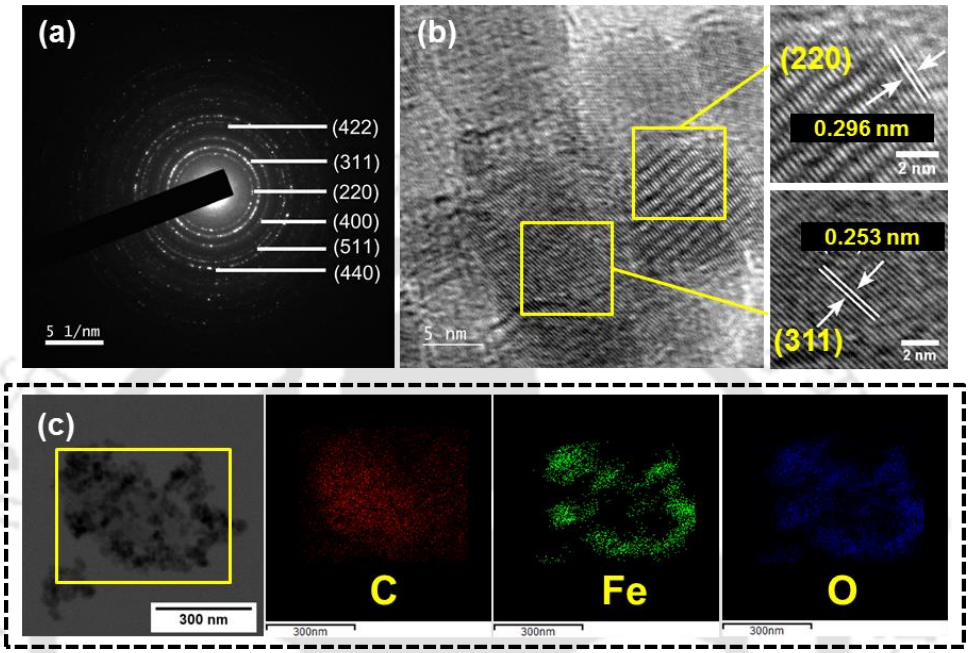


**Figure 2.4** (a) SAED pattern (d) HRTEM and (e) elemental mapping of $Fe_3O_4$/rGO nanocomposite (carbon in red, iron in green, and oxygen in blue)

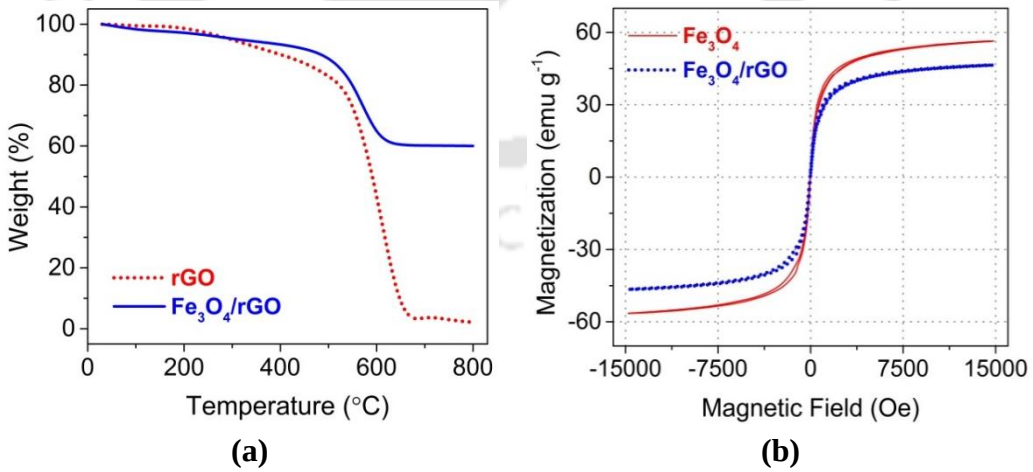


**Figure 2.5** (a) TG plots of rGO and $Fe_3O_4$/rGO nanocomposite (air atmosphere) (b) magnetization dependence of $Fe_3O_4$ and $Fe_3O_4$/rGO nanocomposite

The TGA was used to study the thermal stability and the mass loading of $Fe_3O_4$ in the $Fe_3O_4$/rGO composite. **Figure 2.5a** shows the TG curves of rGO and $Fe_3O_4$/rGO nanocomposite in the oxidative environment (air). The first stage of weight loss for rGO was witnessed in the temperature range of 30 – 350 °C with a minor reduction of ~ 7.5 wt%, which could be attributed to the vaporization of moisture in solids, and decomposition of residual functional groups in rGO. In the second stage, i.e. 350 – 680 °C, sharp weight loss of ~91.3 wt% was seen, which could be attributed to the decomposition of the carbon frame of rGO to $CO_2$.[38] The $Fe_3O_4$/rGO composite also shows weight loss in two stages, viz. 30 – 350 °C (~6.2 wt%) and 350 – 680 °C (~34.7 wt%), respectively. The first stage of weight loss in the $Fe_3O_4$/rGO nanocomposite is possibly due to the combination of moisture removal and oxidation of $Fe_3O_4$ to $Fe_2O_3$ in the 200 – 300 °C temperature range.[22] The second stage of weight loss from 350 to 680 °C could be ascribed to the oxidation of rGO into $CO_2$. After 680 °C, the $Fe_3O_4$/rGO composite does not show any significant weight loss. Several studies have reported the complete phase transition of $Fe_3O_4$ to $Fe_2O_3$ in oxidative thermal degradation.[23] Therefore, without considering any phase transformation the mass loading of $Fe_3O_4$ in the composite was found to be ~59 wt. % from the TG curves.[23]

The magnetic behaviour of the $Fe_3O_4$ particles and that of the $Fe_3O_4$/rGO composite was characterized using a vibrating sample magnetometer and the magnetic field was varied in the range of -15000 to 15000 Oe. The hysteresis loops (*M–H* curves) of both pristine $Fe_3O_4$ and the $Fe_3O_4$/rGO nanocomposite indicated ferromagnetic behaviour (**Figure 2.5b**).[24] The saturation magnetization ($M_s$) values of 56.44 and 46.48 emu $g^{-1}$ were obtained for $Fe_3O_4$ and $Fe_3O_4$/rGO, respectively (**Table A1.3, Appendix 1**). The lesser value of magnetization for the $Fe_3O_4$/rGO composite is

due to the reduced magnetite content (59 wt%) in the composite as compared to pristine magnetite (100 wt%) particles. Earlier studies have reported the application of an external magnetic field in $Fe_3O_4$ and composite increased its electrochemical performance.[25,26] Therefore, the high value of magnetization reported in this study is expected to improve the electrochemical performance of SC devices fabricated from as-synthesized materials in presence of an external magnetic field. Moreover, the high magnetization value enables easy collection of the composite using an external magnet.

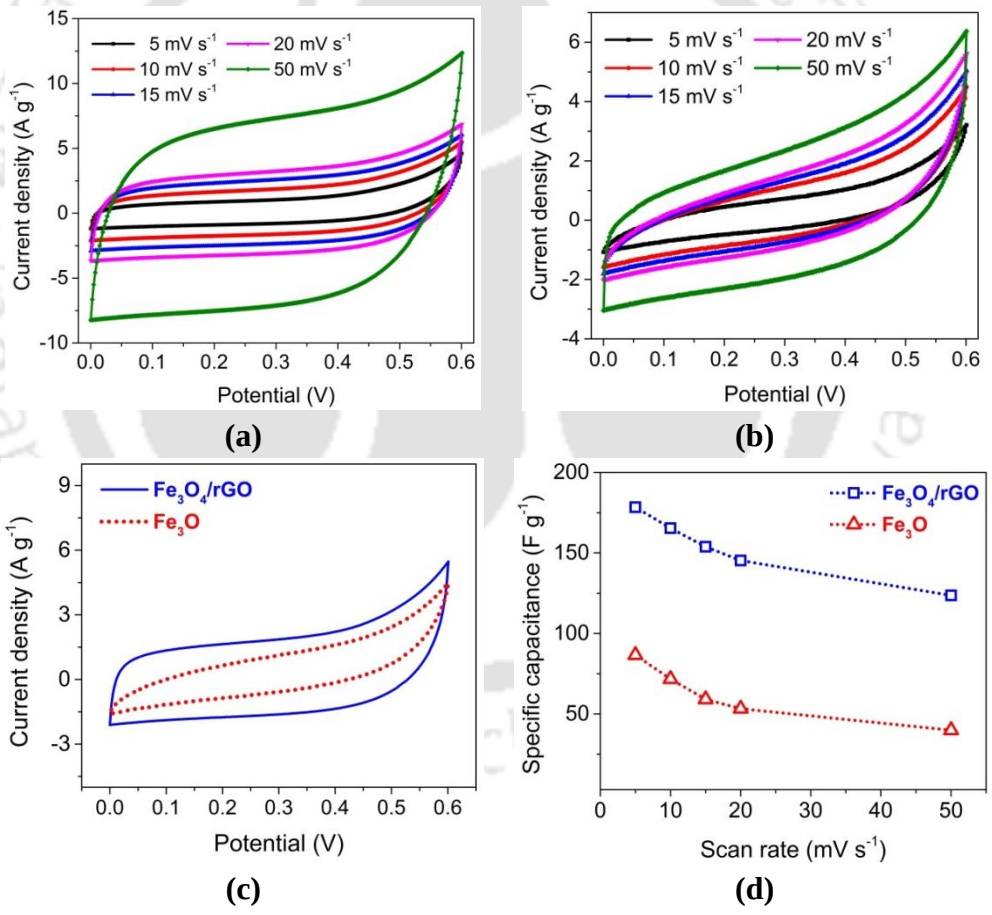


**Figure 2.6** CV curves of (a) $Fe_3O_4$/rGO, (b) $Fe_3O_4$ ASSCs at different scan rates, (c) CV curves of ASSCs at 10 mV $s^{-1}$, and (d) specific capacitance as a function of scan rate.

### 2.3.2 Electrochemical Performance

To investigate the capacitive performance of the synthesized nanomaterials, ASSCs were fabricated as described in section 2.2.6 and **Figure 2.1**. The CV curves of $Fe_3O_4$/rGO ASSC at different scan rates (viz. 5, 10, 15, 20, and 50 mV $s^{-1}$) are shown in **Figure 2.6a**. The CV curves of $Fe_3O_4$/rGO ASSC (in the voltage window of 0-0.6 V) were quasi–rectangular lacking any redox peaks and indicated good capacitive behavior.[20] The quasi–rectangular, symmetric CV curves of $Fe_3O_4$/rGO ASSC indicated the presence of both EDLC and pseudocapacitive behaviour with EDLC being the more dominant one.[27] The rGO present in the composite mostly contributed to EDLC behaviour demonstrated by the $Fe_3O_4$/rGO ASSC. The increase in voltage scan rate induced deviation in CV curves from their near rectangular shape, which could be attributed to increased electrochemical polarization.[28] It was observed that the deviation of CV curve at a higher scan rate (50 mV $s^{-1}$) was very less in the case of $Fe_3O_4$/rGO ASSC, which is conceivably due to the lesser degree of polarization, fast and reversible charge-discharge at a constant rate. But the CV curves of $Fe_3O_4$ ASSC at higher scan rates (**Figure 2.6b**) deviated more from the rectangular shape and showed a stronger degree of polarization. The CV curves of the rGO ASSC at different voltage scan rates are shown in **Figure A1.5a (Appendix 1)**. The quasi-rectangular shape of these CV curves indicated EDLC behaviour of the rGO. The $Fe_3O_4$/rGO ASSC demonstrated a high value of specific capacitance ~ 178.4 F $g^{-1}$ at 5 mV $s^{-1}$, whereas the $Fe_3O_4$ ASSC exhibited a specific capacitance of 86.6 F $g^{-1}$ at the same scan rate. **Figure 2.6c** shows the CV curves of both $Fe_3O_4$/rGO and $Fe_3O_4$ ASSCs at the scan rate of 10 mV $s^{-1}$. It was observed that the area under the CV curve of $Fe_3O_4$/rGO ASSC is more than the area of $Fe_3O_4$ ASSC. This result indicated better capacitive behaviour of $Fe_3O_4$/rGO ASSCs, as the average value of the area under the

CV curves is directly related to capacitance value. The larger area under the CV curves is indicative of a greater amount of charge stored in SC devices. The high capacitance value of the $Fe_3O_4$/rGO ASSCs is essentially due to the high specific surface area reported for composite, and the high conductivity of rGO in the composite.[29] When the voltage scan rate was increased gradual decrease in the specific capacitance values was observed for both the ASSCs (**Figure 2.6d**). The specific capacitance values of $Fe_3O_4$/rGO and $Fe_3O_4$ SC at 50 mV $s^{-1}$ are 123.63 (69.3 % retention) and 39.92 (46.1 % retention) F $g^{-1}$. In addition, the specific capacitances of rGO ASSC were 96.35, and 75.66 F $g^{-1}$ at scan rates of 5 and 50 mV $s^{-1}$, respectively (**Figure A1.5b, Appendix 1**).The decrease in capacitance value with increasing scan rate is a common phenomenon caused by insufficient time for electrolyte ion diffusion and charge storage is limited to the outer surface area only.[30] A similar kind of trend in specific capacitance values was also observed in our study.

The electrochemical performances of the ASSCs were also investigated by galvanostatic charge-discharge under different current densities. **Figure 2.7a-b** shows the symmetric GCD curves and the linearity of the curves indicates the good capacitive performance of the fabricated SCs.[31] The very low *iR* drop present in the GCD curves indicated the low internal resistance present in the $Fe_3O_4$/rGO supercapacitor device.[32] The gravimetric capacitance values of the ASSCs at different current densities were calculated from the discharge curves. At a current density of 1 A $g^{-1}$, the capacitance of the $Fe_3O_4$/rGO and $Fe_3O_4$ ASSCs were found to be 169.2 and 79.8 F $g^{-1}$, respectively. The specific capacitance of $Fe_3O_4$/rGO ASSC decreased as 147.5, 132.25, 118.6, and 109.25 F $g^{-1}$ (**Figure 2.7c**) corresponding to increased current density viz. 2, 3, 4, and 5 A $g^{-1}$, respectively. This decrease in specific capacitance values was visible from the decrease in the discharge time of GCD

curves. This decrease in specific capacitance at higher current density could be ascribed to the limited movement of electrolyte ions into the inner side of the active material.[33] A similar decreasing capacitance trend was also observed in the case of $Fe_3O_4$ ASSC.

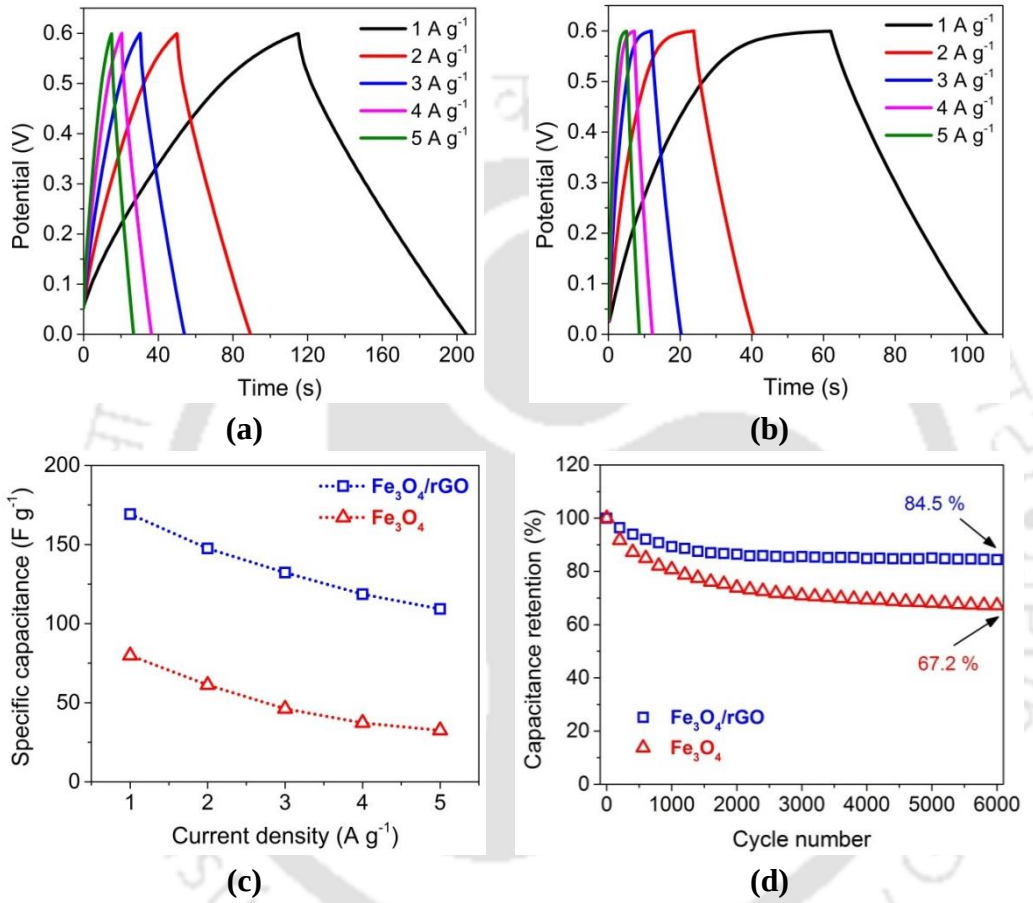


**Figure 2.7** (a) Galvanostatic charge-discharge curves of (a) $Fe_3O_4$/rGO, (b) $Fe_3O_4$ ASSCs at different current densities, (c) specific capacitance vs. current density, and (d) cyclic performance of ASSCs

Furthermore, the near-linear and symmetric charge-discharge curves of the rGO ASSC (**Figure A1.5c, Appendix 1**) suggest fast charge storage characteristics with EDLC behaviour. This behaviour could be attributed to the high surface area and mesoporous structure of rGO. The capacitance of the rGO ASSC was calculated to be

92.80 F $g^{-1}$ at a current density of 1 A $g^{-1}$, which reduces to 72.85 F $g^{-1}$ at 5 A $g^{-1}$ (**Figure A1.5d, Appendix 1**).

The specific capacitance values of $Fe_3O_4$/rGO ASSC were considerably higher than that of both $Fe_3O_4$ ASSC and rGO ASSC in all the current densities, demonstrating superior electrochemical performance. This observation further indicates the synergistic effect of rGO present in the nanocomposite owing to the high conductivity and surface area of rGO, which lowers the charge transfer resistance.[13] The capacitive performance demonstrated by the $Fe_3O_4$/rGO ASSC is highly competitive with the symmetric solid-state supercapacitor devices reported in previous literature (**Table A1.4, Appendix 1**). The gravimetric capacitance of the synthesized $Fe_3O_4$/rGO nanocomposite was also estimated and found to superior to those of other iron oxide carbon-based materials (**Table A1.5, Appendix 1**).

**Figure 2.7d** depicts the variation in measured capacitance values over 6000 cycles for both $Fe_3O_4$/rGO and $Fe_3O_4$ ASSCs (at 5 A $g^{-1}$). The specific capacitance values of both the devices decrease with the increase in the number of charge-discharge cycles. The $Fe_3O_4$/rGO ASSC retained 84.5% of its initial capacitance whereas the $Fe_3O_4$ ASSC retained 67.2% of its capacitance at the end of 6000 charge-discharge cycles. The rGO ASSC device demonstrated high electrochemical stability and retained 96.4 % of its initial capacitance after 6000 charge-discharge cycles (**Figure A1.6a, Appendix 1**). These obtained results indicated the superior electrochemical stability of the $Fe_3O_4$/rGO ASSC due to the addition of rGO. This result is similar to the existing literature, which reports that incorporation of carbon-based materials into pseudocapacitive materials as composite increases the cycle life of the latter.[34]

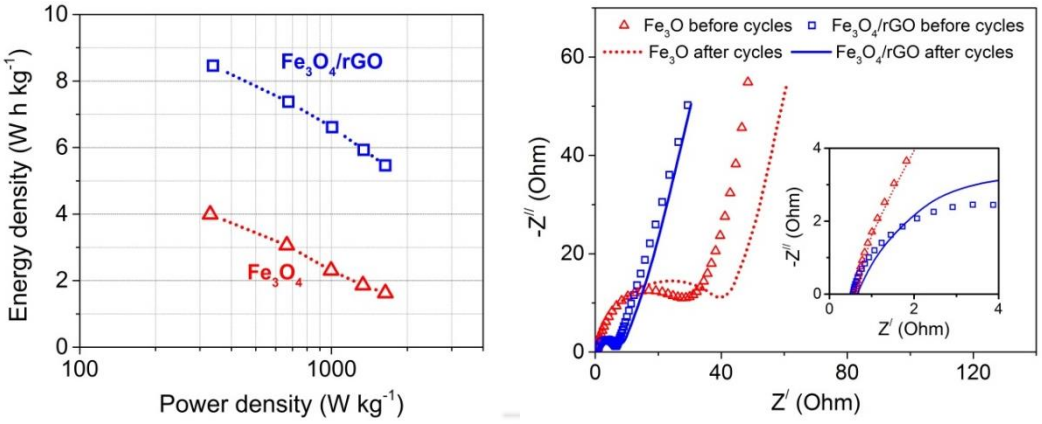


**(a)** **(b)**

**Figure 2.8** (a) Ragone plot and (b) Nyquist plot of $Fe_3O_4$ and $Fe_3O_4$/rGO ASSCs

The Ragone plot of energy versus power densities under different current densities of fabricated supercapacitor devices is shown in **Figure 2.8a**. The $Fe_3O_4$/rGO ASSC demonstrated relatively higher values of energy density of 8.46 W h $kg^{-1}$ at a power density of ~338 W $kg^{-1}$, and this value of energy density is about 2.12× the value of energy density demonstrated by the $Fe_3O_4$ ASSC. At a power density of 1636.36 W $kg^{-1}$ the $Fe_3O_4$/rGO ASSC exhibits an energy density of 5.46 W h $kg^{-1}$. The high values of energy and power densities of the $Fe_3O_4$/rGO ASSC are possibly due to enhanced conductivity and the high surface area of the $Fe_3O_4$/rGO nanocomposite which provides more channels for the electrolyte to access and enables faster charge transfer.

The EIS data of the SC devices were studied in the frequency range of 0.1 - $10^5$ Hz using a 10 mV $s^{-1}$ signal. **Figure 2.8b** represents the Nyquist plot of the ASSCs and the equivalent circuit is shown in **Figure A1.7 (Appendix 1)**. The impedance data for supercapacitors represent a semi-circular arc in the higher frequency region whereas in the low-frequency region a straight line was obtained. The $Z'$ intercept represents the series resistance ($R_s$), i.e. the combination of resistance

originating from electrolyte and contact resistance of current collector and electrode material.[35,36] The semi-circular arc of the Nyquist plot originated from the transfer of charge at the interface (electrolyte-electrode) and was used to evaluate the charge transfer resistance ($R_{ct}$) using an equivalent circuit.[37] The obtained values of $R_s$ and $R_{ct}$ for $Fe_3O_4$/rGO ASSC are 0.51 and 6.25 Ω, respectively, while the corresponding values for $Fe_3O_4$ ASSC are 0.57 and 32.8 Ω. The Nyquist plot of the rGO ASSC is also shown in **Figure A1.6b (Appendix 1)** and the values of $R_s$ and $R_{ct}$ were found to be 0.47 and 5.1 Ω. The rGO sheets in the $Fe_3O_4$/rGO nanocomposite act as conductive support to facilitate the charge transportation on the well-distributed $Fe_3O_4$ nanoparticles and significantly improve the ion mobility. EIS of the SC devices was also performed after the cycle stability test (i.e. after 6000 charge-discharge cycles). The $R_{ct}$ value for the $Fe_3O_4$/rGO ASSC increased slightly to 8.5 Ω whereas the $R_{ct}$ value for $Fe_3O_4$ ASSC increased to 45.8 Ω after the cycling test. Additionally, the $R_s$ value for both the ASSCs after cycling was found to be almost equal (~ 0.60 Ω). These results revealed the enhanced conductivity of the $Fe_3O_4$/rGO as compared to $Fe_3O_4$.

Trasatti and Lee developed a neat method to separate the capacitive elements from the insertion process (diffusion-controlled).[37,38] This method demonstrates that by plotting capacity as an appropriate function of the scan rate, the capacitive contributions can be separated. It is well–known that the capacitance values decrease when the voltage scan rate increases and the same is also evident in the current study. The capacitance values are plotted as a function of $\lambda^{1/2}$ and $\lambda^{-1/2}$ and the $C_{sp}$ values are extrapolated to $\lambda = 0$ and $\lambda =$ infinity. If sufficient time is allowed for all the reactions to take place, the $C_{sp}$ value at $\lambda = 0$ will give the value of the total capacitance ($C_t$), and the $C_{sp}$ value at infinite scan rate is the charge stored at the surface ($C_{su}$). The

difference ($C_t$ – $C_{su}$) of total capacitance to the surface capacitance provides the capacitance resulting from the insertion processes ($C_i$). The contributions of surface charges were obtained by plotting $C_s$ versus $\lambda^{-1/2}$ for both $Fe_3O_4$/rGO and $Fe_3O_4$ ASSCs. To obtain a linear fit, a semi-infinite linear diffusion was assumed.[38]

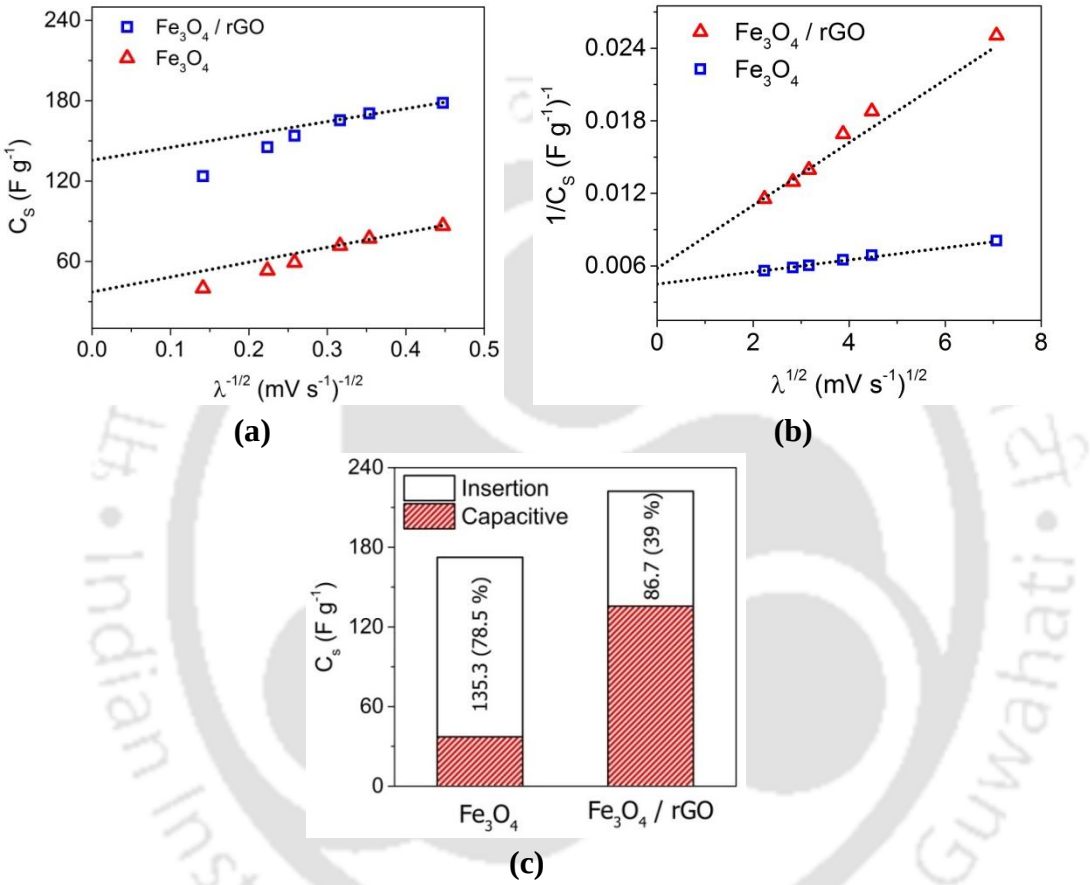


**Figure 2.9** (a) $C_s$ as a function of $\lambda^{-1/2}$, (b) $1/C_s$ as a function of $\lambda^{1/2}$, and (c) capacitance contribution from insertion and surface charges for ASSCs

It was seen from **Figure 2.9a,b** that the straight line could be properly fitted at low scan rates (≤ 10 mV $s^{-1}$), while the linearity deviates at higher scan rates owing to ohmic drops and irreversible redox reactions.[39] The value of $C_{su}$ was obtained from the intercept of the line at $\lambda^{-1/2}$ = 0 (shown by the hatched area in **Figure 2.9c**). Moreover, $1/C_s$ versus $\lambda^{1/2}$ were plotted and the maximum capacitance was obtained

by the extrapolation of the fitted line at $\lambda^{1/2} = 0$. The $C_i$ values were calculated and represented by the white area in the bar graph. The results of the Trasatti and Lee method infer that the capacitance of $Fe_3O_4$/rGO ASSC is mostly contributed by surface charges while the capacitance of $Fe_3O_4$ ASSC is contributed by the charge stored via insertion process. This could be a possible reason for the high rate capability of the $Fe_3O_4$/rGO ASSC as the major contribution of its capacitance comes from surface charges which is a faster process as compared to diffusion-controlled insertion process.

Like other metal oxide electrodes, the electrochemical performance of magnetite electrodes is also influenced by particle size, surface area, particle distribution, etc. When synthesized at nanoscale the conductivity of $Fe_3O_4$ increases due to reduced average solid-state diffusion length.[1] But the major difficulty is in the synthesis procedure as the magnetic $Fe_3O_4$ nanoparticles particles tend to aggregate thereby reducing the surface area. The sonication of reaction mixture employed in the present study generates intense microconvection in the system through physical phenomena of microstreaming and acoustic waves. Two important manifestations of this microconvection are: exfoliation and unfolding of the graphene nanosheets and uniform nucleation of $Fe_3O_4$ nanoparticles on the nanosheets. The microconvection also reduces agglomeration of the $Fe_3O_4$ nanoparticles with improved spatial distribution of $Fe_3O_4$ on rGO. These effects in the synthetic procedure have resulted in the high surface area of nanocomposite which in turn is responsible for the improved capacitive performance of the $Fe_3O_4$/rGO ASSC.

***Comparison with nanocomposites synthesized without ultrasound:*** In order to assess the beneficial effect of sonication, the $Fe_3O_4$/rGO samples were also synthesized without application of ultrasound, and the characterization of the sample is given in

**Appendix 1**. The major changes in properties of the $Fe_3O_4$/rGO samples were as follows:

(i) The BET surface area $Fe_3O_4$/rGO samples synthesized without ultrasound was 227.18 $m^2$ $g^{-1}$ (**Table A1.2 and Figure A1.9, Appendix 1**), as against surface area of 332.34 $m^2$ $g^{-1}$ for the $Fe_3O_4$/rGO samples synthesized with ultrasound. As a consequence, these samples were expected to demonstrate relatively inferior electrochemical performance due to the reduction in electroactive sites available for electrolytes.

(ii) Moreover, the area under the CV curve (**Figure A1.10a, Appendix 1**) of the ASSC fabricated with $Fe_3O_4$/rGO without ultrasound was relatively much smaller. The capacitance of the $Fe_3O_4$/rGO (synthesized without ultrasound) ASSC at 10 mV $s^{-1}$ was 129.82 F $g^{-1}$ which was 22.5 % lesser than $Fe_3O_4$/rGO (synthesized with ultrasound) ASSC.

(iii) A similar observation can also be made from the GCD curves (**Figure A1.10b, Appendix 1**) of the $Fe_3O_4$/rGO (synthesized without ultrasound) ASSC, which demonstrated a specific capacitance of 139.75 F $g^{-1}$ at 1 A $g^{-1}$ which was 17.4 % lesser than the $Fe_3O_4$/rGO (synthesized with ultrasound) ASSC.

## 2.4 CONCLUSIONS

In summary, high surface area $Fe_3O_4$ decorated rGO nanocomposites were synthesized using an ultrasound-assisted low-temperature protocol. $Fe_3O_4$ nanoparticles were uniformly grown on the surface of highly porous rGO that facilitated faster charge transfer in the electrode. The solid-state symmetric supercapacitor fabricated using the $Fe_3O_4$/rGO nanocomposite demonstrated excellent electrochemical properties (specific capacitance of 169.2 F $g^{-1}$ at 1 A $g^{-1}$) and high

stability. $Fe_3O_4$/rGO device retained 64.6 % of its capacitance at 5 A $g^{-1}$ current density. The $Fe_3O_4$/rGO ASSC device exhibited a power density of ~338 W $kg^{-1}$ at an energy density of 8.46 W h $kg^{-1}$. Moreover, the $Fe_3O_4$/rGO ASSC showed ~84.5% capacitance retention after 6000 cycles at a high current density of 5 A $g^{-1}$. The capacitance of $Fe_3O_4$/rGO device was mostly contributed by the surface charges. These effects are attributed to the high surface area of the nanocomposites resulted from the application of sonication. The superior performance of the $Fe_3O_4$/rGO nanocomposite could be attributed to the exfoliation and nucleation induced by intense microconvection generated by sonication, and the synergism achieved through large specific capacitance and energy density of $Fe_3O_4$ and high surface area and conductivity of rGO.

## REFERENCES

(1) Nithya, V. D.; Sabari Arul, N. Progress and Development of Fe3O4 Electrodes for Supercapacitors. *J. Mater. Chem. A* **2016**, *4* (28), 10767–10778.

(2) Das, A. K.; Sahoo, S.; Arunachalam, P.; Zhang, S.; Shim, J. J. Facile Synthesis of Fe3O4 Nanorod Decorated Reduced Graphene Oxide (RGO) for Supercapacitor Application. *RSC Adv.* **2016**, *6* (108), 107057–107064.

(3) Kumar, R.; Singh, R. K.; Vaz, A. R.; Savu, R.; Moshkalev, S. A. Self-Assembled and One-Step Synthesis of Interconnected 3D Network of Fe3O4/Reduced Graphene Oxide Nanosheets Hybrid for High-Performance Supercapacitor Electrode. *ACS Appl. Mater. Interfaces* **2017**, *9* (10), 8880–8890.

(4) Yan, F.; Ding, J.; Liu, Y.; Wang, Z.; Cai, Q.; Zhang, J. Fabrication of Magnetic Irregular Hexagonal-Fe3O4 Sheets/Reduced Graphene Oxide Composite for Supercapacitors. *Synth. Met.* **2015**, *209*, 473–479.

(5) Kassaee, M. Z.; Motamedi, E.; Majdi, M. Magnetic Fe3O4-Graphene Oxide/Polystyrene: Fabrication and Characterization of a Promising Nanocomposite. *Chem. Eng. J.* **2011**, *172* (1), 540–549.

(6) Baptista, J. M.; Sagu, J. S.; KG, U. W.; Lobato, K. State-of-the-Art Materials for High Power and High Energy Supercapacitors: Performance Metrics and Obstacles for the Transition from Lab to Industrial Scale – A Critical Approach. *Chem. Eng. J.* **2019**, *374*, 1153–1179.

(7) Kumar, R.; Sahoo, S.; Joanni, E.; Singh, R. K.; Tan, W. K.; Kar, K. K.; Matsuda, A. Recent Progress in the Synthesis of Graphene and Derived Materials for next Generation Electrodes of High Performance Lithium Ion Batteries. *Prog. Energy Combust. Sci.* **2019**, *75*, 100786.

(8) Kumar, R.; Singh, R. K.; Singh, D. P.; Joanni, E.; Yadav, R. M.; Moshkalev, S. A. Laser-Assisted Synthesis, Reduction and Micro-Patterning of Graphene: Recent Progress and Applications. *Coord. Chem. Rev.* **2017**, *342*, 34–79.

(9) Xu, J.; Gai, S.; He, F.; Niu, N.; Gao, P.; Chen, Y.; Yang, P. A Sandwich-Type Three-Dimensional Layered Double Hydroxide Nanosheet Array/Graphene Composite: Fabrication and High Supercapacitor Performance. *J. Mater. Chem. A* **2014**, *2* (4), 1022–1031.

(10) Kumar, R.; Singh, R. K.; Dubey, P. K.; Singh, D. P.; Yadav, R. M.; Tiwari, R. S. Freestanding 3D Graphene-Nickel Encapsulated Nitrogen-Rich Aligned Bamboo Like Carbon Nanotubes for High-Performance Supercapacitors with Robust Cycle Stability. *Adv. Mater. Interfaces* **2015**, *2* (15), 1500191.

(11) Kumar, R.; Singh, R. K.; Dubey, P. K.; Singh, D. P.; Yadav, R. M. Self-Assembled Hierarchical Formation of Conjugated 3D Cobalt Oxide Nanobead-CNT-Graphene Nanostructure Using Microwaves for High-Performance Supercapacitor Electrode. *ACS Appl. Mater. Interfaces* **2015**, *7* (27), 15042–15251.

(12) Kumar, R.; Matsuo, R.; Kishida, K.; Abdel-Galeil, M. M.; Suda, Y.; Matsuda, A. Homogeneous Reduced Graphene Oxide Supported NiO-MnO 2 Ternary Hybrids for Electrode Material with Improved Capacitive Performance. *Electrochim. Acta* **2019**, *303*, 246–256.

(13) Li, L.; Gao, P.; Gai, S.; He, F.; Chen, Y.; Zhang, M.; Yang, P. Ultra Small and Highly Dispersed Fe3O4 Nanoparticles Anchored on Reduced Graphene for Supercapacitor Application. *Electrochim. Acta* **2016**, *190*, 566–573.

(14) Yang, S.; Gao, P.; Bao, D.; Chen, Y.; Wang, L.; Yang, P.; Li, G.; Sun, Y. Mechanical Ball-Milling Preparation of Mass Sandwich-like Cobalt-Graphene Nanocomposites with High Electrochemical Hydrogen Storage Ability. *J.*

*Mater. Chem. A* **2013**, *1* (23), 6731–6735.

(15) Shi, W.; Zhu, J.; Sim, D. H.; Tay, Y. Y.; Lu, Z.; Zhang, X.; Sharma, Y.; Srinivasan, M.; Zhang, H.; Hng, H. H.; Yan, Q. Achieving High Specific Charge Capacitances in Fe3O4/Reduced Graphene Oxide Nanocomposites. *J. Mater. Chem.* **2011**, *21* (10), 3422–3427.

(16) Park, S.; An, J.; Piner, R. D.; Jung, I.; Yang, D.; Velamakanni, A.; Nguyen, S. B. T.; Ruoff, R. S. Aqueous Suspension and Characterization of Chemically Modified Graphene Sheets. *Chem. Mater.* **2008**, *20* (21), 6592–6594.

(17) Das, A. K.; Srivastav, M.; Layek, R. K.; Uddin, M. E.; Jung, D.; Kim, N. H.; Lee, J. H. Iodide-Mediated Room Temperature Reduction of Graphene Oxide: A Rapid Chemical Route for the Synthesis of a Bifunctional Electrocatalyst. *J. Mater. Chem. A* **2014**, *2* (5), 1332–1340.

(18) Shebanova, O. N.; Lazor, P. Raman Spectroscopic Study of Magnetite (FeFe2O4): A New Assignment for the Vibrational Spectrum. *J. Solid State Chem.* **2003**, *174* (2), 424–430.

(19) Li, L.; Li, R.; Gai, S.; Gao, P.; He, F.; Zhang, M.; Chen, Y.; Yang, P. Hierarchical Porous CNTs@NCS@MnO2 Composites: Rational Design and High Asymmetric Supercapacitor Performance. *J. Mater. Chem. A* **2015**, *3* (30), 15642–15649.

(20) Yan, J.; Liu, J.; Fan, Z.; Wei, T.; Zhang, L. High-Performance Supercapacitor Electrodes Based on Highly Corrugated Graphene Sheets. *Carbon N. Y.* **2012**, *50* (6), 2179–2188.

(21) Choudhury, H. A.; Malani, R. S.; Moholkar, V. S. Acid Catalyzed Biodiesel Synthesis from Jatropha Oil: Mechanistic Aspects of Ultrasonic Intensification. *Chem. Eng. J.* **2013**, *231*, 262–272.

(22) Wu, Q. H.; Qu, B.; Tang, J.; Wang, C.; Wang, D.; Li, Y.; Ren, J. G. An Alumina-Coated Fe3O4-Reduced Graphene Oxide Composite Electrode as a Stable Anode for Lithium-Ion Battery. *Electrochim. Acta* **2015**, *156*, 147–153.

(23) Latorre-Sanchez, M.; Primo, A.; Garcia, H. Green Synthesis of Fe 3O 4 Nanoparticles Embedded in a Porous Carbon Matrix and Its Use as Anode Material in Li-Ion Batteries. *J. Mater. Chem.* **2012**, *22* (40), 21373–21375.

(24) Ren, Y. L.; Wu, H. Y.; Lu, M. M.; Chen, Y. J.; Zhu, C. L.; Gao, P.; Cao, M. S.; Li, C. Y.; Ouyang, Q. Y. Quaternary Nanocomposites Consisting of Graphene, Fe3O 4@Fe Core@Shell, and ZnO Nanoparticles: Synthesis and Excellent

Electromagnetic Absorption Properties. *ACS Appl. Mater. Interfaces* **2012**, *4* (12), 6436–6442.

(25) Zhu, J.; Chen, M.; Qu, H.; Luo, Z.; Wu, S.; Colorado, H. A.; Wei, S.; Guo, Z. Magnetic Field Induced Capacitance Enhancement in Graphene and Magnetic Graphene Nanocomposites. *Energy Environ. Sci.* **2013**, *6* (1), 194–204.

(26) Pal, S.; Majumder, S.; Dutta, S.; Banerjee, S.; Satpati, B.; De, S. Magnetic Field Induced Electrochemical Performance Enhancement in Reduced Graphene Oxide Anchored Fe3O4 Nanoparticle Hybrid Based Supercapacitor. *J. Phys. D. Appl. Phys.* **2018**, *51* (37), 375501–375511.

(27) Liu, T.; Yan, R.; Huang, H.; Pan, L.; Cao, X.; deMello, A.; Niederberger, M. A Micromolding Method for Transparent and Flexible Thin-Film Supercapacitors and Hybrid Supercapacitors. *Adv. Funct. Mater.* **2020**, *30* (46), 2004410.

(28) Chen, J.; Fang, K.; Chen, Q.; Xu, J.; Wong, C. P. Integrated Paper Electrodes Derived from Cotton Stalks for High-Performance Flexible Supercapacitors. *Nano Energy* **2018**, *53*, 337–344.

(29) Sawangphruk, M.; Srimuk, P.; Chiochan, P.; Krittayavathananon, A.; Luanwuthi, S.; Limtrakul, J. High-Performance Supercapacitor of Manganese Oxide/Reduced Graphene Oxide Nanocomposite Coated on Flexible Carbon Fiber Paper. *Carbon N. Y.* **2013**, *60*, 109–116.

(30) Yan, J.; Wei, T.; Qiao, W.; Shao, B.; Zhao, Q.; Zhang, L.; Fan, Z. Rapid Microwave-Assisted Synthesis of Graphene Nanosheet/Co 3O4 Composite for Supercapacitors. *Electrochim. Acta* **2010**, *55* (23), 6973–6978.

(31) Yu, G.; Hu, L.; Liu, N.; Wang, H.; Vosgueritchian, M.; Yang, Y.; Cui, Y.; Bao, Z. Enhancing the Supercapacitor Performance of Graphene/MnO2 Nanostructured Electrodes by Conductive Wrapping. *Nano Lett.* **2011**, *11* (10), 4438–4442.

(32) Pettong, T.; Iamprasertkun, P.; Krittayavathananon, A.; Sukha, P.; Sirisinudomkit, P.; Seubsai, A.; Chareonpanich, M.; Kongkachuichay, P.; Limtrakul, J.; Sawangphruk, M. High-Performance Asymmetric Supercapacitors of MnCo2O4 Nanofibers and N-Doped Reduced Graphene Oxide Aerogel. *ACS Appl. Mater. Interfaces* **2016**, *8* (49), 34045–34053.

(33) Wu, R.; Wang, D. P.; Kumar, V.; Zhou, K.; Law, A. W. K.; Lee, P. S.; Lou, J.; Chen, Z. MOFs-Derived Copper Sulfides Embedded within Porous Carbon Octahedra for Electrochemical Capacitor Applications. *Chem. Commun.* **2015**,

*51* (15), 3109–3112.

(34) Zhu, S.; Fan, L.; Lu, Y. Highly Uniform Fe3O4 Nanoparticle-RGO Composites as Anode Materials for High Performance Lithium-Ion Batteries. *RSC Adv.* **2017**, *7* (87), 59939–59946.

(35) Zhi, J.; Zhao, W.; Liu, X.; Chen, A.; Liu, Z.; Huang, F. Highly Conductive Ordered Mesoporous Carbon Based Electrodes Decorated by 3D Graphene and 1D Silver Nanowire for Flexible Supercapacitor. *Adv. Funct. Mater.* **2014**, *24* (14), 2013–2019.

(36) Zhi, J.; Deng, S.; Wang, Y.; Hu, A. Highly Ordered Metal Oxide Nanorods inside Mesoporous Silica Supported Carbon Nanomembranes: High Performance Electrode Materials for Symmetrical Supercapacitor Devices. *J. Phys. Chem. C* **2015**, *119* (16), 8530–8536.

(37) Zhi, J.; Reiser, O.; Huang, F. Hierarchical MnO2 Spheres Decorated by Carbon-Coated Cobalt Nanobeads: Low-Cost and High-Performance Electrode Materials for Supercapacitors. *ACS Appl. Mater. Interfaces* **2016**, *8* (13), 8452–8459.

(38) Shao, J.; Zhou, X.; Liu, Q.; Zou, R.; Li, W.; Yang, J.; Hu, J. Mechanism Analysis of the Capacitance Contributions and Ultralong Cycling-Stability of the Isomorphous MnO2@MnO2 Core/Shell Nanostructures for Supercapacitors. *J. Mater. Chem. A* **2015**, *3* (11), 6168–6176.

(39) De Pauli, C. P.; Trasatti, S. Electrochemical Surface Characterization of IrO2 + SnO2 Mixed Oxide Electrocatalysts. *J. Electroanal. Chem.* **1995**, *396* (1–2), 161–168.

भारतीय प्रौद्योगिकी संस्थान गुवाहाटी
Indian Institute of Technology Guwahati

# CHAPTER 3

## Ultrasound-Assisted One-Pot Synthesis of Ternary MWCNT/$MnO_2$/rGO Nanocomposite for Supercapacitors with Commercial-Level Mass Loadings

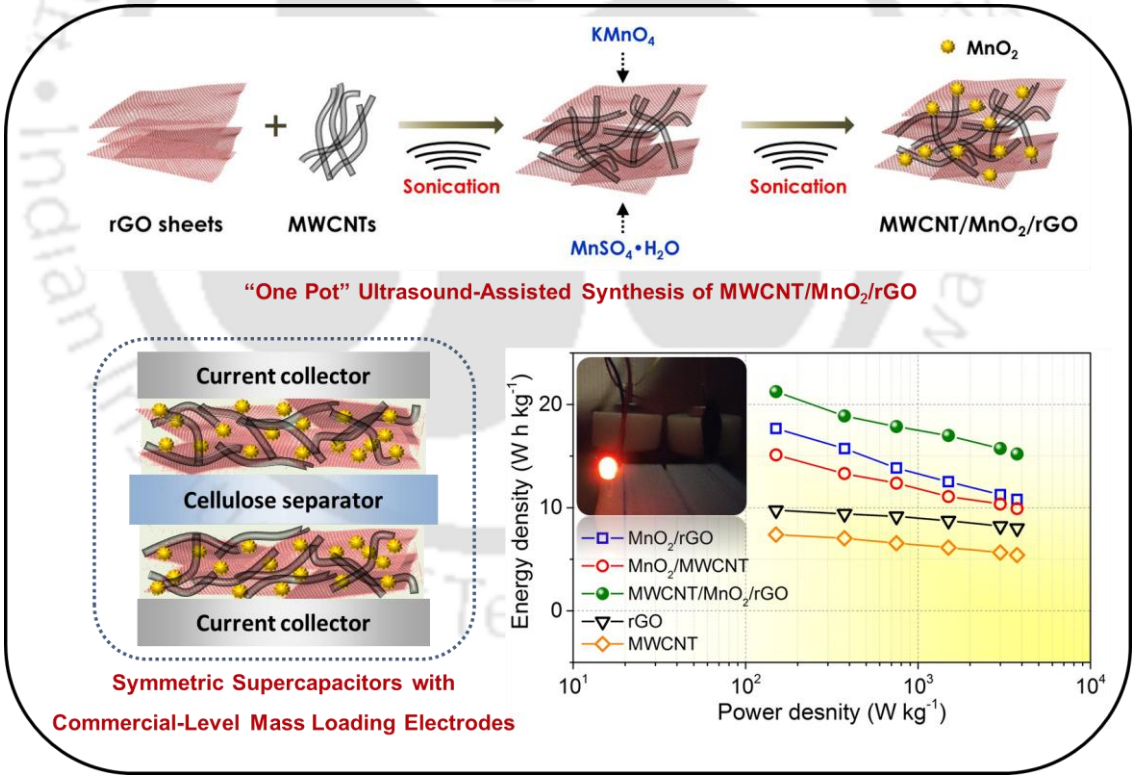

# CHAPTER 3

# ULTRASOUND-ASSISTED ONE-POT SYNTHESIS OF TERNARY MWCNT/$MnO_2$/rGO NANOCOMPOSITE FOR SUPERCAPACITORS WITH COMMERCIAL-LEVEL MASS LOADINGS

## 3.1 INTRODUCTION

Manganese dioxide ($MnO_2$) is a pseudocapacitive material that has shown great promise due to its wide working potential (especially in neutral aqueous electrolytes), high theoretical capacitance, low production cost, and eco–friendly merits.[1] However, the low electrical conductivity of $MnO_2$ ($10^{-5}$ – $10^{-6}$ S $cm^{-1}$) hinders its charge transfer dynamics of $MnO_2$. As a result, specific capacitances reported in the literature for pristine $MnO_2$ (200 – 400 F $g^{-1}$) electrodes are far less compared to its theoretical limit (1380 F $g^{-1}$).[1,2] Therefore, nanocomposites of $MnO_2$ with various conductive materials viz. $MnO_2$/activated carbon,[3,4] $MnO_2$/graphene,[5,6] $MnO_2$/conducting polymers,[7] $MnO_2$/CNT[8,9] have been extensively explored in the literature to obtain enhanced electrochemical properties. In this context, nanocomposites of graphene/CNTs and $MnO_2$ have proven their effectiveness to overcome the difficulties of poor electrical conductivity, cycle stability of pristine $MnO_2$, and the low energy density of carbon components via synergistic effects.

The binary nanocomposites $MnO_2$ with graphene or CNTs for SC applications have been well reported in the existing literature.[6,10–17] On the other hand, literature on SCs based on ternary nanocomposites of graphene, CNTs, and $MnO_2$ are relatively small. The previous literature[12,18–21] on ternary composites showed superior

electrochemical performance as compared to binary nanocomposite as SC electrodes. Lei et al.[18] synthesized a ternary nanocomposite by intercalating graphene sheets via $MnO_2$-CNTs functionalized with poly(diallyldimethylammonium chloride) via a multistep process and demonstrated enhanced capacitive properties. Cheng et al. used a sonochemical approach to prepare rGO/$MnO_2$ composite and later added functionalized few-walled CNTs (fFWNTs) to fabricate graphene/$MnO_2$/fFWNTs films through a vacuum filtration method.[19] Jin et al. electrodeposited $MnO_2$ on a CNT buckypaper paper, and then soaked as-prepared $MnO_2$/CNT paper on graphene dispersion for adsorption of rGO on its surface.[12] In another study, Zhu et al. synthesized 3D CNT–graphene–Ni hybrids through a two-step chemical vapor deposition (CVD) process and later used poly ethylene glycol (PEG) based reduction of $KMnO_4$ to obtain 3D $MnO_2$–CNT–graphene–Ni hybrids.[20] Similarly, Jiang et al. first synthesized rGO/CNTs-Ni composite via an annealing and CVD based process followed by a hydrothermal method to deposit $MnO_2$ on the surface of rGO/CNTs-Ni.[21] The synthesis methods presented in these previous studies were either multi-step or often involve complex procedures and high temperatures. Therefore, a simple and fast synthesis process for the ternary composites is very essential. Furthermore, previous studies have shown that the undesired restacking of graphene layers due to their π–π interaction and van der Waals forces leads to a substantial reduction in the active surface area of graphene-based electrodes, which significantly reduces the performance.[22,23] Interestingly, addition of various nanomaterials, viz. as 1-D CNTs, metal oxide nanoparticles) in the graphene framework could work as spacers to prevent the restacking of graphene sheets and consequently improved capacitive performance can be obtained.[23,24]

Although $MnO_2$/carbon–based nanocomposites reported in the literature have demonstrated remarkable enhancement in capacitive performance, most of these studies were performed at very low electrode mass loadings (~ 1 – 2 mg $cm^{-2}$). In low mass loading electrodes, the actual amount of energy stored is very low, thereby limiting their practical application in energy storage devices.[25] Usually, for practical/commercial applications the mass loading of the electrodes should be ~10 mg $cm^{-2}$.[26–28] A substantial reduction in the capacitance and energy density is observed for the commercial level electrode mass loading, particularly at high current densities. This is a collective consequence of blocked ion transportation pathways, poor electrolyte accessibility, poor wetting of electrodes, increased electrical resistance, and ultra–long ion transport channels.[26,29] Therefore, achieving high energy density simultaneously with high power density is a challenge in the fabrication of SC electrodes with commercial level mass loadings.

Herein, we have reported a "one-pot" ultrasound-assisted synthesis of $MnO_2$ decorated rGO/MWCNT based ternary nanocomposite for SCs. The ternary MWCNT/$MnO_2$/rGO (MnGC) nanocomposite possessed a mesoporous structure with abundant ion diffusion channels together with a high electrochemically active surface area. When SCs were assembled using MnGC as electrodes, the device exhibited a high cell voltage of 1.5 V in a 1 M $Na_2SO_4$ electrolyte. Moreover, the device demonstrated high gravimetric capacitance and energy density along with excellent cycle stability (no loss of capacitance after 5000 cycles). It is noteworthy that the high supercapacitive performances of the devices were obtained at commercial-level electrode mass loadings (~12 mg $cm^{-2}$). The capacitance and energy density of the ternary MnGC based SC was substantially higher than those of the SCs with binary MnC ($MnO_2$/MWCNTs) and MnG ($MnO_2$/rGO) composites synthesized by us.

## 3.2 EXPERIMENTAL SECTION

### 3.2.1 Materials

Manganese (II) sulphate monohydrate ($MnSO_4 \cdot H_2O$), potassium permanganate ($KMnO_4$), were acquired from Himedia Ltd. (India). Nitric acid ($HNO_3$, 70%) was purchased from Merck (India). Multi-walled carbon nanotubes (outer diameter: 5–20 nm; inner diameter: 2–6 nm; length: 1–10 µm) were obtained from Reinste Nano Ventures Ltd. (India). Carbon black (Super P® Conductive) was obtained from Alfa-Aesar (USA). Polytetrafluoroethylene (PTFE, 60 wt% dispersion in $H_2O$) was procured from Sigma Aldrich (India). Ultrapure water was used for all experiments.

### 3.2.2 Synthesis of Ternary MWCNT/$MnO_2$/rGO Nanocomposite

Reduced graphene oxide (rGO) was synthesized as described in **Chapter 2**. The multi-walled carbon nanotubes (MWCNTs) were purified and functionalized with nitric acid to improve their dispersion (as described in **Appendix 2**).

The prepared rGO and MWCNTs were added to 200 mL ultrapure water (rGO:MWCNTs = 8:2 ratio) and vigorously sonicated (100 W, 37 kHz) for 30 min to exfoliate the rGO and to obtain a homogeneous dispersion (3 mg $mL^{-1}$) of rGO/MWCNTs. Then, $MnSO_4 \cdot H_2O$ (3 mmol) was added to the above dispersion under sonication. An aqueous solution of $KMnO_4$ (80 mL, 0.025 M) was added drop-wise to the reaction mixture under continuous sonication. The reaction mixture was further sonicated for another 30 min and then allowed to settle. The settled precipitate was filtered, washed with excess water, and oven-dried at 70 °C to obtain the MWCNT/$MnO_2$/rGO (MnGC) nanocomposite.

### 3.2.3 Synthesis of $MnO_2$/MWCNT and $MnO_2$/rGO Nanocomposites

Binary nanocomposites viz. $MnO_2$/MWCNT (MnC) and $MnO_2$/rGO (MnG), were also synthesized using the same ultrasound-assisted method. In the case of the binary composites, 3 mg $mL^{-1}$ dispersion of either MWCNTs or rGO was first prepared in 200 mL ultrapure water using sonication. Afterward, $MnSO_4 \cdot H_2O$ and $KMnO_4$ were added as described in the previous section. Finally, the precipitate was separated, washed, and dried to obtain the binary nanocomposites.

Pristine $MnO_2$ was also synthesized without adding any carbon material in the synthesis procedure. The method of the pristine $MnO_2$ synthesis is described in section **A2.2 in Appendix 2**.

### 3.2.4 Characterization Techniques

The synthesized materials were characterized using XRD, Raman spectroscopy, FESEM, TEM, EDS, and BET surface area analysis. The instruments used in these analyses are the same as described in **Chapter 2**.

### 3.2.5 Electrochemical Measurements

The electrode slurry was prepared by homogeneously mixing electro-active material (80 wt%), carbon black (10 wt%), and PTFE (10 wt%) in ethanol. The slurry was then coated on stainless steel foil (current collector) and dried overnight at 80 °C. Subsequently, disc electrodes (diameter 1.5 cm) were punched out after drying. The active mass loadings of the electrodes were ~ 12 mg $cm^{-2}$. Electrochemical tests were performed in a two-electrode configuration using a split-type coin cell (MTI Corporation, USA) assembly. Two-electrode symmetric cells were constructed with two similar electrodes, a cellulose separator, and $Na_2SO_4$ (300 μL) as the electrolyte.

Electrochemical measurements, viz. CV, GCD, and EIS, were performed using a M204 Potentiostat/Galvanostat (Metrohm Autolab). The specific capacitance of a single electrode ($C_g$, F $g^{-1}$) was calculated from the CV and GCD curves using equations 1.7 and 1.8, respectively as described in section 1.4.1 in **Chapter 1**. The energy density (E, W h $kg^{-1}$), and power density (P, W $kg^{-1}$) of the cells were calculated from GCD curves using equations 1.9 and 1.10, respectively (described in section 1.4.1 in **Chapter 1)**.

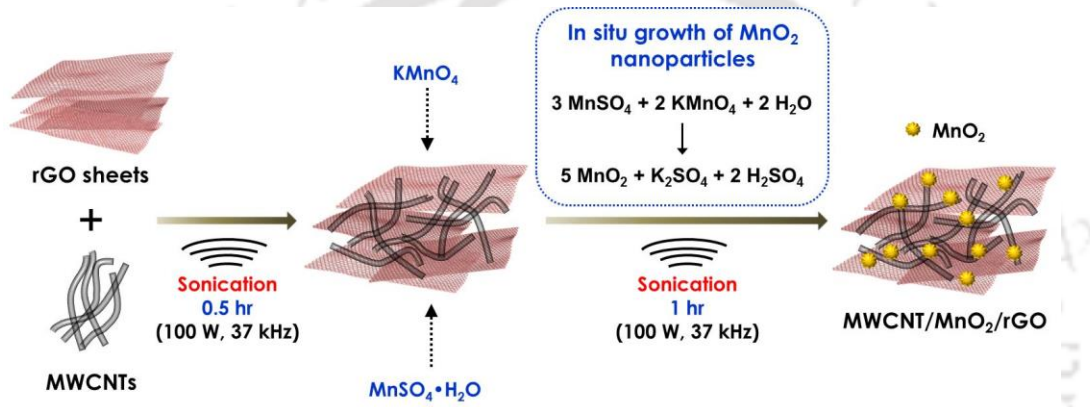


**Figure 3.1** Schematic illustration of "one-pot" ultrasound-assisted synthesis of the MWCNT/$MnO_2$/rGO nanocomposite

## 3.3 RESULTS AND DISCUSSION

### 3.3.1 Materials Characterization

The $MnO_2$ nanoparticles were grown on the surface of MWCNTs and rGO via an ultrasound–assisted redox reaction. The growth of $MnO_2$ nanostructures on the carbon substrates (viz. MWCNTs and rGO) was achieved through the formation of $Mn^{4+}$ as a result of oxidation/reduction reaction between $Mn^{2+}$ and $Mn^{7+}$ ions.[30] The loadings of $MnO_2$ on the synthesized nanocomposites, i.e. MnC, MnG, and MnGC nanocomposites were ~ 37 – 39 wt%. The $MnO_2$ content was calculated from the

weight difference before and after the growth of $MnO_2$ on the rGO/MWCNTs. Moreover, we also calculated the $MnO_2$ content by dissolving the composite in 1 M HCl solution followed by filtering and weighing the undissolved rGO/MWCNTs as reported in the literature[10] and obtained similar results. **Figure 3.1** represents the process of MnGC nanocomposite synthesis and the schematic illustration of the experimental setup used for the synthesis is shown in **Figure A2.1** (**Appendix 2**).

The X–ray diffraction patterns were recorded over the range of $2\theta = 10 - 70°$ (at a scan rate of 5° $min^{-1}$) and shown in **Figure 3.2a**. MWCNTs exhibited a high–intensity characteristic peak at $2\theta = 26°$ and a smaller peak at $2\theta = 43°$ conforming to (0 0 2) and (1 0 0) graphitic carbon peaks, respectively. Similarly, the pristine reduced graphene oxide also showed the (0 0 2) and (1 0 0) peaks at $2\theta = 24.8°$ and 43°. The diffraction peak corresponding to (0 0 2) plane of the rGO was broader, whereas it was sharper in the case of MWCNTs supporting the higher crystallinity of the carbon nanotubes. The XRD patterns of binary nanocomposites, MnC and MnG prominently showed the (0 0 2) peaks of both MWCNT and rGO, respectively. The MnGC nanocomposite showed a combination of broader and an adjacent sharper peak ascertaining the (0 0 2) planes of both rGO and MWCNT. The intensity of (0 0 2) plane at $2\theta = 26°$ was reduced in the composites due to the growth of $MnO_2$ on the surface of MWCNTs/rGO. Moreover, the intensity of the (1 0 0) plane was also low in the nanocomposites. The presence of two small and broad peaks at $2\theta = 37°$ and 66.3° could be related to the (2 1 1) and (0 0 2) planes of $MnO_2$, respectively. The XRD patterns of the pristine $MnO_2$ (synthesized via the same method without any carbon substrates) were also compared with the XRD patterns of the composite, and two similar peaks were observed at $2\theta = 37°$ and 66.3° corresponding to (2 1 1) and (0 0 2) planes of poorly crystalline $MnO_2$.[30] Thus, the XRD results confirmed the

existence of $MnO_2$ in the nanocomposite. The weak intensity of $MnO_2$ referred to its poor crystallinity, which could be due to the small size of $MnO_2$ particles.[8] Additionally, amorphous manganese oxides are expected to have higher capacitance than their crystalline counterparts due to shorter length of diffusion and high ionic conductivity.[9]

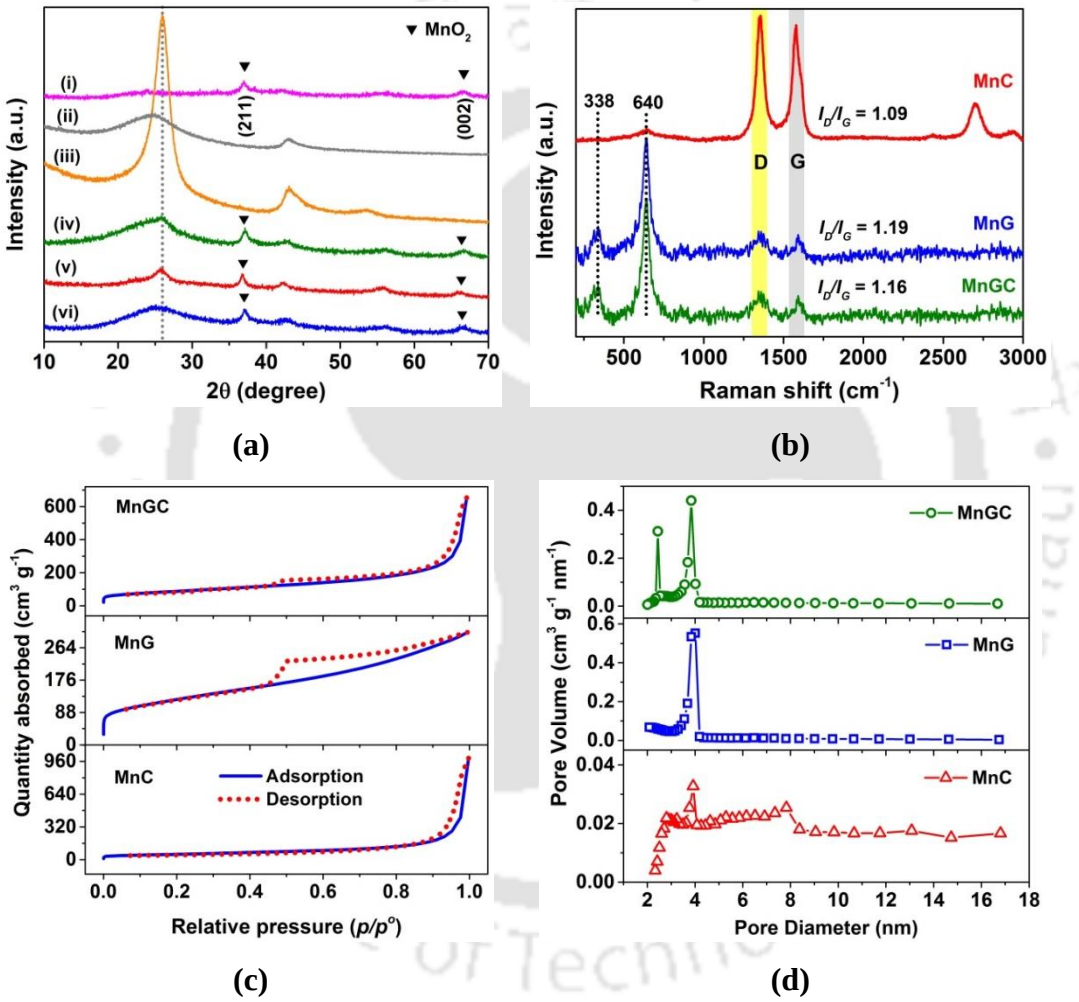


**Figure 3.2** (a) XRD patterns of (i) $MnO_2$, (ii) rGO, (iii) MWCNT, (iv) MnGC, (v) MnC, (vi) MnG; (b) Raman spectra, (c) nitrogen adsorption-desorption isotherms, and (d) pore size distribution of MnC, MnG, and MnGC nanocomposites

The structural features and composition of the nanomaterials were further characterized using the Raman spectroscopy technique. Raman spectra of MWCNTs

and rGO (**Figure A2.2, Appendix 2**) exhibited two distinct D and G bands. The G band characterizes the vibrational mode of $sp^2$ hybridized carbon atoms whereas the D band signifies defects present in the $sp^2$ carbon rings. The bands of MWCNTs were sharp and observed at 1350 (D band) and 1574 (G band) $cm^{-1}$, respectively. The rGO exhibited relatively broader peaks at 1352 $cm^{-1}$ (D band) and 1598 $cm^{-1}$ (G band). The intensity ratio of D and G bands ($I_D/I_G$) corresponds to the degree of disorder present in the carbon frameworks. The $I_D/I_G$ values for the MWCNTs and rGO were 1.05 and 1.18, respectively; indicating the higher degree of structural defects present in rGO, which were introduced during the hydrazine reduction process. The D and G bands were present in the Raman spectra of all the nanocomposites and the $I_D/I_G$ ratios were 1.09 (MnC), 1.19 (MnG), and 1.16 (MnGC), respectively (**Figure 3.2b**). A prominent peak at ~ 640 $cm^{-1}$ was observed for all the nanocomposites, which could be attributed to the Mn–O vibration in $MnO_2$. Whereas another weak peak at ~ 338 $cm^{-1}$ originating from O–Mn–O vibration mode is also observed in the Raman spectra of MnG and MnGC.[5,9,31] The presence of Mn–O, and O–Mn–O vibration modes supported the XRD results, and thus, confirmed the presence of $MnO_2$ in the nanocomposite.

The BET measurements were performed to find the specific surface area pore size of the synthesized samples. **Figure 3.2c** shows the $N_2$ adsorption–desorption isotherms of the nanocomposites. A surface area of ~ 434 $m^2\ g^{-1}$ was obtained for MnG, as compared to ~ 189 $m^2\ g^{-1}$ of MnC and ~ 313 $m^2\ g^{-1}$ of MnGC. The adsorption–desorption isotherms of all three nanocomposites were observed to be type IV isotherms with hysteresis loops due to capillary condensation in the mesopores after monolayer–multilayer adsorption. The H1 type hysteresis loop observed for MnC sample could be attributed to the presence of cylindrical pores with facile pore

connectivity. The MnG sample showed an H2 type of hysteresis loop possibly due to the presence of uniform channel–like networks of mesopores with narrow openings. Interestingly, the hysteresis loop of the MnGC could be correlated to both H1 and H2 type hysteresis loops. The influence of H1 and H2 type loops is essentially due to the presence of both cylindrical pores and narrow channel–like mesoporous channels. The respective surface areas of MWCNTs and $MnO_2$ were ~ 252 and 175 $m^2$ $g^{-1}$, respectively. The surface area of pristine rGO was ~ 555 $m^2$ $g^{-1}$ as reported in our previous study.[32] Adsorption–desorption isotherms of MWCNTs and $MnO_2$ (**Figures A2.3a-b, Appendix 2**) were found to be type IV isotherms with H1 and H2 type of hysteresis loops, respectively. The H2 type hysteresis loop of $MnO_2$ indicated the presence of narrow slit–like pores with irregularly shaped voids. The Barrett–Joyner–Halenda (BJH) model was used to obtain the pore–size distributions (**Figure 3.2.d** and **Figures A2.3c-d, Appendix 2**) of the synthesized nanomaterials. The nanocomposites along with the pristine MWCNTs and $MnO_2$ demonstrated mesoporous distribution in 2 – 18 nm range. The average pore diameters of the $MnO_2$, MWCNTs, MnC, MnG, and MnGC were found to be 4.40, 6.32, 7.42, 4.05, and 4.59 nm, respectively. The narrow pore size distribution of the samples is beneficial for better transport of electrolyte ions. Several studies have revealed that mesopore networks in the range of 2 – 5 nm could provide efficient pathways for easier ion diffusion to the core of electrodes.[33,34] Improved ion transport essentially augments the capacitive performance of the electrode material. Moreover, the high pore volumes of nanocomposites (**Table A2.1, Appendix 2**) could be expected to provide abundant active sites for surface redox reactions and double–layer formation.

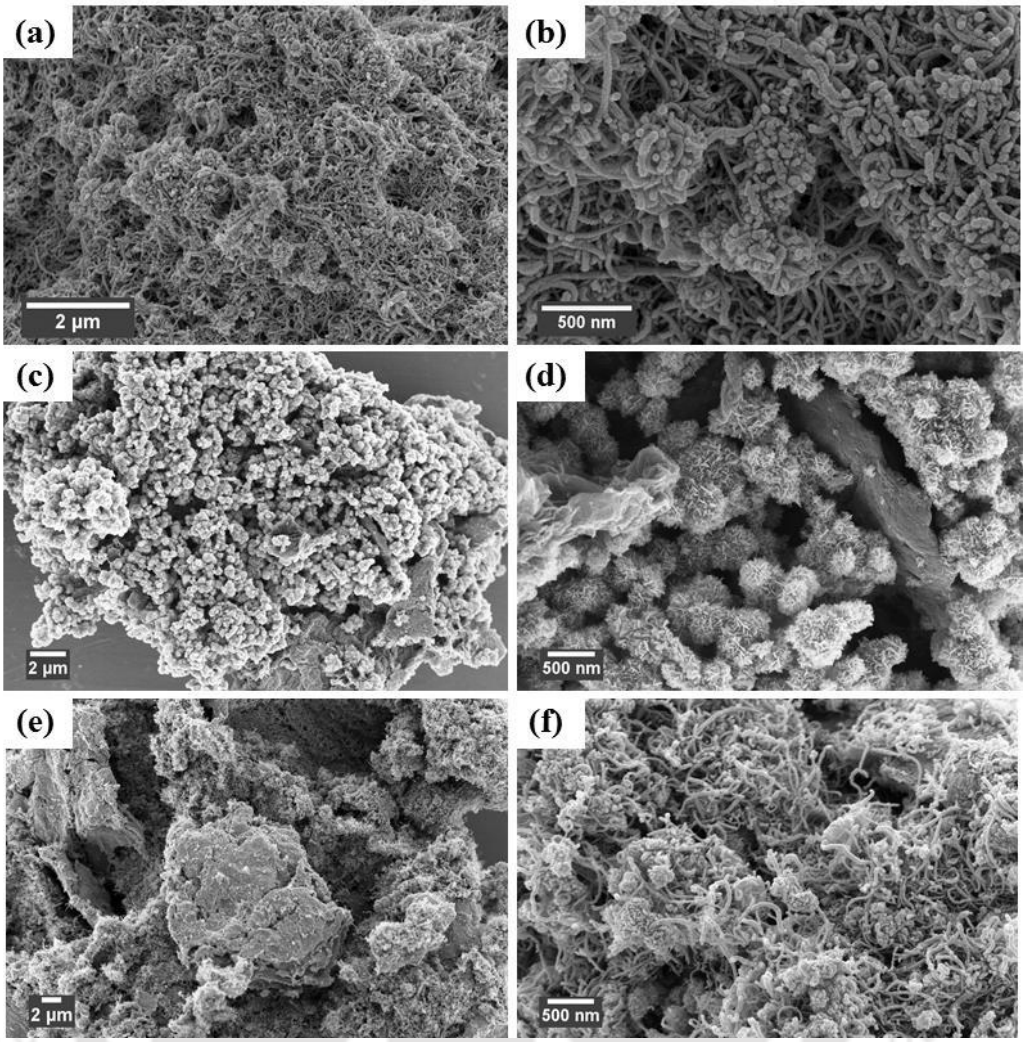


**Figure 3.3** FE-SEM images of (a-b) MnC, (c-d) MnG, and (e-f) MnGC nanocomposites in low and high resolution

The morphologies of the synthesized nanomaterials were studied using FE–SEM and TEM images. The MWCNTs had tubular structures with an outer diameter of 5 – 30 nm and a smooth surface (**Figures A2.4a-b, Appendix 2**). **Figures A2.4c-d** (**Appendix 2**) revealed the crumpled sheet–like morphology of synthesized rGO. The FE–SEM and TEM images (**Figures A2.4e-f, Appendix 2**) indicate that the $MnO_2$ nanoparticles were aggregates of grain–like structures, which apparently look like a

spiked $MnO_2$ sphere. These nanograins have varying diameters (10–30 nm) and lengths varying from 60 nm to sometimes more than 100 nm.

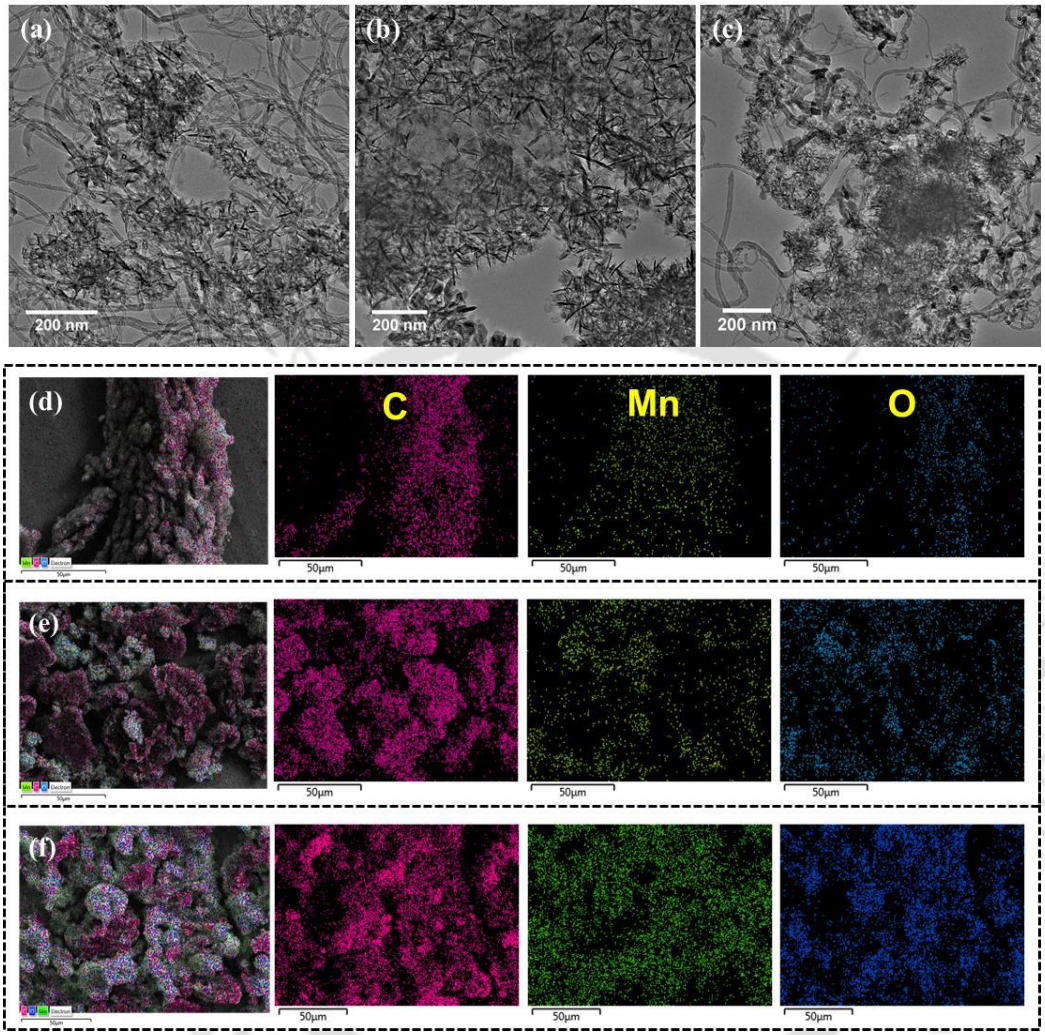


**Figure 3.4** TEM images of (a) MnC, (b) MnG, and (c) MnGC composites; elemental mapping of (d) MnC, (e) MnG, and (f) MnGC nanocomposites (carbon in maroon, manganese in green, and oxygen in blue).

The FE–SEM images of the nanocomposites (**Figure 3.3**) clearly show the presence of $MnO_2$ in the carbon substrates. The morphologies of the $MnO_2$ in the MnG were similar to the pristine $MnO_2$ with densely aggregated grains on the rGO surface. Whereas in the MnC composite the loosely aggregated grains of $MnO_2$ was observed

on the surface of MWCNTs which could be due to the relatively lesser packing density of the MWCNTs as compared to rGO. In the MnGC nanocomposite, the $MnO_2$ grains were efficiently grown on the surface of both rGO and MWCNTs with relatively lesser aggregation than MnG nanocomposite. The TEM images of the nanocomposites (**Figures 3.4a-c**) show that $MnO_2$ particles were grown on the external surface of the MWCNTs and rGO in the nanocomposites. The relatively dense distribution of $MnO_2$ in MnG as compared to MnGC and MnC nanocomposites was also evident from the TEM images, thus supporting the FE–SEM results. The growth of $MnO_2$ on the carbon substrates (viz. MWCNTs and rGO) could form hierarchal mesoporous networks. As a result, the electroactive surface area available for electrolyte ions would increase and facilitate EDL formation and surface redox reactions. The elemental mappings (**Figures 3.4d-f**) and EDX spectra (**Figures A2.5a-c, Appendix 2**) of the MnGC, MnC, and MnG nanocomposites also confirmed the presence of Mn, C, and O elements in the nanocomposites.

### 3.3.2 Electrochemical Performance

To study the electrochemical performance of the nanocomposites, symmetric SCs were fabricated using two identical electrodes, a cellulose separator soaked in 1 M $Na_2SO_4$ electrolyte (cell assembly is shown in **Figure 3.5**). The mass loading of each electrode was ~ 12 mg $cm^{-2}$. In symmetric SCs, the charge stored in the positive and the negative electrodes are similar, and therefore, the potential window of the device is limited by the dissociation of the electrolyte. Typically, the potential window of common acidic and basic aqueous electrolytes is limited to 1 V due to $O_2$ and $H_2$ gas evolution from the electrolysis of water. Conversely, in neutral aqueous electrolytes such as $Na_2SO_4$, higher working potentials could be achieved as the low concentration of $H^+$ and $OH^-$ ions delays the gas evolution reactions.[35,36] In our study,

we were able to achieve a wide potential window of 1.5 V in 1 M $Na_2SO_4$ for the symmetric SCs (**Figure A2.6, Appendix 2**). This potential window is relatively wider as compared to other similar studies in the existing literature (**Tables A2.2-2.3, Appendix 2**).

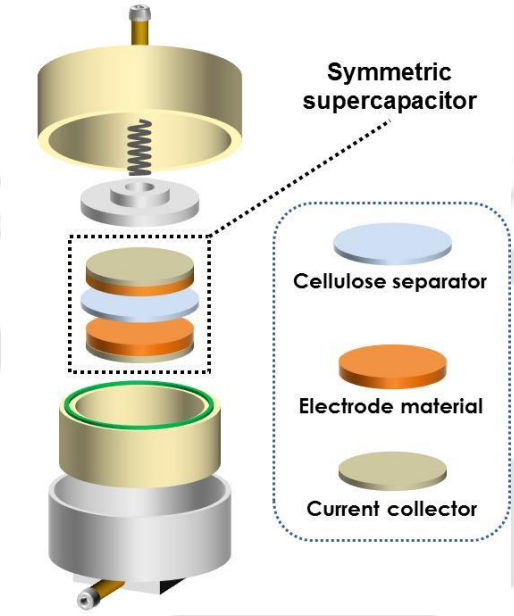


**Figure 3.5** Schematic of the two-electrode symmetric SC cell and the split-type cell assembly

The assembled SC cells were subjected to cyclic voltammetry (CV) tests at scan rates of 5 – 50 mV $s^{-1}$. The CV curves of the pristine MWCNTs, rGO, MnC, MnG, and MnGC at a scan rate of 10 mV $s^{-1}$ are shown in **Figure 3.6a**. It can be observed that the CV curves of the nanocomposites are quasi–rectangular, indicating superior capacitive behavior of the nanocomposites.[37] There is a presence of very weak redox peak in the CV curves, which could be attributed to the oxygen–containing groups present in the MWCNTs and rGO. The CV curves of the MnC, MnG, and MnGC nanocomposites did not show much distortion and maintained a fairly rectangular shape even at higher scan rates (**Figures 3.6b-d**). These results

indicate that the nanocomposite electrodes possessed superior charge storage behavior with quick time response.[38]

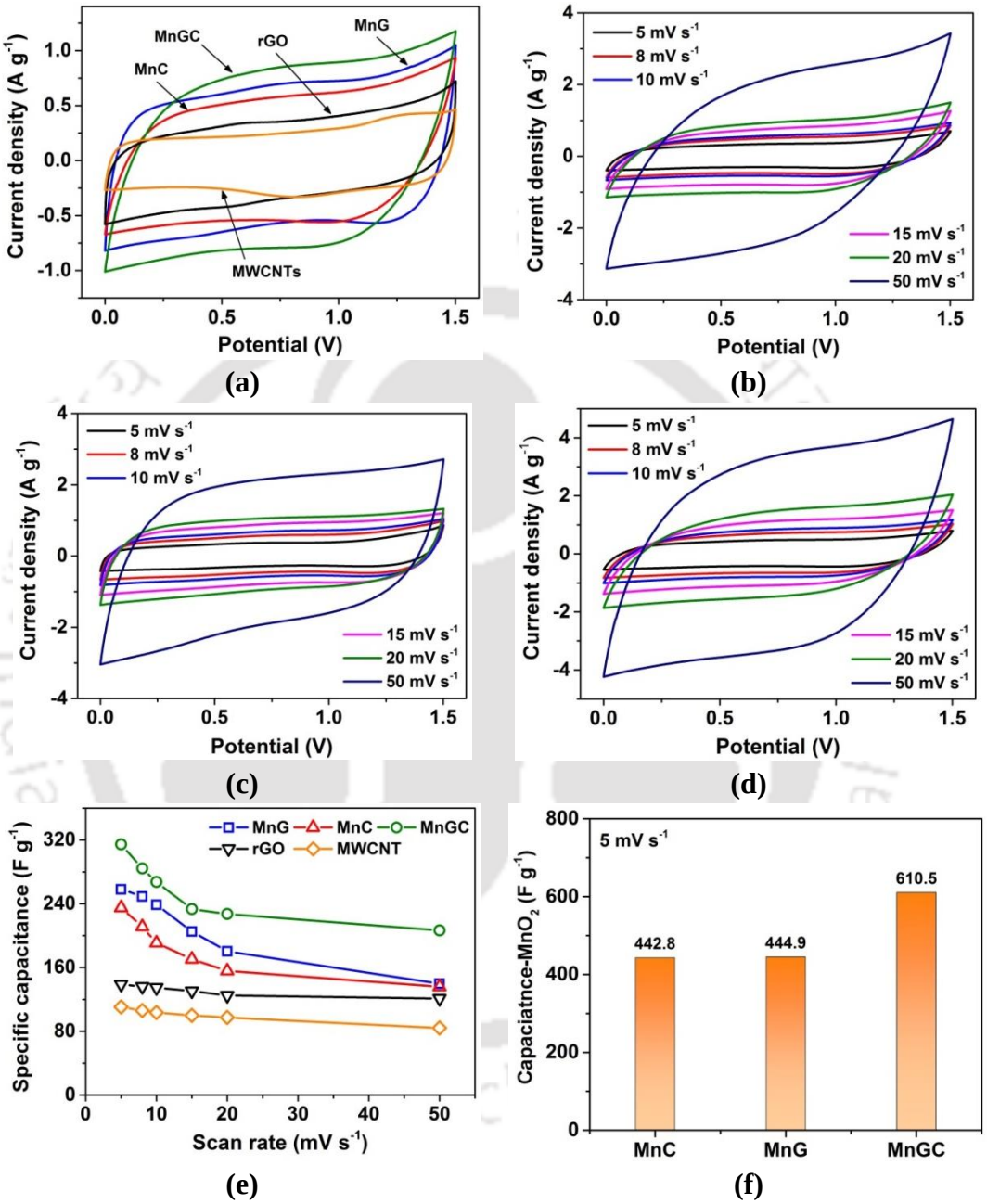


**Figure 3.6** (a) Comparison of the CV curves of SCs at 10 mV $s^{-1}$; CV curves of (b) MnC, (c) MnG, and (d) MnGC SCs at various scan rates; (e) specific capacitance of the SC electrodes as a function of scan rate; (f) capacitance contribution of $MnO_2$ at 5 mV $s^{-1}$

Moreover, CV curves of MWCNT and rGO indicated redox behavior together with double layer charge storage, which could be attributed to the presence of surface oxygen–containing groups in the samples (**Figures A2.7a** and **A2.7c, Appendix 2**). CV curves of MWCNT and rGO show negligible polarization at higher scan rates, which suggests reversible and efficient charge transfer. The larger area under the CV curves of the MnGC, MnC, and MnG, as compared to pristine rGO and MWCNT, indicated the increase in capacitance of nanocomposites due to the addition of $MnO_2$. These results indicated that the capacitance of the MnGC, MnC, and MnG electrodes was a combined contribution of double–layer capacitance of carbon components (MWCNTs and rGO) and pseudocapacitance from the $MnO_2$ and surface oxygen groups present in the carbon components. The charge storage of $MnO_2$ could take place via either rapid adsorption of electrolyte cations ($Na^+$) on the surface (surface faradaic reaction) of the $MnO_2$ or intercalation/deintercalation of cations in the bulk $MnO_2$ (bulk faradaic reaction).[39,40]

$$(MnO_2)_{surface} + Na^+ + e^- \longleftrightarrow (MnOONa)_{surface} \quad \text{(R 3.1)}$$

$$MnO_2 + Na^+ + e^- \longleftrightarrow MnOONa \quad \text{(R 3.2)}$$

The gravimetric capacitances of the electrodes at different scan rates were calculated and are presented in **Figure 3.6e**. The MnGC nanocomposite electrodes demonstrated a high gravimetric capacitance of 314.6 F $g^{-1}$ at 5 mV $s^{-1}$, and this value is 1.34× and 1.22× higher than the capacitance of the MnC (235.1 F $g^{-1}$) and MnG (258.2 F $g^{-1}$) electrodes. Additionally, the capacitances of rGO and MWCNTs electrodes at 5 mV $s^{-1}$ were calculated as 138.9 and 110.5 F $g^{-1}$, respectively. Notably, the specific capacitance obtained for the synthesized MnGC nanocomposites at commercial-level electrode mass loadings is superior to many earlier reports (**Tables A2.2 and A2.3, Appendix 2**). Although some studies have reported

astonishing capacitances for composites of graphene/CNTs with $MnO_2$, electrode mass loadings in these studies were very low (≤ 1 – 2 mg $cm^{-2}$). Despite their extraordinary capacitances, the low mass loading electrodes cannot be used in commercial applications due to their poor actual capacity (as a result of the low ratio of active materials to a full cell). When the mass loading of the electrodes is increased, rapid fading of the capacitance is observed along with poor rate capability as evident in most of the studies.[10,27] As shown in **Figure 3.6e**, the capacitances of the nanocomposite electrodes decreased at increased scan rates as the charge storage gets limited to the outer surface only at higher scan rates. The MnGC nanocomposite displayed a capacitance of 207 F $g^{-1}$ at 50 mV $s^{-1}$ and retained ~ 67 % of initial capacitance. Conversely, the MnC and MnG electrodes were able to retain 57.8 and 54.1 % of their capacitance when the scan rate was increased to 50 mV $s^{-1}$. Although the MnG electrodes exhibited superior capacitance as compared to MnC electrodes, the rate performance of the MnC electrodes was slightly better than the MnG. The relatively worse rate capability of MnG could be due to the dense aggregation of $MnO_2$ nanostructures on the surface of crumpled rGO resulting in sluggish ion transport dynamics. The relatively lower aggregation of $MnO_2$ on the MWCNTs surface has helped the MnC electrodes to retain comparatively better capacitance. Moreover, the superior rate capability of MnGC electrodes could be ascribed to the synergistic effect resulting from simultaneous growth of $MnO_2$ on the surfaces of both rGO and MWCNTs. The specific capacitances contributed by only $MnO_2$ (pseudocapacitance) in the nanocomposite electrodes were also calculated.[1] As shown in **Figure 3.6f**, the capacitance of $MnO_2$ in the MnGC electrodes was 610.5 F $g^{-1}$ at 5 mV $s^{-1}$, which was much higher compared to the MnC (442.8 F $g^{-1}$) and MnG (444.9 F $g^{-1}$) electrodes at similar conditions. It is noteworthy that the MnGC electrodes

exhibited superior capacitive response compared to MnG electrodes despite its relatively lower specific surface than MnG nanocomposite. This excellent capacitance of the MnGC could be ascribed to its unique microstructure that allowed maximum electrochemical utilization of the $MnO_2$ nanostructures and the reduction in diffusion length promoted faster charge transport. As a result, the $MnO_2$ nanostructures of MnGC effectively participated in the charge storage/delivery process exhibiting high pseudocapacitance, thereby enhancing the overall capacitance of the MnGC electrodes.

The electrochemical performance of the nanocomposite electrodes was further investigated by galvanostatic charge–discharge (GCD) at different current densities ranging from 0.2 – 5 A $g^{-1}$. The SC electrodes could work up to the potential of 1.5 V as observed in CV curves. The GCD curves of the SCs at 1 A $g^{-1}$ are shown in **Figure 3.7a**. The symmetric and linear GCD curves indicated the good capacitive behavior of the electrode materials.[41] Additionally, the absence of any voltage plateaus inferred that there is no bulk redox reaction during the charge–discharge process. The GCD curves of the SCs (**Figures 3.7b-d** and **Figures A2.7b, d in appendix 2**) at varying current densities did not deviate from the symmetric and linear nature suggesting high reversibility of the charge storage process. The *IR* drop values were calculated from the GCD curves and found to be 0.09, 0.06, 0.09, 0.02, and 0.08 V for the MnC, MnG, MnGC, rGO, and MWCNT SCs, respectively. The capacitances of the electrodes were also evaluated from the GCD curves. At a current density of 0.2 A $g^{-1}$, the capacitance of MnGC was calculated to be ~ 271.8 F $g^{-1}$ which is 1.2×, 1.4×, 2.2×, 2.9× the capacitance of the MnG (226.2 F $g^{-1}$), MnC (193.5 F $g^{-1}$), rGO (124.7 F $g^{-1}$), and MWCNT (94.5 F $g^{-1}$) electrodes, respectively. The decrease in capacitance of the electrodes for higher current density is evident from the smaller

charge–discharge time of the GCD curves. This decreased capacitance could be ascribed to inadequate ion migration to the inner core of the electrodes and thereby impeding the charge transfer process.[42]

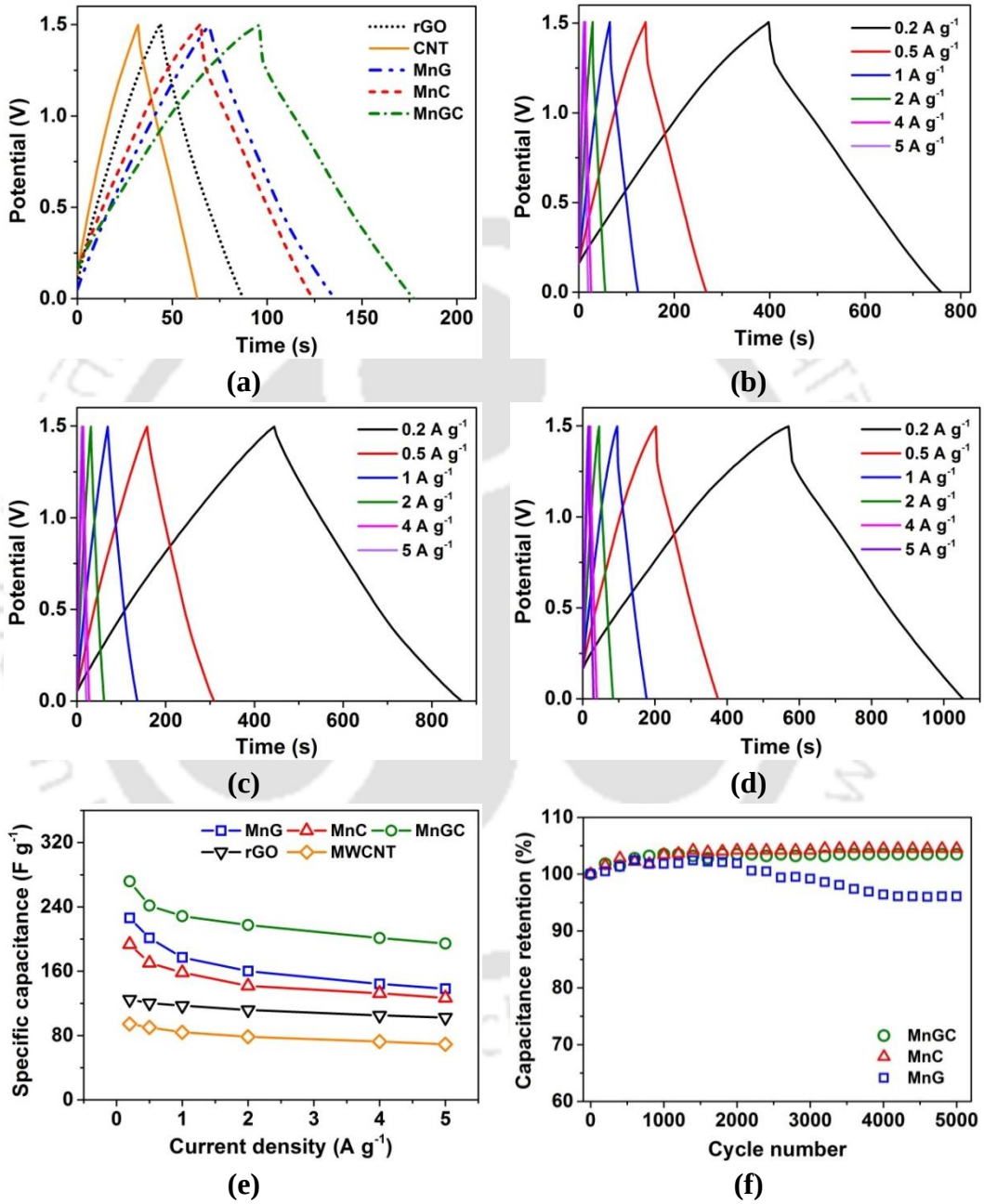


**Figure 3.7** (a) Comparison of GCD curves of SCs at 1 A $g^{-1}$; GCD curves of (b) MnC, (c) MnG, and (d) MnGC SCs at different current densities; (e) specific capacitance of the SC electrodes as a function of current density; (f) long-term cyclic stability of SC cells

Furthermore, the MnGC nanocomposites exhibited superior capacitance values as compared to the MnG and MnC even at high current densities (**Figure 3.7e**). The MnGC electrode retained a capacitance of 194.6 F $g^{-1}$ (71.5%) at 5 A $g^{-1}$ demonstrating the superior rate capability as compared to the MnG (61.4%) and MnC (65.5%) electrodes. The unique structure of MnGC has efficient pore networks for rapid charge transfer, which results in its superior capacitance retention at high current densities.

The fabricated SCs were subjected to repetitive charge–discharge cycles at 5 A $g^{-1}$ to study the electrochemical stability of the electrode materials. As shown in **Figure 3.7f**, there was no prominent degradation in the capacitance for the MnGC and MnC SCs, demonstrating excellent electrochemical stability even after 5000 charge–discharge cycles. The capacitance of the MnGC SC increased 103.4 % after 5000 cycles, as the electrode capacitance increased to 201.2 F $g^{-1}$ from 194.6 F $g^{-1}$. The MnC SC demonstrated 104.5% of initial capacitance after charge–discharge tests. Conversely, MnG SC was able to retain about 96.1% of its initial capacitance. Plausibly the electrolyte ions could not utilize the maximum available electrochemical area of the thicker (due to high mass loading) electrodes at the initial charge–discharge cycles. When the SCs were cycled for a few hundred cycles, the electrolyte ions were able to penetrate deeper into the pore structure as a result of the continuous charge–discharge process (and application of voltage). Thus the electrochemically active area for charge storage must have increased and as a result, the capacitances of the electrodes were gradually increased up to ~ 1000 cycles. The MnGC and MnC SCs were able to retain the increased capacitance whereas the MnG SC suffered a 3.9% loss in capacitance after 5000 charge-discharge cycles. This loss of capacitance could be due to poor capacitance retention of densely grown $MnO_2$ in the MnG

nanocomposite.[43] Furthermore, excellent capacitance retention was exhibited by the pristine rGO and MWCNT SCs, maintaining approximately 100% of their initial capacitance after cycle tests (**Figure A2.8a, Appendix 2**). The capacitive performance of the MnGC nanocomposites was compared with the existing reports of $MnO_2$–carbon based composites and found to be superior to many studies despite high electrode mass loading of 12 mg $cm^{-2}$ (**Tables A2.2 and A2.3**, **Appendix 2**).

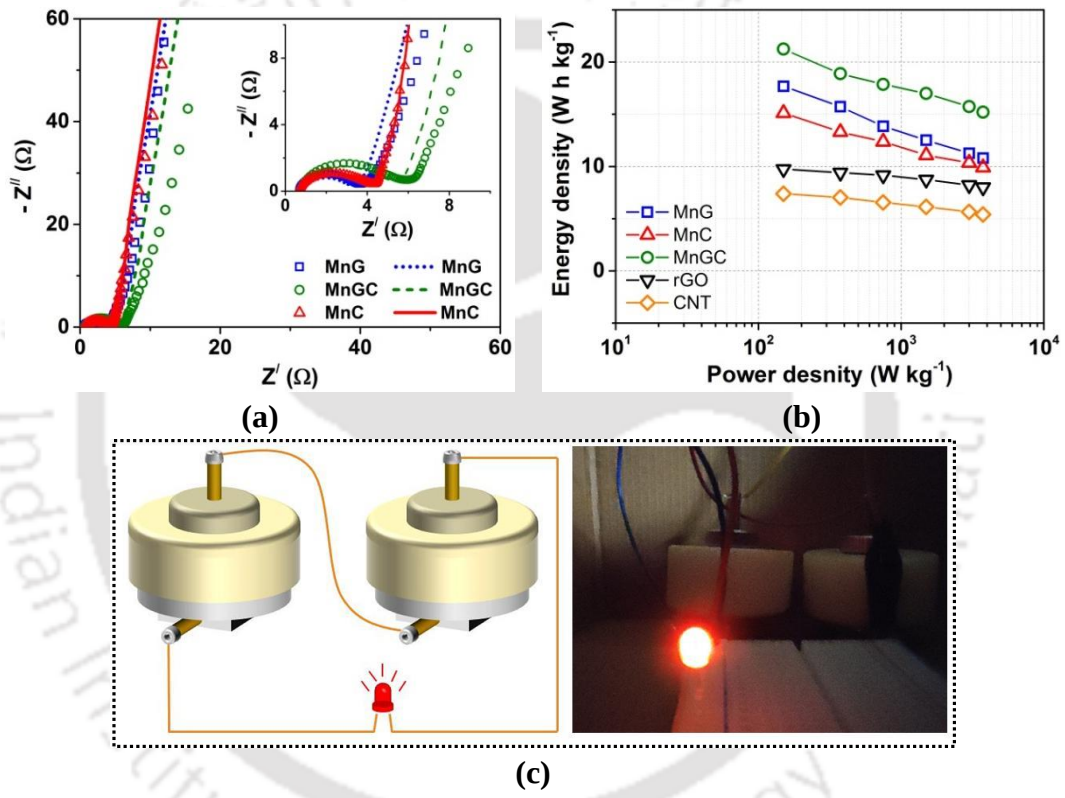


**Figure 3.8** (a) Nyquist plots (lines – EIS data recorded after 5000 cycles) and (b) Ragone plot of MnC, MnG, and MnGC SCs; (c) schematic diagram and photo of the red LED powered by two MnGC SCs connected in series

The electrochemical impedance data of the SCs was recorded using a sinusoidal signal of 10 mV $s^{-1}$ in the frequency range of $10^5$ – 0.01 Hz. The Nyquist plots of MnGC, MnC, and MnG SCs are shown in **Figure 3.8a**. The points in **Figure 3.8a** represent the impedance data recorded before cycle stability tests, whereas the

lines denote impedance data recorded after cycle stability tests, i.e. after 5000 charge–discharge cycles. In the high–frequency region, the impedance spectra of the SCs form a semi–circular arc and a straight line in the low–frequency region.[44] The intercept in the real $Z^{/}$ axis at very high frequency denotes a series resistance ($R_s$), which originates from the combined effect of electrolyte resistance, and other intrinsic resistances of the system.[45] The semi–circle of the Nyquist plot accounts for the charge transfer resistance ($R_{ct}$) associated with the charge transfer via double layer formation and faradaic redox reactions at the electrode/electrolyte interface [46,47]. The equivalent circuit for the impedance data is shown in the inset of **Figure A2.8b** (**Appendix 2**). Before cycle stability tests, the $R_s$ values for the MnC, MnG, and MnGC SCs were in the range of ~ 0.67 - 0.7 Ω, indicating high ionic conductivity and low resistance in the system. After the charge–discharge cycles, the measured $R_s$ values were 0.83, 0.87, and 0.69 Ω, respectively for MnC, MnG, and MnGC. The charge transfer resistances were calculated from the semicircular arc and the MnG sample showed the least charge transfer resistance with an initial $R_{ct}$ value of 2.92 Ω as compared to MnC (3.45 Ω), and MnGC (4.87 Ω). After being subjected to charge–discharge cycles, the charge transfer resistance was reduced to 3.31, 2.32, and 4.39 Ω, respectively for MnC, MnG, and MnGC SCs. Reduction in $R_{ct}$ values indicted the improved charge transport in the electrodes during charge–discharge tests. In the high–frequency region, the impedance spectra of all three SCs showed vertical lines, exhibiting ideal supercapacitive behavior. These lines became more vertical after cycle stability tests, which indicated smaller diffusion resistance as a result of faster ion transfer dynamics after repetitive charge–discharge cycles. A similar observation of reduced charge transfer resistance after cycle stability tests was also noticeable in the Nyquist plots of the rGO and MWCNT SCs, as shown in **Figure A2.9b**

(**Appendix 2**). The reduction in charge transfer and diffusion resistance value supports the observation that the capacitances of the SCs increased after the initial ~ 1000 charge–discharge cycles.

The electrochemical performance of the pristine $MnO_2$ is illustrated in **section A2.3 and Figure A2.9** (**Appendix 2**). The pristine $MnO_2$ electrodes exhibited sluggish charge transport, very poor rate capability (20% capacitance retention when current density increases from 0.1 to 1 A $g^{-1}$), and high charge transfer resistance. This unsatisfactory performance could be ascribed to the high mass loadings (~12 mg $cm^{-2}$) of the $MnO_2$ electrodes. High electrode mass loadings cause severely blocked pores, reduction in electro-active sites, and sluggish charge transport dynamics which ultimately result in poor capacitive performance.

The performances of the fabricated SCs were also compared based on energy and power densities. Ragone plots of the MnC, MnG, MnGC, MWCNT, and rGO based SC cells are shown in **Figure 3.8b**. The energy density of the MnGC SC was calculated to be 21.2 W h $kg^{-1}$ (at a power density of 150 W $kg^{-1}$), and this value is 1.4×, 1.2×, 2.9×, and 2.2× higher than the energy densities of MnC (15.12 W h $kg^{-1}$), MnG (17.67 W h $kg^{-1}$), MWCNT (7.38 W h $kg^{-1}$), and rGO (9.74 W h $kg^{-1}$) SCs, respectively. The MnGC SC was able to maintain its superior energy density as compared to the MnG and MnC SCs even at higher power densities and delivered an energy density of 15.2 W h $kg^{-1}$ at 3750 W $kg^{-1}$. The high energy density of the nanocomposite SCs could be ascribed to the improved capacitance of nanocomposites with high pseudocapacitive contribution from $MnO_2$. Additionally, the energy density of the MnGC SC is superior to many $MnO_2$/carbon-based SCs reported elsewhere.[19,48–51] As a practical demonstration, two MnGC SCs were connected in series for powering a red LED. **Figure 3.8c** depicts the schematic illustration and

digital photograph of two MnGC SCs cells (in series) powering a red LED for a few minutes.

### 3.3.3 Physical Explanation for the Influence of Ultrasound

The ultrasonic irradiation during synthesis creates intense microconvection in the system. Propagation of ultrasound waves induces high-frequency oscillations of fluid elements at a very small spatial scale. The amplitude of oscillation ($a$) of fluid elements in our system was calculated to be $a$ = 0.43 μm (as described in **Chapter 2**). As a result of this intense microconvection at a very small spatial scale, the rGO is efficiently exfoliated and MWCNTs could be uniformly intercalated as spacers to prevent restacking of rGO sheets that facilitate easier diffusion of ions. Additionally, sonication lowers the aggregation of $MnO_2$ nanostructure and promotes simultaneous growth of $MnO_2$ on rGO and MWCNTs resulting in the formation of the ternary MnGC nanocomposite. The superior electrochemical performance displayed by the MnGC nanocomposite could be attributed to its porous microstructure. The self–assembly of the $MnO_2$ nanostructures on the surface of rGO and MWCNTs reduced aggregation and created abundant pores resulting in improved diffusion of electrolyte ions (i.e. $Na^+$) inside the whole composite electrode. Moreover, the addition of MWCNTs to rGO increased the electrochemically active surface area of the MnGC nanocomposite as well as the $MnO_2$ nanostructures. As a result, the diffusion length for the electrolyte ions gets reduced and more electrolyte ions could participate in charge storage and this was reflected in the superior rate capability of the MnGC electrodes. The carbon components in the nanocomposites (i.e. rGO and MWCNTs) act as conductive substrates for $MnO_2$ growth that provide excellent interfacial contact and facilitate easier electron transfer in the whole electrode. This interfacial synergism between individual components of the MnGC nanocomposite, in

conjunction with the morphological features contributing to rapid charge transport, results in its excellent electrochemical performance.

## 3.4 CONCLUSIONS

In summary, a ternary nanocomposite of MWCNT/$MnO_2$/rGO (MnGC) was synthesized via a novel one–pot ultrasound–assisted method. The synthesized MnGC nanocomposite possessed a mesoporous structure with a high BET surface area of ~313.2 $m^2$ $g^{-1}$. The abundant pores present in the MnGC nanocomposite facilitated better electrolyte diffusion, maximum utilization of active surface area of $MnO_2$, reduced diffusion length, and rapid electron transport via its conductive network. As a whole, the synergistic interaction of all the individual components enhanced the energy storage capacity of MnGC electrodes. The symmetric SC fabricated with commercial-level mass loading MnGC electrodes, demonstrated notable enhancement in the capacitive behavior compared to binary nanocomposite (i.e. $MnO_2$/MWCNT and $MnO_2$/rGO) based SCs. The MnGC based SC displayed a wide operating voltage of 1.5 V in the $Na_2SO_4$ electrolyte and high gravimetric capacitance of 314.6 F $g^{-1}$ (at 5 mV $s^{-1}$) was obtained for the MnGC electrodes. Moreover, the SC displayed excellent cycle stability with ~ 103.4 % capacitance retention after 5000 cycles at 5 A $g^{-1}$. The MnGC based SC delivered energy density as high as 21.2 W h $kg^{-1}$ at a power density of 150 W $kg^{-1}$, which was 1.4×, 1.2×, 2.9×, and 2.2× higher than the energy density of $MnO_2$/MWCNT, $MnO_2$/rGO, MWCNT, and rGO based symmetric SCs, respectively. The results of the present study clearly show the potential of ternary MnGC nanocomposite-based aqueous supercapacitors for applications in commercial-scale energy storage systems.

## REFERENCES


(1) Zhi, J.; Reiser, O.; Huang, F. Hierarchical MnO2 Spheres Decorated by Carbon-Coated Cobalt Nanobeads: Low-Cost and High-Performance Electrode Materials for Supercapacitors. *ACS Appl. Mater. Interfaces* **2016**, *8* (13), 8452–8459.

(2) Wei, W.; Cui, X.; Chen, W.; Ivey, D. G. Manganese Oxide-Based Materials as Electrochemical Supercapacitor Electrodes. *Chem. Soc. Rev.* **2011**, *40* (3), 1697–1721.

(3) Liu, Y.-H.; Hsi, H.-C.; Li, K.-C.; Hou, C.-H. Electrodeposited Manganese Dioxide/Activated Carbon Composite As a High-Performance Electrode Material for Capacitive Deionization. *ACS Sustain. Chem. Eng.* **2016**, *4* (9), 4762–4770.

(4) Lin, Z.; Xiang, X.; Chen, K.; Peng, S.; Jiang, X.; Hou, L. Facile Synthesis of MnO2 Nanorods Grown on Porous Carbon for Supercapacitor with Enhanced Electrochemical Performance. *J. Colloid Interface Sci.* **2019**, *540*, 466–475.

(5) Wang, Y.; Guan, H.; Du, S.; Wang, Y. A Facile Hydrothermal Synthesis of MnO2 Nanorod–Reduced Graphene Oxide Nanocomposites Possessing Excellent Microwave Absorption Properties. *RSC Adv.* **2015**, *5* (108), 88979–88988.

(6) Yao, J.; Pan, Q.; Yao, S.; Duan, L.; Liu, J. Mesoporous MnO2 Nanosphere/Graphene Sheets as Electrodes for Supercapacitor Synthesized by a Simple and Inexpensive Reflux Reaction. *Electrochim. Acta* **2017**, *238*, 30–35.

(7) Liu, R.; Duay, J.; Lee, S. B. Electrochemical Formation Mechanism for the Controlled Synthesis of Heterogeneous MnO2/Poly(3,4-Ethylenedioxythiophene) Nanowires. *ACS Nano* **2011**, *5* (7), 5608–5619.

(8) Wang, J. W.; Chen, Y.; Chen, B. Z. Synthesis and Control of High-Performance MnO2/Carbon Nanotubes Nanocomposites for Supercapacitors. *J. Alloys Compd.* **2016**, *688*, 184–197.

(9) Wang, J.; Guo, X.; Cui, R.; Huang, H.; Liu, B.; Li, Y.; Wang, D.; Zhao, D.; Dong, J.; Li, S.; Sun, B. MnO2/Porous Carbon Nanotube/MnO2 Nanocomposites for High-Performance Supercapacitor. *ACS Appl. Nano Mater.* **2020**, *3* (11), 11152–11159.

(10) Wang, Y.; Lai, W.; Wang, N.; Jiang, Z.; Wang, X.; Zou, P.; Lin, Z.; Fan, H. J.; Kang, F.; Wong, C.-P.; Yang, C. A Reduced Graphene Oxide/Mixed-Valence Manganese Oxide Composite Electrode for Tailorable and Surface Mountable Supercapacitors with High Capacitance and Super-Long Life. *Energy Environ. Sci.* **2017**, *10* (4), 941–949.

(11) Xia, H.; Wang, Y.; Lin, J.; Lu, L. Hydrothermal Synthesis of MnO2/CNT Nanocomposite with a CNT Core/Porous MnO2 Sheath Hierarchy Architecture for Supercapacitors. *Nanoscale Res. Lett. 2012 71* **2012**, *7* (1), 1–10.

(12) Jin, Y.; Chen, H.; Chen, M.; Liu, N.; Li, Q. Graphene-Patched CNT/MnO2 Nanocomposite Papers for the Electrode of High-Performance Flexible Asymmetric Supercapacitors. *ACS Appl. Mater. Interfaces* **2013**, *5* (8), 3408–3416.

(13) Wei, B.; Wang, L.; Miao, Q.; Yuan, Y.; Dong, P.; Vajtai, R.; Fei, W. Fabrication of Manganese Oxide/Three-Dimensional Reduced Graphene Oxide Composites as the Supercapacitors by a Reverse Microemulsion Method. *Carbon N. Y.* **2015**, *85*, 249–260.

(14) Unnikrishnan, B.; Wu, C.-W.; Chen, I.-W. P.; Chang, H.-T.; Lin, C.-H.; Huang, C.-C. Carbon Dot-Mediated Synthesis of Manganese Oxide Decorated Graphene Nanosheets for Supercapacitor Application. *ACS Sustain. Chem. Eng.* **2016**, *4* (6), 3008–3016.

(15) Liu, Y.; Miao, X.; Fang, J.; Zhang, X.; Chen, S.; Li, W.; Feng, W.; Chen, Y.; Wang, W.; Zhang, Y. Layered-MnO2 Nanosheet Grown on Nitrogen-Doped Graphene Template as a Composite Cathode for Flexible Solid-State Asymmetric Supercapacitor. *ACS Appl. Mater. Interfaces* **2016**, *8* (8), 5251–5260.

(16) Yao, B.; Chandrasekaran, S.; Zhang, J.; Xiao, W.; Qian, F.; Zhu, C.; Duoss, E. B.; Spadaccini, C. M.; Worsley, M. A.; Li, Y. Efficient 3D Printed Pseudocapacitive Electrodes with Ultrahigh MnO2 Loading. *Joule* **2019**, *3* (2), 459–470.

(17) Hu, L.; Chen, W.; Xie, X.; Liu, N.; Yang, Y.; Wu, H.; Yao, Y.; Pasta, M.; Alshareef, H. N.; Cui, Y. Symmetrical MnO2–Carbon Nanotube–Textile Nanostructures for Wearable Pseudocapacitors with High Mass Loading. *ACS Nano* **2011**, *5* (11), 8904–8913.

(18) Lei, Z.; Shi, F.; Lu, L. Incorporation of MnO2-Coated Carbon Nanotubes

between Graphene Sheets as Supercapacitor Electrode. *ACS Appl. Mater. Interfaces* **2012**, *4* (2), 1058–1064.

(19) Cheng, Y.; Lu, S.; Zhang, H.; Varanasi, C. V.; Liu, J. Synergistic Effects from Graphene and Carbon Nanotubes Enable Flexible and Robust Electrodes for High-Performance Supercapacitors. *Nano Lett.* **2012**, *12* (8), 4206–4211.

(20) Zhu, G.; He, Z.; Chen, J.; Zhao, J.; Feng, X.; Ma, Y.; Fan, Q.; Wang, L.; Huang, W. Highly Conductive Three-Dimensional MnO2–Carbon Nanotube–Graphene–Ni Hybrid Foam as a Binder-Free Supercapacitor Electrode. *Nanoscale* **2013**, *6* (2), 1079–1085.

(21) Jiang, H.; Dai, Y.; Hu, Y.; Chen, W.; Li, C. Nanostructured Ternary Nanocomposite of RGO/CNTs/MnO2 for High-Rate Supercapacitors. *ACS Sustain. Chem. Eng.* **2013**, *2* (1), 70–74.

(22) Li, J.; Östling, M. Prevention of Graphene Restacking for Performance Boost of Supercapacitors—A Review. *Cryst. 2013, Vol. 3, Pages 163-190* **2013**, *3* (1), 163–190.

(23) Zhou, Y.; Hu, X. C.; Guo, S.; Yu, C.; Zhong, S.; Liu, X. Multi-Functional Graphene/Carbon Nanotube Aerogels for Its Applications in Supercapacitor and Direct Methanol Fuel Cell. *Electrochim. Acta* **2018**, *264*, 12–19.

(24) Yang, S. Y.; Chang, K. H.; Tien, H. W.; Lee, Y. F.; Li, S. M.; Wang, Y. S.; Wang, J. Y.; Ma, C. C. M.; Hu, C. C. Design and Tailoring of a Hierarchical Graphene-Carbon Nanotube Architecture for Supercapacitors. *J. Mater. Chem.* **2011**, *21* (7), 2374–2380.

(25) Zhang, Y.; Cui, X.; Fu, J.; Liu, Y.; Wu, Y.; Zhou, J.; Zhang, Z.; Xie, E. Commercial-Level Mass-Loading MnO2 with Ion Diffusion Channels for High-Performance Aqueous Energy Storage Devices. *J. Mater. Chem. A* **2021**, *9* (33), 17945–17954.

(26) Dong, Y.; Zhu, J.; Li, Q.; Zhang, S.; Song, H.; Jia, D. Carbon Materials for High Mass-Loading Supercapacitors: Filling the Gap between New Materials and Practical Applications. *J. Mater. Chem. A* **2020**, *8* (42), 21930–21946.

(27) Guo, W.; Yu, C.; Li, S.; Qiu, J. Toward Commercial-Level Mass-Loading Electrodes for Supercapacitors: Opportunities, Challenges and Perspectives. *Energy Environ. Sci.* **2021**, *14* (2), 576–601.

(28) Zheng, W.; Halim, J.; Sun, Z. M.; Rosen, J.; Barsoum, M. W. MXene—Manganese Oxides Aqueous Asymmetric Supercapacitors with High Mass

Loadings, High Cell Voltages and Slow Self-Discharge. *Energy Storage Mater.* **2021**, *38*, 438–446.

(29) Chen, R.; Yu, M.; Sahu, R. P.; Puri, I. K.; Zhitomirsky, I. The Development of Pseudocapacitor Electrodes and Devices with High Active Mass Loading. *Adv. Energy Mater.* **2020**, *10* (20), 1903848.

(30) Devaraj, S.; Munichandraiah, N. Effect of Crystallographic Structure of MnO2 on Its Electrochemical Capacitance Properties. *J. Phys. Chem. C* **2008**, *112* (11), 4406–4417.

(31) Shah, H. U.; Wang, F.; Javed, M. S.; Ahmad, M. A.; Saleem, M.; Zhan, J.; Khan, Z. U. H.; Li, Y. In-Situ Growth of MnO2 Nanorods Forest on Carbon Textile as Efficient Electrode Material for Supercapacitors. *J. Energy Storage* **2018**, *17*, 318–326.

(32) Choudhury, B. J.; Roy, K.; Moholkar, V. S. Improvement of Supercapacitor Performance through Enhanced Interfacial Interactions Induced by Sonication. *Ind. Eng. Chem. Res.* **2021**, *60* (20), 7611–7623.

(33) Xu, J.; Gai, S.; He, F.; Niu, N.; Gao, P.; Chen, Y.; Yang, P. A Sandwich-Type Three-Dimensional Layered Double Hydroxide Nanosheet Array/Graphene Composite: Fabrication and High Supercapacitor Performance. *J. Mater. Chem. A* **2013**, *2* (4), 1022–1031.

(34) Li, L.; Li, R.; Gai, S.; Gao, P.; He, F.; Zhang, M.; Chen, Y.; Yang, P. Hierarchical Porous CNTs@NCS@MnO 2 Composites: Rational Design and High Asymmetric Supercapacitor Performance. *J. Mater. Chem. A* **2015**, *3* (30), 15642–15649.

(35) Zhong, C.; Deng, Y.; Hu, W.; Qiao, J.; Zhang, L.; Zhang, J. A Review of Electrolyte Materials and Compositions for Electrochemical Supercapacitors. *Chem. Soc. Rev.* **2015**, *44* (21), 7484–7539.

(36) Zhao, X.; Zhang, L.; Murali, S.; Stoller, M. D.; Zhang, Q.; Zhu, Y.; Ruoff, R. S. Incorporation of Manganese Dioxide within Ultraporous Activated Graphene for High-Performance Electrochemical Capacitors. *ACS Nano* **2012**, *6* (6), 5404–5412.

(37) Yan, J.; Liu, J.; Fan, Z.; Wei, T.; Zhang, L. High-Performance Supercapacitor Electrodes Based on Highly Corrugated Graphene Sheets. *Carbon N. Y.* **2012**, *50* (6), 2179–2188.

(38) Chen, J.; Fang, K.; Chen, Q.; Xu, J.; Wong, C. P. Integrated Paper Electrodes

Derived from Cotton Stalks for High-Performance Flexible Supercapacitors. *Nano Energy* **2018**, *53*, 337–344.

(39) Zhu, J.; Shi, W.; Xiao, N.; Rui, X.; Tan, H.; Lu, X.; Hng, H. H.; Ma, J.; Yan, Q. Oxidation-Etching Preparation of MnO2 Tubular Nanostructures for High-Performance Supercapacitors. *ACS Appl. Mater. Interfaces* **2012**, *4* (5), 2769–2774.

(40) Zhang, Q.-Z.; Zhang, D.; Miao, Z.-C.; Zhang, X.-L.; Chou, S.-L. Research Progress in MnO2–Carbon Based Supercapacitor Electrode Materials. *Small* **2018**, *14* (24), 1702883.

(41) Yu, G.; Hu, L.; Liu, N.; Wang, H.; Vosgueritchian, M.; Yang, Y.; Cui, Y.; Bao, Z. Enhancing the Supercapacitor Performance of Graphene/MnO2 Nanostructured Electrodes by Conductive Wrapping. *Nano Lett.* **2011**, *11* (10), 4438–4442.

(42) Wu, R.; Wang, D. P.; Kumar, V.; Zhou, K.; Law, A. W. K.; Lee, P. S.; Lou, J.; Chen, Z. MOFs-Derived Copper Sulfides Embedded within Porous Carbon Octahedra for Electrochemical Capacitor Applications. *Chem. Commun.* **2015**, *51* (15), 3109–3112.

(43) Zhu, S.; Fan, L.; Lu, Y. Highly Uniform Fe3O4 Nanoparticle-RGO Composites as Anode Materials for High Performance Lithium-Ion Batteries. *RSC Adv.* **2017**, *7* (87), 59939–59946.

(44) Ping, Z.; XiaoJing, L.; Anye, R.; Peng, G. Preparation of a Novel Porous Gel Electrolyte and Its Application in Micro Supercapacitor. *J. Electroanal. Chem.* **2016**, *782*, 154–160.

(45) Zhi, J.; Reiser, O.; Huang, F. Hierarchical MnO2 Spheres Decorated by Carbon-Coated Cobalt Nanobeads: Low-Cost and High-Performance Electrode Materials for Supercapacitors. *ACS Appl. Mater. Interfaces* **2016**, *8* (13), 8452–8459.

(46) Zhi, J.; Zhao, W.; Liu, X.; Chen, A.; Liu, Z.; Huang, F. Highly Conductive Ordered Mesoporous Carbon Based Electrodes Decorated by 3D Graphene and 1D Silver Nanowire for Flexible Supercapacitor. *Adv. Funct. Mater.* **2014**, *24* (14), 2013–2019.

(47) Zhi, J.; Deng, S.; Wang, Y.; Hu, A. Highly Ordered Metal Oxide Nanorods inside Mesoporous Silica Supported Carbon Nanomembranes: High Performance Electrode Materials for Symmetrical Supercapacitor Devices. *J.*

*Phys. Chem. C* **2015**, *119* (16), 8530–8536.

(48) Miniach, E.; Śliwak, A.; Moyseowicz, A.; Fernández-Garcia, L.; González, Z.; Granda, M.; Menendez, R.; Gryglewicz, G. MnO2/Thermally Reduced Graphene Oxide Composites for High-Voltage Asymmetric Supercapacitors. *Electrochim. Acta* **2017**, *240*, 53–62.

(49) Liu, Y.; He, D.; Wu, H.; Duan, J.; Zhang, Y. Hydrothermal Self-Assembly of Manganese Dioxide/Manganese Carbonate/Reduced Graphene Oxide Aerogel for Asymmetric Supercapacitors. *Electrochim. Acta* **2015**, *164*, 154–162.

(50) Lee, D. G.; Kim, Y. A.; Kim, B. H. Capacitive Properties of Hierarchically Structured Carbon Nanofiber/Graphene/MnO2 Hybrid Electrode with Nitrogen and Oxygen Heteroatoms. *Carbon N. Y.* **2016**, *107*, 783–791.

(51) Deng, L.; Zhu, G.; Wang, J.; Kang, L.; Liu, Z. H.; Yang, Z.; Wang, Z. Graphene–MnO2 and Graphene Asymmetrical Electrochemical Capacitor with a High Energy Density in Aqueous Electrolyte. *J. Power Sources* **2011**, *196* (24), 10782–10787.

भारतीय प्रौद्योगिकी संस्थान गुवाहाटी
Indian Institute of Technology Guwahati

# CHAPTER 4

## Improved Energy Density of Reduced Graphene Oxide based Aqueous Symmetric Supercapacitors in Redox–Active and Water–in–Salt Electrolytes

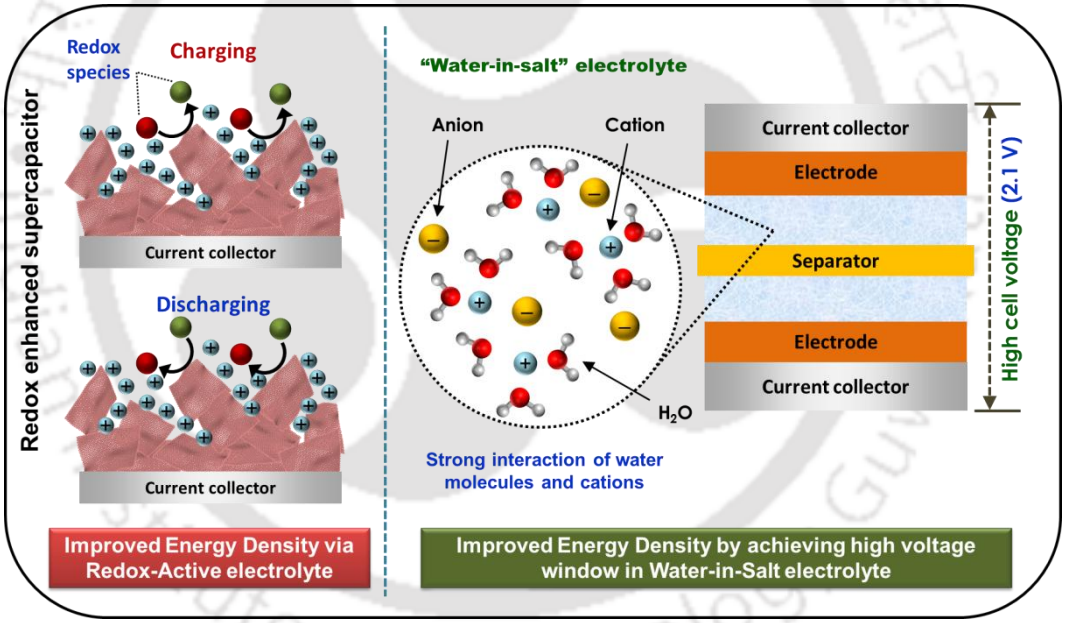

# CHAPTER 4

# IMPROVED ENERGY DENSITY OF REDUCED GRAPHENE OXIDE BASED AQUEOUS SYMMETRIC SUPERCAPACITORS IN REDOX–ACTIVE AND WATER–IN–SALT ELECTROLYTES

## 4.1 INTRODUCTION

Carbon–based EDLCs dominate the commercial market of SCs with ~ 80% of worldwide market revenue. However, these commercial SCs can deliver only a limited amount of energy density (5 – 10 W h $kg^{-1}$) as compared to batteries (100 – 260 W h $kg^{-1}$).[1] As demonstrated by previous authors, the cost of energy (per kW h) provided by SCs is 10× higher compared to that of lithium–ion batteries (LIBs) [2]. Therefore, it is essential to improve the energy density of SCs using inexpensive strategies to widen the commercial applications of SCs.

The energy density ($E_{cell} = \frac{1}{2}CV^2$) of the SCs can be boosted by either enhancing the capacitance ($C$) or by widening the cell voltage ($V$).[3,4] Electrolytes play a vital role in the electrochemical performance as well as in the operational safety of SCs. The organic electrolytes used in commercial EDLCs can provide wide operating voltages (≤ 2.7 V).[1,5] However, organic electrolytes are flammable and suffer from low ionic conductivity and toxicity. Moreover, salt used for making the organic electrolyte raises the cost of the SC.[2] In addition, the manufacturing of organic SCs is sophisticated and expensive due to the high moisture sensitivity of the electrolytes.[5] In this context, low–cost and environment–friendly aqueous electrolytes are appealing and safer alternatives to organic electrolytes.[2,5] Intriguingly, SCs exhibit considerably

higher capacitance, enhanced power density, and superior rate capability in aqueous electrolytes as compared to non–aqueous electrolytes. This superior performance could be attributed to the inherent features of aqueous electrolytes, viz. high ionic conductivity, smaller ionic size, and lower resistance. However, the cell voltages in aqueous electrolytes (especially acidic/alkaline) are limited to 1.23 V due to the thermodynamic decomposition of water. Interestingly, neutral aqueous electrolytes (viz. $Na_2SO_4$, $Li_2SO_4$, and $K_2SO_4$) have shown high electrochemical stability at operating voltages well beyond water–splitting potential and thereby alleviating energy density for aqueous SCs. The enlarged potential windows in neutral aqueous electrolytes can be attributed to raised hydrogen/oxygen evolution overpotentials resulting from the low concentration of $H^+$ and $OH^-$ ions.[1,6]

Among the EDLC materials, graphene is of special interest due to its exceptional properties encompassing $sp^2$ hybridized carbon atoms along with excellent conductivity (charge carrier mobility = 250000 $cm^2\ V^{-1}\ s^{-1}$), mechanical strength (mechanical stiffness = 1 TPa), large surface area (2630 $m^2\ g^{-1}$) and favorable pore size distributions.[7–9] Although graphene materials synthesized via different methods have been reported for EDLCs (please refer to the literature summary given in **Table A3.1, Appendix 3**), however, most of these studies have investigated the electrochemical performances at low electrode mass loadings (< 5 mg $cm^{-2}$). Essentially, the electrode mass loading should be as high as ~ 10 mg $cm^{-2}$ considering the practical/commercial application and to ensure high total capacitance and energy density of SCs.[10] In view of this, we have investigated the electrochemical performances of reduced graphene oxide (rGO)–based aqueous SCs (rGO–SCs) at commercial–level electrode mass loadings. Furthermore, we propose two inexpensive strategies for enhancing the energy density of rGO–SCs. The first strategy implicates

the use of a neutral redox–active aqueous electrolyte to increase the capacitance via soluble redox reactions. The second strategy focuses on extending the cell voltage of rGO–SCs by using water–in–salt (WIS) electrolyte.

Incorporating redox–additives in the electrochemically inert electrolyte to augment the electrochemical performance has gained popularity in recent times.[11–14] The redox additives can participate in electron transfer reactions based on their redox states and improve the energy density of SCs with pseudo–faradaic charge storage as illustrated in **Figure 4.1a**. Previous studies have reported the use of various redox-additives, viz. hydroquinone,[11] viologens,[14] indigo carmine,[12] $K_3Fe(CN)_6$,[15] etc. to augment the energy density of carbon-based EDLCs. Abbas et al.[16] reported enhancement in capacitance of commercial activated carbon (DLC Supra 30) using sodium molybdate ($Na_2MoO_4$) as the redox-additive in $Li_2SO_4$ electrolyte. They showed that the $MoO_4^{2-}$ ions originating from sodium molybdate can provide pseudo-faradaic contributions via redox reactions that increase the capacitance. Moreover, sodium molybdate has various other advantages, including its environmentally friendly nature, low cost, corrosion inhibition of steel, and high water solubility.

The newly introduced "water–in–salt" (WIS) electrolytes have garnered immense attention due to their safe and high operating voltages (> 2 V).[5,17,18] The salt content in the WIS electrolytes surpasses the water content in both mass and volume.[17,19] The strong interactions between water molecules and the cations at such high concentrations decrease the activity of water molecules at the electrode surface; thus preventing the breakdown of the electrolyte as schematically depicted in **Figure 4.1b**.[20,21] Initial studies on WIS electrolytes have focused on the bis(trifluoromethane)–sulfonimide lithium salt (LiTFSI) due to its excellent solubility and stability in the aqueous medium.[22–24] WIS electrolytes based on sodium

perchlorate ($NaClO_4$),[21,25,26] potassium acetate,[27] and sodium nitrate ($NaNO_3$)[28] have been explored very recently. Among these, $NaNO_3$ based WIS electrolyte has high solubility, in addition to relatively high conductivity and superior electrochemical performances.[28]

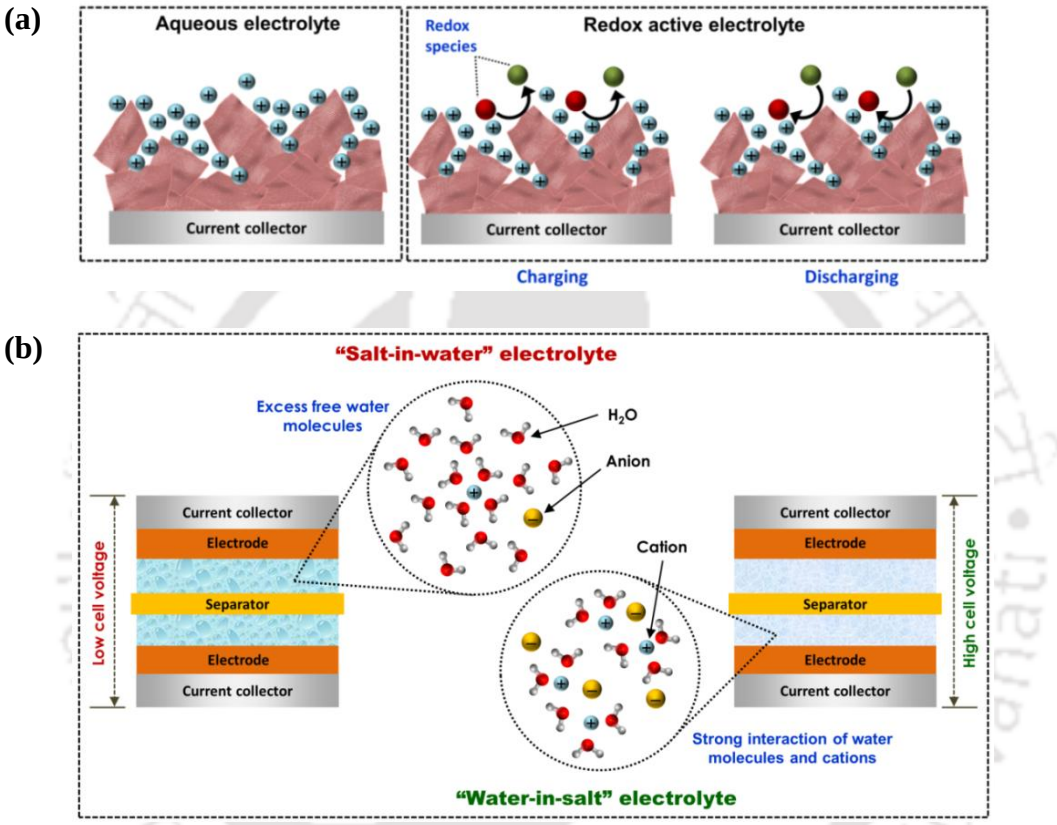


**Figure 4.1** (a) Illustration of charge storage mechanisms of SCs with aqueous and redox–active electrolytes; (b) schematic representation of interactions between water molecules and cations in conventional aqueous (salt–in–water) and "water–in–salt" electrolytes.

Herein, we investigate the performance of rGO based symmetric SCs (rGO–SCs) in aqueous electrolytes (viz. 1 M $H_2SO_4$, 6 M KOH, 1 M $Li_2SO_4$) at commercial–level mass loadings (~ 10 mg $cm^{-2}$). As compared to $H_2SO_4$ and KOH electrolytes, a relatively high energy density (15.39 W h $kg^{-1}$) was obtained for the SC

in $Li_2SO_4$ electrolyte due to the extended cell voltage of 1.8 V. Furthermore, the energy density of rGO–SCs was enhanced to 21.42 and 22.87 W h $kg^{-1}$ via two inexpensive strategies: (i) employing a redox–active electrolyte (0.1 M $Na_2MoO_4$ + 1 M $Li_2SO_4$), and (ii) achieving a high cell voltage of 2.1 V in a WIS electrolyte (11 M $NaNO_3$), respectively. The practical feasibility of the fabricated high energy density SCs was demonstrated by illuminating light–emitting diodes (LEDs).

## 4.2 Experimental Section

### 4.2.1 Materials

Lithium sulfate ($Li_2SO_4$) was procured from Sigma Aldrich, India. Potassium hydroxide (KOH) flakes, sodium molybdate ($Na_2MoO_4$), sodium nitrate ($NaNO_3$), and sulphuric acid ($H_2SO_4$, 98%) were purchased from Merck, India. Ultrapure water was used for all the experiments. Reduced graphene oxide (rGO) was synthesized in our laboratory as described in **Chapter 2**. The synthesis of rGO is schematically illustrated in **Figure 4.2**.

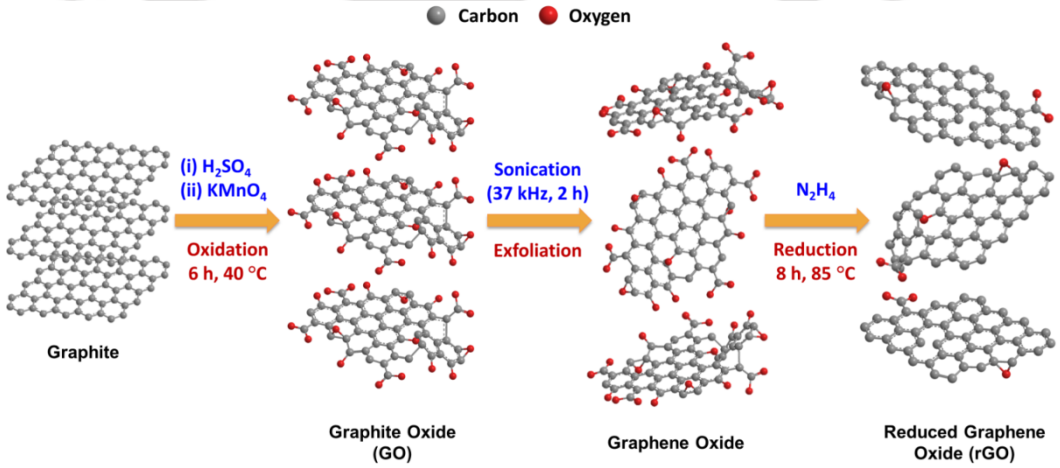


**Figure 4.2** Schematic illustration of reduced graphene oxide (rGO) synthesis

### 4.2.2 Electrochemical Measurements

The electrochemical investigations were performed in both three–electrode and two–electrode (symmetric supercapacitor) cells using a M204 Potentiostat/Galvanostat (Metrohm Autolab). In the three–electrode setup, an Ag/AgCl (3 M KCl) and a platinum rod were used as the reference and counter electrodes, respectively. To make the working electrodes, a uniform slurry was prepared by mixing the rGO (80 wt%) with carbon black (10 wt%), and PTFE binder (10 wt%) in ethanol. The homogeneous electrode slurry was then coated on a 1×1 $cm^2$ area of stainless steel foil (current collector) and dried at 100 °C. The mass of active material on the working electrodes was ~ 7 – 9 mg. The electrodes for symmetric supercapacitors were prepared by casting the aforementioned electrode slurry on a stainless steel foil and disc electrodes of diameter ~ 1.5 cm were punched out after drying. As–prepared disc electrodes had active mass loadings of 9 – 10 mg $cm^{-2}$. Finally, symmetric supercapacitors (rGO–SCs) were assembled using two identical rGO disc electrodes with a cellulose separator (saturated with electrolyte) sandwiched between them. As described in **Chapter 3**, symmetric supercapacitor cells were assembled inside a split–type coin cell assembly.

The electrochemical tests were conducted in different aqueous electrolytes, viz. 1 M $H_2SO_4$, 6 M KOH, 1 M $Li_2SO_4$, 0.1 M $Na_2MoO_4$ + 1 M $Li_2SO_4$ (redox–active electrolyte), and 11 M $NaNO_3$ (water–in–salt electrolyte). The electrochemical parameters were assessed by CV, GCD, and EIS techniques. In three-electrode measurements, specific capacitance ($C_g$, F $g^{-1}$) was calculated from the CV and GCD curves using equations 1.5 and 1.6, respectively as described in section 1.4.1 in **Chapter 1**. The specific capacitance of a single electrode ($C_g$, F $g^{-1}$) of the supercapacitors cells was calculated from the CV and GCD curves using equations

1.7 and 1.8, respectively as described in section 1.4.1 in **Chapter 1**. The energy density (E, W h $kg^{-1}$), and power density (P, W $kg^{-1}$) of the cells were calculated from GCD curves using equations 1.9 and 1.10, respectively (section 1.4.1 in **Chapter 1)**.

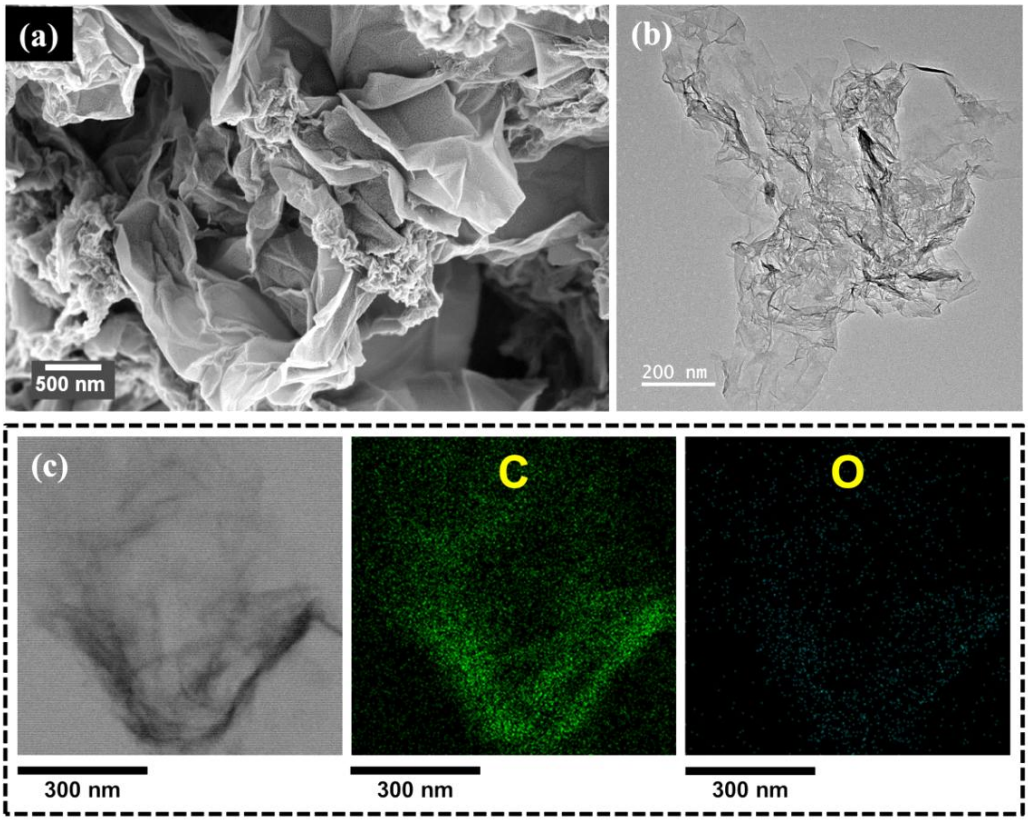


**Figure 4.3** (a) FE–SEM, (b) TEM, and (c) elemental mapping (carbon in green, and oxygen in blue) images of rGO.

## 4.3 RESULTS AND DISCUSSION

### 4.3.1 Physicochemical Characterization of rGO

Various characterizations of rGO such as XRD, Raman spectroscopy, BET surface area measurements have been previously discussed in **Chapter 2** (section 2.31). However, the results of these characterizations are presented in **Figure A3.1** (**Appendix 3**). The FE–SEM and TEM images of the synthesized rGO are shown in

**Figure 4.3a–b**, which reveal the crumpled sheet-like morphology of the synthesized rGO. The crumpled morphology is beneficial for preventing the restacking of rGO. Elemental mapping shown in **Figure 4.3c** indicates the presence of small amount of residual oxygen-containing groups on the surface rGO and these groups could add pseudocapacitive contributions.

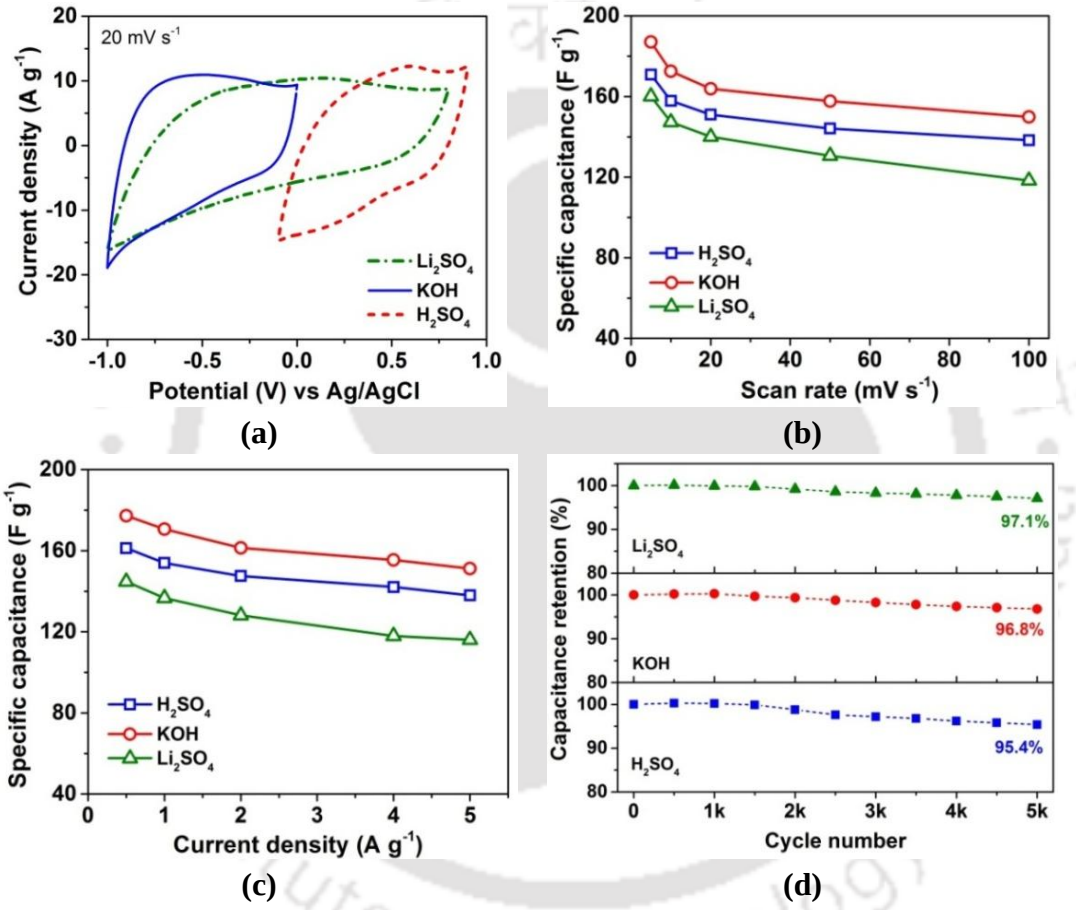


**Figure 4.4** Electrochemical performance of rGO electrodes using a three–electrode system in different aqueous electrolytes viz. 1 M $H_2SO_4$, 6 M KOH, and 1 M $Li_2SO_4$: (a) CV in different electrolytes at a scan rate of 20 mV $s^{-1}$; (b) specific capacitance as a function of scan rate; (c) specific as a function of current density; (d) cycle stability in the different electrolytes.

### *4.3.2* Electrochemical Performance in Acidic, Alkaline, and Neutral Aqueous Electrolytes

#### *4.3.2.1 Three–electrode cell characterization of rGO electrodes*

The electrochemical investigations of single rGO electrodes were performed using a three–electrode setup in different aqueous electrolytes, viz. 1 M $H_2SO_4$, 6 M KOH, and 1 M $Li_2SO_4$. The cyclic voltammetry (CV) curves of the rGO electrodes in the above–mentioned aqueous electrolytes are shown in **Figure 4.4a**. A potential window of −0.1 V to 0.9 V (vs. Ag/AgCl) was obtained for the rGO in the acidic $H_2SO_4$ electrolyte. The hydrogen evolution reaction (HER) was found to occur at a negative potential of −0.1 V (vs. Ag/AgCl) in the $H_2SO_4$ electrolyte, which is due to the high concentration of $H^+$ ions in the electrolyte. In the alkaline KOH electrolyte, a stable potential window was obtained in the range of −1 V to 0 V (vs. Ag/AgCl). It was observed that oxygen evolution reaction (OER) occurs at about 0 V (vs. Ag/AgCl) in the KOH electrolyte, which could be attributed to the higher concentration of $OH^-$ ions in the electrolyte. **Figure A3.2** (**Appendix 3**) shows the CV curves of rGO recorded at different potential windows in $Li_2SO_4$ electrolyte. Firstly the CV curves were recorded in the potential range of −0.6 V to 0.8 V (vs. Ag/AgCl). When the potential range was extended to the negative range, the increase in negative current and the formation of the reduction peak signifies the beginning of the hydrogen storage.[29,30] The sharp rise in negative current at potentials lower than −1 V (vs. Ag/AgCl) indicated increased $H_2$ evolution and a probable limit for negative polarization.[29] As evident from **Figure A3.2** (**Appendix 3**), the potential window of rGO in $Li_2SO_4$ electrolyte can be extended up to ~ 2 V. However, the rate capability was significantly reduced at higher scan rates when the negative potential was lower than −1 V (vs. Ag/AgCl). Therefore, the potential window of −1 V to 0.8 V (vs.

Ag/AgCl) was used for the capacitive measurements in the $Li_2SO_4$ electrolyte. The electrochemical behavior of the rGO was further investigated using CV at various scan rates (5, 10, 20, 50, and 100 mV $s^{-1}$). The CV curves in the $H_2SO_4$ (**Figure A3.3a, Appendix 3**) and KOH (**Figure A3.4a, Appendix 3**) electrolytes have distorted rectangular shapes with redox peaks suggesting pseudocapacitive contributions from surface functionalities along with double–layer behavior. In $Li_2SO_4$ electrolyte, the total capacitance is contributed by double layer capacitance in conjunction with pseudo–capacitance originating from reversible hydrogen storage, which is apparent from the CV curves (**Figure A3.5a, Appendix 3**).[29] **Figure 4.4b** summarizes the specific capacitances of rGO electrodes calculated from the CV curves. At a scan rate of 5 mV $s^{-1}$, specific capacitances were calculated as 187.1, 170.9, and 160.1 F $g^{-1}$ in KOH, $H_2SO_4$, and $Li_2SO_4$ electrolytes, respectively. The specific capacitance values decreased with the increasing scan rates, which could be attributed to the inadequate mitigation of electrolyte ions into active sites of rGO at high scan rates.[31] Interestingly, the rGO electrodes displayed fairly high specific capacitance retentions of 81.2%, 80%, and 73.4% in $H_2SO_4$, KOH, and $Li_2SO_4$ electrolytes, respectively at a high scan rate of 100 mV $s^{-1}$.

The galvanostatic charge–discharge (GCD) curves of rGO (**Figures A3.3b, A3.4b, A3.5b** in **Appendix 3**) display near–linear and triangular curved shapes indicating contributions from both electrical double–layer and pseudocapacitance that originate from surface oxygen groups of rGO and/or reversible hydrogen storage. The negligible voltage drops of GCD curves suggest very low resistance and efficient charge transfer at the electrode–electrolyte interface.[32] The GCD measurements further confirm that the rGO electrodes can be steadily charged and discharged in the potential range of −0.1 V to 0.9 V, −1 V to 0 V, and −1 V to 0.8 V (vs. Ag/AgCl) in

$H_2SO_4$, KOH, and $Li_2SO_4$ electrolytes, respectively, which is in agreement with the CV results. The specific capacitances of rGO electrodes at a current density of 0.5 A $g^{-1}$were 177.3, 161.4, and 144.8 F $g^{-1}$ in KOH, $H_2SO_4$, and $Li_2SO_4$ electrolytes, and corresponding capacitance retentions at 5 A $g^{-1}$ were 85.5%, 85.2%, and 80.1%, respectively (**Figure 4.4c**). The superior rate capability of rGO electrodes in $H_2SO_4$ and KOH electrolytes could be attributed to the smaller ionic diameter and high mobility of the $H^+$ and $K^+$ ions.[33] Moreover, the wettability of the electrodes by the electrolyte plays a pivotal role in the capacitive performance. Better wetting of the electrodes increases the surface area accessible for the electrolytes and thereby improves the capacitance. The wettability of the electrodes was studied using contact angle measurements (**Figure A3.6, Appendix 3**). The wettability of the rGO electrodes decreased as indicated by the contact angles: 6 M KOH (124.6°) > 1 M $H_2SO_4$ (132.5°) > 1 M $Li_2SO_4$ (142.5°). Therefore, it can be inferred that the better wettability of the rGO electrodes by the 6 M KOH in addition to its high ionic conductivity resulted in the highest specific capacitance in the alkaline electrolyte. The specific capacitances obtained for rGO in this work is at par with the previously published data on graphene–based SC electrodes (**Table A3.1, Appendix 3**). Most of the previous studies in the literature have reported electrochemical performances at low electrode mass loadings (< 5 mg $cm^{-2}$). The low active mass loading results in low total capacity and energy density for SCs due to the low mass ratio of active material to cell components, which restricts their practical utility for commercial energy storage. The active material loading in commercial supercapacitors is about ~ 10 mg $cm^{-2}$. Moreover, most electrode materials show drastically reduced performance at high active mass loadings due to hindered charge transport. Therefore, it is essential to use commercial–level electrode mass loadings for obtaining reliable

performance parameters suitable for commercial/industrial applications of these supercapacitors. It is noteworthy that the specific capacitance of commercial electrode mass loading rGO electrodes used in the present study is superior to many of the previous studies with low mass loadings (**Table A3.1, Appendix 3**). The well–organized mesoporous structure and high surface area (~ 555 $m^2$ $g^{-1}$) of the synthesized rGO enabled efficient charge transportation inside the electrode, which results in large specific capacitance values for the rGO electrodes at high mass loadings.

The cyclic performance of the rGO electrodes was investigated over 5000 charge–discharge cycles at a current density of 5 A $g^{-1}$. The rGO electrodes retained about 95.4%, 96.8%, and 97.1% of their initial capacitance after 5000 cycles in $H_2SO_4$, KOH, and $Li_2SO_4$ electrolytes, respectively (**Figure 4.4d**). The excellent cyclic stability of the rGO electrodes indicated high reversibility of the charge storage process in the aqueous electrolytes without any significant material degradation. Electrochemical impedance spectroscopy (EIS) was performed using a 10 mV $s^{-1}$ sinusoidal signal in a frequency range of $10^5$ – 0.1 Hz. All Nyquist plots of rGO electrodes (**Figure A3.7, Appendix 3**) consist of a semicircular arc originating from charge transfer resistance ($R_{ct}$) in the high–frequency range and a straight line in the low–frequency range, which indicated a good capacitive response.[34,35] The combined effect of ionic resistance of electrolyte and interfacial system resistance results in a series resistance ($R_s$).[34] The intercept at the real $Z^{/}$ axis in the Nyquist plot gives the value of $R_s$. The values of $R_s$ and $R_{ct}$ were determined using an equivalent circuit shown in the inset of **Figure A3.7** (**Appendix 3**). The $R_s$ values for the rGO electrodes were 0.75, 0.97 and 4.62 Ω in $H_2SO_4$, KOH and $Li_2SO_4$ electrolytes, and the corresponding $R_{ct}$ values were 32.60, 23.31, and 41.38 Ω, respectively. The low $R_s$

and $R_{ct}$ values obtained in the $H_2SO_4$ and KOH electrolytes further confirm the higher ionic conductivity and fast charge transport in acidic/alkaline aqueous electrolytes.

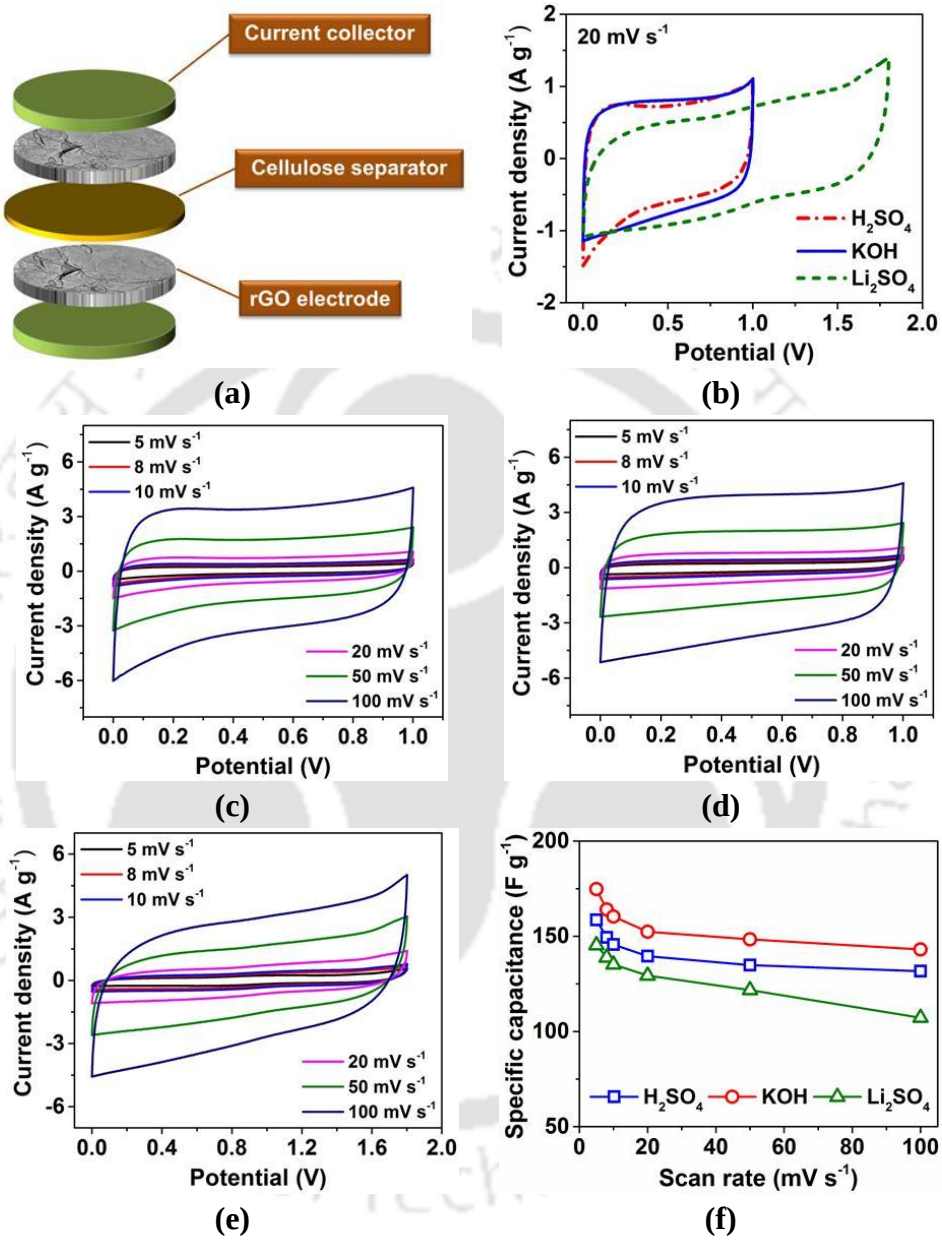


**Figure 4.5** Electrochemical performance of rGO–SCs in different aqueous electrolytes, viz. 1 M $H_2SO_4$, 6 M KOH, and 1 M $Li_2SO_4$: (a) Schematic representation of two–electrode symmetric SC cell; (b) comparison of CV curves of rGO–SCs in different electrolytes; CV curves of rGO–SC in (c) 1 M $H_2SO_4$, (d) 6 M KOH, (e) 1 M $Li_2SO_4$; (f) specific capacitance of rGO electrodes as a function of scan rate.

#### *4.3.2.2 Electrochemical performance of rGO–based symmetric supercapacitors*

To investigate the electrochemical performance in a full cell device, symmetric SCs (rGO–SCs) were fabricated with two identical rGO electrodes partitioned by a cellulose paper separator (**Figure 4.5a**). The separators were impregnated with 300 μL of different electrolyte solutions, including 1 M $H_2SO_4$, 6 M KOH, and 1 M $Li_2SO_4$, respectively. The rGO–SCs were tested at various scan rates ranging from 5 to 100 mV $s^{-1}$. The potential windows of the rGO–SCs were limited to 1 V in $H_2SO_4$ and KOH electrolytes to prevent the thermodynamic decomposition of water, which could potentially damage the SCs, and these potential windows are in agreement with the three–electrode cell measurements. To obtain a relatively wide operating voltage for the rGO–SCs, neutral $Li_2SO_4$ has been used as the electrolyte.[36] As indicated by the CV curves of rGO electrodes in both positive (0 to 0.8 V) and negative (−1 to 0 V) potential ranges (**Figure A3.8a, Appendix 3**), a stable cell voltage of 1.8 V can be obtained for the rGO–SC in $Li_2SO_4$ electrolyte. CV curves of the rGO–SC in $Li_2SO_4$ electrolyte at different potential windows from 1 – 1.9 V are shown in **Figure A3.8b** (**Appendix 3**). The peak at the right side of the CV curves increased with an increase in cell voltage. The peak at 1.9 V is relatively high indicating water decomposition, and therefore, the cell voltage was limited to 1.8 V for the rGO–SC in the $Li_2SO_4$ electrolyte.[37] **Figure 3.5b** shows the CV curves of the rGO–SCs in different electrolytes at a scan rate of 20 mV $s^{-1}$. It can be noted that in the potential window of 1 V, the rGO–SC shows better capacitive responses in $H_2SO_4$ and KOH electrolytes. The CV curves of rGO–SCs at different scan rates of 5 – 100 mV $s^{-1}$ were quasi–rectangular in all three electrolytes (**Figures 3.5c–e**). The rapid current response at the voltage reversal point in the CV curves indicated a superior capacitive response.[38] The quasi rectangular forms of the CV curves were well

retained even at high scan rates in the case of $H_2SO_4$, and KOH electrolytes. These results indicated rapid charge transport inside the rGO electrodes in $H_2SO_4$ and KOH electrolytes.[39] However, relatively larger deviations of CV curves were observed in the $Li_2SO_4$ electrolyte for higher scan rates. This could be attributed to higher diffusion limiting charge storage at increased scan rates in the $Li_2SO_4$ electrolyte. The gravimetric specific capacitances of the rGO electrodes in different electrolytes were calculated from the CV curves of the rGO–SCs. The variations of capacitance at different scan rates are shown in **Figure 4.5f**. The rGO electrodes exhibited the highest capacitance of 174.8 F $g^{-1}$ (at the scan rate of 5 mV $s^{-1}$) in 6 M KOH, followed by 158.6 F $g^{-1}$ in 1 M $H_2SO_4$, and 145.3 F $g^{-1}$ in 1 M $Li_2SO_4$ electrolyte. The decreasing capacitance for higher scan rates could be attributed to the lack of time for diffusion of electrolytes ions inside the pores of crumpled rGO.[31] At a high scan rate of 100 mV $s^{-1}$, the rGO electrodes retained 83% (131.6 F $g^{-1}$) and 81.9% (143.1 F $g^{-1}$) of initial capacitance in $H_2SO_4$ and KOH electrolytes, respectively. In $Li_2SO_4$ electrolyte, 73.8% (107.2 F $g^{-1}$) capacitance was retained at 100 mV $s^{-1}$.

The GCD curves of rGO–SCs obtained at a current density of 1 A $g^{-1}$ are shown in **Figure 4.6a**. The charge–discharge time for the device in KOH electrolyte is longer than that in $H_2SO_4$ electrolyte indicating higher capacitance in KOH electrolyte. The potential window of 1.8 V for the device in $Li_2SO_4$ electrolyte was further confirmed by the GCD results. The GCD curves of the rGO–SCs in the three electrolytes are shown in **Figures 4.6b–d**. The triangular and near–linear nature of GCD curves indicated contributions from both electrical double–layers as well as from pseudocapacitance originating from surface oxygen groups present in the rGO. The negligible voltage drops of the rGO–SCs indicated very low resistance and efficient charge transfer at the electrode–electrolyte interface.[32] At a current density of

0.2 A $g^{-1}$, the highest capacitance of 168.5 F $g^{-1}$ was obtained in the KOH electrolyte. The capacitances of the rGO electrodes were 147.8 and 136.7 F $g^{-1}$ in $H_2SO_4$ and $Li_2SO_4$ electrolytes, respectively (**Figure 4.6e**).

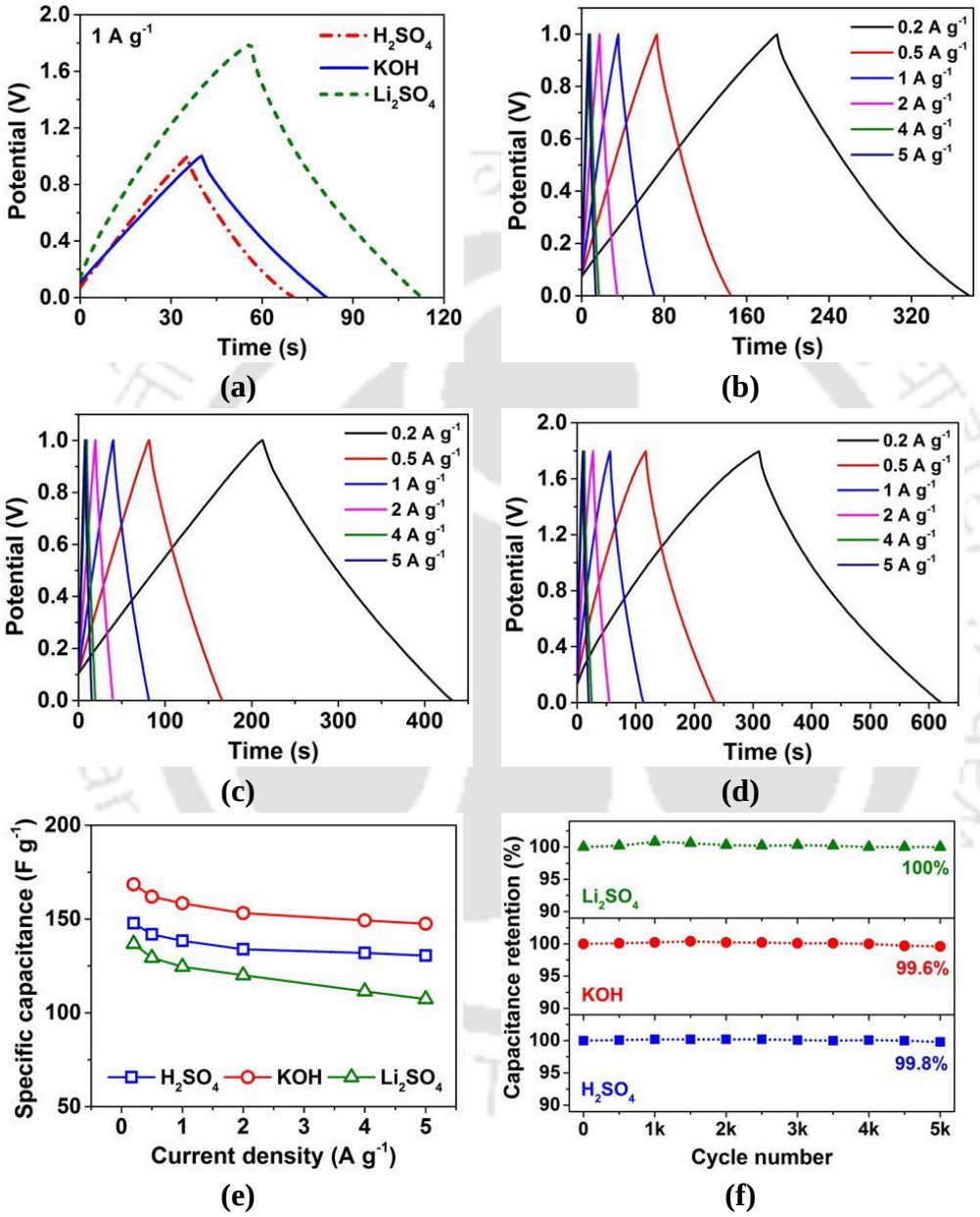


**Figure 4.6** Electrochemical performance of rGO–SCs in different aqueous electrolytes, viz. 1 M $H_2SO_4$, 6 M KOH, and 1 M $Li_2SO_4$: (a) Comparison of GCD curves of rGO–SCs in different electrolytes; GCD curves of rGO–SC in (b) 1 M $H_2SO_4$, (c) 6 M KOH, (d) 1 M $Li_2SO_4$; (e) specific capacitance as a function of current density; (f) cycle stability analysis of the rGO–SCs.

The higher ionic conductivities of KOH and $H_2SO_4$ electrolytes resulted in the high capacitances for the rGO electrodes even at the low potential window of 1 V. The specific capacitances of the rGO electrodes were 130.5 ($H_2SO_4$), 147.5 (KOH), and 107.3 ($Li_2SO_4$) F $g^{-1}$ when the current density was increased to 5 A $g^{-1}$ (**Figure 4.6e**). The smaller ionic size of $H^+$ and $K^+$ ions facilitates rapid charge transport inside the pores of the electrodes. As a result, better rate capacities were obtained in the $H_2SO_4$ (88.33%) and KOH (87.56%) as compared to $Li_2SO_4$ (78.44%) electrolyte. The rGO–SCs demonstrated excellent cyclic stability with almost no loss in capacitance over 5000 GCD cycles at a current density of 5 A $g^{-1}$ (**Figure 4.6f**), which indicates the high reversibility of the charge storage process. In addition, FE–SEM images of the rGO electrodes before, and after cycle stability tests (**Figure A3.9a–d, Appendix 3**) in the three aqueous electrolytes did not show any significant morphological changes. These results further support the high electrochemical stability of the rGO electrodes in the electrolytes. The Nyquist plots of the rGO–SCs are shown in **Figure 4.7a**. The $R_s$ values for rGO–SCs in KOH and $H_2SO_4$ electrolytes were 0.31 and 0.34 Ω, respectively, before cyclic stability tests; whereas, the $R_s$ value in $Li_2SO_4$ electrolyte before the cyclic stability test was ~0.93 Ω. The small $R_s$ values in KOH and $H_2SO_4$ electrolytes could be attributed to their high ionic conductivity as compared to the $Li_2SO_4$ electrolyte. Therefore, high capacitances were obtained in KOH and $H_2SO_4$ electrolytes as a result of the rapid transport of electrolyte ions. The $R_{ct}$ values for rGO–SCs in the KOH, $H_2SO_4$, and $Li_2SO_4$ electrolytes before stability tests were 1.1, 0.97, and 2.1 Ω, respectively. After the stability tests, the rGO–SCs did not show any significant change in $R_s$ values. However, $R_{ct}$ values were reduced to 0.96, 0.96, and 1.6 Ω, respectively in KOH, $H_2SO_4$, and $Li_2SO_4$ electrolytes. These low resistances indicated improved charge transfer in the thick rGO electrodes (due to high mass

loadings) after repetitive charge–discharge as well as high electrochemical stability. In the low–frequency region, the more vertical nature of the impedance spectra in both KOH and $H_2SO_4$ electrolytes indicated rapid diffusion of electrolyte ions inside the pores of rGO electrodes attributed to the smaller cationic sizes.[40,41] However, the diffusion resistance was lower in KOH as compared to that in $H_2SO_4$, which could be attributed to the greater wettability of the rGO electrodes in KOH. The impedance data further supported the high rate capability of rGO–SCs in the KOH and $H_2SO_4$ electrolytes.

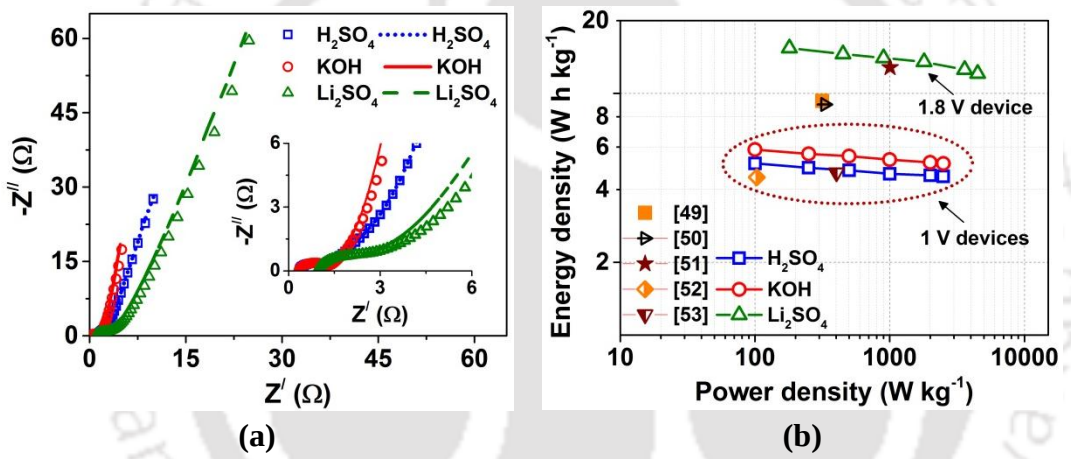


**Figure 4.7** (a) Nyquist plots of rGO–SCs before (denoted by points) and after cycle stability (denoted by lines) tests (inset: high–frequency region); (b) Ragone plot for the rGO–SCs in different aqueous electrolytes and comparison with previously published data.

The Ragone plot in **Figure 4.7b** illustrates the energy and power densities of the rGO–SCs in KOH, $H_2SO_4$, and $Li_2SO_4$ electrolytes. The energy densities of the rGO–SCs in KOH and $H_2SO_4$ electrolytes were 5.85 and 5.13 W h $kg^{-1}$, respectively, at a power density of 100 W $kg^{-1}$. The limited energy density of the rGO–SCs in these two electrolytes is due to the low potential window of 1 V. At the power density of 2500 W $kg^{-1}$, the energy density values were 5.12 and 4.53 W h $kg^{-1}$, respectively, in

KOH and $H_2SO_4$ electrolytes. However, for practical applications higher energy densities are essential. Therefore, the neutral $Li_2SO_4$ electrolyte was used to obtain a greater potential window as well as a higher energy density. The rGO–SCs demonstrated an energy density of 15.39 W h $kg^{-1}$ (180 W $kg^{-1}$) in the $Li_2SO_4$ electrolyte. This is 2.6× and 3× higher than the energy densities in $H_2SO_4$ and KOH electrolytes, respectively. The high energy density of the device in $Li_2SO_4$ could be attributed to the wide voltage window of 1.8 V. The rGO–SC provided an energy density of 12.1 W h $kg^{-1}$ at a high energy density of 4500 W $kg^{-1}$ in $Li_2SO_4$ electrolyte. The high energy density values demonstrated by the rGO–SCs at high power outputs could be ascribed to the superb rate capability and efficient charge transport inside the porous networks present in the electrodes. The energy density of the fabricated neutral SC is superior to many previously published studies (Figure 7b).[42–46]

### 4.3.3 Electrochemical Performance in Redox–Active Electrolyte

#### *4.3.3.1 Three–electrode cell characterization of rGO electrodes*

The redox additives/mediators participate in reversible electron transfer redox reaction at the electrode–electrolyte interface.[47,48] As a result, the surface pseudo-capacitive contribution from the redox additives enhances the performance of the SCs. In the present study, a $Na_2MoO_4$ based redox–active electrolyte (0.1 $Na_2MoO_4$ + 1 M $Li_2SO_4$) has been used to augment the energy density of rGO–SCs. The three–electrode measurements (CV and GCD curves shown in **Figures A3.10a** and **A3.10b**, **Appendix 3**) confirm that the rGO electrodes can be safely charged and discharged in the same potential window of $Li_2SO_4$ electrolyte, i.e. −1 V to 0.8 V (vs. Ag/AgCl). The larger area under the CV curves and the increase in charge–discharge time

indicate the improved charge storage in the redox–active electrolyte. The appearance of the redox peaks and the increase in peaks at voltage reversal indicated pseudo faradaic contributions in the redox–active electrolyte along with double layer charge storage. The redox behavior could be attributed to the following redox reactions of $MoO_4^{2-}$ ions:[16]

$$MoO_4^{2-} + 4H^+ + 2e^- \longleftrightarrow MoO_2 + 2H_2O \quad (4.1)$$

$$MoO_4^{2-} + 8H^+ + 6e^- \longleftrightarrow Mo + 4H_2O \quad (4.2)$$

The CV and GCD curves of the rGO electrode at different scan rates and current densities obtained from three–electrode measurements are shown in **Figures A3.10c** and **A3.10d** (**Appendix 3**), respectively. In the redox–active electrolyte, the rGO electrode exhibited a specific capacitance of 226.9 F $g^{-1}$ at a scan rate of 5 $mVs^{-1}$, which is 1.42× higher than the capacitance in the neat $Li_2SO_4$ electrolyte (**Figure A3.10e, Appendix 3**). When the scan rate was increased to 100 mV $s^{-1}$, about 71.2% (161.5 F $g^{-1}$) of capacitance was retained. In addition, a specific capacitance of 201.5 F $g^{-1}$ was obtained at a current density of 0.5 A $g^{-1}$, which indicated a 1.4× increase in the specific capacitance in the redox–active electrolyte in comparison to the $Li_2SO_4$ electrolyte (**Figure A3.10f, Appendix 3**). The rGO electrodes retained 79.1% (159.5 F $g^{-1}$) of this capacitance at the high current density of 5 A $g^{-1}$ demonstrating a high rate capability in the redox–active electrolyte.

#### *4.3.3.2 Electrochemical performance of rGO–based symmetric supercapacitors*

A symmetric supercapacitor (rGO–SC) was constructed using the redox–active electrolyte, and the electrochemical performance of the device was further investigated. The reversible operational potential window of rGO electrodes in both

positive (0 to 0.8 V) and negative (–1 to 0 V) potential ranges is evident from the CV curves obtained from three–electrode measurements (**Figure A3.11a**, **Appendix 3**).

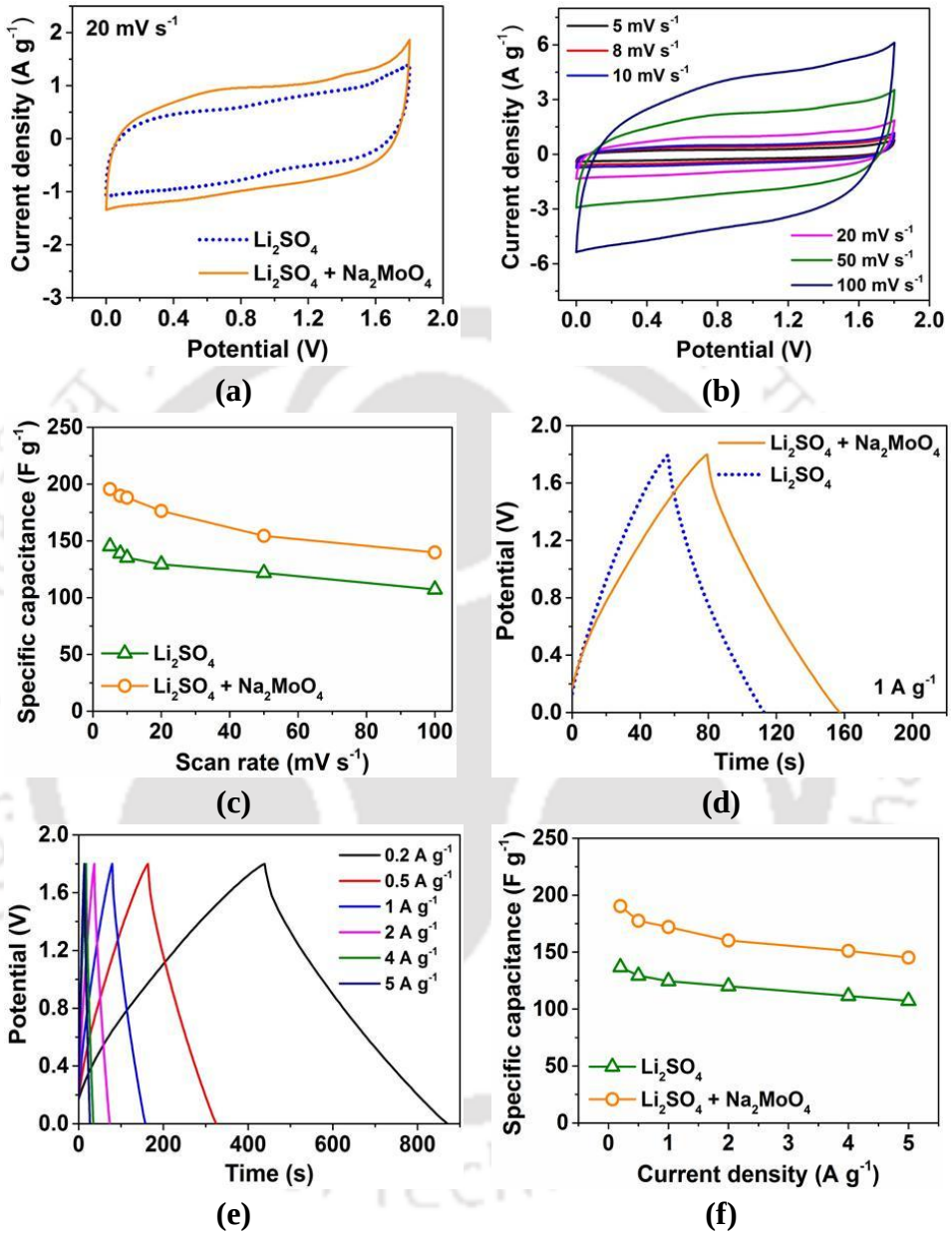


**Figure 4.8** Electrochemical performance of rGO–SC in redox–active electrolyte (0.1 M $Na_2MoO4$ + 1 M $Li_2SO_4$): (a) comparison of the CV curves in redox electrolyte and $Li_2SO_4$; (b) CV curves of rGO–SC at different scan rates; (c) specific capacitance as a function of scan rate; (d) comparison of the GCD curves in redox electrolyte and 1 M $Li_2SO_4$, (e) GCD curves of rGO at different current densities; (f) specific capacitance as a function of current density.

As shown in **Figure A3.11b** (**Appendix 3**), the rGO–SC demonstrated an operating voltage of 1.8 V in the redox–active electrolyte. **Figure 4.8a** shows the CV curves of the rGO–SC in both $Li_2SO_4$ and redox–active electrolyte at a scan rate of 20 mV $s^{-1}$. The increased CV area in the redox–active electrolyte indicated the enhanced charge storage, and this result is in agreement with three–electrode measurements. The plausible redox-reactions for pseudo-faradic contributions have been mentioned in equations (4.1) and (4.2). In addition, a local decrease in pH could take place near the positive electrode resulting from the oxidation of water at high potential windows. If the local pH falls below 6, $MoO_4^{2-}$ ions could transform into $HMoO_4^-$, which could involve further reactions to form $MoO_3$.[16] The CV curves of the rGO–SC (scan rates of 5–100 mV $s^{-1}$) in the redox–active electrolyte are shown in **Figure 4.8b**. The CV curves displayed quasi–rectangular shapes in addition to redox peaks. However, the redox peaks were relatively smaller at 100 mV $s^{-1}$, indicating relatively slow redox kinetics at high scan rates. In the redox–active electrolyte, rGO electrodes exhibited a capacitance of 195.58 F $g^{-1}$ (at 5 mV $s^{-1}$), which is 1.35× higher than the capacitance in the $Li_2SO_4$ electrolyte (**Figure 4.8c**). Moreover, the rGO electrodes exhibited a specific capacitance of 139.82 F $g^{-1}$ at 100 mV $s^{-1}$, which is 71.49% of the capacitance at 5 mV $s^{-1}$.

The GCD curves at a current density of 1 A $g^{-1}$ (**Figure 4.8d**) show a rise in charge–discharge time in the redox–active electrolyte as compared to the $Li_2SO_4$ electrolyte. The GCD curves (current densities of 0.2 – 5 A $g^{-1}$) of the rGO–SC in the redox–active electrolyte are shown in **Figure 4.8e**. The small deviations of GCD curves from linearity indicated pseudocapacitive contributions from redox additive. The rGO electrodes displayed an enhanced capacitance of 268.1 F $g^{-1}$ (at 0.2 A $g^{-1}$) in the redox–active electrolyte (**Figure 4.8f**). In addition, the rGO electrodes retained

76.28% of this capacitance at the high current density of 5 A $g^{-1}$. The redox enhanced rGO–SC demonstrated excellent capacitance retention of 99.3% after 5000 cycles at 5 A $g^{-1}$ (**Figure 4.9a**). Additionally, the morphology of the electrodes did not show any noticeable change after the stability tests (**Figure A3.9e, Appendix 3**). This indicated that the cyclic stability of the rGO–SC was not affected due to the incorporation of the redox additive. The Nyquist plot of the rGO–SC in the redox–active electrolyte (**Figure A3.12**, **Appendix 3**) was similar to that in the $Li_2SO_4$. Before cyclic stability tests, the values of $R_s$ and $R_{ct}$ were 0.76 and 2.68 Ω, respectively. There was no significant change in the $R_s$ after the cyclic stability tests. However, the reduction in $R_{ct}$ value (1.37 Ω) could be ascribed to the improved charge transport inside the pores of the electrodes during repetitive charge–discharge. The redox enhanced rGO–SC displayed an augmented energy density of 21.42 W h $kg^{-1}$ at a power density of 180 W $kg^{-1}$, which is 1.39× higher compared to the energy density of the device in $Li_2SO_4$ electrolyte alone. The Ragone plot in **Figure 4.9b** showed that the energy density of the rGO–SC in redox–active electrolyte is superior to many of the previously published studies on redox–enhanced SCs.[42,43,49–51] At a high power density of 4500 W $kg^{-1}$, the redox enhanced device managed to deliver a high energy density of 12.07 W h $kg^{-1}$. Several redox–active electrolytes (such as hydroquinone/benzoquinone or ferricyanide/ferrocyanide) augment the energy density via additional charge storage, but, cannot hold significant amounts of charge for longer durations. Thus, a large amount of charge dissipates very rapidly due to undesirable cross–diffusion and redox shuttling.[52] The $Na_2MoO_4$ based redox–active electrolyte used in the present study does not suffer from this drawback. In addition, the operational voltage of our redox–enhanced SC is higher than that reported in many previous papers. The inset of **Figure 4.9b** shows a digital photograph of a red LED illuminated by the redox–

enhanced rGO–SC. These results showed that the synergistic interaction among the redox–active electrolyte and mesoporous rGO electrodes improved the energy density via efficient charge mitigation, and reversible and rapid surface redox reactions. The mesopores present in the rGO act as reservoirs of electrolyte as well as redox species and tend to reduce the ion diffusion length thereby increasing the charge storage.[53]

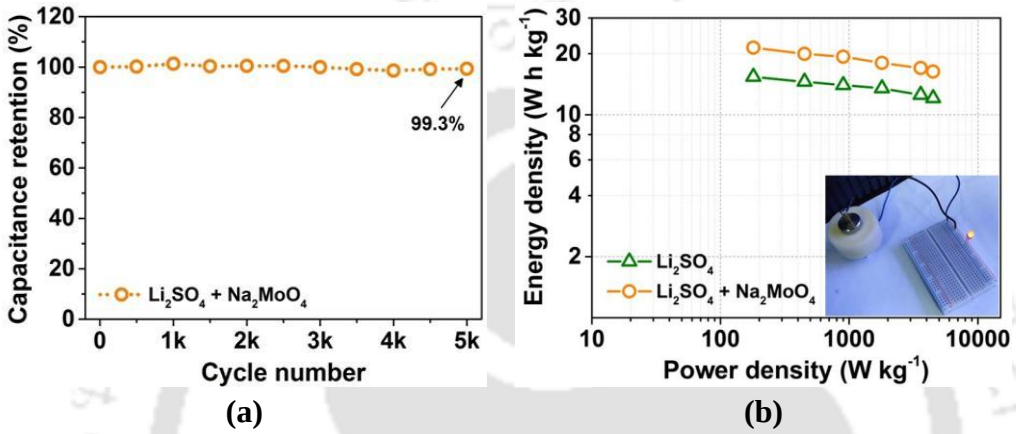


**Figure 4.9** (a) cycle stability analysis of rGO–SC in redox electrolyte; (b) Ragone plot for the rGO–SC in redox electrolyte and 1 M $Li_2SO_4$ (inset: photograph of a red LED powered by the redox enhanced rGO–SC).

### 4.3.4 Electrochemical performance in "water–in–salt" or WIS electrolyte

#### *4.3.4.1 Three–electrode cell characterization of rGO electrodes*

The electrochemical performance of rGO electrodes was investigated in a concentrated 11 M $NaNO_3$ (water–in–salt or WIS) electrolyte. The three–electrode CV measurements revealed that the rGO electrode has a stable potential window of –1.1 V to 1 V (vs. Ag/AgCl) in the WIS electrolyte (**Figure A3.13**, **Appendix 3**). As shown in **Figures A3.14a-b** (**Appendix 2**), the CV and GCD curves of the rGO electrodes indicate predominant double–layer behavior along with pseudocapacitive contributions from reversible hydrogen storage. At a scan rate of 5 mV $s^{-1}$, the rGO

electrode exhibited a specific capacitance of 212.9 F $g^{-1}$ in WIS electrolyte and ~ 67% (142.5 F $g^{-1}$) this capacitance was retained when the scan rate was increased to 100 mV $s^{-1}$ (**Figure A3.14c**, **Appendix 3**). Again from the GCD curves, a specific capacitance of 201.5 F $g^{-1}$ was calculated corresponding to a current density of 0.5 A $g^{-1}$ (**Figure A3.14d**, **Appendix 3**). At a high current density of 5 A $g^{-1}$, the rGO electrode retained 70.8% (140.5 F $g^{-1}$) of its initial capacitance. The rate capability of the rGO electrodes in the WIS electrolyte was comparatively lower than that in the aforementioned aqueous electrolytes and this could be attributed to the high viscosity of the WIS electrolyte.[28]

#### *4.3.4.2 Electrochemical performance of rGO–based symmetric supercapacitors*

To construct a symmetric supercapacitor, rGO electrodes were tested as both positive and negative electrodes separately using the three–electrode setup. As indicated by the CV curves of rGO electrodes in both positive (0 to 1 V) and negative (–1.1 to 0 V) potential ranges (**Figure A3.15a**, **Appendix 3**), a stable cell voltage of 2.1 V can be obtained for the rGO–SC in WIS electrolyte. As shown in **Figure A3.15a** (**Appendix 3**), the potential window of the rGO–SC (in WIS electrolyte) was gradually increased from 1 to 2.2 V and the safe operating voltage was determined to be 2.1 V due to the occurrence of the sharp high polarization peak at 2.2 V. **Figure 4.10a** shows the CV curves at scan rates of 5 – 100 mV $s^{-1}$ in WIS electrolyte and the quasi rectangular shape of the CV curves indicated predominant double–layer charge storage. The CV curves of the device retained similar shape even at a high scan rate of 100 mV $s^{-1}$ indicating good rate capability and small internal resistance. The rGO electrodes displayed a capacitance of 157.95 F $g^{-1}$ at a scan rate of 5 mV $s^{-1}$ in the WIS electrolyte (**Figure 4.10b**). Good capacitance retention of 70% (105.36 F $g^{-1}$) was demonstrated by the rGO electrodes at the high scan rate of 100 mV $s^{-1}$.

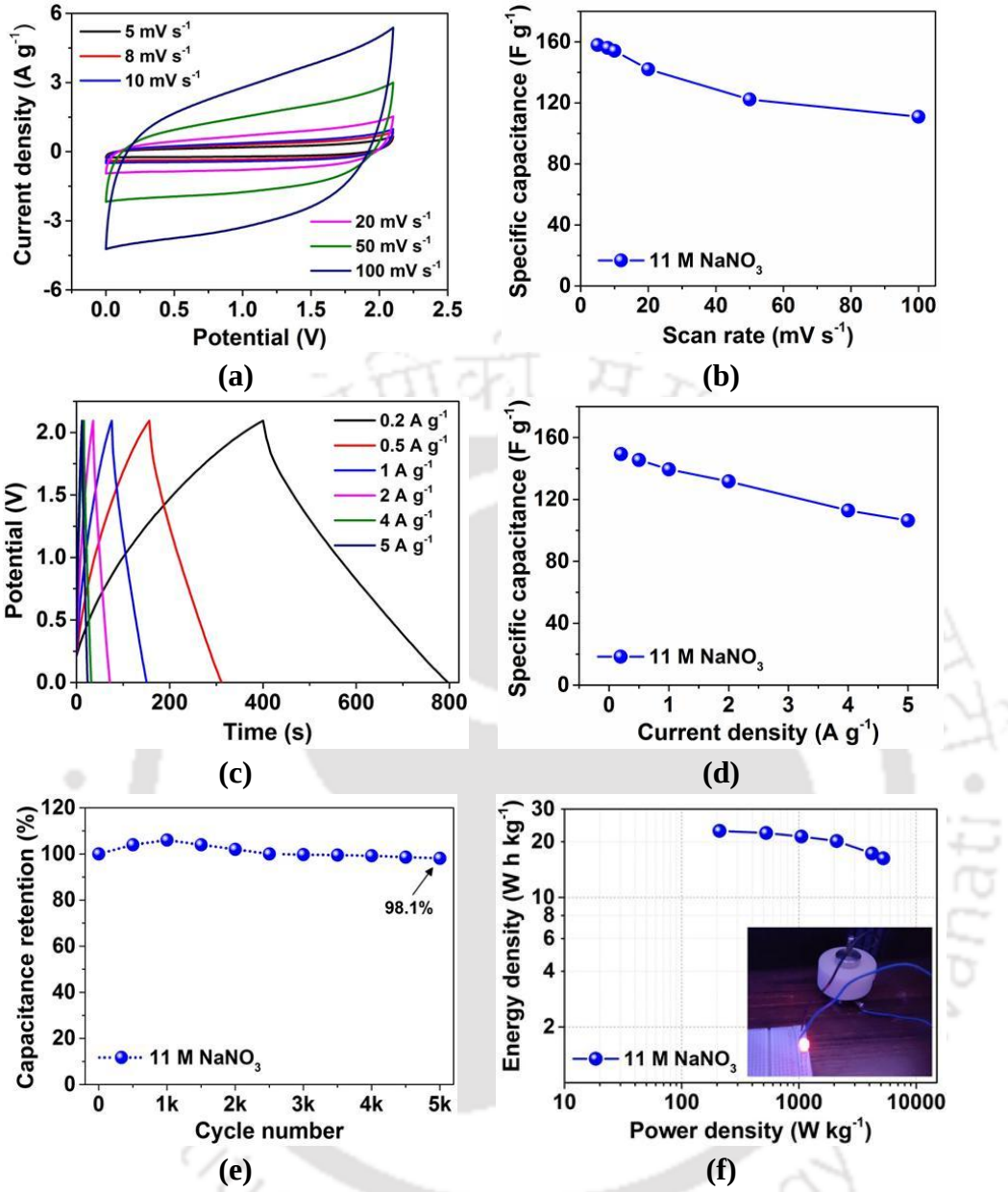


**Figure 4.10** Electrochemical performance of rGO–SC in "water–in–salt" or WIS electrolyte (11 M $NaNO_3$): (a) CV curves of rGO–SC at different scan rates; (b) specific capacitance as a function of scan rate; (c) GCD curves of rGO–SC at different current densities; (d) specific capacitance as a function of current density; (e) cycle stability analysis of the rGO–SC in WIS electrolyte; (f) Ragone plot the rGO–SC in WIS electrolyte (*inset:* photograph of a red LED powered by the 2.1 V device).

The GCD curves of the device shown in **Figure 4.10c** are nearly triangular, which indicated a superior capacitive response. The rGO electrodes exhibited a capacitance of 149.4 F $g^{-1}$ at a current density of 0.2 A $g^{-1}$ and retained 71.2% (106.4 F $g^{-1}$) of this capacitance at 5 A $g^{-1}$ (**Figure 4.10d**). The rGO–SC in WIS electrolyte exhibited superb cyclic stability and retained 98.1% capacitance after 5000 charge–discharge cycles (**Figure 4.10e**). This minor loss of capacitance could be attributed to the degradation of residual surface oxygen groups in rGO due to repetitive charge–discharge at the high cell voltage. However, the electrode morphology did not show any perceptible change after the cycle stability tests (**Figure A3.9f**, **Appendix 3**). The Nyquist plots in **Figure A3.16** (**Appendix 3**) indicated a typical capacitive response. The values of $R_s$ and $R_{ct}$ were calculated as 0.80 and 1.55 Ω, respectively before the cyclic stability tests. A small reduction in both $R_s$ (0.7 Ω) and $R_{ct}$ (1.52 Ω) values was observed after the stability tests. The reduced resistances indicated the improvement of charge transportation inside the pores of the electrodes after repetitive charge–discharge. **Figure 4.10f** shows the Ragone plot for the high voltage rGO–SC with WIS electrolyte. The 2.1 V device delivered a high energy density of 22.47 W h $kg^{-1}$ at a power density of 210 W $kg^{-1}$, which is substantially higher than the energy density of the device in KOH, $H_2SO_4$, and $Li_2SO_4$ electrolytes, and highly competitive with the energy density of previously reported water–in–salt electrolyte based supercapacitors, viz. 21 M LiTFSI (17.2 W h $kg^{-1}$),[54] 17 M $NaClO_4$ (23.7 W h $kg^{-1}$),[54] 12 M $NaNO_3$ (20.5 W h $kg^{-1}$).[28] Moreover, the energy density of the rGO–SC in the WIS electrolyte is marginally higher (< 5%) than that in the redox–active electrolyte. This high energy density is attributed to the larger potential window of 2.1 V compared to the other electrolytes used in this study. Even at a high power delivery of 5250 W $kg^{-1}$, the rGO–SC delivered an energy density of 16.29 W h $kg^{-1}$ in the WIS

electrolyte. The high voltage rGO–SC was used to illuminate a red LED (inset of **Figure 4.10f**). The high cell voltage (2.1 V) and energy density together with excellent rate capability and cyclic stability demonstrated the feasibility of combining mesoporous rGO and $NaNO_3$ based WIS electrolytes for high–performance supercapacitors.

## 4.4 CONCLUSIONS

In summary, symmetric supercapacitors (rGO–SCs) were fabricated using commercial–level mass loading rGO electrodes (9 – 10 mg $cm^{-2}$) in different aqueous electrolytes viz. 1 M $H_2SO_4$, 6 M KOH, and 1 M $Li_2SO_4$. The rGO–SC exhibited a cell voltage of 1.8 V in $Li_2SO_4$ electrolyte and delivered an energy density of 15.39 W h $kg^{-1}$ (at 180 W $kg^{-1}$), which was 2.6× and 3× higher compared to the energy density of the device in KOH, and $H_2SO_4$ electrolyte. Furthermore, the energy densities of the rGO–SCs were augmented with two facile strategies: (i) using pseudo faradaic contributions from redox–active electrolyte, and (ii) widening the cell voltage using a low–cost "water–in–salt" electrolyte. Incorporating $Na_2MoO_4$ (0.1 M) as the redox–additive in $Li_2SO_4$ increased the energy density of the device by 39% (21.42 W h $kg^{-1}$ at 180 W $kg^{-1}$) via redox contributions from the $MoO_4^{2-}$ ions. A high cell voltage of 2.1 V was achieved for the rGO–SC in water–in–salt (11 M $NaNO_3$) electrolyte and the device exhibited a high energy density of 22.87 W h $kg^{-1}$ (at 210 W $kg^{-1}$). In addition, the rGO–SCs demonstrated excellent cyclic stability in both the redox–active and water–in–salt electrolytes. The facile and inexpensive strategies presented in our study have tremendous potential for the development of high energy density EDLCs.

## REFERENCES


(1) Zhong, C.; Deng, Y.; Hu, W.; Qiao, J.; Zhang, L.; Zhang, J. A Review of Electrolyte Materials and Compositions for Electrochemical Supercapacitors. *Chem. Soc. Rev.* **2015**, *44* (21), 7484–7539.

(2) Hwang, J. Y.; Li, M.; El-Kady, M. F.; Kaner, R. B.; Hwang, J. Y.; Li, M.; El-Kady, M. F.; Kaner, R. B. Next-Generation Activated Carbon Supercapacitors: A Simple Step in Electrode Processing Leads to Remarkable Gains in Energy Density. *Adv. Funct. Mater.* **2017**, *27* (15), 1605745.

(3) Burke, A. R&D Considerations for the Performance and Application of Electrochemical Capacitors. *Electrochim. Acta* **2007**, *53* (3), 1083–1091.

(4) Thareja, S.; Kumar, A. High Electrochemical Performance of 2.5 V Aqueous Symmetric Supercapacitor Based on Nitrogen-Doped Reduced Graphene Oxide. *Energy Technol.* **2020**, *8* (5), 1901339.

(5) Liu, J.-C.; Huang, Z.-H.; Ma, T.-Y. Aqueous Supercapacitor with Ultrahigh Voltage Window Beyond 2.0 Volt. *Small Struct.* **2020**, *1* (1), 2000020.

(6) Pal, B.; Yang, S.; Ramesh, S.; Thangadurai, V.; Jose, R. Electrolyte Selection for Supercapacitive Devices: A Critical Review. *Nanoscale Adv.* **2019**, *1* (10), 3807–3835.

(7) Compton, O. C.; Nguyen, S. T. Graphene Oxide, Highly Reduced Graphene Oxide, and Graphene: Versatile Building Blocks for Carbon-Based Materials. *Small* **2010**, *6* (6), 711–723.

(8) Lemine, A. S.; Zagho, M. M.; Altahtamouni, T. M.; Bensalah, N. Graphene a Promising Electrode Material for Supercapacitors—A Review. *Int. J. Energy Res.* **2018**, *42* (14), 4284–4300.

(9) Naderi, H. R.; Sobhani-Nasab, A.; Rahimi-Nasrabadi, M.; Ganjali, M. R. Decoration of Nitrogen-Doped Reduced Graphene Oxide with Cobalt Tungstate Nanoparticles for Use in High-Performance Supercapacitors. *Appl. Surf. Sci.* **2017**, *423*, 1025–1034.

(10) Dong, Y.; Zhu, J.; Li, Q.; Zhang, S.; Song, H.; Jia, D. Carbon Materials for High Mass-Loading Supercapacitors: Filling the Gap between New Materials and Practical Applications. *J. Mater. Chem. A* **2020**, *8* (42), 21930–21946.

(11) Samantray, R.; Karnan, M.; Vivekanand; Subramani, K.; Anjeline, C. J.; Mishra, S. C.; Sathish, M. A Facile Approach to Fabricate Saccharum

Spontaneum-Derived Porous Carbon-Based Supercapacitors for Excellent Energy Storage Performance in Redox Active Electrolytes. *Sustain. Energy Fuels* **2021**, *5* (2), 518–531.

(12) Roldán, S.; González, Z.; Blanco, C.; Granda, M.; Menéndez, R.; Santamaría, R. Redox-Active Electrolyte for Carbon Nanotube-Based Electric Double Layer Capacitors. *Electrochim. Acta* **2011**, *56* (9), 3401–3405.

(13) Lin, K. H.; Lin, L. Y.; Hong, W. L. Incorporating Redox Additives in Sodium Hydroxide Electrolyte for Energy Storage Device with the Nickel Cobalt Molybdenum Oxide Active Material. *J. Energy Storage* **2019**, *25*, 100823.

(14) Sathyamoorthi, S.; Kanagaraj, M.; Kathiresan, M.; Suryanarayanan, V.; Velayutham, D. Ethyl Viologen Dibromide as a Novel Dual Redox Shuttle for Supercapacitors. *J. Mater. Chem. A* **2016**, *4* (12), 4562–4569.

(15) Chodankar, N. R.; Dubal, D. P.; Lokhande, A. C.; Patil, A. M.; Kim, J. H.; Lokhande, C. D. An Innovative Concept of Use of Redox-Active Electrolyte in Asymmetric Capacitor Based on MWCNTs/MnO2 and Fe2O3 Thin Films. *Sci. Reports 2016 61* **2016**, *6* (1), 1–14.

(16) Abbas, Q.; Ratajczak, P.; Béguin, F. Sodium Molybdate – an Additive of Choice for Enhancing the Performance of AC/AC Electrochemical Capacitors in a Salt Aqueous Electrolyte. *Faraday Discuss.* **2014**, *172* (0), 199–214.

(17) Thareja, S.; Kumar, A. "water-In-Salt" Electrolyte-Based High-Voltage (2.7 V) Sustainable Symmetric Supercapacitor with Superb Electrochemical Performance - An Analysis of the Role of Electrolytic Ions in Extending the Cell Voltage. *ACS Sustain. Chem. Eng.* **2021**, *9* (5), 2338–2347.

(18) Yan, X.; Zhao, X.; Liu, C.; Wang, S.; Zhang, Y.; Guo, M.; Wang, Y.; Dai, L.; Yang, X. High-Voltage Bi-Redox Lithium-Ion Capacitor Enabled by Energizing Free Water in "Water-in-Salt" Electrolyte. *J. Power Sources* **2019**, *423*, 331–338.

(19) Dou, Q.; Lei, S.; Wang, D. W.; Zhang, Q.; Xiao, D.; Guo, H.; Wang, A.; Yang, H.; Li, Y.; Shi, S.; Yan, X. Safe and High-Rate Supercapacitors Based on an "Acetonitrile/Water in Salt" Hybrid Electrolyte. *Energy Environ. Sci.* **2018**, *11* (11), 3212–3219.

(20) Martins, V. L.; Torresi, R. M. Water-in-Salt Electrolytes for High Voltage Aqueous Electrochemical Energy Storage Devices. *Curr. Opin. Electrochem.* **2020**, *21*, 62–68.

(21) Bu, X.; Su, L.; Dou, Q.; Lei, S.; Yan, X. A Low-Cost "Water-in-Salt" Electrolyte for a 2.3 V High-Rate Carbon-Based Supercapacitor. *J. Mater. Chem. A* **2019**, *7* (13), 7541–7547.

(22) Hasegawa, G.; Kanamori, K.; Kiyomura, T.; Kurata, H.; Abe, T.; Nakanishi, K. Hierarchically Porous Carbon Monoliths Comprising Ordered Mesoporous Nanorod Assemblies for High-Voltage Aqueous Supercapacitors. *Chem. Mater.* **2016**, *28* (11), 3944–3950.

(23) Lee, W. S. V.; Xiong, T.; Loh, G. C.; Tan, T. L.; Xue, J. Optimizing Electrolyte Physiochemical Properties toward 2.8 v Aqueous Supercapacitor. *ACS Appl. Energy Mater.* **2018**, *1* (7), 3070–3076.

(24) Song, Z.; Duan, H.; Zhu, D.; Lv, Y.; Xiong, W.; Cao, T.; Li, L.; Liu, M.; Gan, L. Ternary-Doped Carbon Electrodes for Advanced Aqueous Solid-State Supercapacitors Based on a "Water-in-Salt" Gel Electrolyte. *J. Mater. Chem. A* **2019**, *7* (26), 15801–15811.

(25) Zhang, L.; Wu, D.; Ma, Q.; Wang, G.; Liu, Z.; Chang, M.; Yan, X. Dual-Strategy to Construct Aqueous-Based Symmetric Supercapacitors with High Volumetric Energy Density. *ChemElectroChem* **2020**, *7* (3), 838–845.

(26) Khademi, B.; Nateghi, M. R.; Shayesteh, M. R.; Nasirizadeh, N. High Voltage Binder Free Hybrid Supercapacitor Based on Reduced Graphene Oxide/Graphene Oxide Electrodes and "Water in Salt" Electrolyte. *J. Energy Storage* **2021**, *43*, 103164.

(27) Lukatskaya, M. R.; Feldblyum, J. I.; Mackanic, D. G.; Lissel, F.; Michels, D. L.; Cui, Y.; Bao, Z. Concentrated Mixed Cation Acetate "Water-in-Salt" Solutions as Green and Low-Cost High Voltage Electrolytes for Aqueous Batteries. *Energy Environ. Sci.* **2018**, *11* (10), 2876–2883.

(28) Guo, J.; Ma, Y.; Zhao, K.; Wang, Y.; Yang, B.; Cui, J.; Yan, X. High-Performance and Ultra-Stable Aqueous Supercapacitors Based on a Green and Low-Cost Water-In-Salt Electrolyte. *ChemElectroChem* **2019**, *6* (21), 5433–5438.

(29) Gao, Q.; Demarconnay, L.; Raymundo-Piñero, E.; Béguin, F. Exploring the Large Voltage Range of Carbon/Carbon Supercapacitors in Aqueous Lithium Sulfate Electrolyte. *Energy Environ. Sci.* **2012**, *5* (11), 9611–9617.

(30) Fic, K.; Płatek, A.; Piwek, J.; Menzel, J.; Ślesiński, A.; Bujewska, P.; Galek, P.; Frąckowiak, E. Revisited Insights into Charge Storage Mechanisms in

Electrochemical Capacitors with Li2SO4-Based Electrolyte. *Energy Storage Mater.* **2019**, *22*, 1–14.

(31) Wei, L.; Sevilla, M.; Fuertes, A. B.; Mokaya, R.; Yushin, G. Hydrothermal Carbonization of Abundant Renewable Natural Organic Chemicals for High-Performance Supercapacitor Electrodes. *Adv. Energy Mater.* **2011**, *1* (3), 356–361.

(32) Chen, J.; Fang, K.; Chen, Q.; Xu, J.; Wong, C. P. Integrated Paper Electrodes Derived from Cotton Stalks for High-Performance Flexible Supercapacitors. *Nano Energy* **2018**, *53*, 337–344.

(33) Zhu, J.; Xu, Y.; Wang, J.; Lin, J.; Sun, X.; Mao, S. The Effect of Various Electrolyte Cations on Electrochemical Performance of Polypyrrole/RGO Based Supercapacitors. *Phys. Chem. Chem. Phys.* **2015**, *17* (43), 28666–28673.

(34) Zhi, J.; Reiser, O.; Huang, F. Hierarchical MnO2 Spheres Decorated by Carbon-Coated Cobalt Nanobeads: Low-Cost and High-Performance Electrode Materials for Supercapacitors. *ACS Appl. Mater. Interfaces* **2016**, *8* (13), 8452–8459.

(35) Zhi, J.; Zhao, W.; Liu, X.; Chen, A.; Liu, Z.; Huang, F. Highly Conductive Ordered Mesoporous Carbon Based Electrodes Decorated by 3D Graphene and 1D Silver Nanowire for Flexible Supercapacitor. *Adv. Funct. Mater.* **2014**, *24* (14), 2013–2019.

(36) Fic, K.; Lota, G.; Meller, M.; Frackowiak, E. Novel Insight into Neutral Medium as Electrolyte for High-Voltage Supercapacitors. *Energy Environ. Sci.* **2012**, *5* (2), 5842–5850.

(37) Zhao, Y.; Liu, J.; Wang, N.; Li, Q.; Hu, M. Rational Selection of Small Aromatic Molecules to Functionalize Graphene for Enhancing Capacitive Energy Storage. *J. Mater. Chem. A* **2018**, *6* (17), 7566–7572.

(38) Dai, S.; Liu, Z.; Zhao, B.; Zeng, J.; Hu, H.; Zhang, Q.; Chen, D.; Qu, C.; Dang, D.; Liu, M. A High-Performance Supercapacitor Electrode Based on N-Doped Porous Graphene. *J. Power Sources* **2018**, *387*, 43–48.

(39) Naderi, H.; Sobati, H.; Sobhani-Nasab, A.; Rahimi-Nasrabadi, M.; Eghbali-Arani, M.; Ganjali, M. R.; Ehrlich, H. Synthesis and Supercapacitor Application of Cerium Tungstate Nanostructure. *ChemistrySelect* **2019**, *4* (10), 2862–2867.

(40) Sawangphruk, M.; Srimuk, P.; Chiochan, P.; Krittayavathananon, A.;

Luanwuthi, S.; Limtrakul, J. High-Performance Supercapacitor of Manganese Oxide/Reduced Graphene Oxide Nanocomposite Coated on Flexible Carbon Fiber Paper. *Carbon N. Y.* **2013**, *60*, 109–116.

(41) Wang, M.; Song, X.; Dai, S.; Xu, W.; Yang, Q.; Liu, J.; Hu, C.; Wei, D. NiO Nanoparticles Supported on Graphene 3D Network Current Collector for High-Performance Electrochemical Energy Storage. *Electrochim. Acta* **2016**, *214*, 68–75.

(42) Senthilkumar, S. T.; Selvan, R. K.; Ponpandian, N.; Melo, J. S.; Lee, Y. S. Improved Performance of Electric Double Layer Capacitor Using Redox Additive (VO2+/VO2+) Aqueous Electrolyte. *J. Mater. Chem. A* **2013**, *1* (27), 7913–7919.

(43) Senthilkumar, S. T.; Selvan, R. K.; Ponpandian, N.; Melo, J. S. Redox Additive Aqueous Polymer Gel Electrolyte for an Electric Double Layer Capacitor. *RSC Adv.* **2012**, *2* (24), 8937–8940.

(44) Jeon, J. W.; Zhang, L.; Lutkenhaus, J. L.; Laskar, D. D.; Lemmon, J. P.; Choi, D.; Nandasiri, M. I.; Hashmi, A.; Xu, J.; Motkuri, R. K.; Fernandez, C. A.; Liu, J.; Tucker, M. P.; McGrail, P. B.; Yang, B.; Nune, S. K. Controlling Porosity in Lignin-Derived Nanoporous Carbon for Supercapacitor Applications. *ChemSusChem* **2015**, *8* (3), 428–432.

(45) Miao, F.; Shao, C.; Li, X.; Lu, N.; Wang, K.; Zhang, X.; Liu, Y. Polyaniline-Coated Electrospun Carbon Nanofibers with High Mass Loading and Enhanced Capacitive Performance as Freestanding Electrodes for Flexible Solid-State Supercapacitors. *Energy* **2016**, *95*, 233–241.

(46) Chang, H. W.; Lu, Y. R.; Chen, J. L.; Chen, C. L.; Chen, J. M.; Tsai, Y. C.; Chou, W. C.; Dong, C. L. Electrochemically Activated Reduced Graphene Oxide Used as Solid-State Symmetric Supercapacitor: An X-Ray Absorption Spectroscopic Investigation. *J. Phys. Chem. C* **2016**, *120* (39), 22134–22141.

(47) Senthilkumar, S. T.; Selvan, R. K.; Melo, J. S. Redox Additive/Active Electrolytes: A Novel Approach to Enhance the Performance of Supercapacitors. *J. Mater. Chem. A* **2013**, *1* (40), 12386–12394.

(48) Evanko, B.; Boettcher, S. W.; Yoo, S. J.; Stucky, G. D. Redox-Enhanced Electrochemical Capacitors: Status, Opportunity, and Best Practices for Performance Evaluation. *ACS Energy Lett.* **2017**, *2* (11), 2581–2590.

(49) Chun, S. E.; Evanko, B.; Wang, X.; Vonlanthen, D.; Ji, X.; Stucky, G. D.;

Boettcher, S. W. Design of Aqueous Redox-Enhanced Electrochemical Capacitors with High Specific Energies and Slow Self-Discharge. *Nat. Commun. 2015 61* **2015**, *6* (1), 1–10.

(50) Yu, H.; Wu, J.; Fan, L.; Lin, Y.; Xu, K.; Tang, Z.; Cheng, C.; Tang, S.; Lin, J.; Huang, M.; Lan, Z. A Novel Redox-Mediated Gel Polymer Electrolyte for High-Performance Supercapacitor. *J. Power Sources* **2012**, *198*, 402–407.

(51) Wang, Y. G.; Cheng, L.; Xia, Y. Y. Electrochemical Profile of Nano-Particle CoAl Double Hydroxide/Active Carbon Supercapacitor Using KOH Electrolyte Solution. *J. Power Sources* **2006**, *153* (1), 191–196.

(52) Evanko, B.; Boettcher, S. W.; Yoo, S. J.; Stucky, G. D. Redox-Enhanced Electrochemical Capacitors: Status, Opportunity, and Best Practices for Performance Evaluation. *ACS Energy Lett.* **2017**, *2* (11), 2581–2590.

(53) Hu, H.; Hu, Y.; Cheng, H.; Dai, S.; Song, K.; Liu, M. Organic Polysulfanes Grafted on Porous Graphene as an Electrode for High-Performance Lithium Organosulfur Batteries. *J. Power Sources* **2021**, *491*, 229617.

(54) Bu, X.; Su, L.; Dou, Q.; Lei, S.; Yan, X. A Low-Cost "Water-in-Salt" Electrolyte for a 2.3 V High-Rate Carbon-Based Supercapacitor. *J. Mater. Chem. A* **2019**, *7* (13), 7541–7547.

# CHAPTER 5

## Biomass Blend derived Porous Carbon for Aqueous Supercapacitors with Commercial-Level Mass Loadings and Enhanced Energy Density in Redox-Active Electrolyte

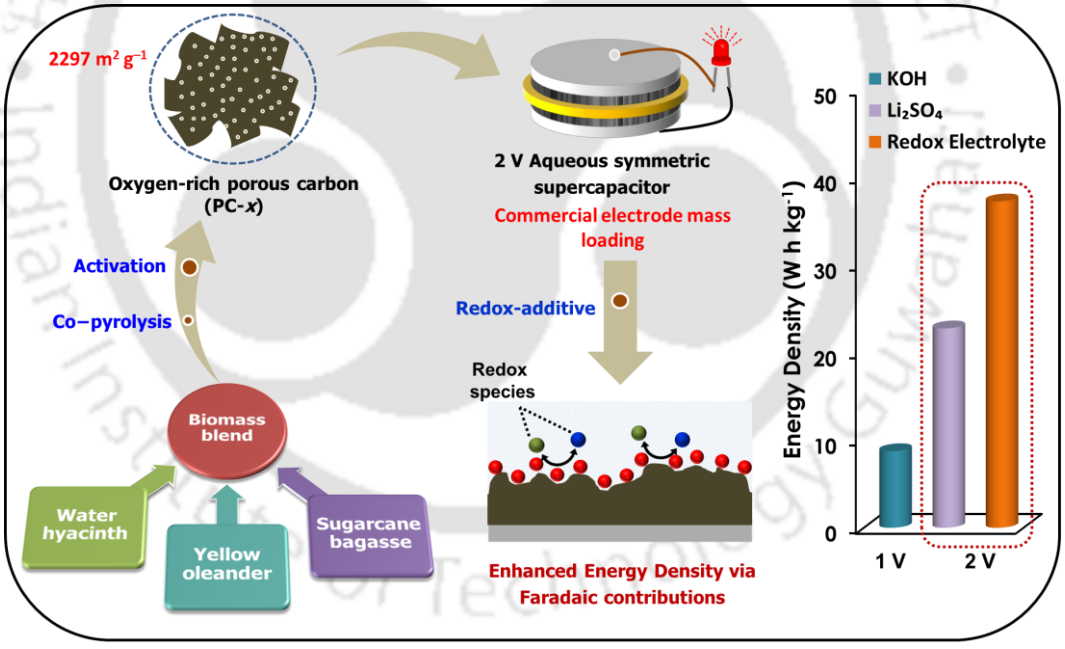

# CHAPTER 5

# BIOMASS BLEND DERIVED POROUS CARBON FOR AQUEOUS SUPERCAPACITORS WITH COMMERCIAL-LEVEL MASS LOADINGS AND ENHANCED ENERGY DENSITY IN REDOX-ACTIVE ELECTROLYTE

## 5.1 INTRODUCTION

Biomass-derived porous carbons have been widely explored as SC electrode materials due to their renewable nature, large surface area, tunable pore size, electrochemical stability, and cost-effectiveness.[1] Varieties of biomass, viz. willow catkins,[2] rice husk,[3] barley grains,[4] cotton waste,[5] phoenix tree leaves [6], etc. have been used to synthesize porous activated carbon for application in SCs. These activated carbons are commonly synthesized by carbonization/pyrolysis followed by either physical activation (in $CO_2$ atmosphere) or chemical activation (using KOH, $H_3PO_4$, $ZnCl_2$, etc.) at high temperatures.[7] The activation process creates abundant porosity (micropores and mesopores) in the carbonized sample (char) resulting in drastically increased surface area for double-layer charge storage. Chemical activation usually creates more porous carbon than physical activation.[7]

Although carbon derived from biomass has proven to be promising for energy storage applications, however, the yield of activated carbon from raw biomass is rather low. Hence, large-scale and sustainable production of activated carbon requires a huge supply of raw materials continuously. In this context, using mixtures of multiple biomass can be a potential solution as it would provide a large quantity of raw material and flexibility in terms of effective utilization of raw materials.

Interestingly, co-pyrolysis of multiple feedstocks (biomass blends/mixtures) have gained popularity for bio-oil and biochar production.[8–10] The biochar obtained from the co-pyrolysis can be further activated to synthesize porous activated carbon. In previous studies of our group, we have reported co-pyrolysis of blends of biomass (viz. water hyacinth, yellow oleander, and sugarcane bagasse).[11,12] These studies revealed advantages such as lowering of activation energy during co-pyrolysis as compared to the pyrolysis of single biomass. The minimum activation energy was obtained for the ternary blend (wt. ratio of 1:1:1) of these three biomass, which is desired for energy-effective thermochemical conversion. Based on these results, the biochar obtained from the co-pyrolysis of this ternary biomass blend was chosen for the synthesis of porous carbon material.

The capacitive performance of activated carbons can be improved by the introduction of heteroatoms (e.g. N, P, S, O, etc.) via doping or attachment of surface functionalities. These heteroatoms provide pseudocapacitive contributions and improve the wettability of the electrode.[13] In this study, we have synthesized oxygen (heteroatom) enriched porous activated carbon via a relatively low-temperature activation process (700 °C) without any external doping agents. Oxygen functionalities increase the wettability of the carbon electrodes and thereby improve the interaction of electrolyte ions at the electrode-electrolyte interface. Additionally, oxygen functional groups are electron-rich and participate in electron transfer resulting in pseudocapacitive contribution.[14] It has been observed that large surface areas are achieved for carbons at high-temperature activation (800 °C or more) however; oxygen functionalities tend to decrease with the increase in temperature.[15] Therefore, it is essential to adopt relatively low-temperature activation to retain

optimal oxygen functionalities in the porous carbon without compromising the porosity.

The present study reports the synthesis of oxygen-enriched porous carbon (PC-*x*) via co-pyrolysis and low-temperature KOH activation (700 °C) from biomass blends (water hyacinth, yellow oleander, and sugarcane bagasse). KOH was chosen as the activating agent to achieve highly micro/mesoporous structures, high pore volumes, and large surface areas along with surface functionalities.[15] The influence of KOH content on micro/mesopore volume, surface functionalities, and capacitive performances has been investigated. The optimized PC-*x* possessed a high surface area of ~2297 $m^2$ $g^{-1}$, hierarchical pore structure with a pore volume of 1.23 $cm^3$ $g^{-1}$, and oxygen functionalities (C/O = 3.05). The PC-*x* electrodes exhibited high specific capacitance, good rate capability along with excellent cyclic stability in 6 M KOH electrolyte at commercial electrode mass loadings (~10 mg $cm^{-2}$), and outperformed various carbon materials with high electrode mass loadings in the literature. The high voltage (2 V) aqueous symmetric SC fabricated in 1 M $Li_2SO_4$ delivered a remarkable energy density of 22.75 W h $kg^{-1}$ (at 200 W $kg^{-1}$) with high cycle stability (96.8 % @ 5 A $g^{-1}$, 10000 cycles). Furthermore, incorporation of $Na_2MoO_4$ (redox-additive) in $Li_2SO_4$ augmented the energy density of the SC by 63.7% (37.24 W h $kg^{-1}$). The enhanced energy density with the redox electrolyte was devised from the redox reactions of $MoO_4^{2-}$ ions.

## 5.2 Experimental Section

### 5.2.1 Material Synthesis

The water hyacinth (*Eichhornia crassipes*) and yellow oleander (*Thevetia peruviana*) were collected from the campus of our institute and the sugarcane (*Saccharum*

*officinarum*) bagasse was obtained from a nearby local market. The biomass samples were extensively washed to remove impurities, chopped, and oven-dried. After drying, samples were grinded using a mixer-grinder and sieved with a 2 mm sieve. A blend of powdered biomass was prepared in the ratio (wt%) of 1:1:1, which was optimized in our previous study.[11] The detailed characterization of the raw biomass and the char of the individual and biomass blends are provided in our earlier studies.[11,12] The ternary biomass blend (500 g) was carbonized at 500 °C for 1 h under argon atmosphere with a heating rate of 10 °C $min^{-1}$. A fixed-batch pyrolyzer was used for the experiments as described in our earlier paper.[16] The as-obtained biochar (20 g) was mixed with KOH at different weight ratios and activated at 700 °C for 1 h in the pyrolyzer under argon atmosphere. The reactor was then allowed to cool down to room temperature in the inert atmosphere. The resulting solids were washed with 0.5 M HCl and deionized water till neutral pH was obtained and finally dried in the oven at 100 °C. The porous carbon samples were named PC-*x*, where *x* indicates the weight ratio of KOH to biochar used during activation (KOH/biochar = 3, 4, and 5). An illustration of the synthesis process for PC-*x* is depicted in **Figure 5.1**.


**Figure 5.1** Synthesis protocol of oxygen-rich porous carbon (PC-*x*) from blends of sugarcane bagasse, water hyacinth, and yellow oleander.

### 5.2.2 Characterization Techniques

The instruments used for XRD, Raman spectroscopy, FESEM, TEM, EDS, and BET surface area analysis were same as described in **Chapter 2**. Additionally, The chemical bonds and the atomic composition were investigated using a Thermo Fisher (ESCALAB Xi+) X-ray photoelectron spectroscope (XPS). The elemental analysis of C, H, N, S, and O contents in the PC-*x* was performed using a Euro EA (Eurovector EA3000) CHNS elemental analyzer. Ash content was obtained according to the ASTM D1102-84 protocol.

### 5.2.3 Electrochemical Measurements

The electrode preparation involved uniform mixing of the PC-*x* (active material), carbon black, and PTFE (in 8:1:1 weight ratio) in ethanol, and coating of the resultant slurry on stainless steel foil followed by drying at 100 °C. The active material loading on the disc electrodes (dia. ~ 1.5 cm) was ~ 10 mg $cm^{-2}$. As described in **Chapter 3**, symmetric SCs (PC-*x*-SCs) were assembled using two identical electrodes and a cellulose separator. Initially, 6 M KOH was used as the electrolyte for the PC-*x*-SCs, and the best sample was tested with 1 M $Li_2SO_4$ and redox-mediated (0.1 M $Na_2MoO_4$ + 1 M $Li_2SO_4$) electrolyte. The amount of electrolyte (300 µL) was consistent throughout all the experiments.

Electrochemical measurements (viz. CV, GCD and EIS) were performed using a M204 Potentiostat/Galvanostat (Metrohm Autolab). The specific capacitance of a single electrode ($C_g$, F $g^{-1}$) was calculated from the CV and GCD curves using equations 1.7 and 1.8, respectively as described in section 1.4.1 in **Chapter 1**. The energy density (E, W h $kg^{-1}$), and power density (P, W $kg^{-1}$) of the cells were

calculated from GCD curves using equations 1.9 and 1.10, respectively (described in section 1.4.1 in **Chapter 1)**.

## 5.3 RESULTS AND DISCUSSION

### 5.3.1 Physicochemical Characterization

As shown in **Figure 5.1**, the ternary biomass blend was co-pyrolyzed and the obtained biochar was activated using KOH to prepare hierarchically porous carbon (PC-*x*). To optimize the pore structure of the PC-*x*, the activation process was performed with varying KOH content. It is noteworthy that the preparation of porous carbon was done on a relatively larger scale. Co-pyrolysis was done for 500 g biomass blend and KOH activation was done for 20 g char and these quantitates are substantially higher (more than 10×) than the previous studies in the existing literature. In our experiments, about 7.6, 7, and 6.2 g of porous carbon were prepared at one time from 20 g of biochar corresponding to *x* (KOH/biochar wt. ratio) = 3, 4, and 5, respectively.

The morphologies of the as-prepared porous carbons were examined using FESEM and TEM (**Figure 5.2**). It was observed that the PC-3 (**Figures 5.2a, d**) sample has a three-dimensional (3D) skeleton formed by carbon sheets. Conversely, some parts of the 3D sheet-like frameworks of the PC-4 (**Figures 5.2b, e**) and PC-5 (**Figures 2c, f**) samples were converted to non-uniform particle-like nanostructures. These particle agglomerates were formed by the partial collapse of carbon walls as a result of etching caused by KOH and this etching of carbon frameworks is aggravated by the increase in KOH content.[17] Therefore, a relatively large amount of particle agglomerates were observed in the PC-5 as compared to the PC-4. Moreover, the high-resolution TEM images (**Figures A4.1**, **Appendix 4**) revealed the presence of

interconnected networks of abundant micropores and mesopores along with the amorphous nature of PC-4. The highly porous network of synthesized PC-*x* makes them potential candidates for energy storage applications.

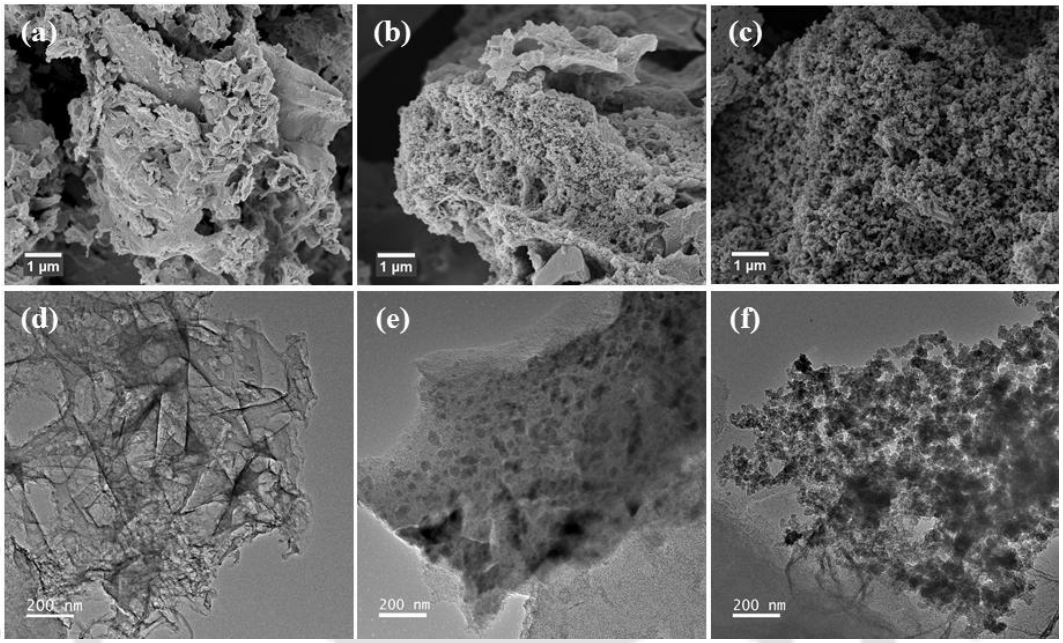


**Figure 5.2** FE-SEM images of (a) PC-3, (b) PC-4, and (c) PC-5. TEM images of (d) PC-3, (e) PC-4, and (f) PC-5 (formation of particulate agglomerates is visible with increasing KOH/biochar ratio)

The formation of these porous carbon samples could be attributed to the following mechanisms:[18] (i) chemical activation (etching of carbon framework) of the carbon samples via redox reactions between the carbon and the activating agents (potassium compounds) as shown in reactions R5.1-R5.6; (ii) physical activation resulting from the gasification of carbon by water vapor and $CO_2$ (reactions R5.5-R5.6); (iii) intercalation of metallic potassium (produced in reactions R5.1, R5.3-R5.4) inside the lattices of the carbon framework resulting in expansion of the carbon lattices.

$$6KOH + 2C \longrightarrow 2K + 3H_2 + 2K_2CO_3 \quad \text{(R5.1)}$$

$$K_2CO_3 \longrightarrow K_2O + CO_2 \quad \text{(R5.2)}$$

$$K_2CO_3 + 2C \longrightarrow 2K + 3CO \quad \text{(R5.3)}$$

$$K_2O + C \longrightarrow 2K + CO \quad \text{(R5.4)}$$

$$CO_2 + C \longrightarrow 2CO \quad \text{(R5.5)}$$

$$C + H_2O \longrightarrow CO + H_2 \quad \text{(R5.6)}$$

The crystallographic structural information of the samples was studied using XRD. The diffraction patterns of the PC-*x* exhibited two broad peaks as shown in **Figure 5.3a**. The diffraction peaks at ~ 24° and ~ 43° correspond to the (0 0 2) and (1 0 0) graphitic planes, respectively. The broad (0 0 2) peak indicated the low degree of graphitization, presence of a large number of pores, and disordered nature of the PC-*x* samples. These results are similar to the previous literature.[19,20] The PC-*x* samples were also studied using Raman spectroscopy. The Raman spectroscopy results showed the existence of two characteristic peaks at ~ 1355 and ~1590 $cm^{-1}$ conforming to D and G bands, respectively (**Figure 5.3b**). The G band characterizes the $E_{2g}$ mode of $sp^2$ hybridized carbon atoms while the D band indicates $A_{1g}$ vibration mode originating from defects present in carbon frameworks.[21] The intensity ratio ($I_D/I_G$) indicates the degree of defects in the carbon materials. The $I_D/I_G$ ratio for PC-3, PC-4, and PC-5 were 1.03, 1.05, and 1.06, respectively. The increase in $I_D/I_G$ ratio could be attributed to the disordered carbon structure resulting from etching by higher quantities of KOH.

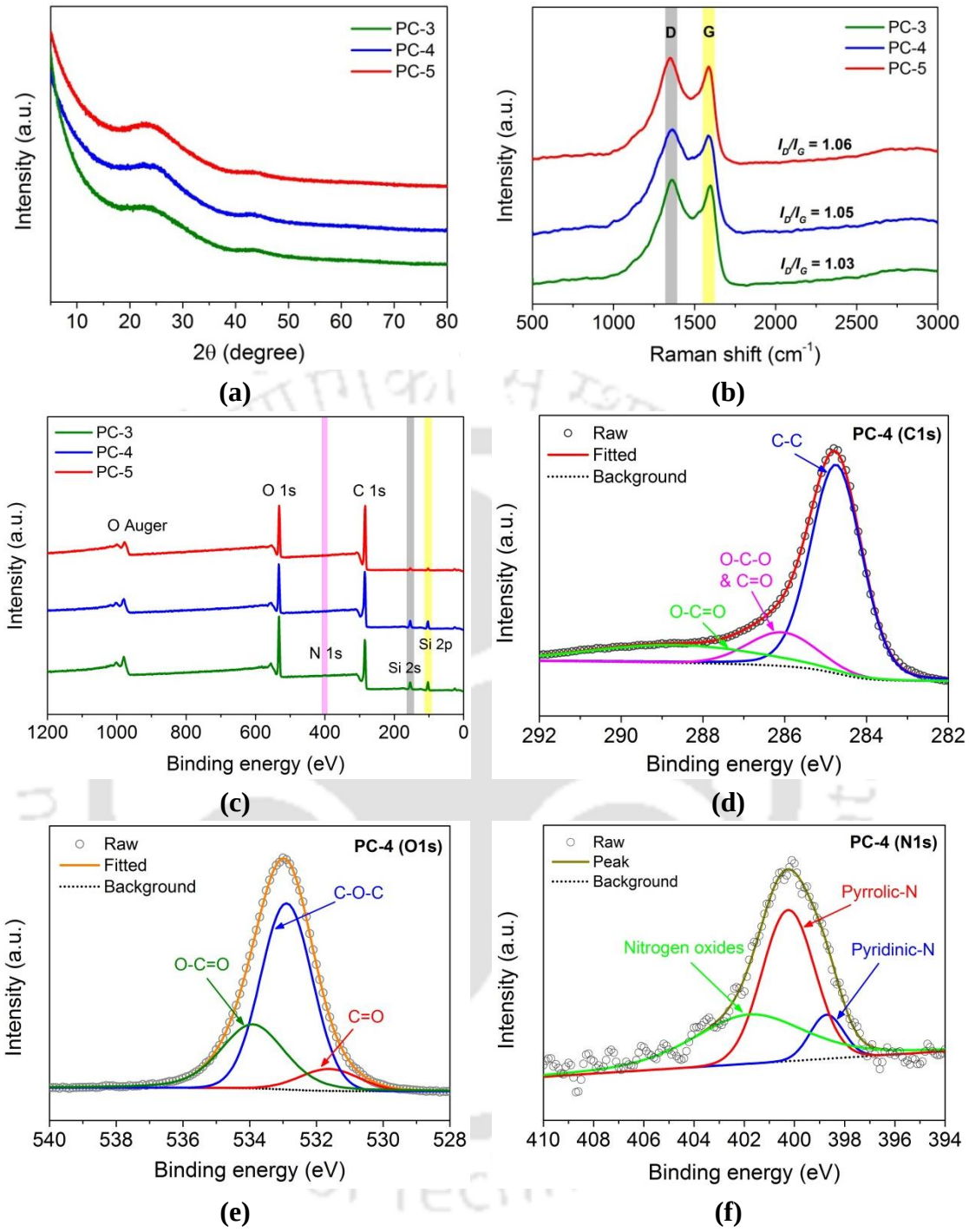


**Figure 5.3** (a) XRD patterns, (b) Raman spectra, and (c) XPS survey spectra of PC-*x* samples; high-resolution (d) C1s, (e) O1s, and (f) N1s spectrum of PC-4.

The elemental composition and the surface chemical composition of the synthesized carbon materials were determined using XPS measurements. **Figure 5.3c** shows the XPS survey spectra of the PC-*x*, which revealed that C and O are the main

constituents of the carbon samples. Along with C and O, small quantities of N and Si were also detected in the samples. The Si content could be residual from water hyacinth and small peaks at 103 and 155 eV could be attributed to the Si 2p and Si 2s, respectively (**Figure 5.3c**). **Table 5.1** shows the elemental compositions of the PC-*x* obtained from XPS. The carbon contents of PC-3, PC-4, and PC-5 were 67.28, 71.56, and 72.82 at%, while the oxygen contents were 26.91, 23.45, and 23.24 at%, respectively. The C/O ratio of the samples varies as 2.5, 3.05, and 3.13 for PC-3, PC-4, and PC-5, respectively. This indicated that the oxygen content in the samples decreased as the KOH content increased during activation. The deconvoluted C1s spectra of PC-*x* showed three peaks centered at 284.8, 286.1, and 288.5 eV (**Figure 5.3d**, and **Figures A4.2a-b** in **Appendix 4**) conforming to C–C, C–O–C, and O–C=O functional groups, respectively.[22,23] The O1s spectra were deconvoluted into three peaks at 531.2, 532.8, and 534.2 eV, which could be attributed to C=O, C–O–C, and O–C=O groups, respectively (**Figure 5.3e**, and **Figures A4.2c-d** in **Appendix 4**).[22,23] Additionally, the composition of nitrogen in the PC-3, PC-4, and PC-5 samples were 0.71, 0.39, and 0.44 at%, respectively (**Table 5.1**). Three peaks were obtained from the deconvoluted N1s spectra at 398.7, 400.3, and 402.2 eV, which corresponds to pyridinic-N (N6), Pyrrolic-N (N5), and oxides of nitrogen (N-X), respectively (**Figure 5.3f**, and **Figures A4.2e-f** in **Appendix 4**).[24] The N6 and N5 functionalities can contribute electron lone pairs to conjugated carbon systems and consequently induce faradaic pseudocapacitance. On the other hand, N-X offers high charge mobility and is an efficient electron donor.[25] Therefore, the introduced nitrogen heteroatoms could significantly enhance the capacitance of the PC-*x*. **Table 5.1** also shows the chemical composition of PC-*x* samples detected by CHNS elemental analysis. The CHNS elemental analysis further supports the high oxygen content of

the carbon samples (29.54, 26.71, and 25.98 wt% for PC-3, PC-4, and PC-5, respectively).

**Table 5.1** Elemental compositions (from XPS and CHNS analysis) and ash contents of PC-*x* samples

| Sample | Elemental composition from XPS (at%) | | | | Elemental composition from CHNS (wt%) | | | | Ash [%] |
|---|---|---|---|---|---|---|---|---|---|
| | C | O | N | Si | C | H | #O | N | |
| PC-3 | 67.28 | 26.91 | 0.71 | 5.1 | 58.96 | 2.19 | 32.24 | 1.08 | 5.53 |
| PC-4 | 71.56 | 23.45 | 0.39 | 4.6 | 61.60 | 3.57 | 27.71 | 1.68 | 5.44 |
| PC-5 | 72.82 | 23.24 | 0.44 | 3.5 | 64.63 | 1.78 | 26.99 | 1.23 | 5.37 |

# calculated by difference

It is noteworthy that the high oxygen content was achieved via self-doping at a relatively low activation temperature of 700 °C without any additional reagents. Previous studies have reported that carbon materials derived from biomass having high lignin content may have abundant oxygen functionalities.[26,27] This could be due to the relatively complex and thermally stable structure of lignin as compared to cellulose and hemicellulose. The compositions of cellulose, hemicellulose, and lignin in the three biomass used in this study are listed in **Table A4.1**, **Appendix 4** (reported in our previous study).[11] It could be seen that the lignin content of the sugarcane bagasse (19.89±0.52 wt%) and yellow oleander (15.76±1.29 wt%) was significantly higher than that of water hyacinth (5.65±0.63 wt%). Therefore, the major portion of the oxygen content in PC-*x* has plausibly come from sugarcane bagasse and yellow oleander due to their high lignin content. The presence of such high content of oxygen functionalities is most likely to improve the wettability of the PC-*x* electrodes, and thus, increases the surface area accessed by the electrolyte. Interestingly, these oxygen-containing groups could also participate in reversible surface redox reactions contributing to pseudocapacitance to increase the overall capacitive performance. In

addition, the ash contents of PC-3, PC-4, and PC-5 were found to be 5.23, 5.44, and 5.38 wt %, respectively (**Table 5.1**). These ash content values are comparable to that of the wood-based activated carbon available commercially.

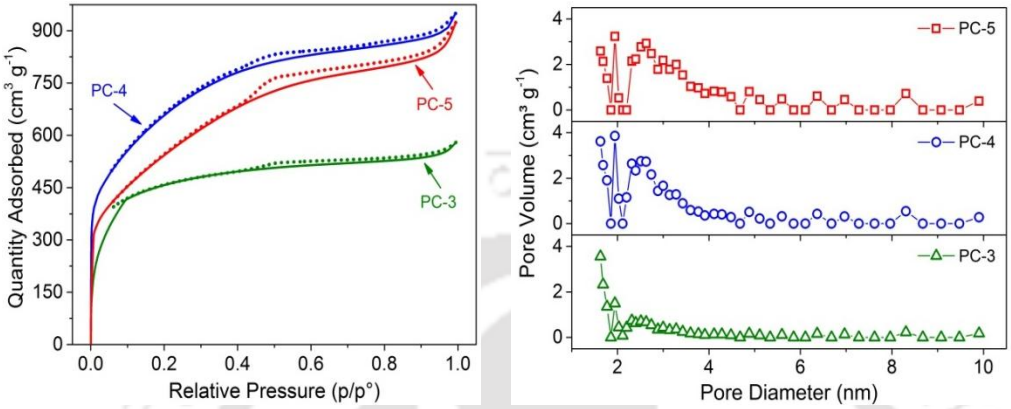


**(a)** **(b)**

**Figure 5.4** (a) $N_2$ adsorption-desorption isotherms, and (b) pore size distribution (PSD) curves of the PC-*x* samples.

**Table 5.2** Porosity parameters of PC-*x* samples

| Sample | $S_{BET}$ ($m^2\ g^{-1}$) | $V_t$ ($cm^3\ g^{-1}$) | $V_{mic}$ ($cm^3\ g^{-1}$) | $V_{meso}$ ($cm^3\ g^{-1}$) | $L = V_{meso}/V_{mic}$ | $D_A$ (nm) |
|---|---|---|---|---|---|---|
| PC-3 | 1439.22 | 0.73 | 0.43 | 0.30 | 0.70 | 2.4 |
| PC-4 | 2297.68 | 1.24 | 0.51 | 0.73 | 1.43 | 2.5 |
| PC-5 | 1949.53 | 1.18 | 0.42 | 0.76 | 1.80 | 2.9 |

$S_{BET}$ - BET surface area; $V_t$ - total pore volume; $V_{mic}$ - micropore volume; $V_{meso}$ -mesopore volume; *L*-ratio of mesopore/micropore volume; $D_A$ - average pore diameter

To examine the porosity parameters of the synthesized PC-*x* samples, the $N_2$ adsorption-desorption measurements were performed. As shown in **Figure 5.4a**, the $N_2$ adsorption-desorption isotherms of the PC-*x* samples exhibit combined characteristics of both type I and IV isotherms. The rapid $N_2$ uptake at low relative pressure ($P/P_0 < 0.1$) and the almost horizontal nature of the adsorption curve at high relative pressure indicate the presence of micropores (pore size < 2 nm) in the PC-*x*

samples [28,29]. H4 type hysteresis loops were observed between $0.4 < P/P_0 < 0.95$ for PC-3, and $0.3 < P/P_0 < 0.95$ for PC-4 and PC-5 samples, which further reveals the existence of mesopores.[30–32] The presence of micropores in PC-*x* could provide a large surface area for charge separation, while the mesopores could act as rapid charge transport pathways and charge assimilation reservoirs.[33,34] The detailed textural properties of the PC-*x* samples are illustrated in **Table 5.2**. The BET specific surface areas of PC-3, PC-4, and PC-5 were found to be 1439, 2297, and 1950 $m^2 g^{-1}$, respectively. **Figure 5.4b** shows the pore size distribution (PSD) curves of PC-*x* samples obtained using the non-local density functional theory (NL-DFT) method. The PSD curves indicate the presence of micropores and mesopores of 1.6 - 1.94 nm and 2 - 10 nm sizes, respectively (**Figure 5.4b**). Total pore volumes of PC-3, PC-4, and PC-5 were 0.73, 1.24, and 1.18 $cm^3 g^{-1}$, respectively, with corresponding micropore volumes of 0.43, 0.51, and 0.42 $cm^3 g^{-1}$ (**Table 5.2**). An increasing trend was observed for both mesopore volume and average pore diameter for PC-*x* when the KOH/biochar ratio (*x*) was gradually increased (**Table 5.2**). The corresponding increase in mesopore volume is evident from the rise in the peak of the PSD curve at ~2.5 nm. Seemingly the BET specific surface area and the total pore volume of PC-*x* increase with *x* increasing from 3 to 4, which could be attributed to the development of hierarchical porous structure constituting micro and mesopores. However, a further rise in KOH content (i.e. $x = 5$) resulted in a reduced micropore volume, and consequently the total pore volume and the BET specific surface area of PC-5 were lower than PC-4. Thus, the optimal amount of KOH was found to be 4× the amount of biochar that resulted in the highest specific surface area. Notably, PC-*x* samples possess high surface area, despite being activated in relatively large quantities (20 g), and at low activation temperature (700 °C) in a large reactor. Additionally, these PC-*x*

are rich in oxygen functionalities besides having large surface areas. Combining all these features of large surface area, favorable micro/mesopore distribution, and heteroatom doping, the synthesized PC-*x* are expected to demonstrate a superior capacitive response.

### 5.3.2 Electrochemical Performance in 6 M KOH

To evaluate the electrochemical performances, symmetric SC cells (as shown in **Figure 5.5a**) were assembled using PC-*x* electrodes and cellulose separators soaked in 6 M KOH electrolyte and termed as PC-*x*-SC. The electrode mass loadings were ~ 10 mg $cm^{-2}$ to commensurate with commercial SC electrodes. The capacitive responses of the PC-*x*-SC were first reordered using CV at voltage scan rates of 5 - 100 mV $s^{-1}$. **Figure 5.5b** depicts the CV curves of the PC-*x*-SCs over the potential widow of 0 - 1 V at 20 mV $s^{-1}$. The quasi-rectangular CV curves indicate excellent capacitive behavior and predominant double-layer characteristics. However, the CV curve of PC-3 shows a small deviation from the rectangular shape, which could be attributed to the high content of oxygen present in the sample contributing pseudocapacitance. The PC-4-SC demonstrated superior capacitive response as compared to PC-3-SC and PC-5-SC and it is evident from the highest area under the CV curve in Figure 5b. The better capacitive response of the PC-4 could be attributed to its exceptionally high surface area (2297.45 $m^2$ $g^{-1}$) and optimal heteroatom (O and N) doping. The large surface area of PC-4 enables higher ion adsorption for double-layer capacitance and the heteroatoms contribute pseudocapacitance as well as improve the wettability of the electrodes. At higher scan rates, the CV curves of the PC-*x*-SCs (**Figure 5.5c-e**) slightly deviate from the ideal rectangular shape, which could be attributed to the insufficient time for diffusion of electrolyte ions to the inner pores of electrode material.[35]

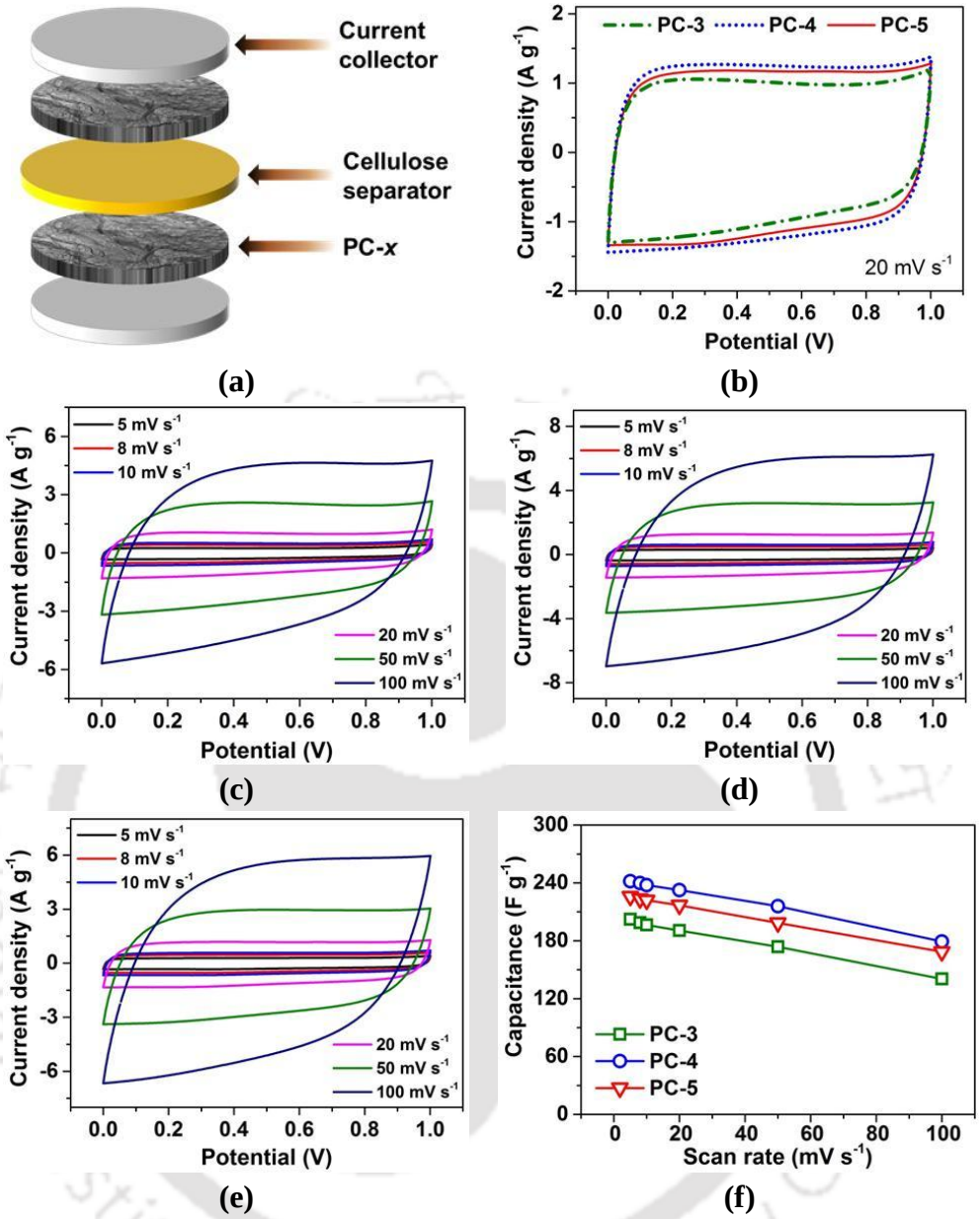


**Figure 5.5** Electrochemical performance of PC-*x*-SCs in 6 M KOH electrolyte: (a) schematic of symmetric supercapacitors, (b) CV curves of PC-*x*-SCs at 20 mV $s^{-1}$; CV curves of (c) PC-3-SC, (d) PC-4-SC, and (e) PC-5-SC at different scan rates; (f) specific capacitances of PC-*x* electrodes at different scan rates

At 100 mV $s^{-1}$, the distortion of CV curves was relatively high confirming the diffusion-limited behavior of the charge storage process.[36] Considering the high mass loading of the PC-*x* electrodes, the distortion of CV curves at high scan rates is not

very significant. Therefore, it could be assumed that the well-distributed pore channels inside the PC-*x* electrodes serve as efficient charge transfer pathways resulting in faster ion transport kinetics. At a scan rate of 5 mV $s^{-1}$, the specific capacitances of the PC-3, PC-4, and PC-5 electrodes were calculated as 241.8, 202.2, and 225.9 F $g^{-1}$, respectively. The variation of capacitance with the change in scan rate is shown in **Figure 5.5f**. The decreasing capacitance trend corresponding to increased scan rates could be attributed to insufficient time for electrolyte ion diffusion, which limits the charge storage to the outer surface only.[35] However, at a high scan rate of 100 mV $s^{-1}$, the PC-3, PC-4, and PC-5 electrodes showed superb capacitance retention of 69.47, 74.15, and 74.62%, respectively.

The PC-*x*-SCs were also subjected to GCD measurements at different current densities (0.2 - 10 A $g^{-1}$). **Figure 5.6a** shows the GCD curves of the PC-*x*-SCs at a current density of 1 A $g^{-1}$. The longer discharge time for the PC-4-SC indicated its superior capacitance compared to the PC-3-SC and PC-5-SC. The GCD curves of the three PC-*x*-SCs (**Figure 5.6b-d**) were of linear and triangular symmetric shape that displays superior capacitive behavior with a major contribution from double-layer charge storage. The gravimetric capacitance of PC-4 electrodes were found to be 251.6 F $g^{-1}$ at 0.2 A $g^{-1}$, which was 21.8% and 10.4% higher than the respective capacitances of PC-3 (206.5 F $g^{-1}$) and PC-5 (227.9 F $g^{-1}$) electrodes at similar conditions. The surface area of PC-4 and PC-5 were 60% and 35.4% higher than that of PC-3. However, the capacitances of PC-4 and PC-5 were only 21.8% and 10.3% higher compared to the capacitance of PC-3. This behavior can be explained by the higher pseudocapacitance contributed by the relatively larger number of oxygen functionalities of PC-3 (C/O = 2.5) as compared to PC-4 (C/O = 3.05) and PC-5 (C/O = 3.13).

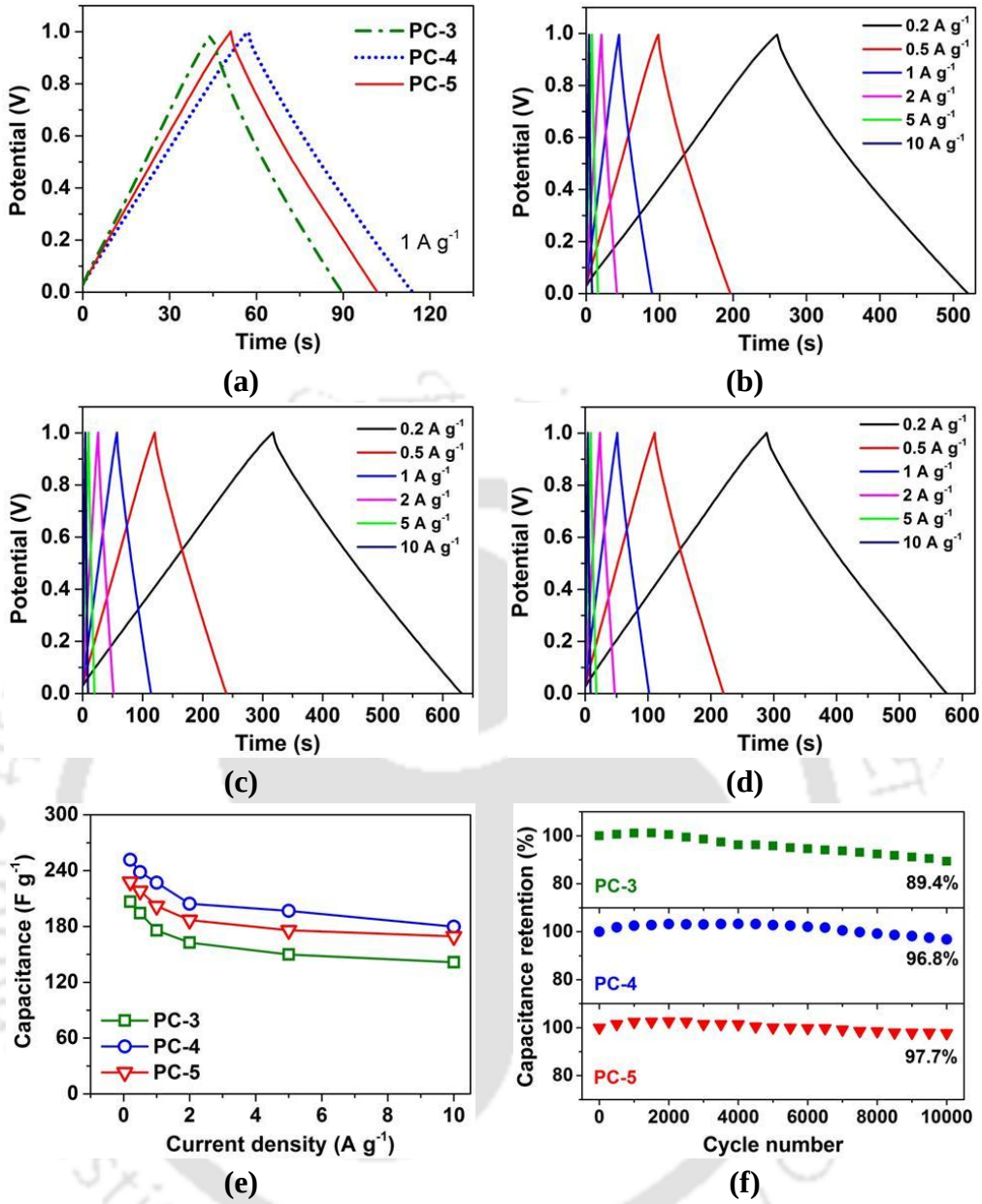


**Figure 5.6** Electrochemical performance of PC-*x*-SCs in 6 M KOH electrolyte: (a) GCD curves of PC-*x*-SCs at 1 A $g^{-1}$; GCD curves of (b) PC-3-SC, (c) PC-4-SC, and (d) PC-5-SC at different current densities; (e) specific capacitances of PC-*x* electrodes at different current densities, (f) cycle stability of PC-*x*-SCs

The capacitances of PC-*x*-SCs decreased with increasing current densities, and the same is visible from the shorter periods for charge-discharge in GCD curves (**Figures 5.6b-d**) at higher current densities. This decreasing capacitance trend could be

attributed to insufficient time for ion diffusion during charge storage and hindered ion propagation during the delivery due to the resistance devising from the interaction of the functional groups attached to carbon (or dangling bonds) and the electrolyte.[37] **Figure 5.6e** depicts the capacitance variation of PC-*x* electrodes with current densities. The PC-5 electrodes showed the best rate capability among all and retained about 74.29% (169.30 F $g^{-1}$) capacitance with an increase in current density from 0.2 to 10 A $g^{-1}$. Whereas, the PC-4 (179.73 F $g^{-1}$) and PC-3 (141.52 F $g^{-1}$) electrodes exhibited capacitance retention of 71.43% and 65.61%, respectively at 10 A $g^{-1}$ (**Figure 5.6e**). The lower rate capability of the PC-3 electrodes could be credited to its low mesopore/micropore volume ($L$ = 0.7) and relatively high content of surface oxygen groups, which leads to sluggish kinetics of charge storage at high current densities. The mesopore/micropore volume of PC-4 ($L$ = 1.43) is lower than PC-5 ($L$ = 1.80), and oxygen-containing groups in PC-4 are marginally higher than PC-5. Therefore, PC-4 electrodes showed slightly reduced rate capability as compared to PC-5 electrodes. Rise in rate capability with an increase in mesopore/micropore volume could be attributed to the fact that mesopores act as ion reservoirs during charge storage and reduce the ion diffusion length to facilitate rapid charge transport at high current densities. The large surface, optimal oxygen and nitrogen functionalities along the favorable micro/mesoporous structure of the PC-4 resulted in its high capacitive performance by balancing the contribution from double-layer capacitance and pseudocapacitance. The IR drop (voltage drop) values for the PC-*x*-SCs were obtained from the GCD curves. At the current density of 0.2 A $g^{-1}$, the IR drop values for the PC-3-SC, PC-4-SC, and PC-5-SC were 0.051, 0.036, and 0.030 V, respectively. The IR drop values increased to 0.11, 0.087, and 0.082 V, respectively for the PC-3-SC, PC-4-SC, and PC-5-SC when the current density was increased to

10 A $g^{-1}$. The low IR drop values of the SCs suggest rapid charge transport at the electrode-electrolyte interface and very insignificant capacitance loss due to internal resistance originating from the electrode-current collector interface.[22] Furthermore, the high Columbic efficiencies ($\eta = \frac{\Delta t_d}{\Delta t_c} \times 100\%$; where $\Delta t_c$ and $\Delta t_d$ are the charge time and discharge time, respectively) of ~ 99.10, 99.34, and 99.55% (average values), respectively for PC-3-SC, PC-4-SC, and PC-5-SC indicate the excellent charge and discharge reversibility of the devices. The specific capacitance values obtained for the PC-4 electrodes are at par with the supercapacitors fabricated using carbon derived from individual biomass, as evident from previous literature summarized in **Table A4.2** (**Appendix 4**). Although many studies in the literature have reported very high specific capacitance values, these have been restricted by low electrode mass loadings (< 5 mg $cm^{-2}$). The low active mass loadings result in poor actual capacity (due to the low mass ratio of active material to cell components) restricting their practical utility in commercial energy storage devices. Typically, high active mass loading of 10 mg $cm^{-2}$ or higher should be used considering commercial/practical applications.[38] Nevertheless, at high active mass loadings, capacitance, as well as the rate capability of electrode materials, decreases drastically due to a reduction in electro-active sites due to severe pore blockage.[38] Remarkably, the capacitive performance of PC-*x* with commercial level mass loadings was superior compared to that of the previous carbon-based materials with high mass loadings as shown in **Table A4.3** (**Appendix 4**). The well-designed pore structure with optimal mesopore/micropore volume of the synthesized PC-*x* enabled efficient charge transportation inside the electrode, and therefore, high capacitance values were obtained at high electrode mass loadings. Additionally, the comparative evaluation of the supercapacitor properties revealed that mixing of different biomass during the

synthesis of porous carbon precursor does not compromise the properties of a supercapacitor. This result is important as it clearly reveals the flexibility of synthesis in terms of the raw materials and paves way for scalable production of mixed biomass-based carbon materials.

The cycle stability of SCs is an essential parameter that indicates the capacitance retention ability of the active materials over prolonged charge-discharge cycles. The cyclic performances of the PC-*x*-SCs (in 6 M KOH electrolyte) were evaluated over 10000 GCD cycles at 5 A $g^{-1}$. After 10000 continuous charge-discharge cycles, PC-3-SC, PC-4-SC, and PC-5-SC retained about 89.4, 96.8, and 97.7% of their initial capacitance, respectively (**Figure 5.6f**). These results indicated the high cycle stability of the fabricated PC-*x*-SCs using KOH electrolyte. Relatively lower capacitance retention of PC-3-SC could be attributed to the fact that more oxygen-containing functional groups were contributing to the charge storage process of PC-3 via pseudocapacitance, which faded over the repetitive charge-discharge cycles. It was also observed that the specific capacitances of the PC-*x*-SCs gradually increased in the initial GCD cycles, which could be attributed to the process of self-activation.[22] The electrolyte ions could not use the pore structure of the high mass loading PC-*x* electrodes at the beginning of the cycle stability tests. As the charge-discharge process progresses, the electrolyte ions can infiltrate deeper into the pore-structure of the electrode material, which increases the electrochemically active area. Consequently, the additional charge can be stored, and the capacitance increases which is referred to as the self-activation process.

The impedance features of the PC-*x*-SCs were studied using EIS in the range of $10^5$ - 0.1 Hz with a signal of 10 mV $s^{-1}$. The Nyquist plots of the PC-*x*-SCs obtained from EIS measurements are depicted in **Figure A4.3a** (**Appendix 4**). A

series resistance ($R_s$), representing the combination of ionic resistance of electrolyte and any resistances of cell components can be obtained from the intercept of EIS spectra in the real $Z^{/}$ axis (at high frequency).[39] Afterward, the impedance spectra of the PC-*x*-SCs display a circular arc and a straight line (at the low-frequency), exhibiting an ideal supercapacitive response. The semi-circle relates to the charge transfer resistance ($R_{ct}$) during the charge transport process.[39,40] The $R_s$ values for the PC-*x*-SCs were 0.27 - 0.31 Ω before cycle stability tests, which indicated high ionic conductivity of the electrolyte and low intrinsic resistance. The $R_{ct}$ values were obtained using the equivalent circuit shown in inset of **Figure A4.3a** (**Appendix 4**). The $R_{ct}$ values for PC-3-SC, PC-4-SC, and PC-5-SC before stability tests were 0.93, 0.76, and 0.89 Ω, respectively. After 10000 GCD cycles, the $R_s$ values (0.26 - 0.30 Ω) did not change much whereas the $R_{ct}$ values were reduced to 0.61, 0.54, and 0.62 Ω, respectively for PC-3-SC, PC-4-SC, and PC-5-SC. Low $R_s$ and $R_{ct}$ values are indicative of fast charge transfer kinetics and excellent electrochemical stability of PC-*x* electrodes over repetitive charge-discharge tests. Moreover, the impedance spectra of the PC-4-SC and PC-5-SC in the low-frequency region were more vertical than those of the PC-3-SC demonstrating relatively low diffusion resistance that facilitates better charge transfer dynamics inside the porous electrodes.[41] Conversely, the PC-3-SC exhibits slightly higher diffusion resistance in the high-frequency region owing to relatively more surface oxygen groups participating in the charge storage. The EIS results further support the better rate capability of the PC-4-SC and PC-5-SC resulting from efficient and rapid ion transportation.

The PC-4-SC revealed the highest energy density of 8.74 W h $kg^{-1}$ (at a power density of 100 W $kg^{-1}$), which is 1.22× and 1.1× the energy density of PC-3-SC (7.17 W h $kg^{-1}$), and PC-5-SC (7.91 W h $kg^{-1}$) at the same power density (**Figure A4.3b**,

**Appendix 4**). This high energy density of the PC-4-SC could be correlated to the large surface area of PC-4 enabling the storage of a large amount of charge and pseudocapacitive contribution from heteroatom doping. At a high power density of 5000 W $kg^{-1}$, the PC-4-SC could still deliver 6.24 W h $kg^{-1}$ of energy density. Additionally, the PC-3-SC and PC-4-SC exhibited energy densities of 4.71 and 5.88 W h $kg^{-1}$, respectively at 5000 W $kg^{-1}$. These high energy densities at high power densities suggest efficient and rapid charge delivery of the PC-*x*-SCs due to the presence of favorable pore networks. **Figure A4.3b** (**Appendix 4**) depicts the comparison of energy and power densities of PC-*x*-SCs in a Ragone plot. Moreover, the inset in **Figure A4.3b** (**Appendix 4**) shows a red LED powered by two PC-*x*-SC cells.

### 5.3.3 Electrochemical Performance in 1 M $Li_2SO_4$ Electrolyte

The energy density of SCs can be greatly enhanced by widening the cell voltage. Neutral aqueous electrolytes have shown high electrochemical stability and could operate beyond the decomposition potential of water (1.23 V) due to their ability to suppress gas evolution reactions.[42] Among these neutral aqueous electrolytes, $Li_2SO_4$ has demonstrated excellent electrochemical stability at wide operating voltages (~2 V).[43] Therefore, we tested the PC-4-SC using 1 M $Li_2SO_4$ as the electrolyte in different potential windows (1 - 2 V), and the results are presented in **Figure 5.7a**. The CV curves of the device retained their quasi rectangular shapes even at 2 V. This indicates a high working potential window of 2 V for the symmetric device in $Li_2SO_4$ electrolyte. **Figure 5.7b** shows the CV curves of PC-4-SC at scan rates of 5 - 100 mV $s^{-1}$. At high scan rates, the small deviation of CV curves from the quasi-rectangular shape showed the stability and efficient charge transport behavior of the PC-4

electrodes at a high operating voltage of 2 V. The specific capacitances of PC-4 at different scan rates are shown in **Figure 5.7c**.

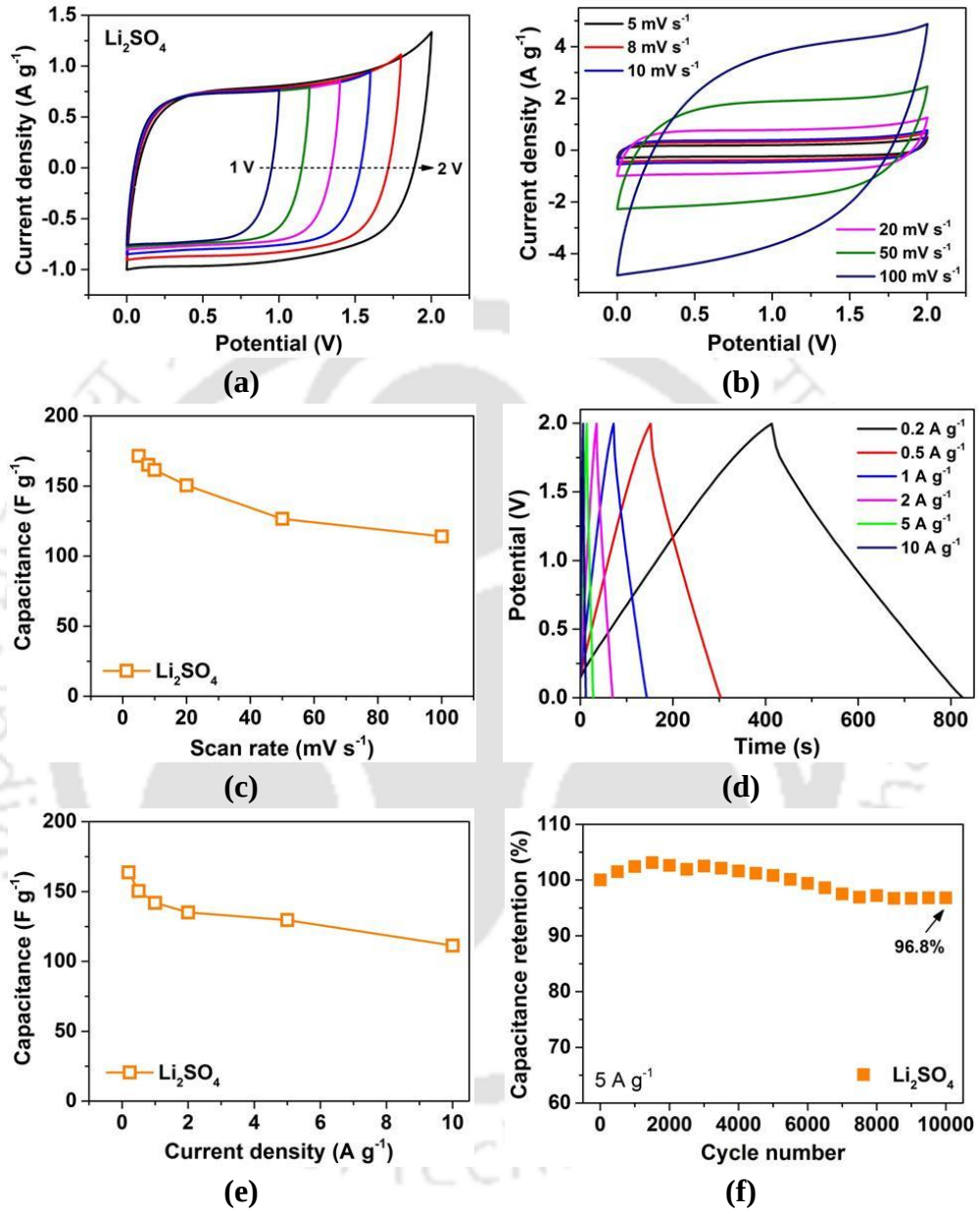


**Figure 5.7** Electrochemical performance of PC-4-SC in 1 M $Li_2SO_4$: (a) CV curves of the SC at different potential windows; (b) CV of the SC curves at different scan rates; (c) specific capacitances of PC-4 electrodes at different scan rates; (d) GCD curves of the SC at different current densities; (e) specific capacitances of PC-4 electrodes at different current densities; (f) long-term cycle stability of the SC.

In $Li_2SO_4$ electrolyte, the PC-4 electrodes exhibited a specific capacitance of 171.5 F $g^{-1}$ at 5 mV $s^{-1}$, which reduced to 114 F $g^{-1}$ (66.5%) at 100 mV $s^{-1}$. The symmetric and linear GCD curves (at 0.2 - 20 A $g^{-1}$) of the PC-4-SC suggest a superior capacitive response of the device in the neutral $Li_2SO_4$ electrolyte (**Figure 5.7d** and **Figure A4.4a**, **Appendix 4**). The gravimetric specific capacitance of the PC-4 electrodes was calculated to be 163.8 F $g^{-1}$ at 0.2 A $g^{-1}$ (**Figure 5.7e**). As the current density of the device was gradually increased to 20 A $g^{-1}$, the capacitance of PC-4 electrodes reduced to 108.5 F $g^{-1}$ (66.25% of capacitance at 0.2 A $g^{-1}$). This high rate capability could be attributed to the rapid charge transfer inside the electrodes. The IR drop of the device increases from 0.082 to 0.183 V with the corresponding increase in current density from 0.2 to 20 A $g^{-1}$. An excellent Coulombic efficiency of ~ 99.42% (average value) demonstrates the high charge and discharge reversibility of the PC-4-SC in $Li_2SO_4$ electrolyte. Moreover, the neutral SC demonstrated excellent cycle stability with 96.8% capacitance retention over 10000 cycles at 5 A $g^{-1}$ (**Figure 5.7f**). The Nyquist plots (**Figure A4.5**, **Appendix 4**) also indicated superb capacitive behavior of the device along with low resistance. $R_s$ value increased from 0.86 to 1 Ω and the $R_{ct}$ value increased from 0.97 to 0.98 Ω at the end of cyclic stability tests. This increase in resistances could be ascribed to the degradation of active material. The PC-4-SC in $Li_2SO_4$ electrolyte delivered a superb energy density of 22.75 W h $kg^{-1}$ (at 200 W $kg^{-1}$), which is considerably higher than the energy density of the device in KOH electrolyte (8.74 W h $kg^{-1}$ at 100 W $kg^{-1}$). The Ragone plot in **Figure 5.8a** illustrates that the energy density values of the neutral PC-4-SC are superior to many of the earlier reports on carbon-based supercapacitors.[44–52] At a high power density of 10000 W $kg^{-1}$, PC-4-SC delivered a noticeable energy density of 15.62 W h $kg^{-1}$. The use of $Li_2SO_4$ as the electrolyte extended the cell voltage up to 2 V in contrast to 1 V with

KOH as electrolyte. By virtue of this wide potential window, the energy density of the device was augmented by multiple folds. The applicability of the fabricated 2 V device was practically demonstrated by powering a red LED for more than 8 minutes (schematic and photograph shown in **Figure 5.8b**).

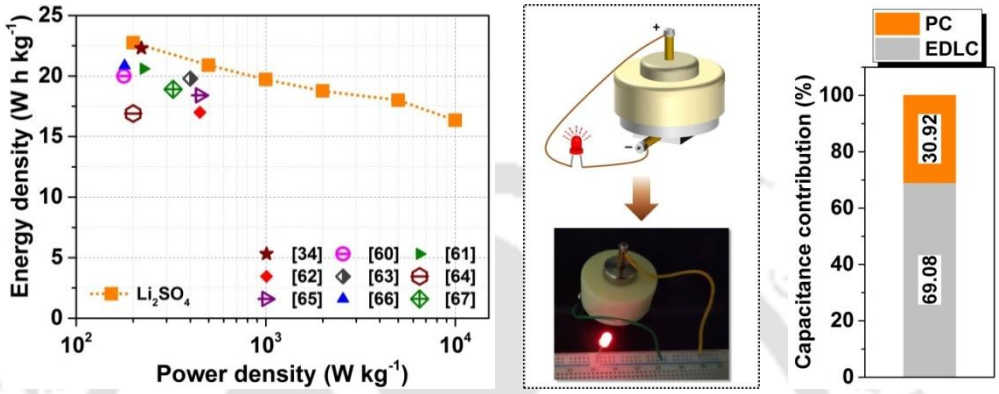


**Figure 5.8** (a) Ragone plot of PC-4-SC in 1 M $Li_2SO_4$ and comparison with carbon-based SCs in literature; (b) schematic and a digital photograph of a LED powered by PC-4-SC in 1 M $Li_2SO_4$; (c) percentage of the capacitance contribution evaluated for PC-4 in $Li_2SO_4$ electrolyte based on Trasatti's method.

It is essential to comprehend the capacitive behavior of PC-4 as it is expected to demonstrate both double-layer capacitance and pseudocapacitance. The double-layer capacitance would be contributed from the carbon matrices whereas the pseudocapacitance originates from the heteroatom (O and N) containing surface functionalities. Therefore, the capacitive contributions from surface-controlled processes (electrical double layer formation) and diffusion-controlled processes (pseudo-capacitive reactions) for the PC-4-SC were investigated using the Trasatti method.[53,54] The Trasatti's method has been already described in **Chapter 2**. The plots $\frac{1}{C(\lambda)}$ versus $\lambda^{1/2}$ and $C(\lambda)$ versus $\lambda^{-1/2}$ (where, C is the capacitance and λ is the

scene voltage scan rate) are shown in **Figures 4.6a-b** (**Appendix 4**), respectively, and capacitance contributions for the PC-4-SC were calculated from these plots. As shown in **Figure 4.8c**, the double layer charge storage contributes 69.08% of the total capacitance of the device whereas the pseudocapacitance (PC) accounts for 30.92%.

The superior capacitive performance of the PC-4 can be attributed to the following facets: (i) heteroatom (oxygen and nitrogen) doping in PC-4, which contributes pseudocapacitance and improves the wettability of the electrodes, and (ii) large surface area and hierarchical pore structure of PC-4 with optimal micro- and mesopore distribution that facilitates rapid and efficient ion diffusion.

### 5.3.4 Electrochemical Performance in Redox-Mediated/Active electrolyte

The use of redox additives can augment the performance of the SCs with additional faradaic charge storage via redox reactions. In redox-enhanced SCs, the dead weight of the electrolyte is effectively used to host redox couples, and the pores of electrodes act as reservoirs for redox couples.[55] For augmenting the energy density of the neutral aqueous PC-4-SC, $Na_2MoO_4$ (0.1 M) was used as the redox additive in the 1 M $Li_2SO_4$ electrolyte. The capacitive performance of the PC-4-SC was investigated in the novel redox-mediated/active electrolyte (0.1 $Na_2MoO_4$ + 1 M $Li_2SO_4$) and the results are presented in **Figure 5.9**. As shown in **Figure A4.7** (**Appendix 4**), the redox-enhanced device could also operate in the high potential window of 2 V. The CV curves of the PC-4-SC in both $Li_2SO_4$ and redox-active electrolyte are compared at a scan rate of 20 mV $s^{-1}$ (**Figure 5.9a**). The larger CV area for the device in redox-mediated electrolyte indicated the enhancement in the capacitive response due to the addition of $Na_2MoO_4$.

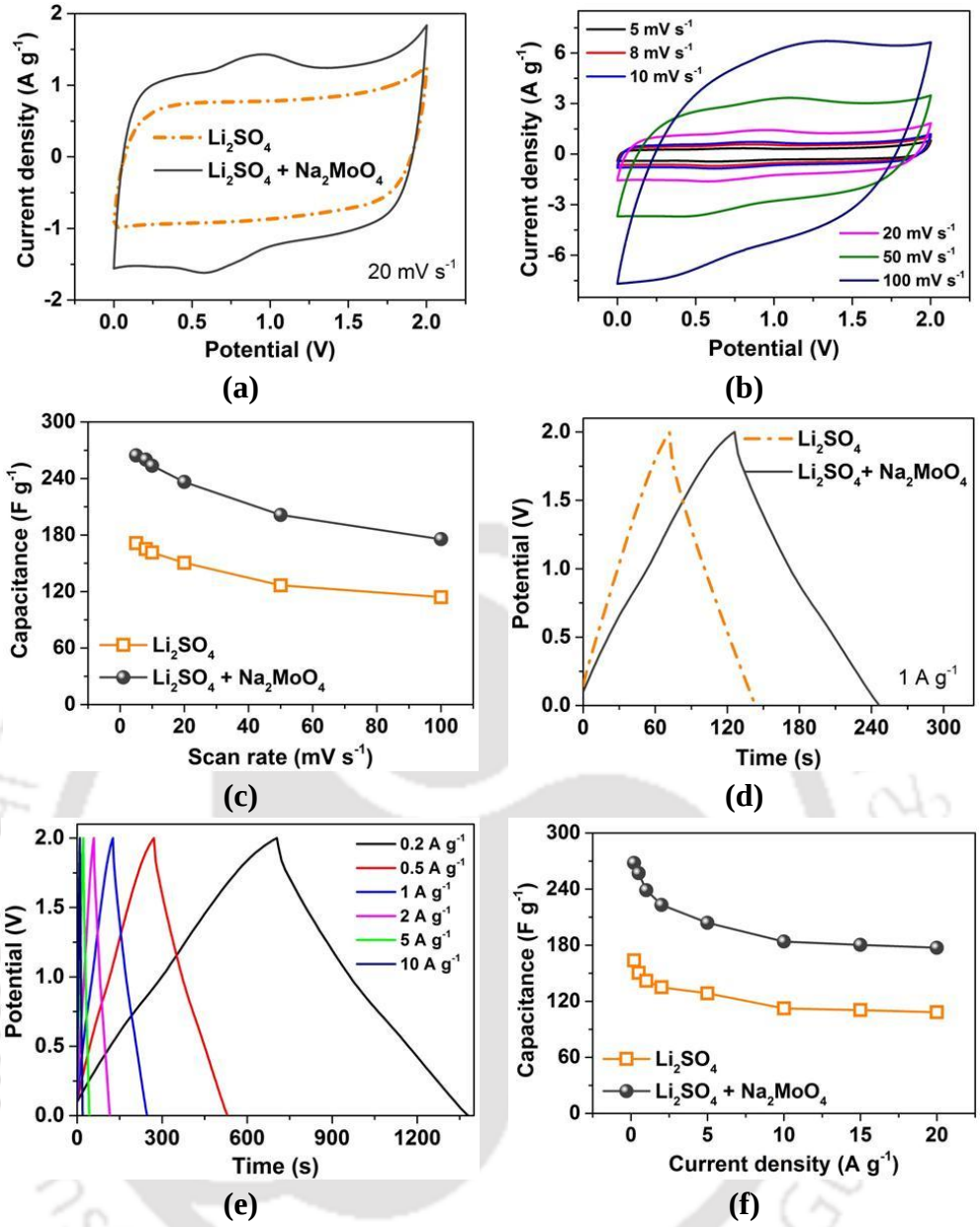


**Figure 5.9** Electrochemical performance of PC-4-SC in the redox-mediated electrolyte (0.1 $Na_2MoO_4$ + 1 M $Li_2SO_4$): (a) comparison of CV curves of the SC in redox and $Li_2SO_4$ electrolyte; (b) CV curves at different scan rates; (c) specific capacitances of PC-4 electrodes at different scan rates (comparison with $Li_2SO_4$); (d) comparison of GCD curves of the SC in redox and $Li_2SO_4$ electrolyte; (e) GCD curves of the SC at different current densities; (f) specific capacitances of PC-4 electrodes at different current densities (comparison with $Li_2SO_4$).

A pair of redox peaks appeared in the redox-active electrolyte, which could be attributed to the reactions of $MoO_4^{2-}$ ions:[56]

$$MoO_4^{2-} + 8H^+ + 6e^- \longleftrightarrow Mo + 4H_2O \quad \text{(R5.1)}$$

However, at the positive electrode oxidation of water can occur (at high cell voltages), which reduces the local pH. As a result, the $MoO_4^{2-}$ could also transform into $HMoO_4^-$ (at pH < 6) and ultimately form $MoO_3$.[56] Essentially, the appearance of the redox peaks, as well as the increase in anodic peak, revealed the contribution from pseudocapacitance along with the double-layer capacitance. **Figure 5.9b** shows the CV curves (at 5-100 mV $s^{-1}$) of the PC-4-SC in the redox-mediated electrolyte. The CV curves of the device retained a similar shape at higher scan rates but the redox peaks were relatively low at 100 mV $s^{-1}$, suggesting the relatively slow redox kinetics. The PC-4 electrodes exhibited high capacitance of 264.5 F $g^{-1}$ at 5 mV $s^{-1}$ in the redox-active electrolyte, which is 1.54× higher than the capacitance in $Li_2SO_4$ electrolyte (**Figure 5.9c**). In the redox-active electrolyte, the PC-4 electrodes retained 66.38% (175.6 F $g^{-1}$) of its capacitance at 100 mV $s^{-1}$. The enhancement in the capacitance due to the redox mediator ($Na_2MoO_4$) is also evident from the comparison of GCD curves (at 1 A $g^{-1}$) of the PC-4-SC in $Li_2SO_4$ and redox-mediated electrolyte (**Figure 5.9d**). The GCD curves of the PC-4-SC in redox electrolyte (**Figure 5.9e** and **Figure A4.4b**, **Appendix 4**) were quasi-linear and also show influence of redox behavior. In the redox-mediated electrolyte, the PC-4 electrodes displayed a remarkable capacitance of 268.1 F $g^{-1}$ at 0.2 A $g^{-1}$, which is 1.63× the capacitance in $Li_2SO_4$ electrolyte (**Figure 5.9f**). The electrodes could retain 66.16% (177.4 F $g^{-1}$) of their initial capacitance at 20 A $g^{-1}$ in the redox-mediated electrolyte. The high rate capability in the redox-active electrolyte could be attributed to the efficient pore structure (having abundant micro- and mesopores) of PC-4. The mesopores of PC-4 serve as the reservoirs for electrolyte and redox species, which could reduce the length of ion diffusion inside the micropores and augment the charge storage capacity.

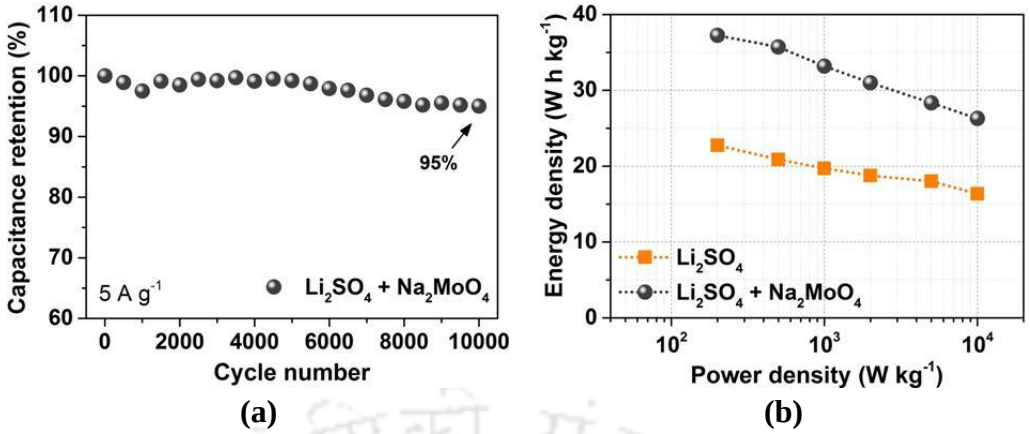


**Figure 5.10** (a) Long-term cycle stability and (b) Ragone plot (comparison with $Li_2SO_4$) of the PC-4-SC in the redox-mediated electrolyte (0.1 $Na_2MoO_4$ + 1 M $Li_2SO_4$)

It was observed that the IR drop (0.09 - 0.185 V at 0.2 - 20 A $g^{-1}$) of the PC-4-SC in the redox-active electrolyte was comparable to that in the $Li_2SO_4$ electrolyte. The Coulombic efficiency of the redox-enhanced PC-4-SC was 96.84% (average value), which is slightly lower than that of the device in $Li_2SO_4$ electrolyte. The redox-enhanced PC-4-SC demonstrated superb cycle stability with 95.1% capacitance retention over 10000 cycles at 5 A $g^{-1}$ (**Figure 5.10a**). This indicated that the stability of the device was not affected due to the addition of redox additive. The redox-enhanced PC-4-SC exhibited significantly improved energy density due to the redox reactions originating from the redox-active electrolyte (**Figure 5.10b**). The redox-enhanced device delivered a markedly high energy density of 37.24 W h $kg^{-1}$ (at 200 W $kg^{-1}$), which was 1.64× higher compared to the energy density of the device with neat $Li_2SO_4$ (22.75 W h $kg^{-1}$) at similar conditions. Remarkably, the energy density of the redox-enhanced SC was as high as 25.55 W h $kg^{-1}$ at the high power density of 10000 W $kg^{-1}$. The Nyquist plots did not show any significant change in the impedance behavior of the device after adding $Na_2MoO_4$ in the $Li_2SO_4$ (**Figure A4.5**,

**Appendix 4**). The charge transfer resistance of the device increased marginally after cycle stability tests. These results indicate synergistic interactions of the redox-active electrolyte and the highly porous PC-4 electrodes, which boosted the energy density the device through efficient charge transportation as well as reversible and quick surface redox reactions.

## 5.4 CONCLUSIONS

In summary, we have demonstrated a scalable preparation of high surface area oxygen rich porous carbon (PC-*x*) from biomass blends via co-pyrolysis, and facile low-temperature activation. The oxygen functionalities were achieved via self-doping at a low activation temperature of 700 °C without any additional reagents. The optimized PC-4 possessed a surface area of 2297 $m^2 g^{-1}$, pore volume of 1.23 $cm^3 g^{-1}$, micro/mesopore distribution, and surface oxygen functional groups. In KOH electrolyte, the PC-4 demonstrated capacitance of 251.6 F $g^{-1}$ (at 0.2 A $g^{-1}$) and excellent cycle stability at commercial-level electrode mass loading of ~10 mg $cm^{-2}$. The PC-4 based symmetric SC achieved a high cell voltage of 2 V in $Li_2SO_4$ electrolyte and delivered an energy density of 22.75 W h $kg^{-1}$ (at 200 W h $kg^{-1}$). Moreover, the device showed high capacitance retention of 96.8% over 10000 GCD cycles at 5 A $g^{-1}$. Using a redox-mediated electrolyte ($Na_2MoO_4$ + $Li_2SO_4$), the energy density of the device was enhanced to 37.24 W h $kg^{-1}$, which was 1.64× and 4.3× higher than the energy density in $Li_2SO_4$ and KOH. The supercapacitor fabrication route demonstrated in this study is sustainable as it is based on carbon derived from renewable source of biomass. Secondly, the performance of the supercapacitor fabricated with biomass blend-derived carbon is at par with those fabricated with single biomass-derived carbon. This feature has important implications from

viewpoint of large-scale manufacture of biomass-based energy storage devices, as it offers the flexibility in terms of raw materials (or feedstocks).

## REFERENCES


(1) Jiang, G.; Senthil, R. A.; Sun, Y.; Kumar, T. R.; Pan, J. Recent Progress on Porous Carbon and Its Derivatives from Plants as Advanced Electrode Materials for Supercapacitors. *J. Power Sources* **2022**, *520*, 230886.

(2) Xie, L.; Sun, G.; Su, F.; Guo, X.; Kong, Q.; Li, X.; Huang, X.; Wan, L.; song, W.; Li, K.; Lv, C.; Chen, C.-M. Hierarchical Porous Carbon Microtubes Derived from Willow Catkins for Supercapacitor Applications. *J. Mater. Chem. A* **2016**, *4* (5), 1637–1646.

(3) Teo, E. Y. L.; Muniandy, L.; Ng, E. P.; Adam, F.; Mohamed, A. R.; Jose, R.; Chong, K. F. High Surface Area Activated Carbon from Rice Husk as a High Performance Supercapacitor Electrode. *Electrochim. Acta* **2016**, *192*, 110–119.

(4) Wan, L.; Xiao, R.; Liu, J.; Zhang, Y.; Chen, J.; Du, C.; Xie, M. A Novel Strategy to Prepare N, S-Codoped Porous Carbons Derived from Barley with High Surface Area for Supercapacitors. *Appl. Surf. Sci.* **2020**, *518*, 146265.

(5) Vijayakumar, M.; Santhosh, R.; Adduru, J.; Rao, T. N.; Karthik, M. Activated Carbon Fibres as High Performance Supercapacitor Electrodes with Commercial Level Mass Loading. *Carbon N. Y.* **2018**, *140*, 465–476.

(6) He, J.; Zhang, D.; Wang, Y.; Zhang, J.; Yang, B.; Shi, H.; Wang, K.; Wang, Y. Biomass-Derived Porous Carbons with Tailored Graphitization Degree and Pore Size Distribution for Supercapacitors with Ultra-High Rate Capability. *Appl. Surf. Sci.* **2020**, *515*, 146020.

(7) Yang, I.; Jung, M.; Kim, M. S.; Choi, D.; Jung, J. C. Physical and Chemical Activation Mechanisms of Carbon Materials Based on the Microdomain Model. *J. Mater. Chem. A* **2021**, *9* (15), 9815–9825.

(8) Mallick, D.; Mahanta, P.; Moholkar, V. S. *Synergistic Effects in Gasification of Coal/Biomass Blends: Analysis and Review*; 2018.

(9) Ahmed, M. J.; Hameed, B. H. Insight into the Co-Pyrolysis of Different Blended Feedstocks to Biochar for the Adsorption of Organic and Inorganic Pollutants: A Review. *J. Clean. Prod.* **2020**, *265*, 121762.

(10) Yang, X.; Ng, W.; Wong, B. S. E.; Baeg, G. H.; Wang, C. H.; Ok, Y. S. Characterization and Ecotoxicological Investigation of Biochar Produced via Slow Pyrolysis: Effect of Feedstock Composition and Pyrolysis Conditions. *J. Hazard. Mater.* **2019**, *365*, 178–185.

(11) Muigai, H. H.; Choudhury, B. J.; Kalita, P.; Moholkar, V. S. Co–Pyrolysis of Biomass Blends: Characterization, Kinetic and Thermodynamic Analysis. *Biomass and Bioenergy* **2020**, *143*, 105839.

(12) Muigai, H. H.; Choudhury, B. J.; Kalita, P.; Moholkar, V. S. Physico–Chemical Characterization and Pyrolysis Kinetics of Eichhornia Crassipes, Thevetia Peruviana, and Saccharum Officinarum. *Fuel* **2021**, *289*, 119949.

(13) Teng, W.; Zhou, Q.; Wang, X.; Che, H.; Du, Y.; Hu, P.; Li, H.; Wang, J. Biotemplating Preparation of N,O-Codoped Hierarchically Porous Carbon for High-Performance Supercapacitors. *Appl. Surf. Sci.* **2021**, *566*, 150613.

(14) He, Y.; Zhang, Y.; Li, X.; Lv, Z.; Wang, X.; Liu, Z.; Huang, X. Capacitive Mechanism of Oxygen Functional Groups on Carbon Surface in Supercapacitors. *Electrochim. Acta* **2018**, *282*, 618–625.

(15) Aruchamy, K.; Dharmalingam, K.; Lee, C. W.; Mondal, D.; Sanna Kotrappanavar, N. Creating Ultrahigh Surface Area Functional Carbon from Biomass for High Performance Supercapacitor and Facile Removal of Emerging Pollutants. *Chem. Eng. J.* **2022**, *427*, 131477.

(16) Muigai, H. H.; Bordoloi, U.; Hussain, R.; Ravi, K.; Moholkar, V. S.; Kalita, P. A Comparative Study on Synthesis and Characterization of Biochars Derived from Lignocellulosic Biomass for Their Candidacy in Agronomy and Energy Applications. *Int. J. Energy Res.* **2021**, *45* (3), 4765–4781.

(17) Li, Z.; Bai, Z.; Mi, H.; Ji, C.; Gao, S.; Pang, H. Biowaste-Derived Porous Carbon with Tuned Microstructure for High-Energy Quasi-Solid-State Supercapacitors. *ACS Sustain. Chem. Eng.* **2019**, *7* (15), 13127–13135.

(18) Wang, J.; Kaskel, S. KOH Activation of Carbon-Based Materials for Energy Storage. *J. Mater. Chem.* **2012**, *22* (45), 23710–23725.

(19) Wang, X.; Yun, S.; Fang, W.; Zhang, C.; Liang, X.; Lei, Z.; Liu, Z. Layer-Stacking Activated Carbon Derived from Sunflower Stalk as Electrode Materials for High-Performance Supercapacitors. *ACS Sustain. Chem. Eng.* **2018**, *6* (9), 11397–11407.

(20) Guan, L.; Pan, L.; Peng, T.; Gao, C.; Zhao, W.; Yang, Z.; Hu, H.; Wu, M.

Synthesis of Biomass-Derived Nitrogen-Doped Porous Carbon Nanosheests for High-Performance Supercapacitors. *ACS Sustain. Chem. Eng.* **2019**, *7* (9), 8405–8412.

(21) Hu, W.; Huang, J.; Yu, P.; Zheng, M.; Xiao, Y.; Dong, H.; Liang, Y.; Hu, H.; Liu, Y. Hierarchically Porous Carbon Derived from Neolamarckia Cadamba for Electrochemical Capacitance and Hydrogen Storage. *ACS Sustain. Chem. Eng.* **2019**, *7* (18), 15385–15393.

(22) Chen, J.; Fang, K.; Chen, Q.; Xu, J.; Wong, C. P. Integrated Paper Electrodes Derived from Cotton Stalks for High-Performance Flexible Supercapacitors. *Nano Energy* **2018**, *53*, 337–344.

(23) Chen, J.; Xu, J.; Zhou, S.; Zhao, N.; Wong, C. P. Nitrogen-Doped Hierarchically Porous Carbon Foam: A Free-Standing Electrode and Mechanical Support for High-Performance Supercapacitors. *Nano Energy* **2016**, *25*, 193–202.

(24) Ayiania, M.; Smith, M.; Hensley, A. J. R.; Scudiero, L.; McEwen, J. S.; Garcia-Perez, M. Deconvoluting the XPS Spectra for Nitrogen-Doped Chars: An Analysis from First Principles. *Carbon N. Y.* **2020**, *162*, 528–544.

(25) Zhang, H.; Ling, Y.; Peng, Y.; Zhang, J.; Guan, S. Nitrogen-Doped Porous Carbon Materials Derived from Ionic Liquids as Electrode for Supercapacitor. *Inorg. Chem. Commun.* **2020**, *115*, 107856.

(26) Atika; Dutta, R. K. Oxygen-Rich Porous Activated Carbon from Eucalyptus Wood as an Efficient Supercapacitor Electrode. *Energy Technol.* **2021**, *9* (9), 2100463.

(27) Li, J.; Li, Y.; Wu, Y.; Zheng, M. A Comparison of Biochars from Lignin, Cellulose and Wood as the Sorbent to an Aromatic Pollutant. *J. Hazard. Mater.* **2014**, *280*, 450–457.

(28) Yao, B.; Chandrasekaran, S.; Zhang, J.; Xiao, W.; Qian, F.; Zhu, C.; Duoss, E. B.; Spadaccini, C. M.; Worsley, M. A.; Li, Y. Efficient 3D Printed Pseudocapacitive Electrodes with Ultrahigh MnO2 Loading. *Joule* **2019**, *3* (2), 459–470.

(29) Zhou, H.; Wu, S.; Wang, H.; Li, Y.; Liu, X.; Zhou, Y. The Preparation of Porous Carbon Materials Derived from Bio-Protic Ionic Liquid with Application in Flexible Solid-State Supercapacitors. *J. Hazard. Mater.* **2021**, *402*, 124023.

(30) Wang, H.; Zhou, H.; Wu, S.; Li, Z.; Fan, B.; Li, Y.; Zhou, Y. Facile Synthesis of N/B Co-Doped Hierarchically Porous Carbon Materials Based on Threonine Protic Ionic Liquids for Supercapacitor. *Electrochim. Acta* **2021**, *380*, 138230.

(31) Wu, D.; Ji, C.; Mi, H.; Guo, F.; Cui, H.; Qiu, P.; Yang, N. A Safe and Robust Dual-Network Hydrogel Electrolyte Coupled with Multi-Heteroatom Doped Carbon Nanosheets for Flexible Quasi-Solid-State Zinc Ion Hybrid Supercapacitors. *Nanoscale* **2021**, *13* (37), 15869–15881.

(32) Chen, X.; Chi, M.; Xing, L.; Xie, X.; Liu, S.; Liang, Y.; Zheng, M.; Hu, H.; Dong, H.; Liu, Y.; Jiang, S. P.; Xiao, Y. Natural Plant Template-Derived Cellular Framework Porous Carbon as a High-Rate and Long-Life Electrode Material for Energy Storage. *ACS Sustain. Chem. Eng.* **2019**, *7* (6), 5845–5855.

(33) Wang, C.; Zhou, Y.; Sun, L.; Zhao, Q.; Zhang, X.; Wan, P.; Qiu, J. N/P-Codoped Thermally Reduced Graphene for High-Performance Supercapacitor Applications. *J. Phys. Chem. C* **2013**, *117* (29), 14912–14919.

(34) Li, L.; Li, R.; Gai, S.; Gao, P.; He, F.; Zhang, M.; Chen, Y.; Yang, P. Hierarchical Porous CNTs@NCS@MnO 2 Composites: Rational Design and High Asymmetric Supercapacitor Performance. *J. Mater. Chem. A* **2015**, *3* (30), 15642–15649.

(35) Wu, R.; Wang, D. P.; Kumar, V.; Zhou, K.; Law, A. W. K.; Lee, P. S.; Lou, J.; Chen, Z. MOFs-Derived Copper Sulfides Embedded within Porous Carbon Octahedra for Electrochemical Capacitor Applications. *Chem. Commun.* **2015**, *51* (15), 3109–3112.

(36) Conway, B. E. *Electrochemical Supercapacitors*; Springer US, 1999.

(37) Wei, L.; Sevilla, M.; Fuertes, A. B.; Mokaya, R.; Yushin, G. Hydrothermal Carbonization of Abundant Renewable Natural Organic Chemicals for High-Performance Supercapacitor Electrodes. *Adv. Energy Mater.* **2011**, *1* (3), 356–361.

(38) Dong, Y.; Zhu, J.; Li, Q.; Zhang, S.; Song, H.; Jia, D. Carbon Materials for High Mass-Loading Supercapacitors: Filling the Gap between New Materials and Practical Applications. *J. Mater. Chem. A* **2020**, *8* (42), 21930–21946.

(39) Zhi, J.; Reiser, O.; Huang, F. Hierarchical MnO2 Spheres Decorated by Carbon-Coated Cobalt Nanobeads: Low-Cost and High-Performance Electrode Materials for Supercapacitors. *ACS Appl. Mater. Interfaces* **2016**, *8* (13), 8452–8459.

(40) Zhi, J.; Zhao, W.; Liu, X.; Chen, A.; Liu, Z.; Huang, F. Highly Conductive Ordered Mesoporous Carbon Based Electrodes Decorated by 3D Graphene and 1D Silver Nanowire for Flexible Supercapacitor. *Adv. Funct. Mater.* **2014**, *24* (14), 2013–2019.

(41) Sawangphruk, M.; Srimuk, P.; Chiochan, P.; Krittayavathananon, A.; Luanwuthi, S.; Limtrakul, J. High-Performance Supercapacitor of Manganese Oxide/Reduced Graphene Oxide Nanocomposite Coated on Flexible Carbon Fiber Paper. *Carbon N. Y.* **2013**, *60*, 109–116.

(42) Pal, B.; Yang, S.; Ramesh, S.; Thangadurai, V.; Jose, R. Electrolyte Selection for Supercapacitive Devices: A Critical Review. *Nanoscale Adv.* **2019**, *1* (10), 3807–3835.

(43) Fic, K.; Lota, G.; Meller, M.; Frackowiak, E. Novel Insight into Neutral Medium as Electrolyte for High-Voltage Supercapacitors. *Energy Environ. Sci.* **2012**, *5* (2), 5842–5850.

(44) Yu, P.; Liang, Y.; Dong, H.; Hu, H.; Liu, S.; Peng, L.; Zheng, M.; Xiao, Y.; Liu, Y. Rational Synthesis of Highly Porous Carbon from Waste Bagasse for Advanced Supercapacitor Application. *ACS Sustain. Chem. Eng.* **2018**, *6* (11), 15325–15332.

(45) Cai, Y.; Luo, Y.; Xiao, Y.; Zhao, X.; Liang, Y.; Hu, H.; Dong, H.; Sun, L.; Liu, Y.; Zheng, M. Facile Synthesis of Three-Dimensional Heteroatom-Doped and Hierarchical Egg-Box-Like Carbons Derived from Moringa Oleifera Branches for High-Performance Supercapacitors. *ACS Appl. Mater. Interfaces* **2016**, *8* (48), 33060–33071.

(46) Huang, J.; Liang, Y.; Hu, H.; Liu, S.; Cai, Y.; Dong, H.; Zheng, M.; Xiao, Y.; Liu, Y. Ultrahigh-Surface-Area Hierarchical Porous Carbon from Chitosan: Acetic Acid Mediated Efficient Synthesis and Its Application in Superior Supercapacitors. *J. Mater. Chem. A* **2017**, *5* (47), 24775–24781.

(47) Ran, F.; Yang, X.; Xu, X.; Li, S.; Liu, Y.; Shao, L. Green Activation of Sustainable Resources to Synthesize Nitrogen-Doped Oxygen-Riched Porous Carbon Nanosheets towards High-Performance Supercapacitor. *Chem. Eng. J.* **2021**, *412*, 128673.

(48) Liang, H.; Lu, Z.; Wang, D. A Facile Zn Involved Self-Sacrificing Template-Assisted Strategy towards Porous Carbon Frameworks for Aqueous Supercapacitors with High Ions Diffusion Coefficient. *Diam. Relat. Mater.*

**2020**, *103*, 107696.

(49) Sun, X.; Zhang, X.; Zhang, H.; Zhang, D.; Ma, Y. A Comparative Study of Activated Carbon-Based Symmetric Supercapacitors in Li 2SO 4 and KOH Aqueous Electrolytes. *J. Solid State Electrochem.* **2012**, *16* (8), 2597–2603.

(50) Xu, Z.; Zhang, X.; Liang, Y.; Lin, H.; Zhang, S.; Liu, J.; Jin, C.; Choe, U.; Sheng, K. Green Synthesis of Nitrogen-Doped Porous Carbon Derived from Rice Straw for High-Performance Supercapacitor Application. *Energy and Fuels* **2020**, *34* (7), 8966–8976.

(51) Su, X. L.; Cheng, M. Y.; Fu, L.; Yang, J. H.; Zheng, X. C.; Guan, X. X. Superior Supercapacitive Performance of Hollow Activated Carbon Nanomesh with Hierarchical Structure Derived from Poplar Catkins. *J. Power Sources* **2017**, *362*, 27–38.

(52) Liu, X.; Yu, C.; Chen, Z.; Xu, F.; Liao, W.; Zhong, W. Biomass Peach Gum-Derived Heteroatom-Doped Porous Carbon via in Situ Molten Salt Activation for High-Performance Supercapacitors. *Energy and Fuels* **2021**, *35* (23), 19801–19810.

(53) Huang, Z. H.; Liu, T. Y.; Song, Y.; Li, Y.; Liu, X. X. Balancing the Electrical Double Layer Capacitance and Pseudocapacitance of Hetero-Atom Doped Carbon. *Nanoscale* **2017**, *9* (35), 13119–13127.

(54) Choudhury, B. J.; Roy, K.; Moholkar, V. S. Improvement of Supercapacitor Performance through Enhanced Interfacial Interactions Induced by Sonication. *Ind. Eng. Chem. Res.* **2021**, *60* (20), 7611–7623.

(55) Evanko, B.; Boettcher, S. W.; Yoo, S. J.; Stucky, G. D. Redox-Enhanced Electrochemical Capacitors: Status, Opportunity, and Best Practices for Performance Evaluation. *ACS Energy Lett.* **2017**, *2* (11), 2581–2590.

(56) Abbas, Q.; Ratajczak, P.; Béguin, F. Sodium Molybdate – an Additive of Choice for Enhancing the Performance of AC/AC Electrochemical Capacitors in a Salt Aqueous Electrolyte. *Faraday Discuss.* **2014**, *172* (0), 199–214.

# CHAPTER 6

## Overview and Scope for Future Work

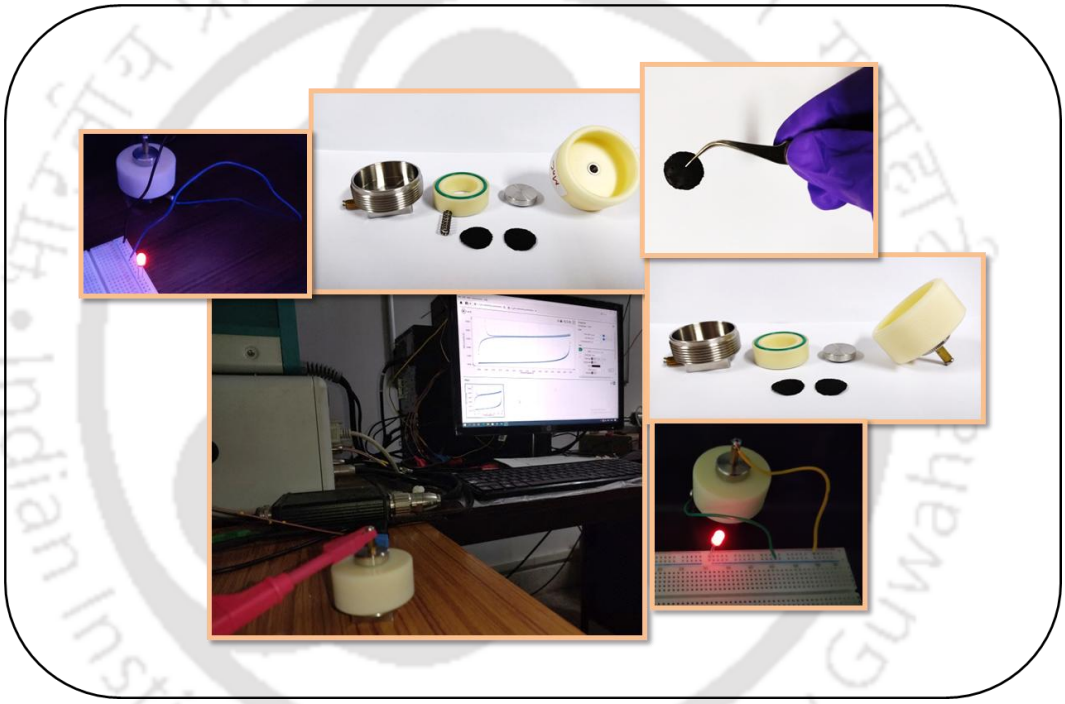

# CHAPTER 6

# OVERVIEW AND SCOPE FOR FUTURE WORK

## 6.1 SUMMARY OF THE MAJOR OUTCOMES

This thesis has presented an investigation in the synthesis of four electrode materials for supercapacitors, including nanocomposites ($Fe_3O_4$/rGO and MWCNT/$MnO_2$/rGO), and carbon materials (rGO and PC–*x*). The two nanocomposites were synthesized via the facile ultrasound–assisted synthesis method. Using ultrasound in the synthesis generates intense microconvection in the reaction system. The propagation of ultrasound waves induces high-frequency oscillations of fluid elements at a very small spatial scale. The amplitude of oscillation (*a*) of fluid elements in our system was calculated to be $a$ = 0.43 μm (as described in **Chapter 2**). This intense microconvection at a small spatial scale is highly effective in unfolding graphene sheets. Subsequently, various nanoparticles can be grown and intercalated in the graphene sheets to synthesize nanocomposites with relatively high surface area. The reduced graphene oxide (rGO) was synthesized via the chemical reduction of highly oxidized graphene oxide (prepared via a modified Hummers' method). Co–pyrolysis and KOH activation process were used to prepare the oxygen-enriched porous carbon (PC–*x*) from a ternary biomass blend. The synthesized materials have been extensively characterized using standard techniques to determine their physicochemical properties. Electrochemical performances of these materials have been investigated in a two–electrode (full-cell) configuration using the CV, GCD, and

EIS techniques. The fabricated supercapacitors have been demonstrated to possess excellent electrochemical properties.

The major conclusions of the studies presented in this thesis are summarized below:

- In Chapter 2, we have reported the ultrasound-assisted synthesis of a $Fe_3O_4$/ rGO nanocomposite having a high BET-specific surface area of ~332 $m^2$ $g^{-1}$ and mesoporous structure. This high surface area of the nanocomposite was achieved through the application of sonication, which induced the unfolding of rGO and generated additional active sites for nucleation of $Fe_3O_4$ nanoparticles. Benefiting from the increased electrochemically active surface area the structural features, the $Fe_3O_4$/rGO based all–solid–state supercapacitor with PVA/KOH polymer–gel electrolyte exhibited high cell-specific capacitance of 169.2 F $g^{-1}$ (at 1 A $g^{-1}$) and ~84.5% capacitance retention over 6000 cycles (at 5 A $g^{-1}$). The all–solid–state supercapacitor displayed an energy density of 8.46 W h $kg^{-1}$ at a power density of 338 W $kg^{-1}$.
- Chapter 3 reported a ternary MWCNT/$MnO_2$/rGO (MnGC) nanocomposite synthesized by a facile ultrasound-assisted one-pot method. The synergistic effect of simultaneous growth of $MnO_2$ on the graphene and MWCNTs under ultrasonic irradiation resulted in the formation of a porous ternary structure with efficient ion diffusion channels, maximum utilization of active surface area of $MnO_2$, reduced diffusion length, and rapid electron transport via its conductive network. As a result, the MnGC nanocomposite demonstrated superior capacitive performance as compared to binary nanocomposites ($MnO_2$/rGO and $MnO_2$/MWCNT). The supercapacitor based on commercial–level mass loading (~12 mg $cm^{-2}$) MnGC electrodes exhibited high electrode-specific capacitance of 314.6 F $g^{-1}$ at 5 mV $s^{-1}$ and excellent cycle stability with no capacitance loss after 5000 cycles (5 A $g^{-1}$).

The MnGC-based supercapacitor exhibited a high energy density of 21.2 W h $kg^{-1}$ at 150 W $kg^{-1}$ at a wide cell voltage of 1.5 V in 1 M $Na_2SO_4$ electrolyte.

- Chapter 4 demonstrated an eco-friendly and sustainable approach for developing high-energy-density aqueous supercapacitors. Firstly, rGO-based supercapacitors (rGO–SCs) having commercial–level electrode mass loadings have been investigated in different aqueous electrolytes viz. 1 M $H_2SO_4$ (0–1 V), 6 M KOH (0–1 V), and 1 M $Li_2SO_4$ (0–1.8 V). The rGO-SCs demonstrated an energy density of 15.39 W h $kg^{-1}$ (at 180 W $kg^{-1}$) in neutral $Li_2SO_4$ electrolyte, which is ~2.6–3× higher compared to the acidic and alkaline electrolyte. This higher energy density was achieved due to the extended cell voltage in the $Li_2SO_4$ electrolyte. Furthermore, the energy densities of the rGO–SC were improved using two facile strategies: (i) using pseudo faradaic contributions from redox–active electrolyte, and (ii) widening the cell voltage using low–cost water–in–salt (WIS) electrolyte. Incorporating $Na_2MoO_4$ (0.1 M) as the redox–additive in $Li_2SO_4$ increased the energy density to 21.42 W h $kg^{-1}$ (at 180 W $kg^{-1}$) via redox contributions from the electrolyte. The high voltage (2.1 V) supercapacitor fabricated with 11 M $NaNO_3$ (WIS) electrolyte delivered an energy density of 22.87 W h $kg^{-1}$ (at 210 W $kg^{-1}$).
- In Chapter 5, oxygen-enriched porous carbon (PC-*x*) was prepared via co-pyrolysis, and activation of a ternary mixture of biomass (viz. sugarcane bagasse, water hyacinth, and yellow oleander). The PC-*x* possessed large surface area (1439 - 2297 $m^2$ $g^{-1}$), high pore volume, rational micro/mesopore distribution, and surface oxygen functionalities (C/O = 2.5 - 3.1). The optimized PC-*x* electrodes at commercial electrode mass loading (~ 10 mg $cm^{-2}$) unveiled a high gravimetric capacitance of 251.6 F $g^{-1}$, high rate capability, and cycle stability in a 6 M KOH

electrolyte. Furthermore, an aqueous symmetric supercapacitor fabricated in 1 M $Li_2SO_4$ electrolyte achieved a high cell voltage of 2 V and energy density of 22.75 W h $kg^{-1}$ (at 200 W $kg^{-1}$) along with 96.8% capacitance retention over 10000 cycles. Using $Na_2MoO_4$ as the redox–additive, the energy density of the device was further augmented to 37.24 W h $kg^{-1}$ (at 200 W $kg^{-1}$) without compromising the cycle stability.

## 6.2 SCOPE FOR FUTURE RESEARCH

This thesis has focused on the development of nanocomposites and carbon materials to fabricate high-performance supercapacitors. The present work can be further advanced in several directions and some suggestions for future work are as follows:

1. The nanocomposites in the present study were synthesized using an ultrasound–assisted approach. In this regard, the effect of various parameters of ultrasound like power and frequency in synthesized materials can be studied. Moreover, multi–transducer ultrasonic reactors can be designed to scale the synthesis process of these nanocomposites.
2. The charge storage reaction mechanisms of the synthesized materials can be further investigated using *in situ/ operando* techniques (*in situ/ operando* XRD, XAS, XPS, AFM, SEM, TEM) without disassembling the device, which could help in revealing of the crucial kinetic information. These *in situ/ operando* characterization techniques enable researchers to identify the detrimental and favorable mechanisms in existing materials and to develop new materials with improved properties.

3. Flexible and micro–supercapacitor configurations are suitable for miniaturization and integration with flexible microcircuits for wearable and implantable biomedical devices, remotely rechargeable sensors, and various Internet of Things (IoT) devices. The aforementioned supercapacitor configurations can be explored for the synthesized materials.
4. Electrode processing techniques (such as laser scribing, plasma treatment, etc.) can be employed to create micro scale trenches on the electrode which can further improve the electrochemical performance.
5. Molecular simulations is a powerful tool and it can be employed to further understand the various parameters such as the roles of mesopores and macropores in ion diffusion, electrode–electrolyte interaction, etc., which could be helpful for designing high–performance electrodes.

भारतीय प्रौद्योगिकी संस्थान गुवाहाटी
Indian Institute of Technology Guwahati

# Appendix 1

**Table A1.1** Elemental compositions of GO and rGO from CHN analysis

| Sample | C (wt. %) | H (wt. %) | N (wt. %) | O (wt. %) |
|---|---|---|---|---|
| GO | 41.5 | 3.2 | 0 | 55.3 |
| rGO | 89.0 | 0.6 | 1.9 | 8.5 |

**Table A1.2** Porosity parameters of the samples

| Sample | $S_{BET}$ ($m^2$ $g^{-1}$) | $V_T$ ($cm^3$ $g^{-1}$) | $D_A$ (nm) |
|---|---|---|---|
| rGO | 555.20 | 0.49 | 3.57 |
| $Fe_3O_4$ | 104.83 | 0.27 | 9.19 |
| $Fe_3O_4$/rGO | 332.34 | 0.36 | 4.34 |
| $Fe_3O_4$/rGO (without ultrasound) | 227.18 | 0.30 | 5.30 |

$S_{BET}$ - BET surface area; $V_T$ - total pore volume; $D_A$ - average pore diameter

**Table A1.3** Magnetic parameters of the of $Fe_3O_4$ NPs and $Fe_3O_4$/rGO nanocomposite measured using vibrating sample magnetometer

| Parameter | $Fe_3O_4$ | $Fe_3O_4$/rGO |
|---|---|---|
| Coercivity (Oe) | 22.37 | 16.57 |
| Magnetization (emu $g^{-1}$) | 56.44 | 46.48 |
| Retentivity (emu $g^{-1}$) | 1.61 | 0.80 |

**Table A1.4** Comparative evaluation of capacitance of symmetric solid-state supercapacitor devices

| Electrode materials | Electrolyte | Voltage window (V) | Specific capacitance | Cycle stability | Ref. |
|---|---|---|---|---|---|
| PEDOT:PSS/MWCNT | PVA/KOH | 1 | 380 F $g^{-1}$ at 0.25 A $g^{-1}$ | 90 % after 1000 cycles | 1 |
| ZnS/CNTs | PVA/KOH | 1 | 159.6 F $g^{-1}$ at 1 A $g^{-1}$ | 91.8 % after 3000 cycles | 2 |
| N-doped cotton-derived carbon frameworks (NCCF)-rGO | PVA/KOH | 1 | 200 F $g^{-1}$ at 0.1 A $g^{-1}$ | 94 % after 10000 cycles | 3 |
| Polyaniline-coated carbon nanofibers | PVA/$H_2SO_4$ | 0.8 | 201 F $g^{-1}$ at 0.25 A $g^{-1}$ | 80 % after 6000 cycles | 4 |
| $ZnCo_2O_4$/rGO | PVA/KOH | 0.4 | 143 F $g^{-1}$ at 1 A $g^{-1}$ | 93.4 % after 5000 cycles | 5 |
| Porous carbon | PVA/KOH | 0.8 | 81.3 F $g^{-1}$ at 0.5 A $g^{-1}$ | 90.2 % after 6000 cycles | 6 |
| MWCNTs/$MnO_2$ | PVA/$Na_2SO_4$ | 1 | 204 F $g^{-1}$ at 1 mA $cm^{-2}$ | 80.36 % after 2500 cycles | 7 |
| Porous single-walled carbon nanotube/poly-(3,4-ethylenedioxythiophene) (SWCNT/PEDOT) | PVA/$H_3PO_4$ | 0.9 | 53 F $g^{-1}$ at 1 A $g^{-1}$ | 100 % after 1000 cycles | 8 |
| $Fe_3O_4$/rGO | PVA/KOH | 0.6 | 169.2 F $g^{-1}$ at 1 A $g^{-1}$ | 84.5 % after 6000 cycles | **This work** |

**Table A1.5** Comparison of electrochemical performance $Fe_3O_4$/rGO electrodes with recently reported iron oxide carbon-based electrodes

| Materials | Method | Electrolyte | Capacitance | Cycle stability | Ref. |
|---|---|---|---|---|---|
| $Fe_3O_4$-carbon nanosheets | Solvothermal | 1 M $Na_2SO_3$ | 163.4 F $g^{-1}$ at 1 A $g^{-1}$ | 93% after 5000 cycles | 9 |
| Carbon nanotube/cubic $Fe_3O_4$ | Hydrothermal | 6 M KOH | 117.2 F $g^{-1}$ at 10 mA $cm^{-2}$ | 91% after 500 cycles at 10 mA $cm^{-2}$ | 10 |
| $FeO_x$/CNF | Electrospinning | 1 M $Na_2SO_4$ | 436 F·$g^{-1}$ at 1 A·$g^{-1}$ | 89% after 5000 cycles at 1 A·$g^{-1}$ | 11 |
| $Fe_3O_4$/graphene | Hydrothermal method | 1 M KOH | 661 F $g^{-1}$ at 1 A·$g^{-1}$ | - | 12 |
| $Fe_3O_4$/graphene | Three step method | 1 M KOH | 368 F $g^{-1}$ at 1 A $g^{-1}$ | - | 13 |
| $Fe_3O_4$/reduced graphene oxide | Solvothermal process | 1 M KOH | 480 F $g^{-1}$ at 5 A $g^{-1}$ | - | 14 |
| $Fe_3O_4$/reduced graphene oxide | Hydrolysis and annealing process | 6 M KOH | 350.6 F $g^{-1}$ at 1 mV $s^{-1}$ | - | 15 |
| $Fe_3O_4$/Nitrogen-Doped Carbon | Reflux and thermal expansion | 3 M KOH | 522.7 F $g^{-1}$ at 0.5 A $g^{-1}$ | 91.9% after 5000 cycles 2 A $g^{-1}$ | 16 |
| $Mn_3O_4$-$Fe_2O_3$/$Fe_3O_4$@rGO | Microwave | 1 M KOH | 590.7 F/g at 5 mV $s^{-1}$ | 64.5% after 1000 cycles at 50 mV $s^{-1}$ | 17 |
| $Fe_3O_4$/rGO | Ultrasound-assisted method | PVA/KOH | #676.8 F $g^{-1}$ at 1 A $g^{-1}$ | 84.5 % after 6000 cycles | This work |

#Gravimetric capacitance ($C_g$) of active material can be expressed as: $C_g = 4\ C_s$ where, $C_s$ = gravemetric specific capacitance of symmetric supercapacitors

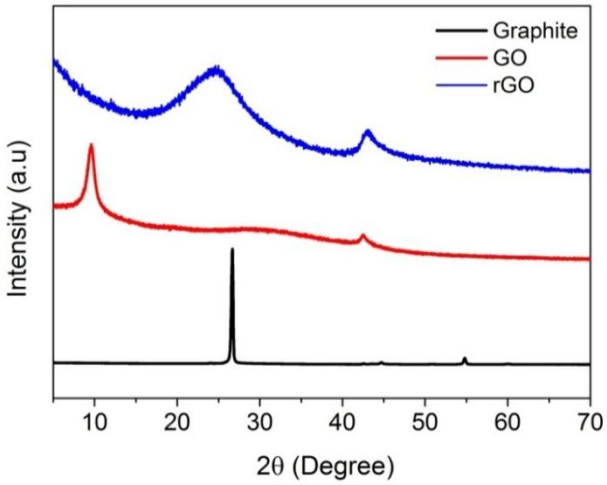


**Figure A1.1** XRD plot of graphite, GO and rGO

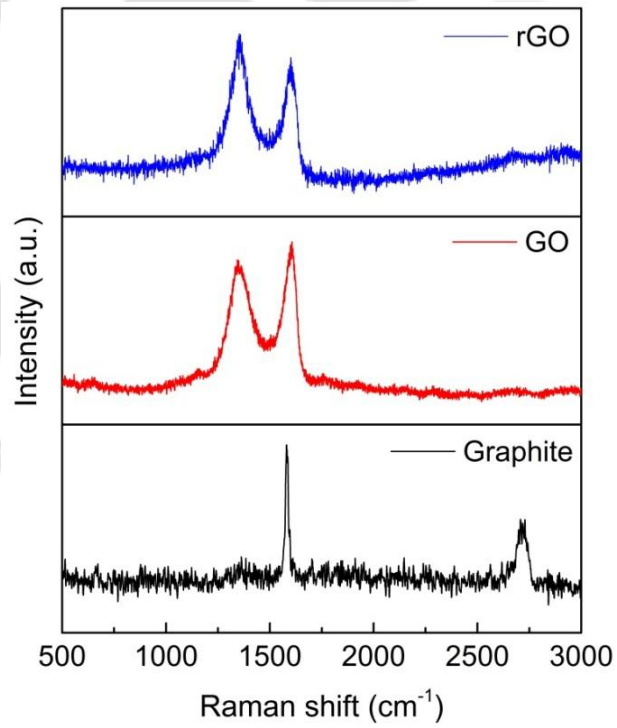


**Figure A1.2** Raman spectra of graphite, GO and rGO

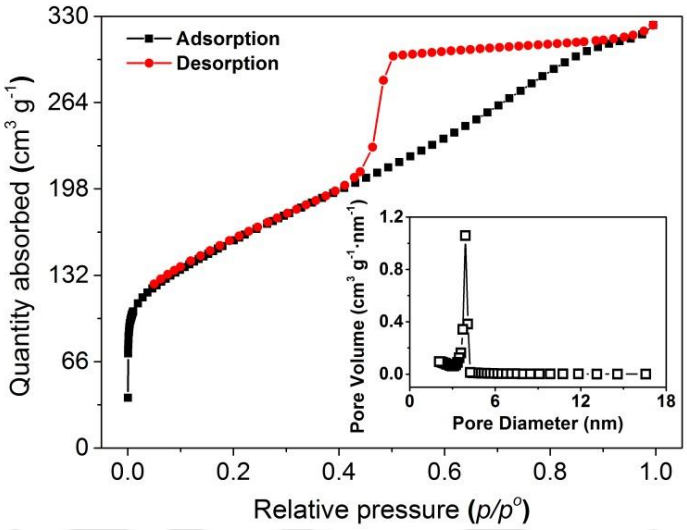


**Figure A1.3** (a) $N_2$ adsorption-desorption isotherms of rGO (inset: BJH pore size distribution).

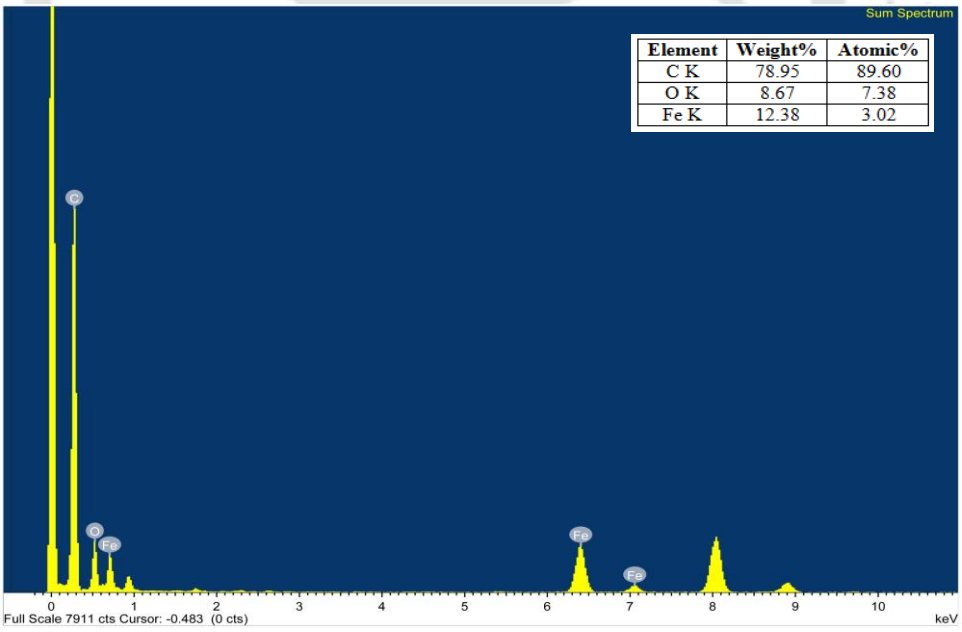


**Figure A1.4** EDS spectrum of $Fe_3O_4$/rGO nanocomposite

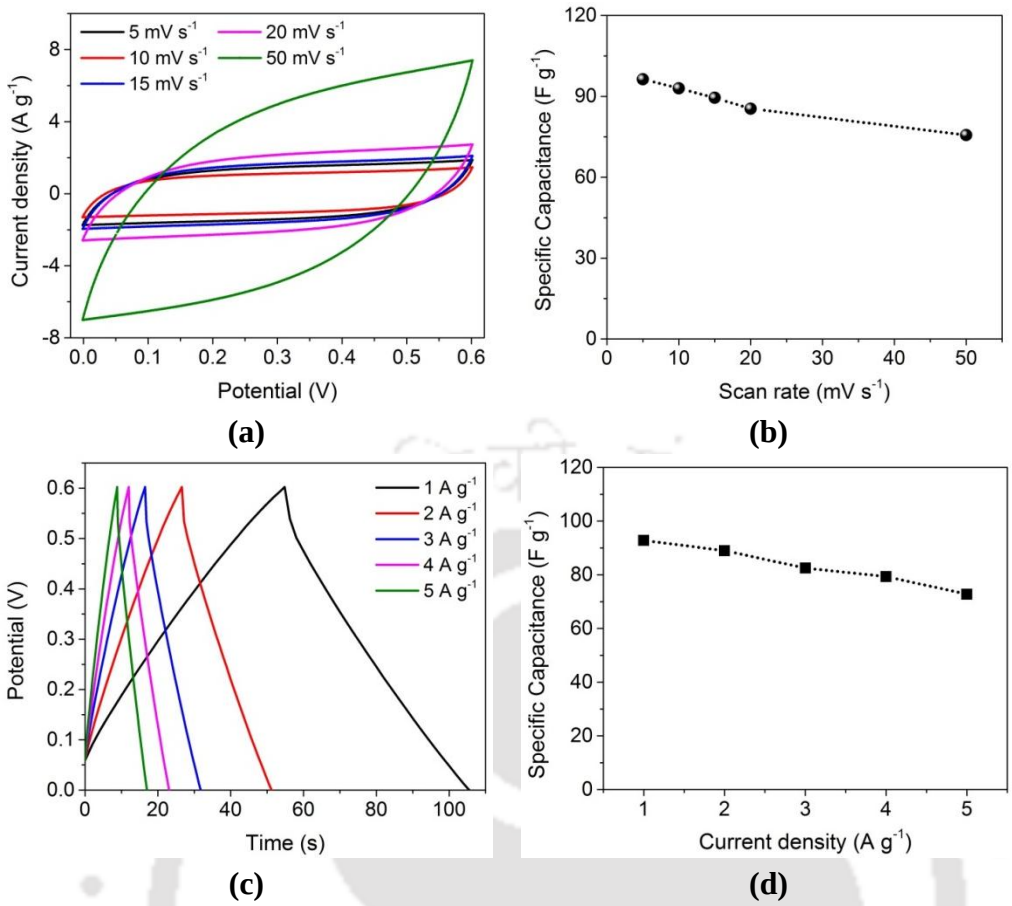


**Figure A1.5** Electrochemical performance of rGO ASSC: (a) Cyclic curves at different scan rates, (b) specific capacitance as a function of scan rate, (c) GCD curves at different current densities, , (d) specific capacitance as a function of current density.

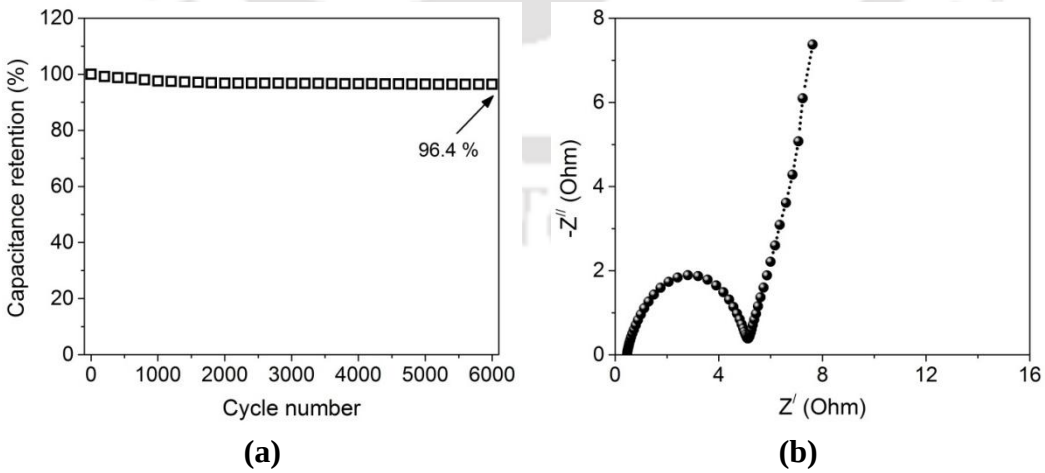


**Figure A1.6** (a) Cyclic performance (at 5 $Ag^{-1}$) and (b) Nyquist plot of rGO ASSC

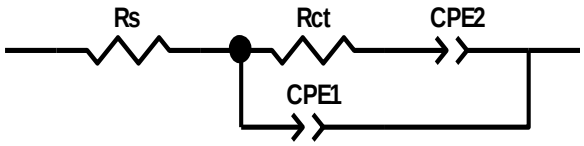


**Figure A1.7** Equivalent circuit of ASSCs

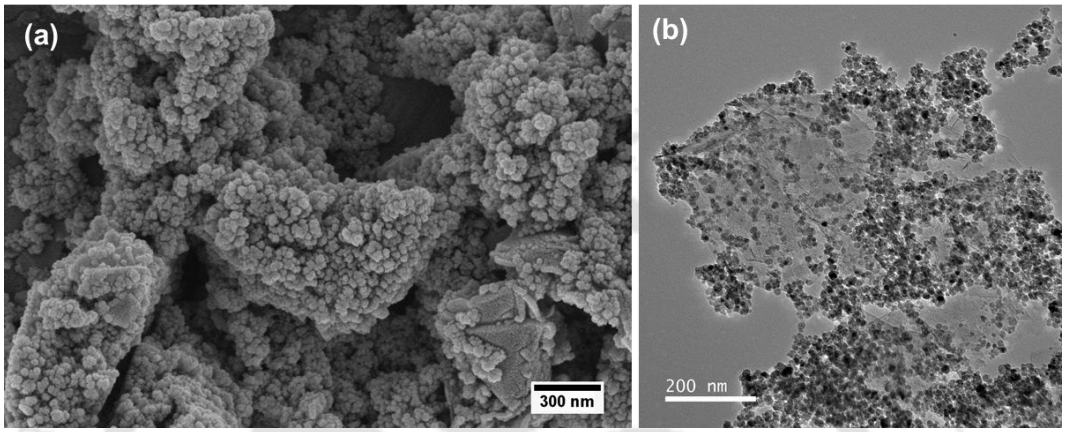


**Figure A1.8** (a) FE-SEM and (b) TEM images $Fe_3O_4$/rGO nanocomposite synthesized without ultrasound

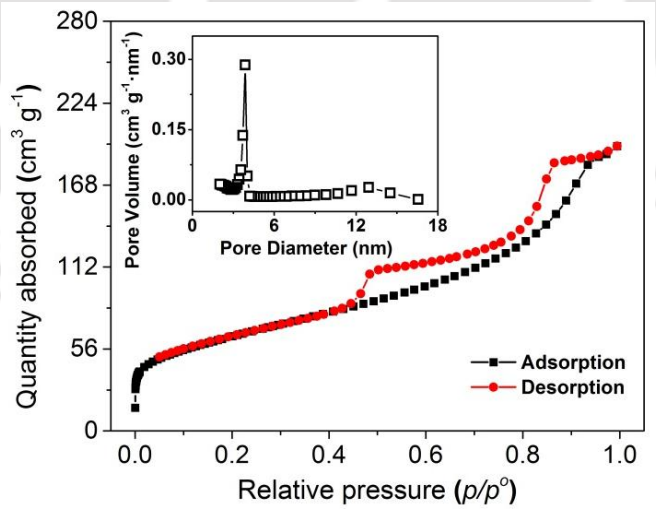


**Figure A1.9** $N_2$ adsorption-desorption isotherms (inset: BJH pore size distribution) of $Fe_3O_4$/rGO nanocomposites synthesized without ultrasound.

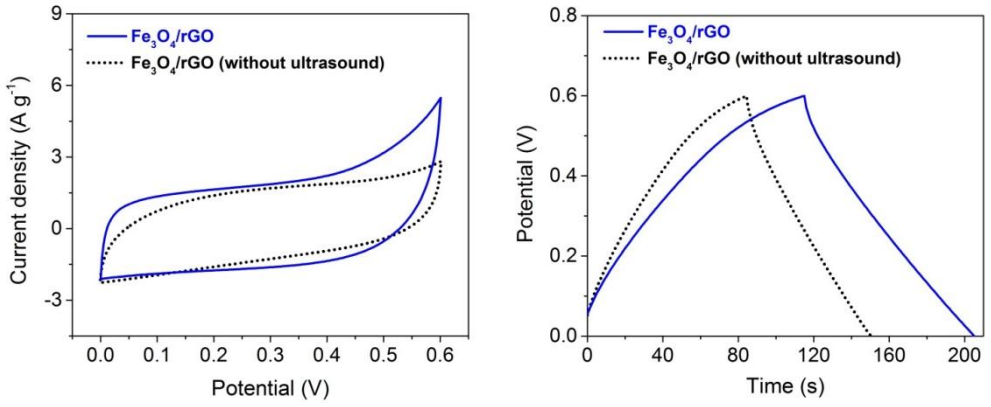


**(a)** **(b)**

**Figure A1.10** Comparison of (a) CV curves at 10 mV $s^{-1}$ and (b) GCD curves at 1 A $g^{-1}$ of ASSCs fabricated with $Fe_3O_4$/rGO synthesized using ultrasound-assisted method and without ultrasound.

**References (Appendix 1)**

(1) Zhao, D.; Zhang, Q.; Chen, W.; Yi, X.; Liu, S.; Wang, Q.; Liu, Y.; Li, J.; Li, X.; Yu, H. Highly Flexible and Conductive Cellulose-Mediated PEDOT:PSS/MWCNT Composite Films for Supercapacitor Electrodes. *ACS Appl. Mater. Interfaces* **2017**, *9* (15), 13213–13222.

(2) Hou, X.; Peng, T.; Cheng, J.; Yu, Q.; Luo, R.; Lu, Y.; Liu, X.; Kim, J. K.; He, J.; Luo, Y. Ultrathin ZnS Nanosheet/Carbon Nanotube Hybrid Electrode for High-Performance Flexible All-Solid-State Supercapacitor. *Nano Res.* **2017**, *10* (8), 2570–2583.

(3) Fan, Y. M.; Song, W. L.; Li, X.; Fan, L. Z. Assembly of Graphene Aerogels into the 3D Biomass-Derived Carbon Frameworks on Conductive Substrates for Flexible Supercapacitors. *Carbon N. Y.* **2017**, *111*, 658–666.

(4) Miao, F.; Shao, C.; Li, X.; Lu, N.; Wang, K.; Zhang, X.; Liu, Y. Polyaniline-Coated Electrospun Carbon Nanofibers with High Mass Loading and Enhanced Capacitive Performance as Freestanding Electrodes for Flexible Solid-State Supercapacitors. *Energy* **2016**, *95*, 233–241.

(5) Moon, I. K.; Yoon, S.; Oh, J. Three-Dimensional Hierarchically Mesoporous $ZnCo_2O_4$ Nanowires Grown on Graphene/Sponge Foam for High-Performance, Flexible, All-Solid-State Supercapacitors. *Chem. - A Eur. J.*

**2017**, *23* (3), 597–604.

(6) Li, X.; Liu, K.; Liu, Z.; Wang, Z.; Li, B.; Zhang, D. Hierarchical Porous Carbon from Hazardous Waste Oily Sludge for All-Solid-State Flexible Supercapacitor. *Electrochim. Acta* **2017**, *240*, 43–52.

(7) Chodankar, N. R.; Ji, S. H.; Kim, D. H. Low-Cost Superior Symmetric Solid-State Supercapacitors Based on MWCNTs/MnO2 Nanocomposite Thin Film. *J. Taiwan Inst. Chem. Eng.* **2017**, *80*, 503–510.

(8) Zhang, N.; Zhou, W.; Zhang, Q.; Luan, P.; Cai, L.; Yang, F.; Zhang, X.; Fan, Q.; Zhou, W.; Xiao, Z.; Gu, X.; Chen, H.; Li, K.; Xiao, S.; Wang, Y.; Liu, H.; Xie, S. Biaxially Stretchable Supercapacitors Based on the Buckled Hybrid Fiber Electrode Array. *Nanoscale* **2015**, *7* (29), 12492–12497.

(9) Liu, D.; Wang, X.; Wang, X.; Tian, W.; Liu, J.; Zhi, C.; He, D.; Bando, Y.; Golberg, D. Ultrathin Nanoporous Fe3O4-Carbon Nanosheets with Enhanced Supercapacitor Performance. *J. Mater. Chem. A* **2013**, *1* (6), 1952–1955.

(10) Guan, D.; Gao, Z.; Yang, W.; Wang, J.; Yuan, Y.; Wang, B.; Zhang, M.; Liu, L. Hydrothermal Synthesis of Carbon Nanotube/Cubic Fe3O4 Nanocomposite for Enhanced Performance Supercapacitor Electrode Material. *Mater. Sci. Eng. B Solid-State Mater. Adv. Technol.* **2013**, *178* (10), 736–743.

(11) Samuel, E.; Joshi, B.; Jo, H. S.; Kim, Y. Il; An, S.; Swihart, M. T.; Yun, J. M.; Kim, K. H.; Yoon, S. S. Carbon Nanofibers Decorated with FeOx Nanoparticles as a Flexible Electrode Material for Symmetric Supercapacitors. *Chem. Eng. J.* **2017**, *328*, 776–784.

(12) Lin, T. W.; Dai, C. S.; Hung, K. C. High Energy Density Asymmetric Supercapacitor Based on NiOOH/Ni3S2/3D Graphene and Fe3O4/Graphene Composite Electrodes. *Sci. Rep.* **2014**, *4* (1), 1–10.

(13) Liu, M.; Sun, J. In Situ Growth of Monodisperse Fe3O4 Nanoparticles on Graphene as Flexible Paper for Supercapacitor. *J. Mater. Chem. A* **2014**, *2* (30), 12068–12074.

(14) Shi, W.; Zhu, J.; Sim, D. H.; Tay, Y. Y.; Lu, Z.; Zhang, X.; Sharma, Y.; Srinivasan, M.; Zhang, H.; Hng, H. H.; Yan, Q. Achieving High Specific Charge Capacitances in Fe3O 4/Reduced Graphene Oxide Nanocomposites. *J. Mater. Chem.* **2011**, *21* (10), 3422–3427.

(15) Qi, T.; Jiang, J.; Chen, H.; Wan, H.; Miao, L.; Zhang, L. Synergistic Effect of Fe3O4/Reduced Graphene Oxide Nanocomposites for Supercapacitors with

Good Cycling Life. *Electrochim. Acta* **2013**, *114*, 674–680.

(16) Li, L.; Jia, C.; Shao, Z.; Wang, J.; Wang, F.; Wang, W.; Wang, H.; Zu, D.; Wu, H. $Fe_3O_4$ /Nitrogen- Doped Carbon Electrodes from Tailored Thermal Expansion toward Flexible Solid- State Asymmetric Supercapacitors. *Adv. Mater. Interfaces* **2019**, *6* (21), 1901250.

(17) Kumar, R.; Youssry, S. M.; Ya, K. Z.; Tan, W. K.; Kawamura, G.; Matsuda, A. Microwave-Assisted Synthesis of Mn3O4-Fe2O3/Fe3O4@rGO Ternary Hybrids and Electrochemical Performance for Supercapacitor Electrode. *Diam. Relat. Mater.* **2020**, *101*, 107622.

# Appendix 2

## A2.1 Purification of Multi-Walled Carbon Nanotubes (MWCNTs)

The MWCNTs obtained from Reinste Nano Ventures Ltd. were purified with nitric acid before use. MWCNTs (2 g) were added to a nitric acid solution (20%) and sonicated for 15 min. The suspension was then refluxed at 80 ºC under continuous stirring for 6 h. Finally, acid-treated MWCNTs were separated via filtration and washed with excess water (to obtain neutral pH), and vacuum dried.

## A2.2 Synthesis of $MnO_2$

$MnO_2$ nanoparticles were synthesized by a redox reaction between $Mn^{2+}$ and $Mn^{7+}$. 3 mmol $MnSO_4 \cdot H_2O$ was dissolved in 200 mL ultrapure water and 80 mL of $KMnO_4$ (0.025 M) solution was added dropwise into the former solution under continuous sonication. After the addition of $KMnO_4$, the solution was further sonicated for 30 min. A dark-brown precipitate was separated after filtration and washed with ultrapure water. The $MnO_2$ powder was obtained after drying the filtrate at 70 °C.

**Table A2.1** BET surface area results of samples

| Sample | $S_{BET}$ ($m^2\ g^{-1}$) | $V_t$ ($cm^3\ g^{-1}$) | $d_A$ (nm) |
|---|---|---|---|
| $MnO_2$ | 175.07 | 0.33 | 4.40 |
| MWCNT | 252.48 | 1.89 | 6.32 |
| MnC | 189.09 | 1.22 | 7.42 |
| MnG | 434.24 | 0.47 | 4.05 |
| MnGC | 313.22 | 0.95 | 4.59 |

$S_{BET}$ – BET surface area; $V_t$ – total pore volume; $d_A$ – average pore diameter

**Table A2.2** Capacitive performance of binary graphene/carbon nanotube based manganese oxide nanocomposites for SCs

| Materials | Mass loading (mg $cm^{-2}$) | Electrolyte | Potential Window | Capacitance | Capacitance retention | Ref. |
|---|---|---|---|---|---|---|
| rGO/$MnO_x$ | 2<br>19 | 0.5 M $Na_2SO_4$ | 0 – 0.8 V | 202 F $g^{-1}$ (1 mV $s^{-1}$)<br>2.5 F $cm^{-2}$ (~ 131.6 F $g^{-1}$) | 106% (115000 cycles at 12 A $g^{-1}$) | [1] |
| $MnO_2$/CNT | ~ 2 – 3 | 1 M $Na_2SO_4$ | 0 – 0.9 V | 223 F $g^{-1}$ (10 mV $s^{-1}$) | | [2] |
| CNT/$MnO_2$ | | 1 M $Na_2SO_4$ | −0.1 – 0.8 V | 257.8 F $g^{-1}$ (2 mV $s^{-1}$) | 63% (800 cycles at 1 A $g^{-1}$) | [3] |
| $MnO_x$−CDGs | 1 | 1 M $Na_2SO_4$<br>$H_3PO_4$/PVA | 0 – 1 V | 480 F $g^{-1}$ (0.2 A $g^{-1}$)<br>280 F $g^{-1}$ (1 A $g^{-1}$) | 94% (5000 cycles at 1 A $g^{-1}$)<br>94.7% (10000 cycles at 1.2 A $g^{-1}$) | [4] |
| $MnO_2$/AG | 7 – 14 | 1 M $H_2SO_4$ | 0 – 1 V | 256 F $g^{-1}$ (0.25 A $g^{-1}$) | 87.7% (1000 cycles at 15 A $g^{-1}$) | [5] |
| $MnO_2$/graphene | 5 | 1 M $Na_2SO_4$ | 0 – 1 V | 466.7 F $g^{-1}$ (1 A $g^{-1}$) | 92% (2000 cycles at 1 A $g^{-1}$) | [6] |
| $MnO_2$/NG | 2 | 5 M LiCl | 0 – 1 V | 305 F $g^{-1}$ (5 mV $s^{-1}$) | 90.511% (1500 cycles at mA $cm^{-2}$) | [7] |
| *3D printed GA/$MnO_2$ | 45.2 | 3 M LiCl | 0 – 0.8 V | 231.9 F $g^{-1}$ (0.5 mA $cm^{-2}$) | 92.9% ( 20,000 cycles at 20 $mVs^{-1}$) | [8] |
| MWCNT/$MnO_2$/rGO | ~12 | 1 M $Na_2SO_4$ | 0 – 1.5 V | 314.6 F $g^{-1}$ (5 mV $s^{-1}$) | 104.5% (5000 cycles at 5 A $g^{-1}$) | **This work** |

CDG – carbon dot/graphene; AG – activated graphene; NG – nitrogen-doped graphene, GA – graphene aerogel
*Mass loading of $MnO_2$ *i.e.* 90.76 % (45.2 mg $cm^{-2}$), 90.83 % (182.2 mg $cm^{-2}$) of electrode mass

**Table A2.3** Capacitive performance of ternary graphene-carbon nanotube based manganese oxide nanocomposites for SCs

| Materials | Mass loading (mg $cm^{-2}$) | Electrolyte | Potential Window | Capacitance | Capacitance retention | Ref. |
|---|---|---|---|---|---|---|
| $MnO_2$-CNTs/rGO | 4 | 1 M $Na_2SO_4$ | 0 – 0.9 V | 193 F $g^{-1}$ (0.2 A $g^{-1}$) | 94–96% (1300 cycles at 2 A $g^{-1}$) | [9] |
| Graphene/$MnO_2$/CNTs | 0.4 | 1 M $Na_2SO_4$ | 0 – 1 V | 288 F $g^{-1}$ (50 mV $s^{-1}$) | 95% (1000 cycles at 4 A $g^{-1}$) | [10] |
| | 2.1 | | | 130 F $g^{-1}$ (50 mV $s^{-1}$) | | |
| CNT/$MnO_2$/GR paper | | 1 M $Na_2SO_4$ | −0.1 – 0.8 V | 486.6 F $g^{-1}$ (2 mV $s^{-1}$) | 92.8% (800 cycles at 1 A $g^{-1}$) | [3] |
| 3D $MnO_2$–CNT–GR–Ni foam | | 1 M $Li_2SO_4$ | −0.2 – 0.8 V | 251 F $g^{-1}$ (1 A $g^{-1}$) | 82% (3000 cycles at 1.0 A $g^{-1}$) | [11] |
| rGO/CNTs/$MnO_2$ | 0.8 | 1 M $Na_2SO_4$ | −0.2 – 0.8 V | 319 F $g^{-1}$ (1 A $g^{-1}$) | 85.4% (3000 cycles at 50 mV $s^{-1}$) | [12] |
| $MnO_2$–rGO/CFP | 4 | 0.5 M $Na_2SO_4$ | 0 – 1 V | 393 F $g^{-1}$ (0.1 A $g^{-1}$) | 98.5% (2000 cycles at 0.1 A $g^{-1}$) | [13] |
| $MnO_2$/CQD/GA | ~1 – 2 | 1 M $Na_2SO_4$ | 0 – 1 V | 721 F $g^{-1}$ (1 A $g^{-1}$) | 92.3% (10,000 at 10 A $g^{-1}$) | [14] |
| MWCNT/$MnO_2$/rGO | ~12 | 1 M $Na_2SO_4$ | 0 – 1.5 V | 314.6 F $g^{-1}$ (5 mV $s^{-1}$) | 104.5% (5000 cycles at 5 A $g^{-1}$) | **This work** |

GR – graphene; CFP – carbon fibre paper; CQD – carbon quantum dots; GA – graphene aerogel

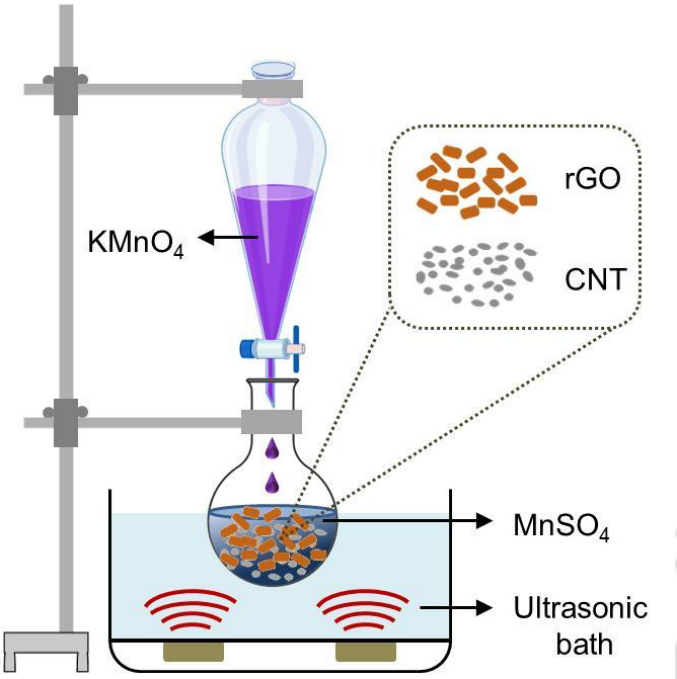


**Figure A2.1** Schematic illustration of the experimental setup for the synthesis of nanocomposites

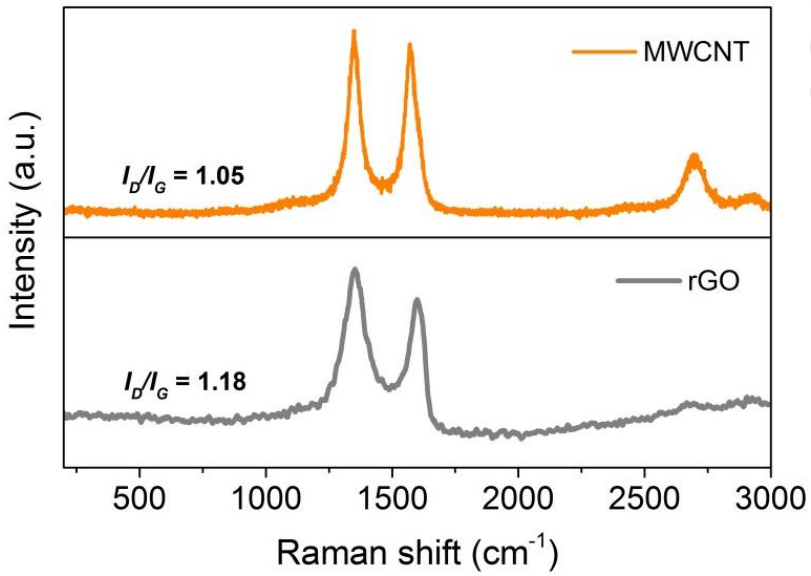


**Figure A2.2** Raman spectra of pristine MWCNT and rGO

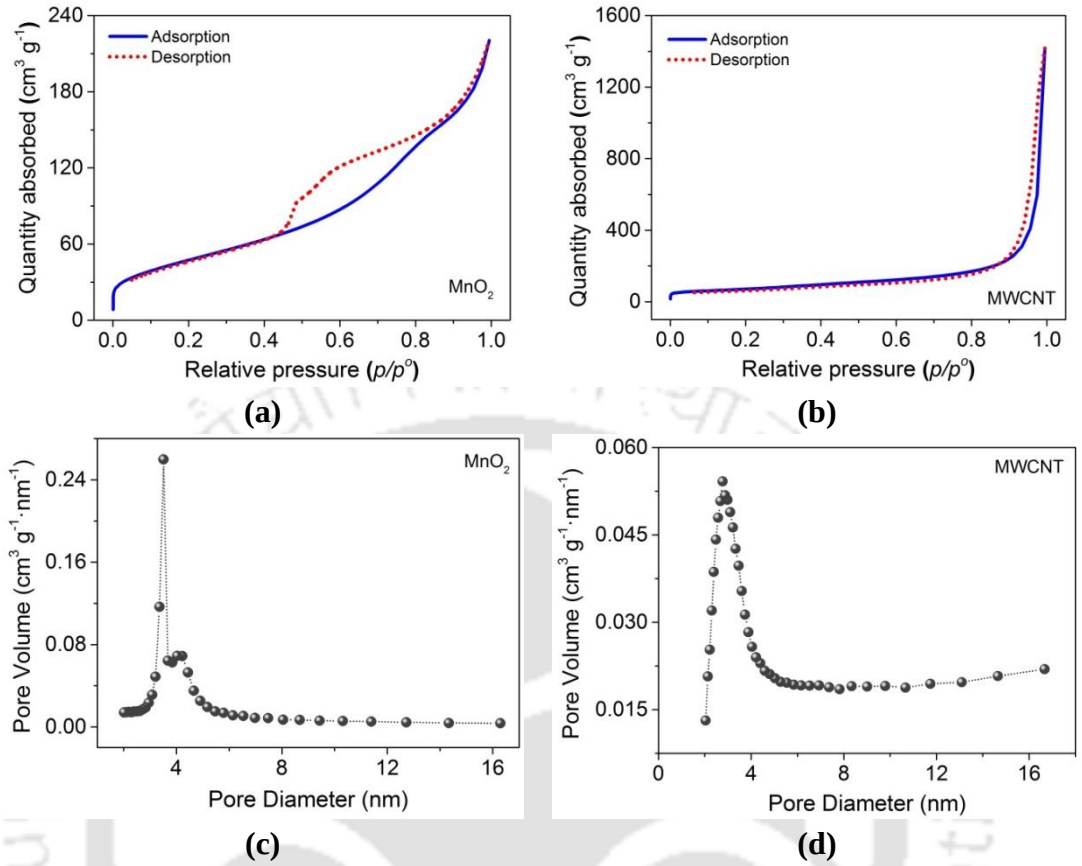


**Figure A2.3** Nitrogen adsorption-desorption isotherms of (a) $MnO_2$, (b) MWCNT; and pore size distribution of (c) $MnO_2$, (d) MWCNT

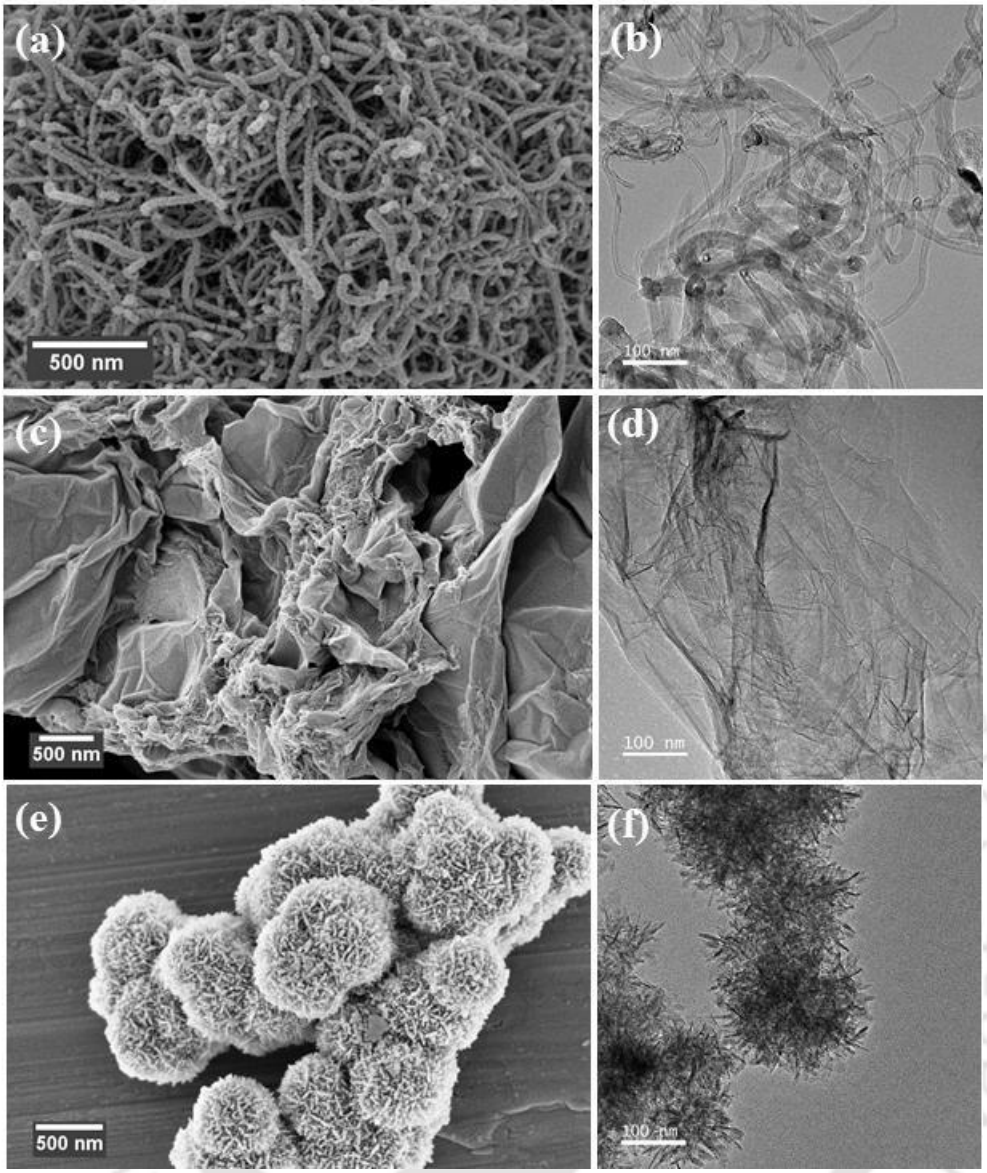


**Figure A2.4** FE-SEM images of (a) CNT (c) rGO (e) $MnO_2$ and TEM images of (b) MWCNT (d) rGO, and (f) $MnO_2$

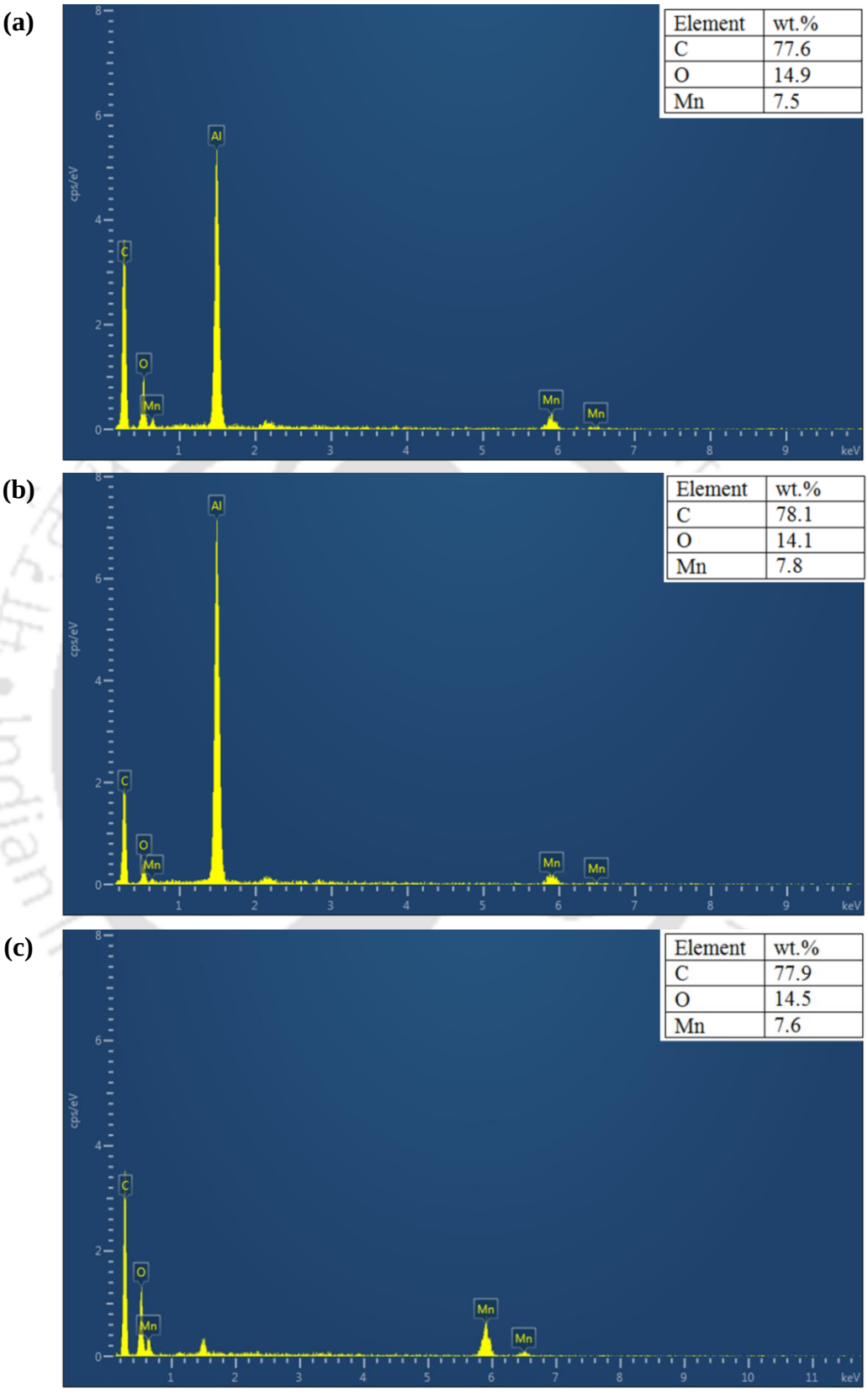


**Figure A2.5** EDX spectra of (a) MnC, (b) MnG, and (c) MnGC (the samples were dropped cast on aluminum foils and therefore a peak of Al was observed)

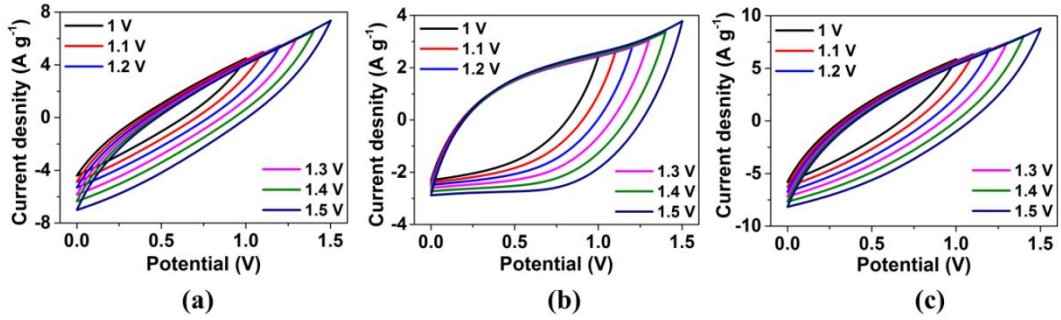


**Figure A2.6** CV curves of the SCs at different potential windows from 1 to 1.5 V at a scan rate of 50 mV $s^{-1}$ (a) MnC, (b) MnG, and (c) MnGC

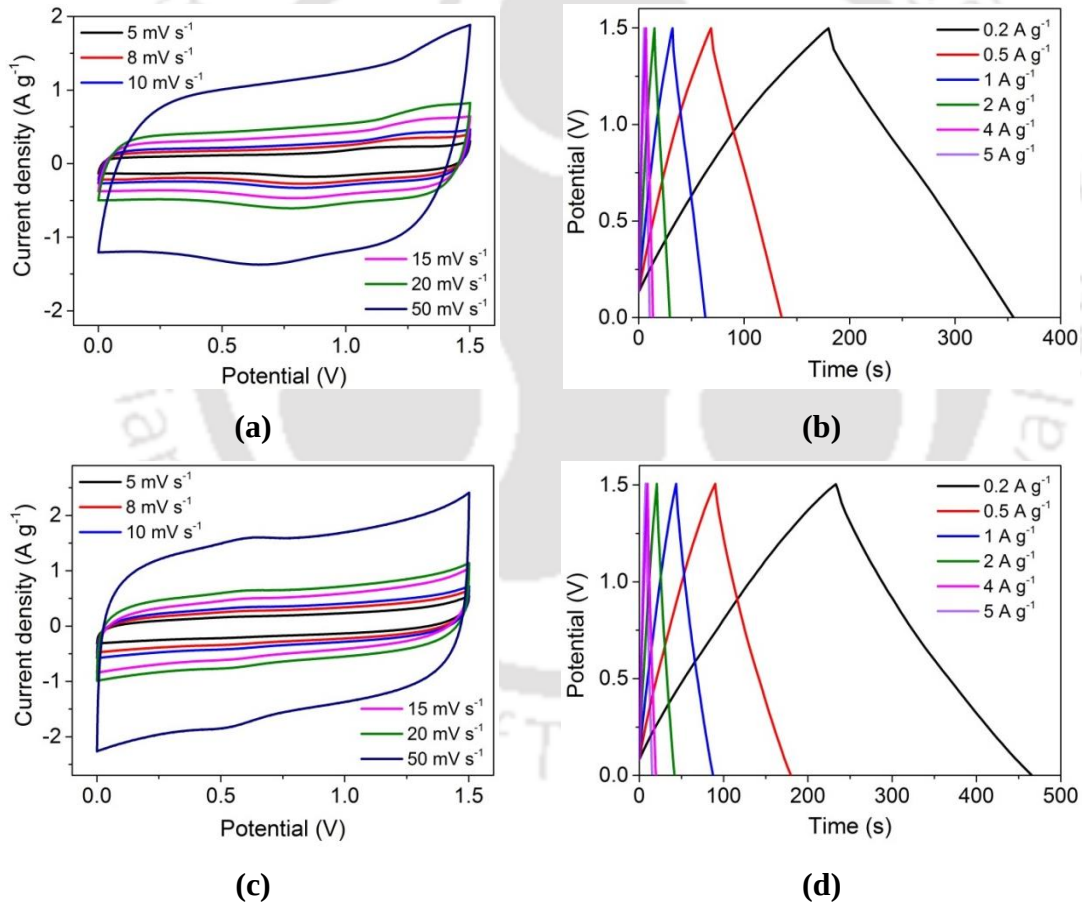


**Figure A2.7** (a) CV and (b) GCD curves of MWCNT SC at different scan rates and current densities; (c) CV and (d) GCD curves of rGO SC at different scan rates and current densities

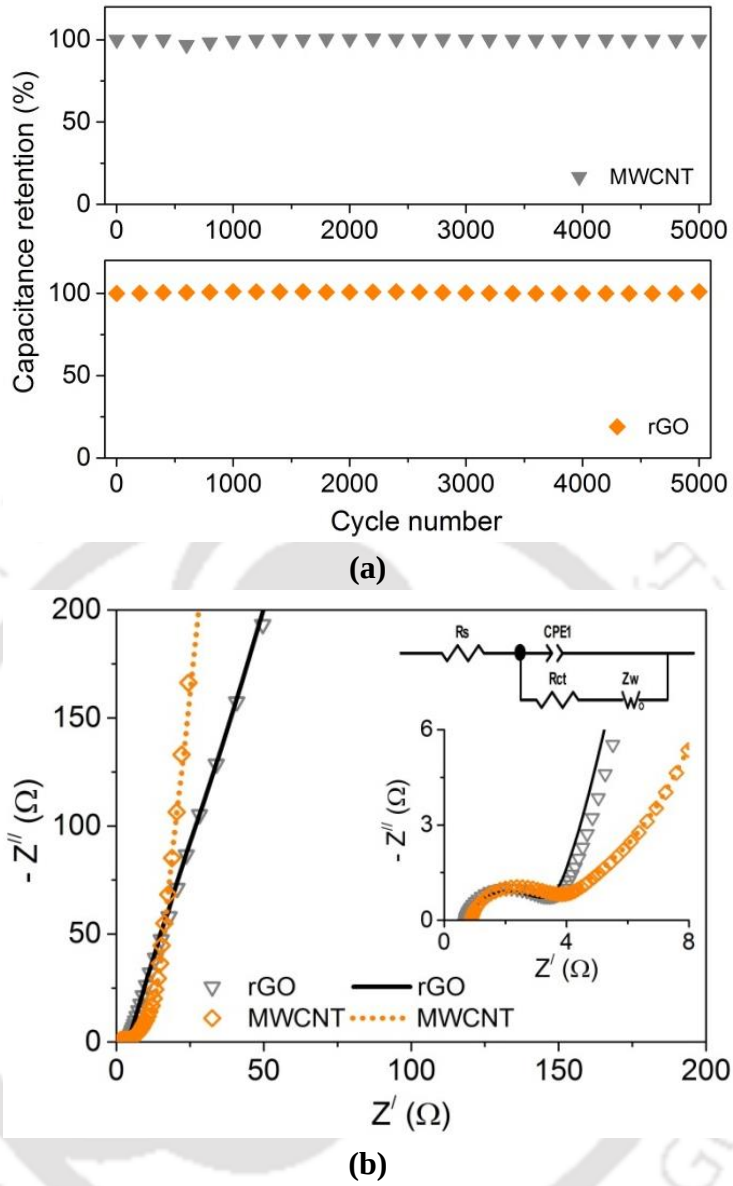


**Figure A2.8** (a) Capacitance retention of MWCNTs and rGO SCs, (b) Nyquist plots of MWCNTs and rGO SC (lines – data after 5000 charge-discharge cycles)

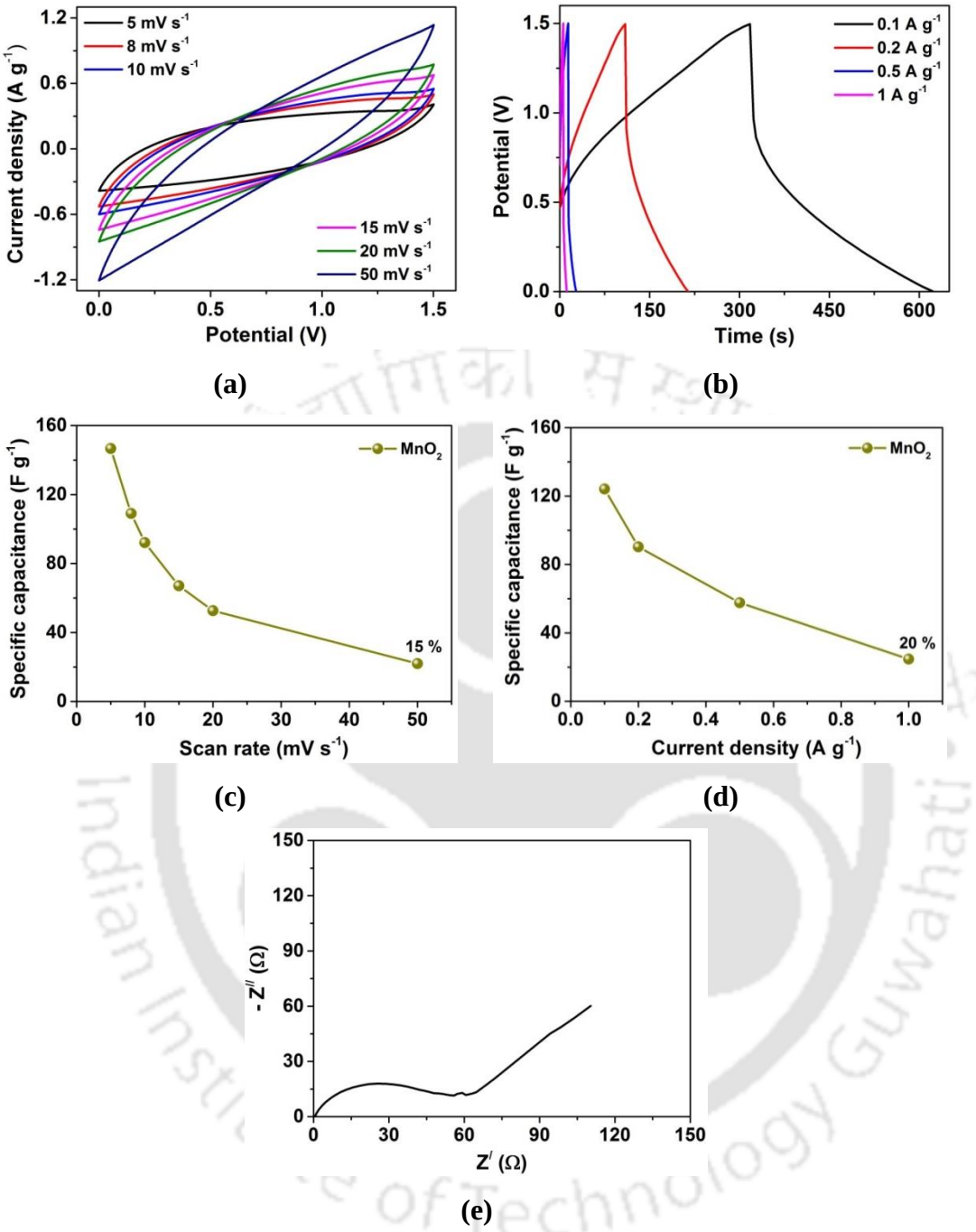


**Figure A2.9** Electrochemical performance of $MnO_2$ SC: (a) CV and (b) GCD curves of $MnO_2$ SC at different scan rates and current densities; specific capacitance of the $MnO_2$ electrodes as a function of (c) scan rate and (d) current density; (e) Nyquist plots of $MnO_2$

### A2.3 Electrochemical performance of $MnO_2$

The electrochemical performance of the $MnO_2$-based SC was investigated in the potential window of 1 to 1.5 V in 1 M $Na_2SO_4$ electrolyte, and the results are depicted in **Figure A2.10**. The CV curves $MnO_2$ SC at varying scan rates (5 to 50 mV $s^{-1}$) are shown in **Figure A2.10a**. The CV curves displayed high deviation from quasi-rectangular shape at high scan rates indicating a diffusion-limited process. The $MnO_2$ electrodes displayed a capacitance of 146.7 F $g^{-1}$ at a scan rate of 5 mV $s^{-1}$, but it could retain only 15% of this capacitance at 50 mV $s^{-1}$ (**Figure A2.10c**). The GCD curves of the $MnO_2$ SC also show a large IR drop indicating poor charge transport (**Figure A2.10b**). The $MnO_2$ electrodes exhibited a capacitance of 124.1 F $g^{-1}$ at a current density of 0.1 A $g^{-1}$ and only 20% of this value is retained when the current density increases to 1 A $g^{-1}$ (**Figure A2.10d**). The high charge transfer resistance of 54 Ω further confirms the poor charge transport characteristics of the $MnO_2$ electrodes (**Figure A2.10e**). At high commercial-level electrode mass loadings, pristine $MnO_2$ (or any metal oxide) based SCs are most likely to suffer from deteriorated charge storage, sluggish charge transport, poor rate capability, etc.[15,16] Therefore, it is necessary to couple these materials with conductive substrates and to create abundant pore channels for effective charge transport. Due to high mass loadings (~ 12 mg $cm^{-2}$) used in our study, the pristine $MnO_2$-based electrodes delivered poor capacitive performance and low rate capability. High electrode mass loadings cause severely blocked pores, reduction in electro-active sites, and sluggish charge transport dynamics, which ultimately result in poor capacitive performance.

### References (Appendix 2)

(1) Wang, Y.; Lai, W.; Wang, N.; Jiang, Z.; Wang, X.; Zou, P.; Lin, Z.; Fan, H. J.; Kang, F.; Wong, C.-P.; Yang, C. A Reduced Graphene Oxide/Mixed-Valence

Manganese Oxide Composite Electrode for Tailorable and Surface Mountable Supercapacitors with High Capacitance and Super-Long Life. *Energy Environ. Sci.* **2017**, *10* (4), 941–949.

(2) Xia, H.; Wang, Y.; Lin, J.; Lu, L. Hydrothermal Synthesis of MnO2/CNT Nanocomposite with a CNT Core/Porous MnO2 Sheath Hierarchy Architecture for Supercapacitors. *Nanoscale Res. Lett. 2012 71* **2012**, *7* (1), 1–10.

(3) Jin, Y.; Chen, H.; Chen, M.; Liu, N.; Li, Q. Graphene-Patched CNT/MnO2 Nanocomposite Papers for the Electrode of High-Performance Flexible Asymmetric Supercapacitors. *ACS Appl. Mater. Interfaces* **2013**, *5* (8), 3408–3416.

(4) Unnikrishnan, B.; Wu, C.-W.; Chen, I.-W. P.; Chang, H.-T.; Lin, C.-H.; Huang, C.-C. Carbon Dot-Mediated Synthesis of Manganese Oxide Decorated Graphene Nanosheets for Supercapacitor Application. *ACS Sustain. Chem. Eng.* **2016**, *4* (6), 3008–3016.

(5) Zhao, X.; Zhang, L.; Murali, S.; Stoller, M. D.; Zhang, Q.; Zhu, Y.; Ruoff, R. S. Incorporation of Manganese Dioxide within Ultraporous Activated Graphene for High-Performance Electrochemical Capacitors. *ACS Nano* **2012**, *6* (6), 5404–5412.

(6) Yao, J.; Pan, Q.; Yao, S.; Duan, L.; Liu, J. Mesoporous MnO2 Nanosphere/Graphene Sheets as Electrodes for Supercapacitor Synthesized by a Simple and Inexpensive Reflux Reaction. *Electrochim. Acta* **2017**, *238*, 30–35.

(7) Liu, Y.; Miao, X.; Fang, J.; Zhang, X.; Chen, S.; Li, W.; Feng, W.; Chen, Y.; Wang, W.; Zhang, Y. Layered-MnO2 Nanosheet Grown on Nitrogen-Doped Graphene Template as a Composite Cathode for Flexible Solid-State Asymmetric Supercapacitor. *ACS Appl. Mater. Interfaces* **2016**, *8* (8), 5251–5260.

(8) Yao, B.; Chandrasekaran, S.; Zhang, J.; Xiao, W.; Qian, F.; Zhu, C.; Duoss, E. B.; Spadaccini, C. M.; Worsley, M. A.; Li, Y. Efficient 3D Printed Pseudocapacitive Electrodes with Ultrahigh MnO2 Loading. *Joule* **2019**, *3* (2), 459–470.

(9) Lei, Z.; Shi, F.; Lu, L. Incorporation of MnO2-Coated Carbon Nanotubes between Graphene Sheets as Supercapacitor Electrode. *ACS Appl. Mater. Interfaces* **2012**, *4* (2), 1058–1064.

(10) Cheng, Y.; Lu, S.; Zhang, H.; Varanasi, C. V.; Liu, J. Synergistic Effects from Graphene and Carbon Nanotubes Enable Flexible and Robust Electrodes for High-Performance Supercapacitors. *Nano Lett.* **2012**, *12* (8), 4206–4211.

(11) Zhu, G.; He, Z.; Chen, J.; Zhao, J.; Feng, X.; Ma, Y.; Fan, Q.; Wang, L.; Huang, W. Highly Conductive Three-Dimensional MnO2–Carbon Nanotube–Graphene–Ni Hybrid Foam as a Binder-Free Supercapacitor Electrode. *Nanoscale* **2013**, *6* (2), 1079–1085.

(12) Jiang, H.; Dai, Y.; Hu, Y.; Chen, W.; Li, C. Nanostructured Ternary Nanocomposite of RGO/CNTs/MnO2 for High-Rate Supercapacitors. *ACS Sustain. Chem. Eng.* **2013**, *2* (1), 70–74.

(13) Sawangphruk, M.; Srimuk, P.; Chiochan, P.; Krittayavathananon, A.; Luanwuthi, S.; Limtrakul, J. High-Performance Supercapacitor of Manganese Oxide/Reduced Graphene Oxide Nanocomposite Coated on Flexible Carbon Fiber Paper. *Carbon N. Y.* **2013**, *60*, 109–116.

(14) Lv, H.; Yuan, Y.; Xu, Q.; Liu, H.; Wang, Y. G.; Xia, Y. Carbon Quantum Dots Anchoring MnO2/Graphene Aerogel Exhibits Excellent Performance as Electrode Materials for Supercapacitor. *J. Power Sources* **2018**, *398*, 167–174.

(15) Dong, Y.; Zhu, J.; Li, Q.; Zhang, S.; Song, H.; Jia, D. Carbon Materials for High Mass-Loading Supercapacitors: Filling the Gap between New Materials and Practical Applications. *J. Mater. Chem. A* **2020**, *8* (42), 21930–21946.

(16) Guo, W.; Yu, C.; Li, S.; Qiu, J. Toward Commercial-Level Mass-Loading Electrodes for Supercapacitors: Opportunities, Challenges and Perspectives. *Energy Environ. Sci.* **2021**, *14* (2), 576–601.

भारतीय प्रौद्योगिकी संस्थान गुवाहाटी
Indian Institute of Technology Guwahati

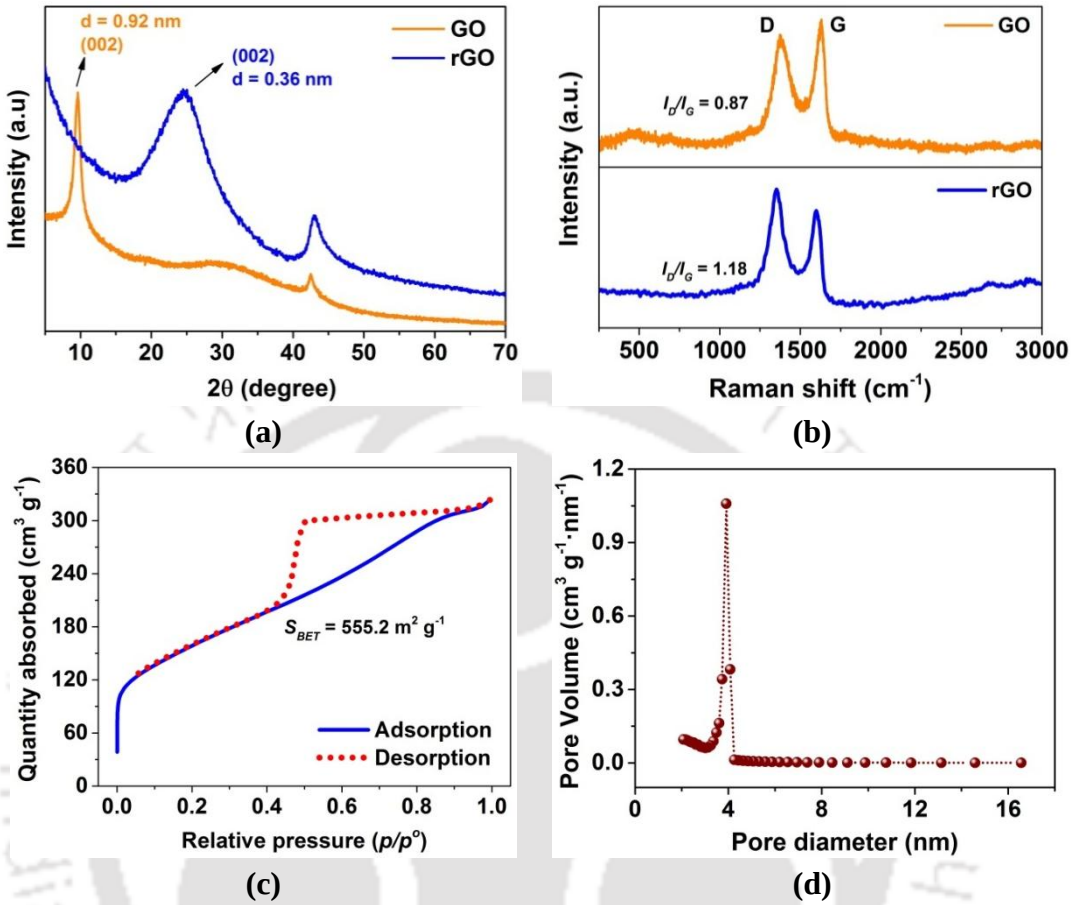


**Figure A3.1** (a) XRD patterns, (b) Raman spectra of graphene oxide (GO) and reduced graphene oxide (rGO); (c) $N_2$ adsorption-desorption isotherms, and (d) BJH pore-size distributions of rGO.

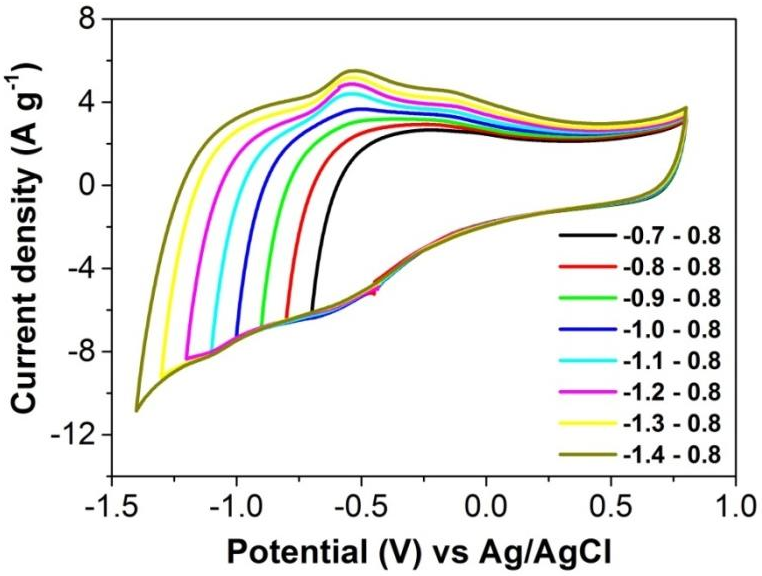


**Figure A3.2** Three-electrode CV curves of rGO electrode recorded at different potential windows in 1 M $Li_2SO_4$ electrolyte

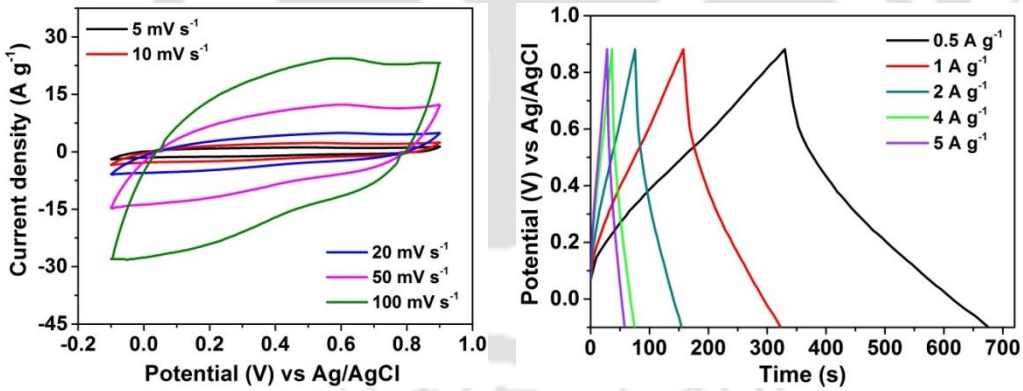


**Figure A3.3** Electrochemical performance of rGO electrodes using three-electrode system in 1 M $H_2SO_4$ electrolyte: (a) CV curves at different scan rates from 5 to 100 mV $s^{-1}$, (b) GCD curves at different current densities from 0.5 to 5 A $g^{-1}$.

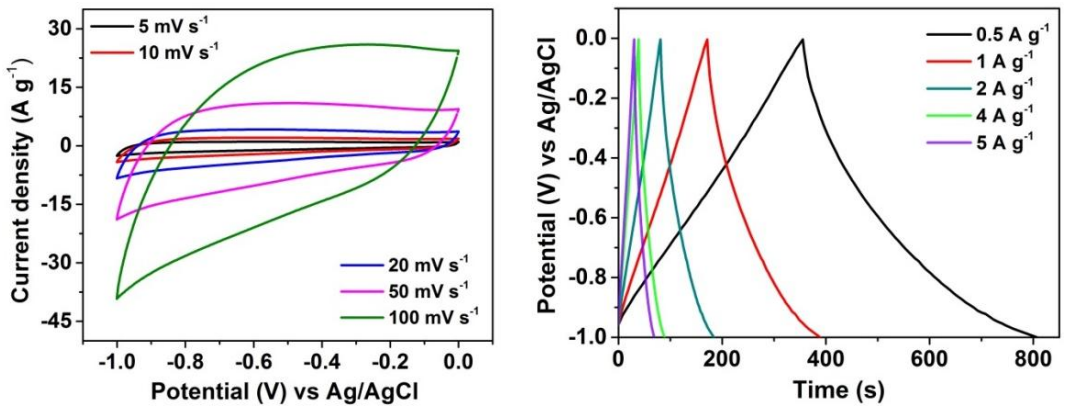


**Figure A3.4** Electrochemical performance of rGO electrodes using three-electrode system in 6 M KOH electrolyte: (a) CV curves at different scan rates from 5 to 100 mV $s^{-1}$, (b) GCD curves at different current densities from 0.5 to 5 A $g^{-1}$.

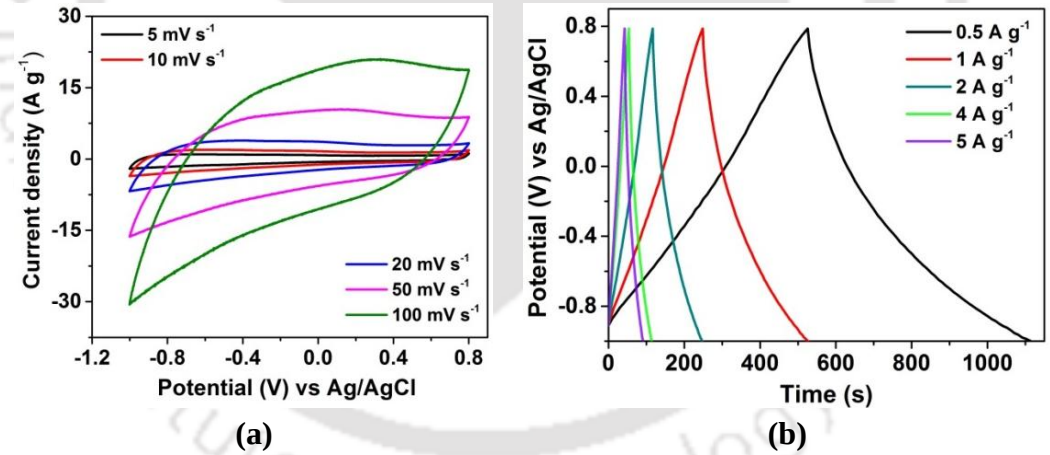


**Figure A3.5** Electrochemical performance of rGO electrodes using three-electrode system in 1 M $Li_2SO_4$ electrolyte: (a) CV curves at different scan rates from 5 to 100 mV $s^{-1}$, (b) GCD curves at different current densities from 0.5 to 5 A $g^{-1}$.

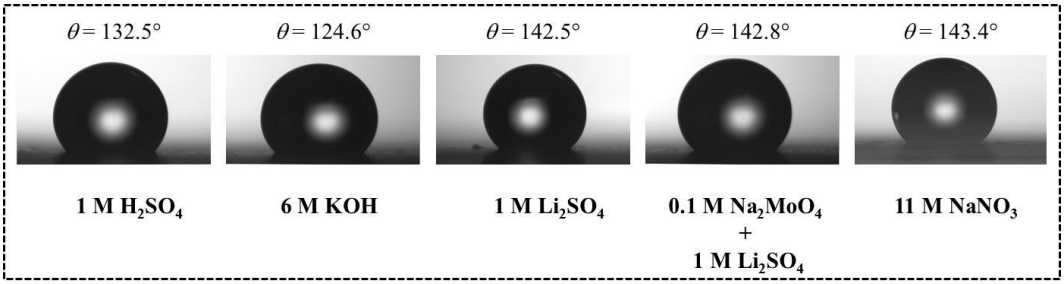


**Figure A3.6** Wettability of different electrolytes on rGO electrode surface (contact angle is denoted as $\theta$)

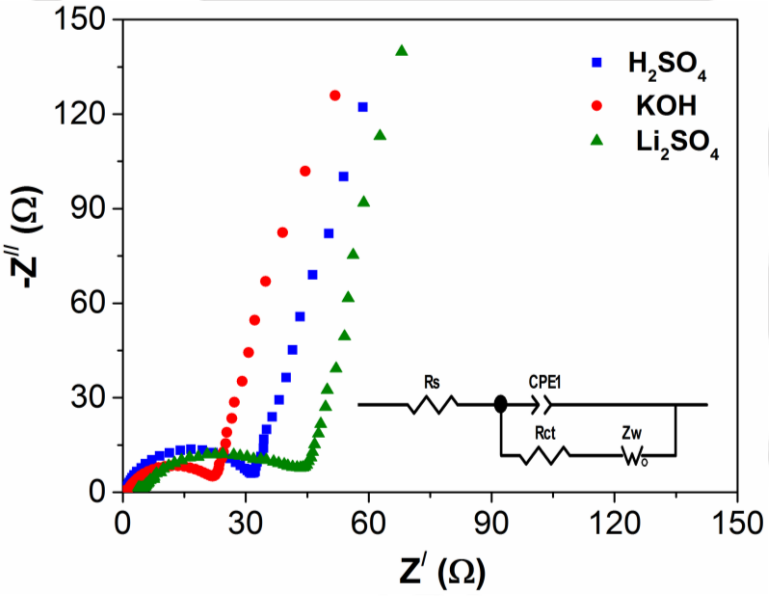


**Figure A3.7** Nyquist plot of the rGO electrodes in three aqueous electrolytes viz. 1 M $H_2SO_4$, 6 M KOH, and 1 M $Li_2SO_4$ (inset: equivalent circuit)

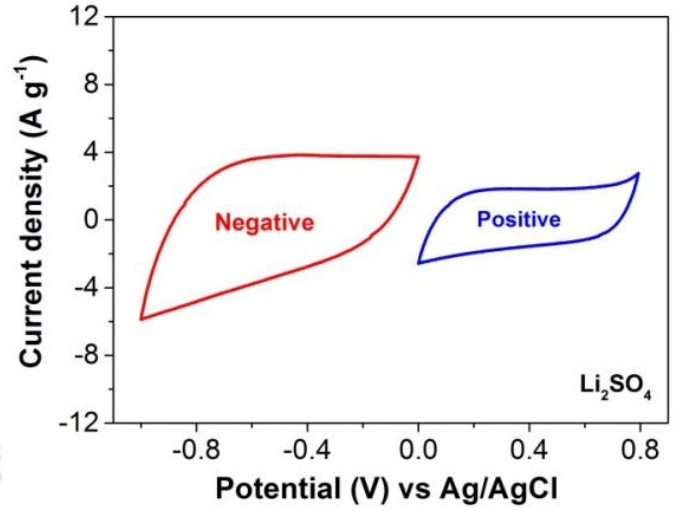


**(a)**

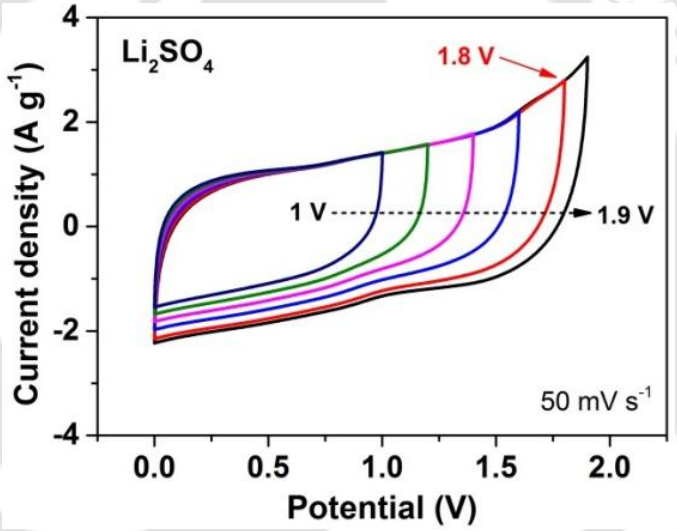


**(b)**

**Figure A3.8** (a) CV curves of rGO in separate potential windows as positive (0 to 0.8 V) and negative (–1.0 V to 0 V) electrodes at a scan rate of 20 mV $s^{-1}$ in 1 M $Li_2SO_4$ electrolyte; (b) CV curves of rGO-SC at different potential windows in 1 M $Li_2SO_4$ electrolyte.

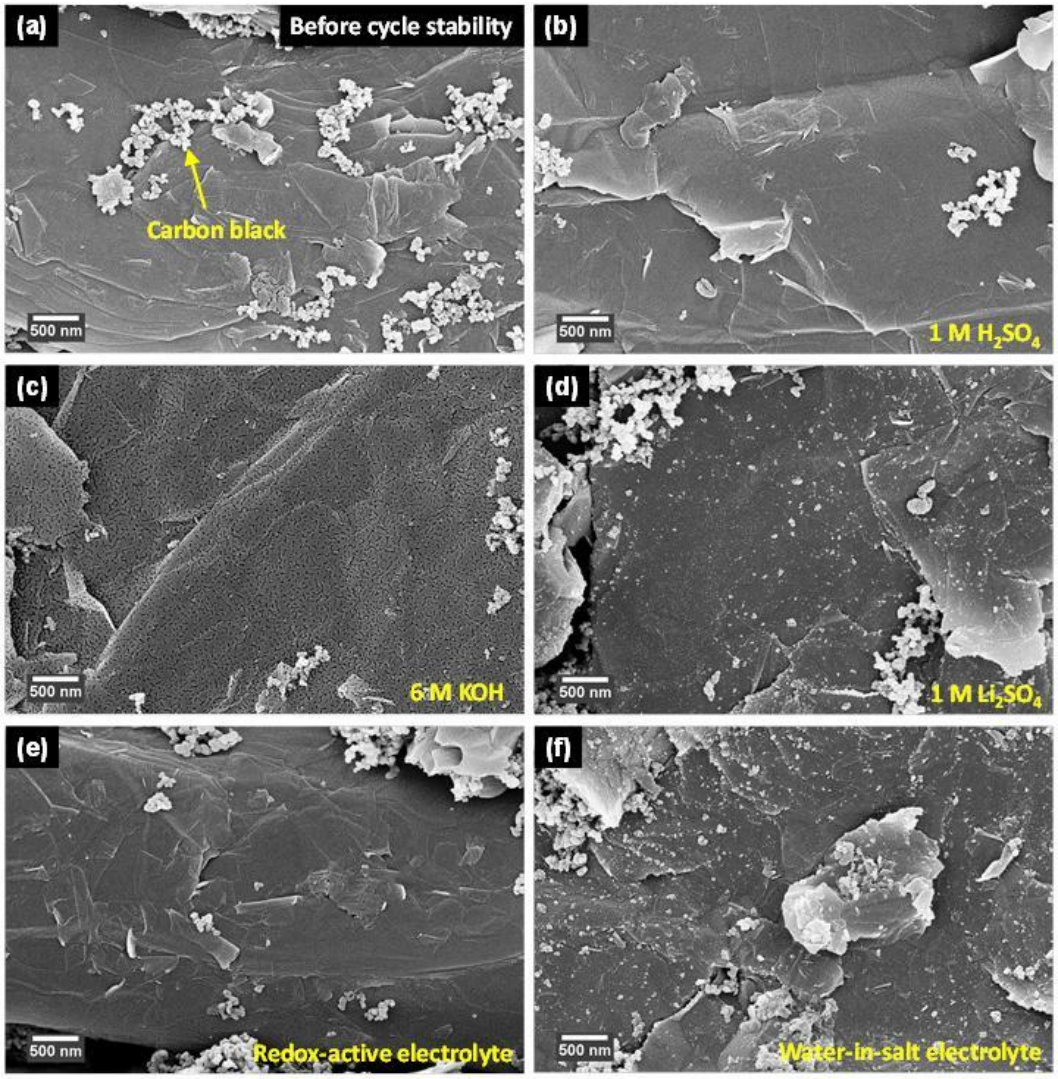


**Figure A3.9** FE-SEM images of rGO electrodes (a) before cycle stability; and after cycle stability tests in (b) $H_2SO_4$, (c) KOH, (d) $Li_2SO_4$, (e) redox-active electrolyte, and (f) water-in-salt electrolytes.

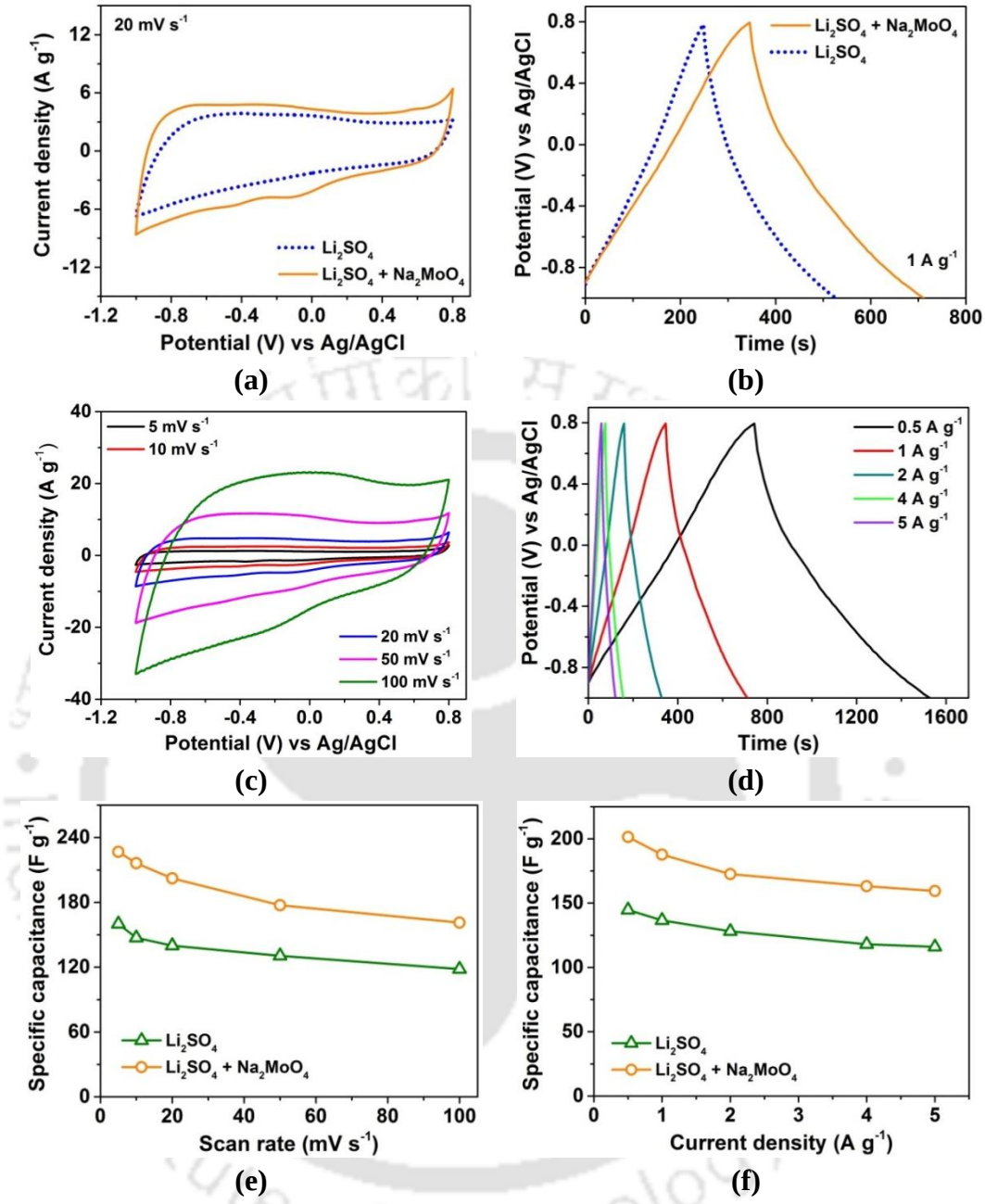


**Figure A3.10** Electrochemical performance of rGO electrodes using three-electrode system in redox-active electrolyte (1 M $Li_2SO_4$ + 0.1 M $Na_2MoO_4$): (a) comparison of CV curves in redox–active electrolyte and 1 M $Li_2SO_4$ at 20 mV $s^{-1}$; (b) comparison of GCD curves in redox electrolyte and 1 M $Li_2SO_4$ at 1 A $g^{-1}$; (c) CV curves at different scan rates from 5 to 100 mV $s^{-1}$, (d) GCD curves at different current densities from 0.5 to 5 A $g^{-1}$ (e) specific capacitance at various scan rates, (f) specific capacitance at various current densities.

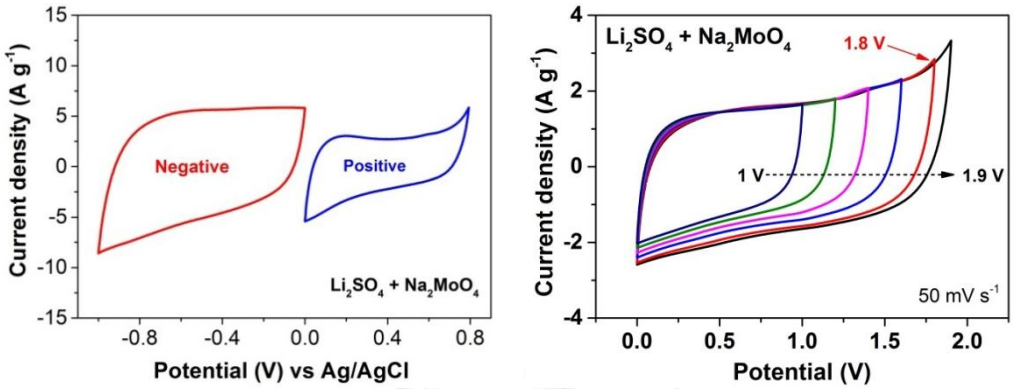


**(a)** **(b)**

**Figure A3.11** (a) CV curves of rGO in separate potential windows as positive (0 to 0.8 V) and negative (–1.0 V to 0 V) electrodes at a scan rate of 20 mV $s^{-1}$ in redox-active electrolyte; (b) CV curves of rGO-SC at different potential windows in redox-active electrolyte.

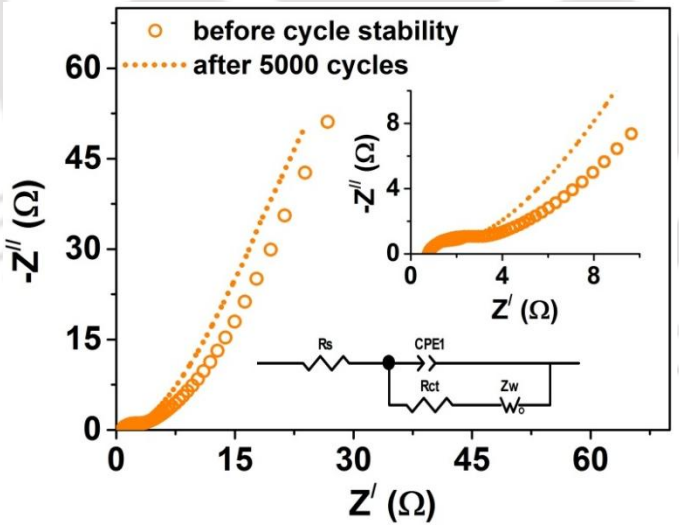


**Figure A3.12** Nyquist plots of rGO–SC in redox-active electrolyte (inset: high frequency region and equivalent circuit)

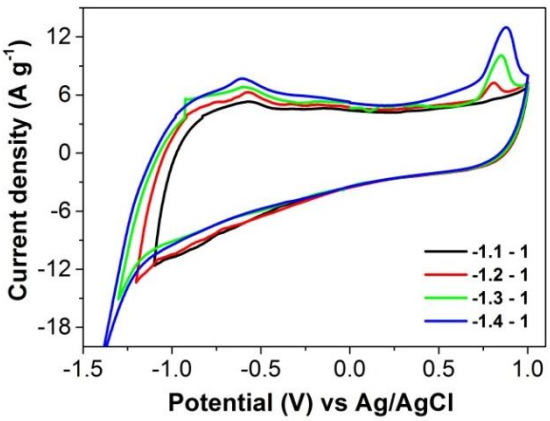


**Figure A3.13** Three-electrode CV curves of rGO electrode recorded at different potential windows in water-in-salt electrolyte (11 M $NaNO_3$).

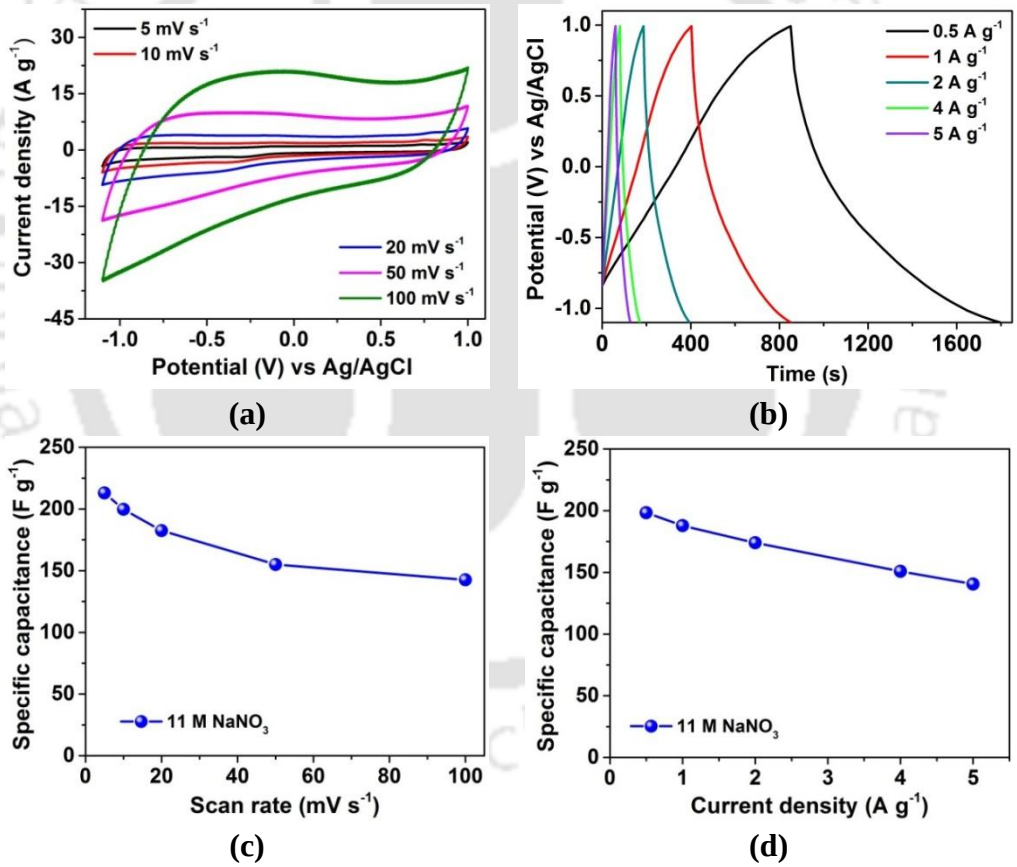


**Figure A3.14** Electrochemical performance of rGO electrodes using three-electrode system in water-in-salt electrolyte (11 M $NaNO_3$): (a) CV curves at different scan rates from 5 to 100 mV $s^{-1}$, (b) GCD curves at different current densities from 0.5 to 5 A $g^{-1}$ (c) specific capacitance at various scan rates, (d) specific capacitance at various current densities.

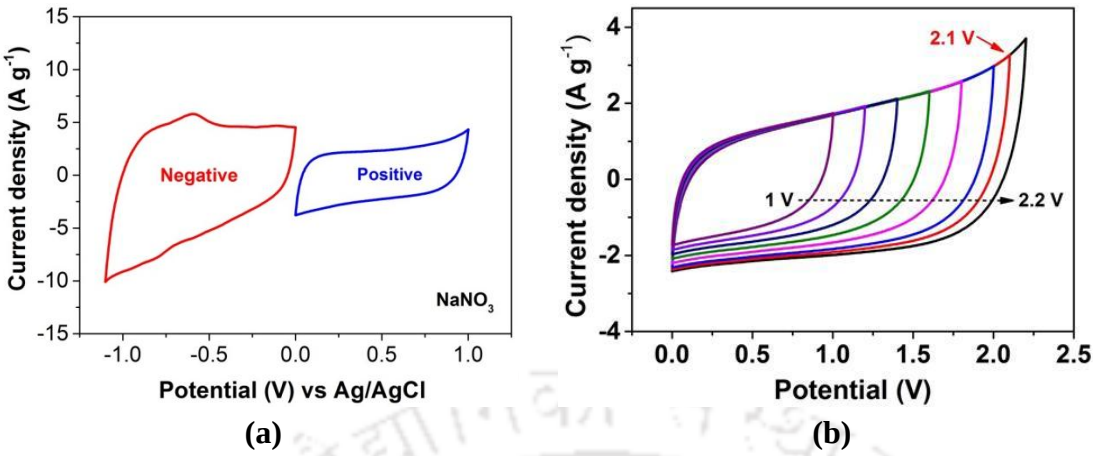


**Figure A3.15** (a) CV curves of rGO in separate potential windows as positive (0 to 1 V) and negative (–1.1 V to 0 V) electrodes at a scan rate of 20 mV $s^{-1}$ in water-in-salt electrolyte; (b) CV curves of rGO-SC at different potential windows from 1 – 2.2 V in water-in-salt electrolyte.

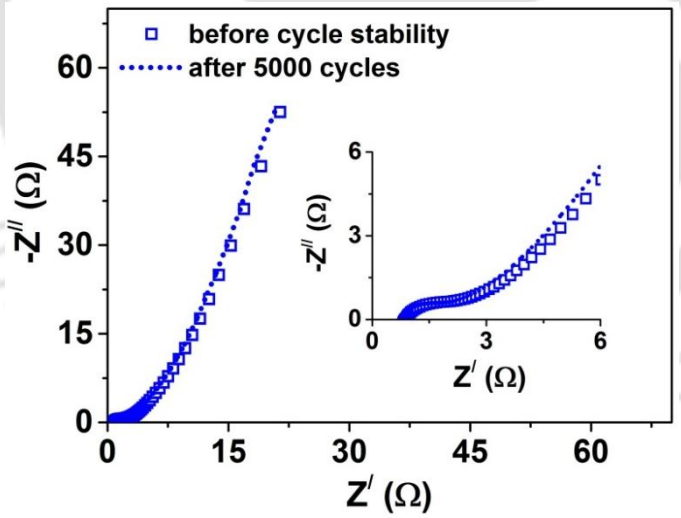


**Figure A3.16** Nyquist plots of rGO-SC in "water–in–salt" electrolyte (inset: high-frequency region)

**Table A3.1** Comparison of capacitive performance of graphene-based electrodes reported in our work with previous literature

| Material | Synthesis method | $S_{BET}$ ($m^2\ g^{-1}$) | Mass loading (mg $cm^{-2}$) | Electrolyte | Capacitance | Cycle stability | Ref. |
|---|---|---|---|---|---|---|---|
| Graphene sheets | Thermal reduction | 524 | 4 | 30 wt.% KOH in $H_2O$ | 150 F $g^{-1}$ (0.1 A $g^{-1}$) | 100% after 500 cycles | 1 |
| MW graphene | Microwave treatment | 463 | – | 5 M KOH | 191 F $g^{-1}$ (0.15 A $g^{-1}$) | | 2 |
| B-doped rGO | Reflux with (borane + THF) | 466 | ~ 2 | 6 M KOH | 200 F $g^{-1}$ (0.1 A $g^{-1}$) | 95% after 4500 cycles | 3 |
| N/P-rGO | Thermal reduction | 355 | – | 6 M KOH | 165 F $g^{-1}$ (0.1 A $g^{-1}$) | 91% after 2000 cycles | 4 |
| rGO | Flow reaction with sodium cholate | – | 1.5 | 1 M $H_3PO_4$ | 94.1 F $g^{-1}$ (0.1 A $g^{-1}$) | 103% after 10000 cycles | 5 |
| rGO | Microwave treatment with sodium cholate | – | 1 – 2 | 1 M $H_2SO_4$ | 182.5 F $g^{-1}$ (0.1 A $g^{-1}$)<br>102.3 F $g^{-1}$ (0.5 A $g^{-1}$)<br>94.1 F $g^{-1}$ (1 A $g^{-1}$) | 104.1% after 5000 cycles | 6 |
| rGO film | Hydrothermal reaction with hydrazine | 0.9067 | 2.8 | 1 M $H_2SO_4$ | 111 F $g^{-1}$ (0.5 A $g^{-1}$) | ~ 90% after 10000 cycles | 7 |
| rGO/CF film | | 184.324 | 4 | | 214 F $g^{-1}$ (0.5 A $g^{-1}$) | | |
| rGO on carbon cloth | Thermal reaction with *Ascorbic acid* | 20.3 | – | 1 M $H_2SO_4$ | 47.2 F $g^{-1}$ (1.3 A $g^{-1}$) | 68.2 after 3000 cycles | 8 |
| | *Sodium borohydride* | 21.2 | | | 87.3 F $g^{-1}$ (1.3 A $g^{-1}$) | 60.9 after 3000 cycles | |
| | *Hydrazine* | 33.6 | | | 185.7 F $g^{-1}$ (1.3 A $g^{-1}$) | 60.5 after 3000 cycles | |
| rGO on Ni foam | Magnetron sputtering | – | ~ 1 | 6 M KOH | 122 F $g^{-1}$ (1 A $g^{-1}$) | 99% after 1000 cycles | 9 |
| **rGO** | **Hydrazine reduction** | **~ 555** | **#7 – 9**<br>**$9 – 10** | **6 M KOH** | **#177.3 F $g^{-1}$ (0.5 A $g^{-1}$)**<br>**$157.4 F $g^{-1}$ (1 A $g^{-1}$)** | **99.6% after 5000 cycles** | **This work** |

$S_{BET}$ – BET specific surface area, MW – microwave, THF – tetrahydrofuran, CF - carbon fiber, Ni – nickel, # - three-electrode measurement, $ - two-electrode measurement

**References (Appendix 3)**


(1) Du, X.; Guo, P.; Song, H.; Chen, X. Graphene Nanosheets as Electrode Material for Electric Double-Layer Capacitors. *Electrochim. Acta* **2010**, *55* (16), 4812–4819.

(2) Zhu, Y.; Murali, S.; Stoller, M. D.; Velamakanni, A.; Piner, R. D.; Ruoff, R. S. Microwave Assisted Exfoliation and Reduction of Graphite Oxide for Ultracapacitors. *Carbon N. Y.* **2010**, *48* (7), 2118–2122.

(3) Han, J.; Zhang, L. L.; Lee, S.; Oh, J.; Lee, K. S.; Potts, J. R.; Ji, J.; Zhao, X.; Ruoff, R. S.; Park, S. Generation of B-Doped Graphene Nanoplatelets Using a Solution Process and Their Supercapacitor Applications. *ACS Nano* **2013**, *7* (1), 19–26.

(4) Wang, C.; Zhou, Y.; Sun, L.; Zhao, Q.; Zhang, X.; Wan, P.; Qiu, J. N/P-Codoped Thermally Reduced Graphene for High-Performance Supercapacitor Applications. *J. Phys. Chem. C* **2013**, *117* (29), 14912–14919.

(5) Lau, K. S.; Ginting, R. T.; Tan, S. T.; Chin, S. X.; Zakaria, S.; Chia, C. H. Sodium Cholate as Efficient Green Reducing Agent for Graphene Oxide via Flow Reaction for Flexible Supercapacitor Electrodes. *J. Mater. Sci. Mater. Electron.* **2019**, *30* (21), 19182–19188.

(6) Aminuddin Rosli, N. H.; Lau, K. S.; Winie, T.; Chin, S. X.; Chia, C. H. Microwave-Assisted Reduction of Graphene Oxide for an Electrochemical Supercapacitor: Structural and Capacitance Behavior. *Mater. Chem. Phys.* **2021**, *262*, 124274.

(7) Huang, Y.; Shen, C.; Tang, Z.; Shi, T.; Zheng, S.; Lin, L. Mass Loading-Independent Energy Storage with Reduced Graphene Oxide and Carbon Fiber. *ChemElectroChem* **2019**, *6* (24), 6009–6015.

(8) Guo, G.; Shen, L.; Li, X.; Cao, Y.; Sun, Y.; Xiong, Z. Tunable Reduction Degree of Stacked Lamellar RGO Film for Application in Flexible All-Solid-State Supercapacitors. *Diam. Relat. Mater.* **2020**, *106*, 107845.

(9) Du, X.; Wu, W.; An, C.; Cheng, Y.; Zhang, X.; Sun, Y.; Liu, Y. Facile Synthesis of Three-Dimensional Graphene Networks by Magnetron Sputtering for Supercapacitor Electrode. *Int. J. Energy Res.* **2016**, *40* (12), 1731–1738.

# Appendix 4

**Table A4.1** Composition analysis of the raw biomass samples

| Composition (wt %) | Water hyacinth | Sugarcane bagasse | Yellow oleander |
|---|---|---|---|
| Cellulose | 30.56±0.34 | 40.59±1.14 | 28.90±0.76 |
| Hemicellulose | 34.79±1.25 | 29.35±0.23 | 21.45±0.19 |
| Lignin | 5.65±0.63 | 19.89±0.52 | 15.76±1.29 |
| Extractives(*) | 29.0±0.87 | 10.17±1.04 | 33.89±0.71 |

**Table A4.2** Comparison of capacitive performance of PC–*x* with different carbon derived from individual biomass

| Biomass | Activating agent | $S_{BET}$ ($m^2\ g^{-1}$) | Mass loading (mg $cm^{-2}$) | Electrolyte | Capacitance | Ref. |
|---|---|---|---|---|---|---|
| Willow catkins | KOH | 1775.7 | 3 | 6 M KOH | 292 F $g^{-1}$ (1 A $g^{-1}$) | 1 |
| Rice husk | KOH | 2696 | < 2 | 6 M KOH | 147 F $g^{-1}$ (0.1 A $g^{-1}$) | 2 |
| Moringa oleifera stems | $ZnCl_2$+ $FeCl_3$ | 2250 | 4 | 6 M KOH | 283 F $g^{-1}$ (0.1 A $g^{-1}$) | 3 |
| Potato waste | $ZnCl_2$ | 1052 | ~ 1 | 2 M KOH | 255 F $g^{-1}$ (1 A $g^{-1}$) | 4 |
| Tobacco Wastes | KOH | 1297 | ~5 | 6 M KOH | 286 F $g^{-1}$ (0.5 A $g^{-1}$) | 5 |
| Sugarcane bagasse | KOH | 3151 | 3.5 | 6 M KOH | 413 F $g^{-1}$ (1 A $g^{-1}$) | 6 |
| Broad bean shells | KOH | 655 | ~5 | 1 M $H_2SO_4$ | 229 F $g^{-1}$ (0.5 A $g^{-1}$) | 7 |
| Soybean lecithin | KOH | 1803 | 5 | 1 M KOH | 285 F g−1 (0.5 A g−1) | 8 |
| Water hyacinth | KOH | 2276 | ~2 | 1 $H_2SO_4$ | 344.9 F $g^{-1}$ (0.5 A $g^{-1}$) | 9 |
| **Biomass blend** | **KOH** | **2297** | **10** | **6 M KOH** | **251.6 F $g^{-1}$ (0.2 A $g^{-1}$) 227 F $g^{-1}$ (1 A $g^{-1}$)** | **This work** |

**Table A4.3** Comparison of electrochemical performance biomass blend derived carbon with recently reported carbon materials at high electrode mass loadings

| **Materials** | **$S_{BET}$ ($m^2$ $g^{-1}$)** | **Mass loading (mg $cm^{-2}$)** | **Electrolyte** | **Capacitance** | **Ref.** |
|---|---|---|---|---|---|
| GQD embedded activated carbon | 2829 | 15 | 6 M KOH | 143 F $g^{-1}$ (1 A $g^{-1}$) | [10] |
| Lignin derived porous carbon | 803 | 14.4 | 6 M KOH | 208 F $g^{-1}$ (0.1 A $g^{-1}$) | [11] |
| Hollow carbon nanoparticles | 753.2 | 15 | 6 M KOH | 154 F $g^{-1}$ (1 A $g^{-1}$) | [12] |
| Activated carbon/CNT | 1889 | 15 | 0.5 M $Na_2SO_4$ | 50.9 F $g^{-1}$ (2 mV $s^{-1}$) | [13] |
| GQD puzzled ultra-microporous carbon | 1730 | 10 | 6 M KOH | 218 F $g^{-1}$ (0.5 A $g^{-1}$) | [14] |
| Porous graphene monoliths | 891 | 10 | EMIMBF4/AN | 186 F $g^{-1}$ (1 A $g^{-1}$) | [15] |
| Graphene with defects | 29.7 | 10 | 6 M KOH | 175 F $g^{-1}$ (1 A $g^{-1}$) | [16] |
| Cotton waste | 1550 | 10 | 6 M KOH | 161 F $g^{-1}$ (1 A $g^{-1}$) | [17] |
| **Biomass blend** | **2297** | **10** | **6 M KOH** | **251.6 F $g^{-1}$ (0.2 A $g^{-1}$)**<br>**227 F $g^{-1}$ (1 A $g^{-1}$)** | **This work** |

GQD – graphene quantum dots

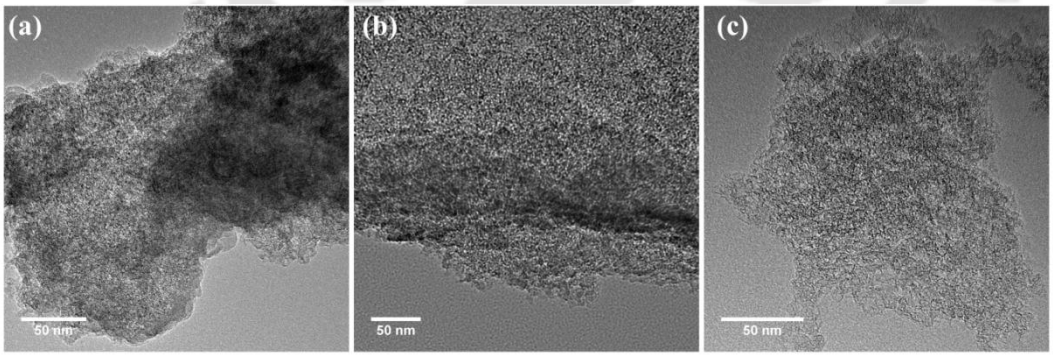


**Figure A4.1** High resolution TEM images of (a) PC-3, (b) PC-4, and (c) PC-5

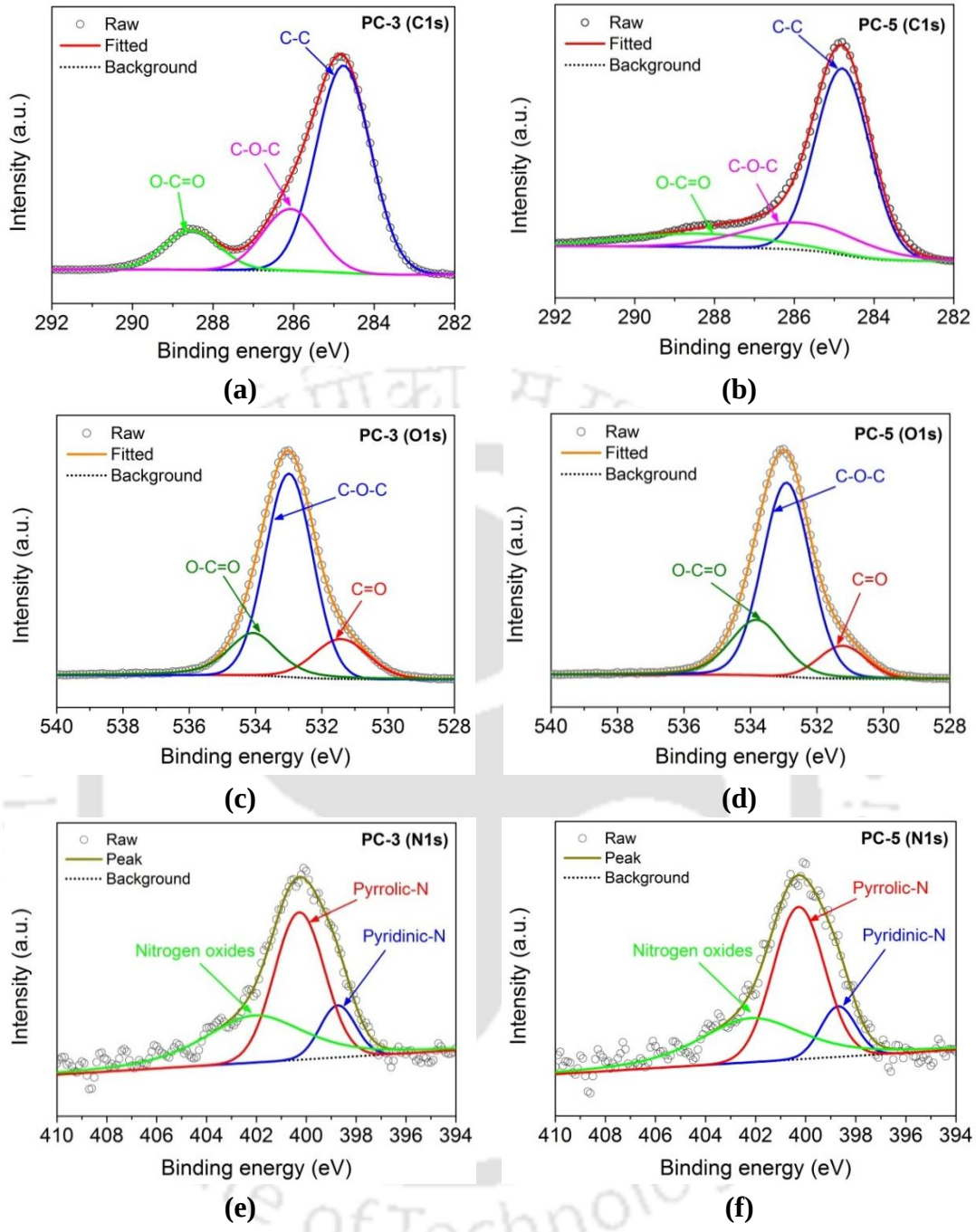


**Figure A4.2** High-resolution (a) C1s, (c) O1s, and (e) N1s spectrum of PC-3; high-resolution (b) C1s, (d) O1s, and (f) N1s spectrum of PC-5

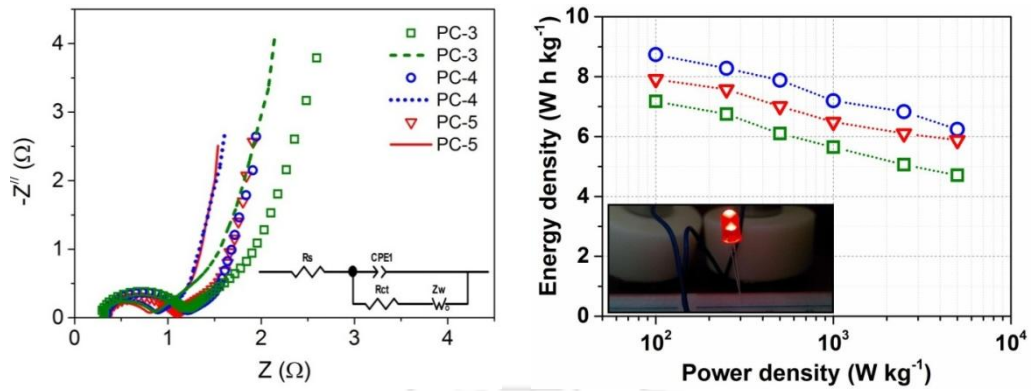


**(a)** **(b)**

**Figure A4.3** Electrochemical performance PC–*x*–SCs in 6 M KOH electrolyte: (a) Nyquist plots of PC–*x*–SCs (lines indicate EIS data after cycle stability tests and *inset*: equivalent circuit); (b) Ragone plot for PC–*x*–SCs (*inset:* a red LED powered by two symmetric PC-*x*-SC cells)

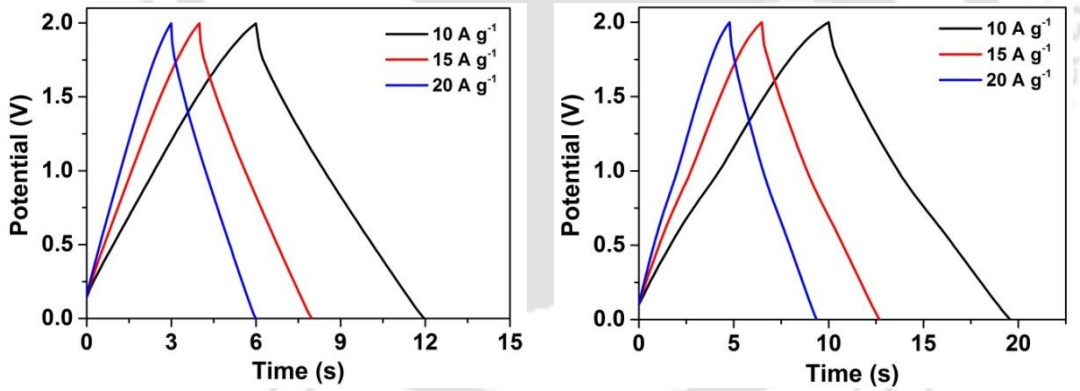


**(a)** **(b)**

**Figure A4.4** GCD curves of PC-4-SC at high current densities from 10 – 20 A $g^{-1}$ in (a) 1 M $Li_2SO_4$ and (b) redox–mediated electrolyte (0.1 $Na_2MoO_4$ + 1 M $Li_2SO_4$)

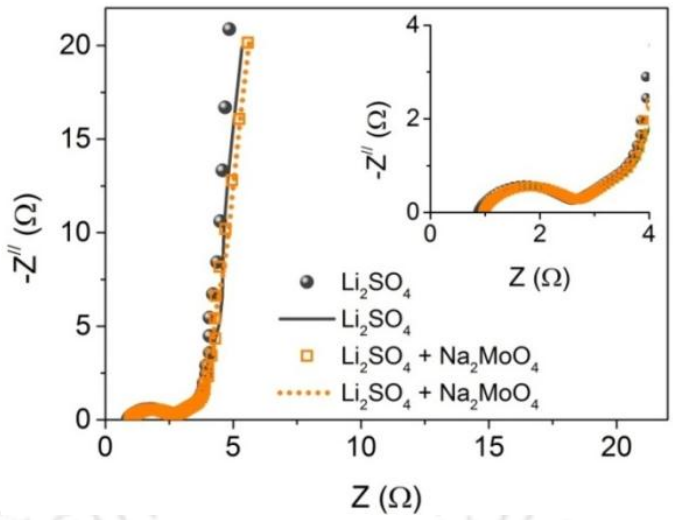


**Figure A4.5** Nyquist plots of the PC-4-SC (lines indicate EIS spectra recorded after cycle stability tests (*inset* shows the high frequency region) in 1 M $Li_2SO_4$ and redox-mediated electrolyte (0.1 $Na_2MoO_4$ + 1 M $Li_2SO_4$).

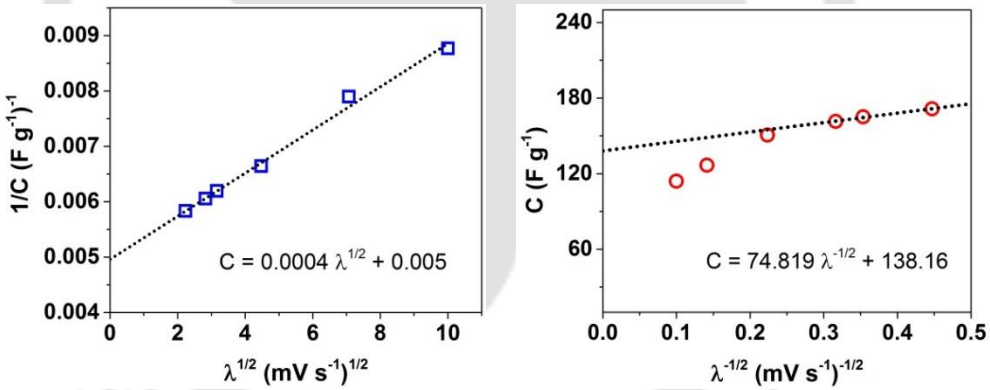


**Figure A4.6** (a) plot of reciprocal of gravimetric capacitance (1/C) vs. square root of scan rate ($\lambda^{1/2}$); (b) plot of gravimetric capacitance (C) vs. reciprocal of square root of scan rate ($\lambda^{-1/2}$). The solid lines are linear fitting lines of data points. The algebraic equations of the fitting lines are shown in the inset.

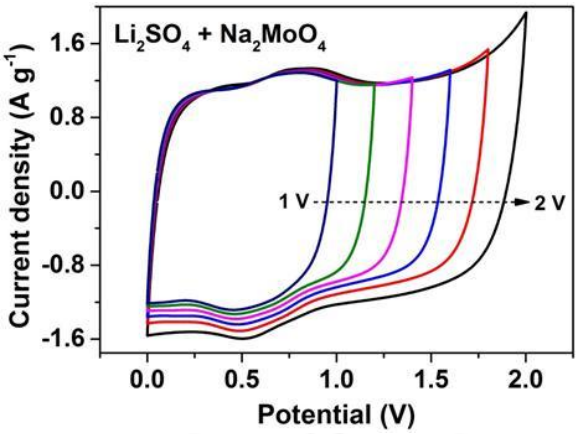


**Figure A4.7** CV curves of the PC-4-SC at different potential windows in redox-mediated electrolyte (0.1 $Na_2MoO_4$ + 1 M $Li_2SO_4$)

**References (Appendix 4)**

(1) Xie, L.; Sun, G.; Su, F.; Guo, X.; Kong, Q.; Li, X.; Huang, X.; Wan, L.; song, W.; Li, K.; Lv, C.; Chen, C.-M. Hierarchical Porous Carbon Microtubes Derived from Willow Catkins for Supercapacitor Applications. *J. Mater. Chem. A* **2016**, *4* (5), 1637–1646.

(2) Teo, E. Y. L.; Muniandy, L.; Ng, E. P.; Adam, F.; Mohamed, A. R.; Jose, R.; Chong, K. F. High Surface Area Activated Carbon from Rice Husk as a High Performance Supercapacitor Electrode. *Electrochim. Acta* **2016**, *192*, 110–119.

(3) Cai, Y.; Luo, Y.; Dong, H.; Zhao, X.; Xiao, Y.; Liang, Y.; Hu, H.; Liu, Y.; Zheng, M. Hierarchically Porous Carbon Nanosheets Derived from Moringa Oleifera Stems as Electrode Material for High-Performance Electric Double-Layer Capacitors. *J. Power Sources* **2017**, *353*, 260–269.

(4) Ma, G.; Yang, Q.; Sun, K.; Peng, H.; Ran, F.; Zhao, X.; Lei, Z. Nitrogen-Doped Porous Carbon Derived from Biomass Waste for High-Performance Supercapacitor. *Bioresour. Technol.* **2015**, *197*, 137–142.

(5) Chen, H.; Guo, Y. C.; Wang, F.; Wang, G.; Qi, P. R.; Guo, X. H.; Dai, B.; Yu, F. An Activated Carbon Derived from Tobacco Waste for Use as a Supercapacitor Electrode Material. *New Carbon Mater.* **2017**, *32* (6), 592–599.

(6) Yu, P.; Liang, Y.; Dong, H.; Hu, H.; Liu, S.; Peng, L.; Zheng, M.; Xiao, Y.; Liu, Y. Rational Synthesis of Highly Porous Carbon from Waste Bagasse for

Advanced Supercapacitor Application. *ACS Sustain. Chem. Eng.* **2018**, *6* (11), 15325–15332.

(7) Xu, G.; Han, J.; Ding, B.; Nie, P.; Pan, J.; Dou, H.; Li, H.; Zhang, X. Biomass-Derived Porous Carbon Materials with Sulfur and Nitrogen Dual-Doping for Energy Storage. *Green Chem.* **2015**, *17* (3), 1668–1674.

(8) Demir, M.; Saraswat, S. K.; Gupta, R. B. Hierarchical Nitrogen-Doped Porous Carbon Derived from Lecithin for High-Performance Supercapacitors. *RSC Adv.* **2017**, *7* (67), 42430–42442.

(9) Zheng, K.; Li, Y.; Zhu, M.; Yu, X.; Zhang, M.; Shi, L.; Cheng, J. The Porous Carbon Derived from Water Hyacinth with Well-Designed Hierarchical Structure for Supercapacitors. *J. Power Sources* **2017**, *366*, 270–277.

(10) Qing, Y.; Jiang, Y.; Lin, H.; Wang, L.; Liu, A.; Cao, Y.; Sheng, R.; Guo, Y.; Fan, C.; Zhang, S.; Jia, D.; Fan, Z. Boosting the Supercapacitor Performance of Activated Carbon by Constructing Overall Conductive Networks Using Graphene Quantum Dots. *J. Mater. Chem. A* **2019**, *7* (11), 6021–6027.

(11) Li, H.; Yuan, D.; Tang, C.; Wang, S.; Sun, J.; Li, Z.; Tang, T.; Wang, F.; Gong, H.; He, C. Lignin-Derived Interconnected Hierarchical Porous Carbon Monolith with Large Areal/Volumetric Capacitances for Supercapacitor. *Carbon N. Y.* **2016**, *100*, 151–157.

(12) Fan, C.; Dong, Y.; Liu, Y.; Zhang, L.; Wang, D.; Lin, X.; Lv, Y.; Zhang, S.; Song, H.; Jia, D. Mesopore-Dominated Hollow Carbon Nanoparticles Prepared by Simple Air Oxidation of Carbon Black for High Mass Loading Supercapacitors. *Carbon N. Y.* **2020**, *160*, 328–334.

(13) Shi, K.; Ren, M.; Zhitomirsky, I. Activated Carbon-Coated Carbon Nanotubes for Energy Storage in Supercapacitors and Capacitive Water Purification. *ACS Sustain. Chem. Eng.* **2014**, *2* (5), 1289–1298.

(14) Zhang, S.; Zhu, J.; Qing, Y.; Wang, L.; Zhao, J.; Li, J.; Tian, W.; Jia, D.; Fan, Z. Ultramicroporous Carbons Puzzled by Graphene Quantum Dots: Integrated High Gravimetric, Volumetric, and Areal Capacitances for Supercapacitors. *Adv. Funct. Mater.* **2018**, *28* (52), 1805898.

(15) Li, H.; Tao, Y.; Zheng, X.; Luo, J.; Kang, F.; Cheng, H. M.; Yang, Q. H. Ultra-Thick Graphene Bulk Supercapacitor Electrodes for Compact Energy Storage. *Energy Environ. Sci.* **2016**, *9* (10), 3135–3142.

(16) Dong, Y.; Zhang, S.; Du, X.; Hong, S.; Zhao, S.; Chen, Y.; Chen, X.; Song, H.;

Dong, Y.; Du, X.; Hong, S.; Zhao, S.; Chen, Y.; Chen, X.; Song, H.; Zhang, S. Boosting the Electrical Double-Layer Capacitance of Graphene by Self-Doped Defects through Ball-Milling. *Adv. Funct. Mater.* **2019**, *29* (24), 1901127.

(17) Vijayakumar, M.; Santhosh, R.; Adduru, J.; Rao, T. N.; Karthik, M. Activated Carbon Fibres as High Performance Supercapacitor Electrodes with Commercial Level Mass Loading. *Carbon N. Y.* **2018**, *140*, 465–476.

# RESEARCH OUTPUT

## Publications

1. **B.J. Choudhury**, K. Roy, V.S. Moholkar, Improvement of Supercapacitor Performance through Enhanced Interfacial Interactions Induced by Sonication, Industrial & Engineering Chemistry Research 2021, 60 (20), 7611–7623. (ACS, IF - 3.72)
2. **B.J. Choudhury**, V.S. Moholkar, Ultrasound-assisted facile one-pot synthesis of ternary MWCNT/$MnO_2$/rGO nanocomposite for high performance supercapacitors with commercial-level mass loadings, Ultrasonics Sonochemistry 2022, 82, 105896. (Elsevier, IF - 9.336)
3. **B.J. Choudhury**, K. Ingtipi, V.S. Moholkar, Improved energy density of reduced graphene oxide based aqueous symmetric supercapacitors in redox-active and "water-in-salt" electrolytes, Journal of Energy Storage 2022, 52, 105006. (Elsevier, IF - 8.907)
4. **B.J. Choudhury**, H. Hihu Muigai, P. Kalita, V.S. Moholkar, Biomass blend derived porous carbon for aqueous supercapacitors with commercial–level mass loadings and enhanced energy density in redox–active electrolyte, Applied Surface Science 2022, 601, 154202. (Elsevier, IF - 7.392)

## Book Chapter

1. **B.J. Choudhury**, V.S. Moholkar, Magnetite–Graphene–Based Composites and Their Potential Application as Supercapacitor Electrode Material, in Handbook of Magnetic Hybrid Nanoalloys and their Nanocomposites, Springer Nature Switzerland AG, 2022, https://doi.org/10.1007/978–3–030–34007–0_34–1

## Other Publications

1. H. Hihu Muigai[#], **B.J. Choudhury**[#], P. Kalita, V.S. Moholkar, Physico–chemical characterization and pyrolysis kinetics of Eichhornia Crassipes, Thevetia Peruviana, and Saccharum Officinarum, Fuel 2021, 289, 119949. (Elsevier, IF – 6.609). [#]*Equal contributon*
2. H.H. Muigai[#], **B.J. Choudhury**[#], P. Kalita, V.S. Moholkar, Co–pyrolysis of biomass blends: Characterization, kinetic and thermodynamic analysis, Biomass and Bioenergy 2020, 143, 105839. (Elsevier, IF – 5.061). [#]*Equal contribution*
3. N. Singh, A.H. Batghare, **B.J. Choudhury**, A. Goyal, V.S. Moholkar, Microalgae based biorefinery: Assessment of wild fresh water microalgal isolate for simultaneous biodiesel and β-carotene production, Bioresource Technology Reports 2020, 11, 100440.